

Modeling of Multi-Dimensional Flow over Heated Rods and Rod Bundle: CFD Simulation and Experimental Validation under Station Black out (SBO) Conditions

By
Mukesh Kumar
ENGG 01201204001

Bhabha Atomic Research Centre, Trombay, Mumbai

A thesis submitted to the
Board of Studies in Engineering Sciences

In partial fulfillment of requirements

for the Degree of

DOCTOR OF PHILOSOPHY

of

HOMI BHABHA NATIONAL INSTITUTE

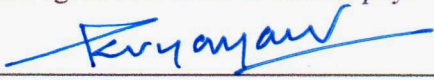
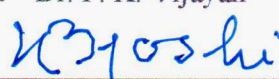
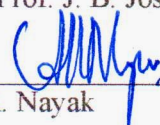
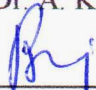
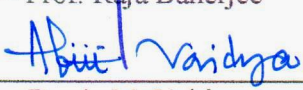
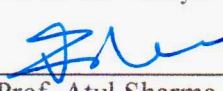


December, 2018

Homi Bhabha National Institute

Recommendations of the Viva Voce Committee

As members of the Viva Voce Committee, we certify that we have read the dissertation prepared by Mukesh Kumar entitled "Modeling of Multi-Dimensional Flow over Heated Rods and Rod Bundle: CFD Simulation and Experimental validation under Station Black Out (SBO) Conditions" and recommend that it may be accepted as fulfilling the thesis requirement for the award of Degree of Doctor of Philosophy.

	15/12/18
Chairman – Dr. P. K. Vijayan	Date:
	15/12/18
Guide / Convener – Prof. J. B. Joshi	Date:
	15/12/18
Co-guide – Dr. A. K. Nayak	Date:
	15/12/2018
Examiner – Prof. Raja Banerjee	Date:
	15/12/18
Member 1- Dr. A. M. Vaidya	Date:
	15/12/18
Member 2- Prof. Atul Sharma	Date:

Final approval and acceptance of this thesis is contingent upon the candidate's submission of the final copies of the thesis to HBNI.

I/We hereby certify that I/we have read this thesis prepared under my/our direction and recommend that it may be accepted as fulfilling the thesis requirement.

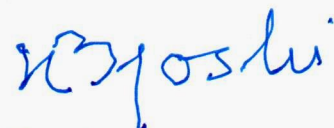
Date: 15/12/2018

Place: MUMBAI



Signature

Co-guide (if applicable)




Signature

Guide

STATEMENT BY AUTHOR

This dissertation has been submitted in partial fulfillment of requirements for an advanced degree at Homi Bhabha National Institute (HBNI) and is deposited in the Library to be made available to borrowers under rules of the HBNI.

Brief quotations from this dissertation are allowable without special permission, provided that accurate acknowledgement of source is made. Requests for permission for extended quotation from or reproduction of this manuscript in whole or in part may be granted by the Competent Authority of HBNI when in his or her judgment the proposed use of the material is in the interests of scholarship. In all other instances, however, permission must be obtained from the author.



Mukesh Kumar

DECLARATION

I, hereby declare that the investigation presented in the thesis has been carried out by me. The work is original and has not been submitted earlier as a whole or in part for a degree / diploma at this or any other Institution / University.



Mukesh Kumar

List of publications arising from the thesis

Publications in Refereed Journal:

a. Published

1. Managing a prolonged Station Blackout condition in AHWR by passive means, Mukesh Kumar, A. K. Nayak, Vikas Jain, P. K. Vijayan, K. K. Vaze, Nuclear Engineering & Technology, 2013.
2. Conceptual design of a passive moderator cooling system for a pressure tube type natural circulation boiling water cooled reactor, Mukesh Kumar, Pal E., Nayak A. K., Vijayan P. K., Nuclear Engineering and Design, 2015, 291, 261-270.
3. Experimental and CFD simulations of fluid flow and temperature distribution in a natural circulation driven Passive Moderator Cooling System of an advanced nuclear reactor, Eshita Pal, Mukesh Kumar, Arun K. Nayak, Jyeshtharaj B. Joshi, Chemical Engineering Science, Volume 155, 22 November 2016, Pages 45-64.
4. Investigations of Natural Convection and Circulation in Passive Moderator Cooling System of an Advanced Reactor in a Scaled Test Facility, Mukesh Kumar, A.K. Nayak, J.B. Joshi, Nuclear Engineering and Design 322-2017 55–67
5. Experimental Demonstration of AHWR Safety during Prolonged Station Black Out (SBO), Mukesh Kumar, P. K. Verma, A. K. Nayak and A. Rama Rao, ASME J of Nuclear Rad Sci, 2017, Paper No: NERS-17-1007; doi: 10.1115/1.4037031
6. CFD simulations of a bubble column with and without internals by using Open-FOAM, V.H. Bhusare, Mukesh Kumar, D.V. Kalaga, S. Roy, J.B. Joshi, Chemical Engineering Journal 317 (2017) 157–174
7. CFD simulation of boiling flows inside fuel rod bundle of a natural circulation based Advanced Reactor, Mukesh Kumar, Avinash Moharana, A. K. Nayak, J. B. Joshi, Nuclear Engineering and Design, Volume 338, November 2018, Pages 300-329

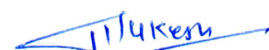
Other Publications:

a. Book/Book Chapter

1. Design of passive safety systems for advanced reactors using CFD; J.B. Joshi, A. K. Nayak, Nitin Minocha, Eshita Pal, Ankur Kumar, Mukesh Kumar, Avinash Moharana, Advances of Computational Fluid Dynamics in Nuclear Reactor Design and Safety Assessment, Woodhead Publishing, Elsevier publication.
2. CFD Model Development for Two-Phase Flows; Marco Colombo, M. Fairweather, S.P. Walker, Mukesh Kumar, Avinash Moharana, A.K. Nayak, J.B. Joshi, A. Dasgupta, D.K. Chandraker, Tanskanen Vesa, Patel Giteshkumar, Advances of Computational Fluid Dynamics in Nuclear Reactor Design and Safety Assessment, Woodhead Publishing, Elsevier publication.

b. Conference/Symposium

1. Safety analysis of AHWR for post-Fukushima type scenario, Mukesh Kumar, Kulkarni, P. P., Kamble, M. T. , Nayak, A. K. , Vijayan, P. K. , Vaze , K. K., Proceedings of the International workshop on new horizons in nuclear reactor thermal hydraulics and safety, 2014, Mumbai, India.
2. Evaluation of scaling adequacy for the Thermal-Hydraulic Test facility of Advanced Heavy Water Reactor, Mukesh Kumar, A. K. Nayak, P. K. Vijayan and K. K. Vaze, Proceedings of the Fortieth National Conference on Fluid Mechanics and Fluid Power (FMFP), December 12-14, 2013, NIT Hamirpur, Himachal Pradesh, India



Mukesh Kumar

DEDICATIONS

To my Guru, my mentor, Prof. J. B. Joshi

“I could complete my thesis work only because of his encouragement”

ACKNOWLEDGEMENTS

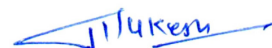
First of all, I express my sincere gratitude to my guide Prof. J. B. Joshi (Padam Bhushan), Emeritus Professor, Homi Bhabha National Institute, Mumbai and my co-guide Dr. A. K. Nayak, Head-Thermal hydraulic section, Bhabha Atomic Research Centre, Mumbai for their invaluable guidance and continuous encouragement.

Besides, I sincerely thank Doctoral Committee Chairman, Dr. P. K. Vijayan and members Dr. K. Velusamy, Prof. Atul Sharma, Dr. A. M. Vaidya, for time-to-time evaluation of the research work and useful suggestions. I pay my sincere thanks to Dr. Eshita Pal, Shri Avinash Moharana, Dr. A. Dasgupta and Dr. Vishal Bhusare for their technical supports and discussions. With pleasure, I would also like to thank Shri Vinay V. Vaze and Shri Vikas Jain for his timely support for thesis enrichments and final defense.

Besides, I would like to thank Dr H. J. Pant, BARC, and Dr. Dinesh Kalga for giving me the opportunity to work on RPT experimental setup for bubble columns. I am also thankful to my department for providing me the necessary infrastructure for carrying out the thesis work.

I wish to acknowledge my parents, for their blessings and for have always supported me in any situations.

Finally, I would also like to thank my wife and my children for their constant support and allow me to impart their time for my research work.



Mukesh Kumar

Table of Contents

Synopsis.....	vii
List of Figures.....	xxvi
List of Tables.....	xxxii
Abbreviations.....	.xxxiii
Nomenclature.....	.xxxiv

CHAPTER-1 Introduction

1.1	Background.....	2
1.2	Motivation.....	4
1.3	Objectives and methodology.....	6
1.4	Outline of Thesis.....	9

CHAPTER-2 Numerical Studies for Decay Heat Removal in AHWR

2.1	Introduction.....	12
2.2	Brief description of the Fukushima event.....	13
2.1	AHWR system description	15
2.2	Description of relevant postulated Fukushima scenarios for AHWR.....	21
2.2.1	Case-a: Prolonged SBO with no loss of GDWP water.....	21
2.2.2	Case-b: Prolonged SBO with partial loss of GDWP water:	21
2.2.3	Case-c: Prolonged SBO with complete loss of GDWP water.....	22
2.2.4	Case-d: Prolonged SBO with loss of GDWP water and dry containment.....	22
2.3	Analysis methodology	23
2.3.1	Description of system code RELAP5	24
2.3.2	Analysis for Case-a: Prolonged SBO with no loss of GDWP water	29
2.3.3	Analysis for Case-b: Prolonged SBO with partial loss of GDWP water.....	32
2.3.4	Analysis for Case-c: Prolonged SBO with complete loss of GDWP water	34
2.3.5	Analysis for Case-d: Prolonged SBO with loss of GDWP & dry containment	35
2.4	Results and discussions.....	36
2.5	Closure	42

CHAPTER-3 Post Fukushima Design Modifications: Experimental Studies

3.1	Introduction.....	45
3.2	Post Fukushima design modifications in AHWR.....	46
3.2.1	Passive Moderator Cooling System (PMCS)	47
3.2.2	Passive End-shield cooling system.....	48
3.2.3	Passive Union of V1 and V2 volume of primary containment (PAUSE)	50
3.2.4	Core catcher.....	51
3.2.5	Hydrogen mitigation system.....	52
3.2.6	Containment Filtered Venting System (CFVS).....	52
3.3	Experimental studies.....	52
3.3.1	Scaling methodology	52
3.3.2	Integrated Scaled Test Facility	56
	<i>Scaled Passive Moderator Cooling System</i>	56
	<i>Scaled Passive Endshield Cooling System</i>	57
	<i>Scaled GDWP tank with simulated Isolation condenser heaters</i>	58
3.3.3	Instrumentation for the Test Facility	58
3.3.4	Scaling adequacy and distortions	59
3.3.6	Experiments conducted.....	60
3.3.6	Experimental results	61
3.4	Closure.....	65

CHAPTER-4 Investigations of Natural Circulation and Convection in PMCS Test Facility

4.1	Introduction.....	67
4.2	PMCS: Calandria and Moderator Heat generation	67
4.3	Integral Analysis of reactor during prolonged SBO with PMCS	70
4.3.1	Performance evaluation of AHWR with PMCS during prolonged SBO	70
4.3.2	Scenarios considered	71
4.3.3	Results and discussions	73
4.4	Experimental studies.....	76
4.4.1	Facility description	76
4.4.2	Instrumentations	78

4.4.3	Experimental methodology.....	79
4.5	Experiments results.....	80
4.5.1	Obtaining the initial prototypic conditions of moderator in the Test Facility	80
4.5.2	Decay heat removal in a scaled test facility for prolonged period	83
4.6	RELAP simulation of the test performed in the scaled facility	87
4.6.1	Nodalisation Scheme	87
4.6.2	RELAP and experimental data comparison.....	88
4.7	CFD simulation of calandria vessel for steady states during the experiment.....	90
4.7.1	Governing equations.....	90
4.7.2	Turbulence model	91
4.7.3	Boundary conditions	92
	<i>Inlet</i>	92
	<i>Outlet</i>	93
	<i>Wall</i>	93
4.7.4	Methodology for analysis	94
	<i>Residual for the simulations</i>	96
4.8	CFD predictions and experimental data comparison	97
4.9	Closure.....	100

CHAPTER-5 CFD of Multi-Phase Flow

5.1	Introduction.....	103
5.2	CFD of two phase flow	104
	<i>Complexity in modeling of two phase flow</i>	106
5.3	Mathematical modeling of two phase flow.....	107
5.3.1	Homogeneous flow model.....	110
5.3.2	Drift flux model.....	111
5.3.3	Separated two fluid model.....	113
5.4	Two fluid model (Euler-Euler formulations).....	113
5.4.1	Governing equations.....	113
5.4.2	Principle of determinism and closure relations	116
5.4.3	Closure in continuity equation.....	117

5.4.4	Closure in momentum equation (Interfacial forces).....	118
	<i>Drag force</i>	119
	<i>Lift force</i>	124
	<i>Virtual mass/ Added mass force</i>	125
	<i>Turbulent dispersion force</i>	125
	<i>Wall lubrication force</i>	126
5.4.5	Closure in energy equation	127
	<i>Heat flux partitioning model</i>	128
	<i>Nucleation site density</i>	131
	<i>Bubble departure frequency</i>	132
	<i>Bubble departure diameter</i>	132
	<i>Interfacial heat transfer</i>	140
5.5	Turbulence modeling	140
	<i>k-ϵ model for two phase flow</i>	142
	<i>Reynolds Stress (R_{ij}-ϵ) Model</i>	144
	<i>Bubble induced turbulence</i>	145
5.6	Closure	146

CHAPTER-6 Studies for Adiabatic Two-Phase Flow

6.1	Introduction.....	149
6.2	Experimental studies of Bubble Column using RPT technique.....	150
6.2.1	Principle of RPT operations	152
6.2.2	Experimental setup	154
6.2.3	Experimental procedure.....	160
6.2.4	Results and discussions	161
	<i>Liquid velocity profiles</i>	161
	<i>Error and uncertainty in the experimental data</i>	163
	<i>Turbulent kinetic energy</i>	169
6.3	Bubble Column simulation using OpenFOAM	171
6.3.1	CFD code validation with literature data.....	171
	<i>Mesh generation and grid sensitivity</i>	172

	<i>Method of solution</i>	173
	<i>Boundary conditions</i>	177
	<i>Results and discussions</i>	180
6.3.2	CFD code validation with RPT data.....	185
	<i>Results and discussions</i>	186
	<i>Turbulent kinetic energy</i>	188
6.4	Closure	191

CHAPTER-7 Studies on Boiling Flows through Rod Bundle

7.1	Introduction.....	194
7.2	CFD model for boiling conditions	200
7.2.1	CFD model details	201
7.2.2	Grid generation and grid independence.....	202
7.2.3	Sub models performance study.....	204
	<i>Turbulence models</i>	204
	<i>Bubble generated turbulence</i>	207
	<i>Momentum closures</i>	210
	<i>Energy closures</i>	213
7.2.4	RELAP modeling for subcooled boiling	218
7.3	Application of the model for high pressure boiling simulation	219
7.4	CFD simulation of thermal hydraulic behavior inside rod bundle	221
7.4.1	CFD Model Setup For Boiling Flows Inside Rod bundle.....	225
7.4.2	Results and discussions	228
	<i>Case#1 (Set-1 models)</i>	228
	<i>RELAP simulation for Case#1</i>	241
	<i>Case#1 (Set 2 models)</i>	243
	<i>Case#2</i>	247
	<i>Case#3</i>	253
	<i>Case#4</i>	253
7.5	Closure	257

CHAPTER-8 Conclusions and Future Directions

8.1	Introduction.....	260
8.2	Major conclusions.....	260
8.2.1	Conclusions from study-1.....	260
	<i>Establishment of decay heat removal capability by natural circulation</i>	
	<i>mode of cooling during Fukushima type of scenario in integral manner</i>	<i>260</i>
8.2.2	Conclusions from study-2.....	261
	<i>Demonstration of grace period of the reactor for ~7 days during SBO.....</i>	<i>261</i>
8.2.3	Conclusions from study-3 and 4.....	261
	<i>Estimation of flow and void distribution inside coolant channel of AHWR</i>	
	<i>during SBO conditions of heat removal</i>	<i>261</i>
8.3	Future directions	262
	References.....	267



Homi Bhabha National Institute

SYNOPSIS OF Ph. D. THESIS

1. **Name of the Student:** Mukesh Kumar
2. **Name of the Constituent Institution:** Bhabha Atomic Research Centre, Mumbai
3. **Enrolment No. :** ENGG 01201204001
4. **Title of the Thesis:** Modeling of Multi-Dimensional Flow over Heated Rods and Rod Bundle: CFD Simulation and Experimental validation under Station Blackout (SBO) conditions

Nuclear is a clean and green option of energy and carries a huge potential for electricity generation without the harmful carbon footprints. This has attracted many countries to consider power production from nuclear energy. However, the accidents happened in past in nuclear industry have put a question mark on its safe disposition. The recent Fukushima accident had an inconceivable effect on nuclear power industry and has led to doubt the reliability of safety systems incorporated in nuclear power plants. The design criteria against natural disaster accidents are being reviewed across the globe and new criteria are being established for newly developed and existing reactors. One such criterion is the need to have longer reactor grace period without operator intervention. In this regard, passive systems demonstrate a promising option in reactor design.

BARC, India has designed an innovative reactor Advanced Heavy Water Reactor (AHWR) (Sinha and Kakodkar, 2006), which is a 920MW_{th}, pressure tube type boiling light water cooled and heavy water moderated reactor. The reactor includes many passive features in its

design. Few new systems are incorporated in reactor design after evaluating the reactor safety against Fukushima accident.

The undertaken research work incorporates establishment of safe decay heat removal capability of AHWR design for Fukushima type of accident. The objectives are achieved by making use of system code for integral behavior studies, experiments in the scaled test facility of AHWR and finally CFD simulations for multidimensional behavior of flow over heated Calandria tubes (inside Calandria Vessel) and fuel rod bundle.

Integral behavior analysis of the reactor confirms capability of reactor design to remove decay heat for more than 7 days. An integral test facility incorporating passive decay heat removal system along with post Fukushima design modification systems is designed and built. Experimental demonstration for a grace period of 7 days is established in the test facility.

Besides, it is apparent that system codes are not capable to estimate the local flow behavior at component level of the reactor system such as inside the calandria vessel and rod bundle of the core. Though, decay heat removal is ensured as predicted by the system code; still there exists a possibility of mal-distribution of flow inside big calandria vessel and local hot spot inside fuel rod bundle, which may lead to fuel failure. This may happen because of the multidimensional local circulation phenomena inside the big vessels and flow scarcity at local level inside the fuel rod cluster of the nuclear reactor. CFD simulations are carried out for estimation of the flow fields inside these components. The thesis involves CFD frame work development, its validations and simulations for the component level hydrodynamics inside the reactor componets viz calandria vessel and fuel rod bundle. CFD simulations give insights for the flow, temperature and void distributions inside the AHWR rod bundle and calandria vessel. In nutshell, the thesis deliberates estimation of AHWR design against Fukushima type of accidents by simulating the reactor systems in integral manner with system code, by

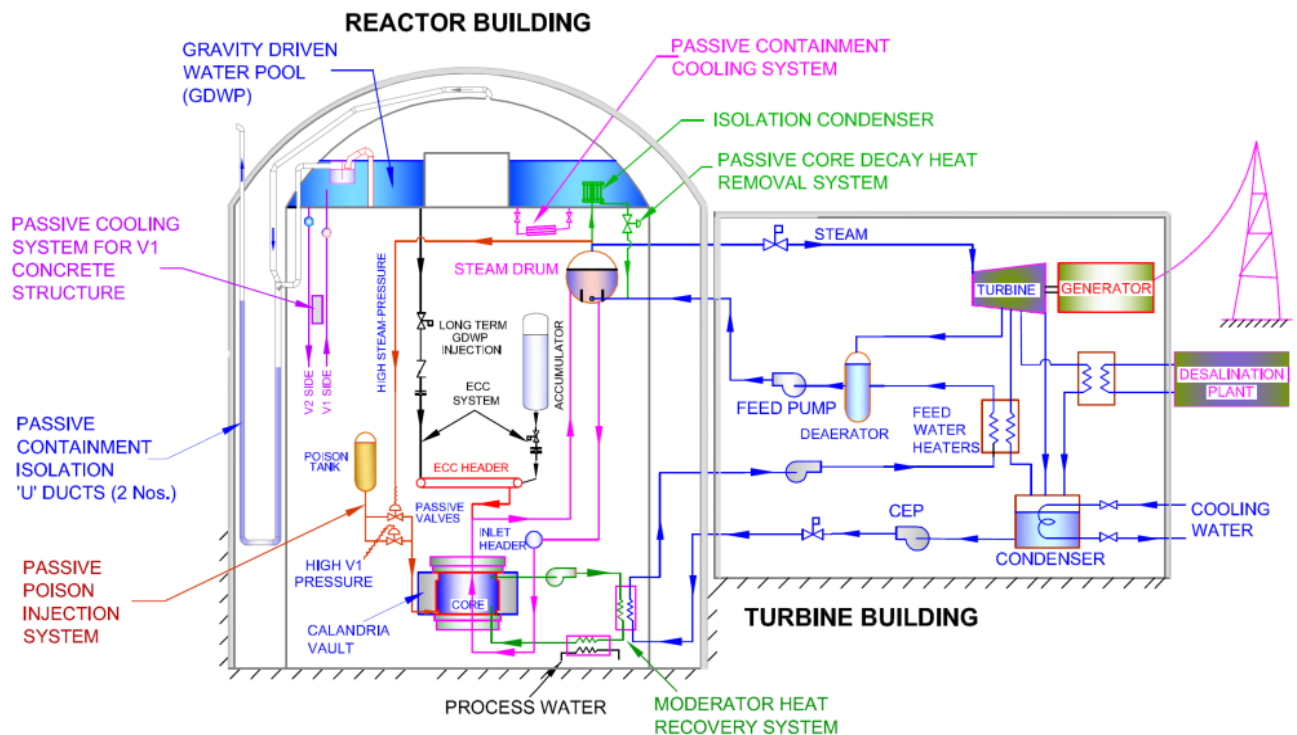
experimental demonstration in a scaled test facility of AHWR and also includes CFD simulations at component scale for calandria vessel and boiling two phase simulations for fuel rod bundle ensuring no local hot spots. An extensive literature survey on the flows inside the big vessels and over rod bundles has been carried out to mark the gray area in CMFD simulation. The research work address following scientific and technical issues:

Study-1: Establishment of decay heat removal capability by natural circulation mode of cooling during Fukushima type of scenario in integral manner.

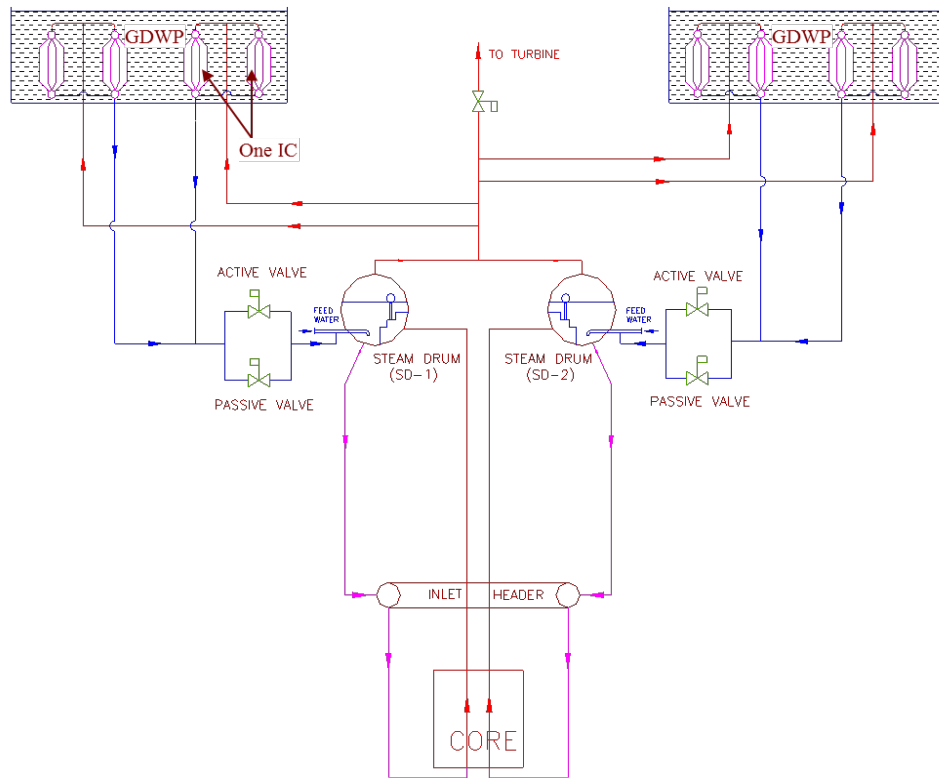
This study includes challenges as natural circulation being the mode of heat transfer, integral behavior assessment of the design, coupling of multiple natural circulation loops. AHWR is equipped with Isolation Condensers (ICs) submerged in Gravity Driven Water Pool (GDWP) to remove decay heat during Station Blackout (SBO). Figure-1 shows the general arrangement of the decay heat removal system. Numerical studies are carried out for evaluating the capability AHWR design against Fukushima type of accident in integral manner. Various systems of the reactor viz. Main Heat Transport System (MHTS), ICs, Containment and GDWP are simulated for a postulated initializing event (Fukushima type) causing prolonged SBO in the reactor. Results indicate (Figure-2) that the reactor design, after being shut down on seismic signal similar to that in Fukushima, is capable of removing decay heat by passive means using ICs by dissipating heat into the GDWP. The large pool of water i.e. GDWP ($\sim 8000 \text{ m}^3$) can absorb decay heat for more than 100 days. The steam generated by boil-off of the water in GDWP, condenses passively on the walls of containment and on tubes of Passive Containment Cooling System (PCCS) without exceeding the containment design pressure for 7 days. If venting is carried out beyond this period, the decay heat removal can be extended for more than 100 days passively.

It may be noted that while removing decay heat by ICs for prolonged period, cooling of moderator and endshield could not be maintained as these systems are cooled by pump

circulation systems. It is important to maintain the temperature of moderator and endshield within design limits (below 100°C) to ensure the reactor integrity. If the temperature and pressure of moderator and endshield is not maintained, moderator can leak out in the containment and radioactivity will be released inside the containment. To cater the issue, new passive systems viz. Passive Moderator and Endshield Cooling systems (PMCS and PECS) are incorporated in the design and integral analysis is carried out after incorporation of PMCS and PECS. Figure-3 shows the schematic of AHWR, incorporating PMCS and PECS as post Fukushima design modifications. The results indicate (Figure-4) safe decay heat removal for more than 7 days without operator intervention. It is also seen that newly incorporated passive systems PMCS and PECS is able to maintain the coolability of the moderator and Endshield. The study confirms capability of reactor design removing decay heat for a prolonged period passively while many passive systems are coupled.



(a)



(b)

Figure-1: (a) General arrangement of AHWR and (b) schematic of decay heat removal by isolation condenser

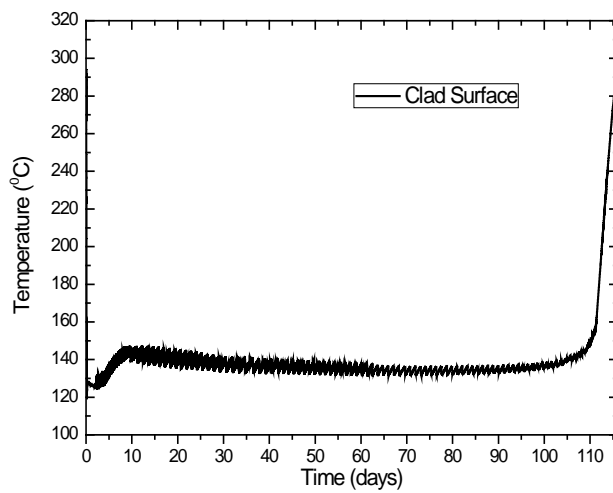


Fig 2a: Clad Surface Temperature variation during prolonged SBO

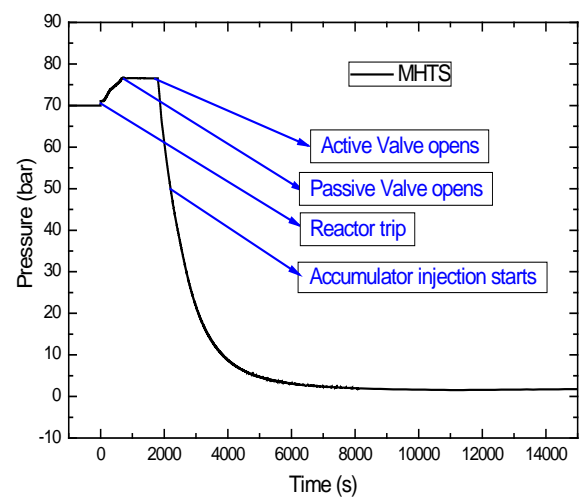
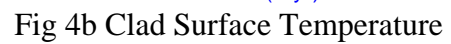


Fig 2b: MHT Pressure variation during prolonged SBO



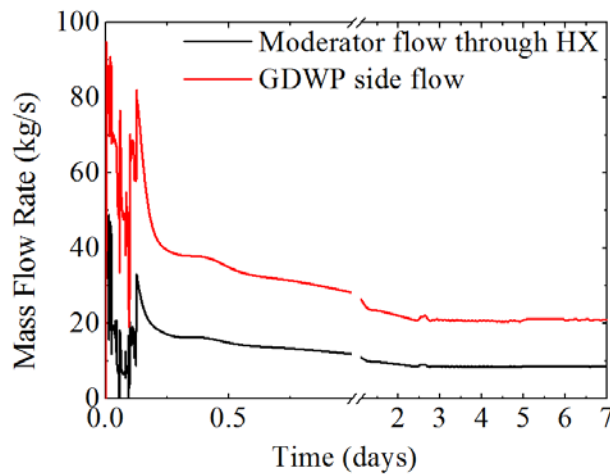


Fig 4g Mass flow rate in moderator and GDWP (Endshield)

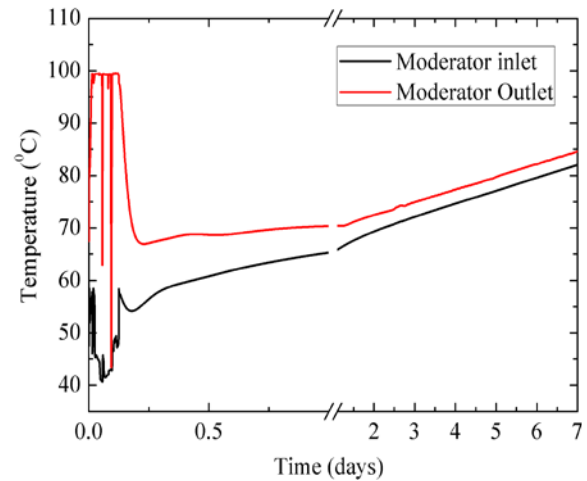


Fig 4h Temperature at inlet and outlet of moderator

Study-2: Experimental demonstration of grace period of the reactor for ~7 days during SBO after incorporation of moderator and end shield cooling systems in reactor design.

This study incorporates challenges as startup behavior of the natural circulation system, flow pattern and temperature distribution inside large calandria vessel, Identifications the hot pockets or dead zones inside the vessel, stratification inside the vessel.

In order to address Fukushima type scenario in AHWR, a scaled integral test facility comprises of Passive Moderator Cooling System (PMCS), Passive Endshield Cooling System (PECS) and GDWP tank with submerged ICs is built (Figure-5). For maintaining the geometrical and dynamic similitude in the facility for accurate predictions, Ishii scaling methodology is adopted for the design of experimental facility. Experiments are conducted for 7 days without operator intervention. Experiment shows successful decay heat removal by GDWP water for a prolonged period. Figure-6 and 7 shows the temperature variation of the moderator and GDWP water for 7 days. The temperature at calandria outlet rises to 60°C after 1 day and reaches to 70°C in 7 days. While GDWP water temperature reaches to 60°C in 7 days. RELAP5 simulations are also carried out for 7 days experiment.

CFD simulations for flow over heated calandria tubes for multidimensional flow distribution inside calandria vessel: To study the multidimensional flow behavior inside the

calandria vessel, experiments are carried out with Passive Moderator Cooling System test facility (PMCSTF) and simulated Isolation Condenser heaters.

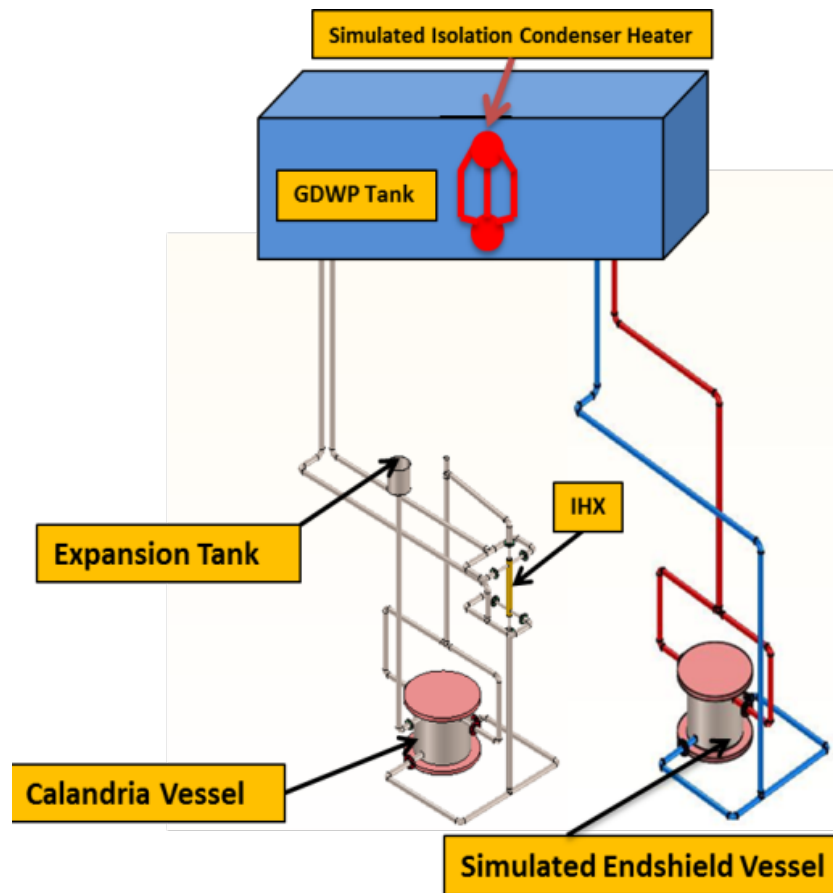


Figure-5 Post Fukushima Test facility of AHWR

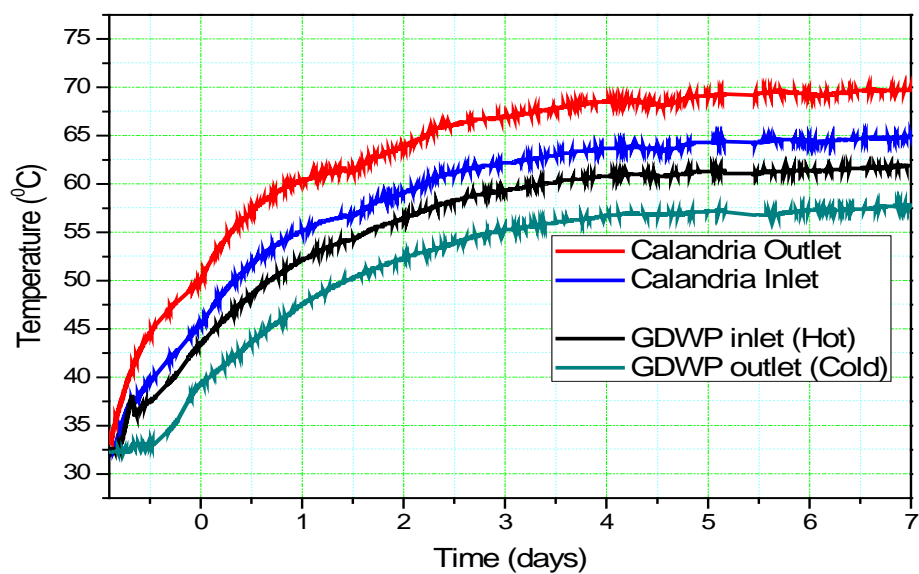


Figure-6 Fluid Temperature Variation at Calandria Inlet/Outlet and GDWP Inlet/Outlet

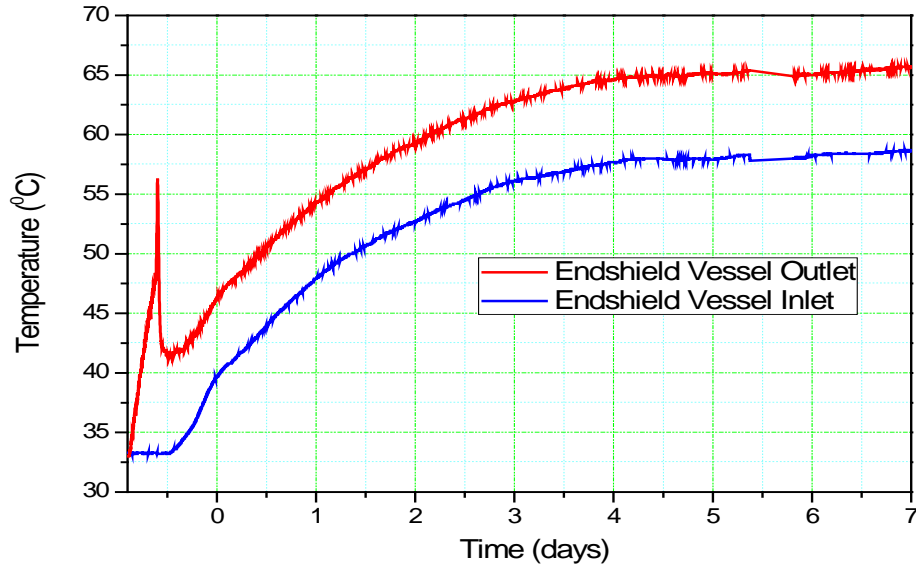


Figure-7 Fluid Temperature Variation at Endshield Vessel Inlet and Outlet

CFD simulations are carried out for the steady state condition of mass in and out to the calandria vessel. Only calandria vessel is simulated with CFD (Open FOAM 2.3.1) to study the multidimensional behaviour inside it. The steady state temperature distribution inside the calandria vessel is obtained from CFD and results are compared with the steady state experimental data of the temperature distribution inside calandria vessel at two time instances during the experiment. Figure 8 shows the fluid temperature distribution as predicted by CFD and compared with experimental data for case#1 (fluid inlet temperature 54°C at time $t=0$ day; A range of temperature from 54.5°C to 63.5°C is observed in both CFD predictions as well as during the experiment for case#1. With almost same average temperature of $\sim 58.5^{\circ}\text{C}$ in CFD and also in experiment for case#1, the temperature contours are identical (qualitatively) with minor difference.

Study-3: Developing understanding of the two phase flow and CFD model for simulation.

This study includes challenges in terms of presence of the multiple phases with vast difference in the physical properties, interphase forces estimation and their implementation in modeling along with turbulence for two phase flows. For studying the multidimensional two

phase behavior inside the fuel rod bundle of AHWR during decay heat removal, a systematic approach is followed. The approach charts the following steps:

1. Development of two fluid model for simulation of adiabatic two phase system (bubble column) using Open FOAM 2.3.1 platform.
2. Validation of the developed CFD model with experimental data available in literature.
3. Experiments for flow distribution inside the bubble column using Radioactive Particle Technique (RPT).
4. Validation of the CFD model with experimental data obtained from RPT

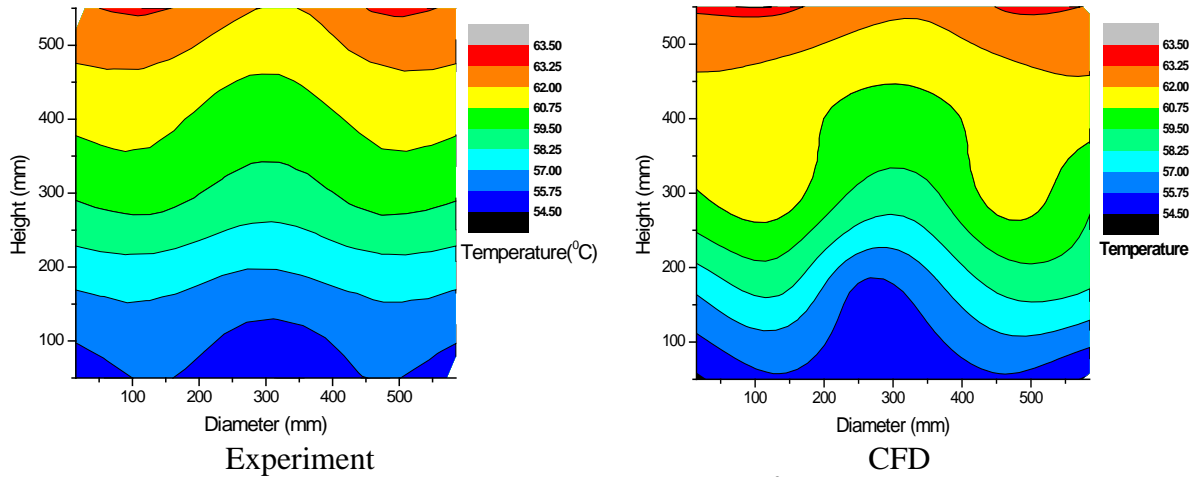


Figure-8 Temperature Distribution at outlet plane @ 54°C inlet temperature (0 day instance)

Development of CFD model for adiabatic two phase flow and its validation: CFD model for adiabatic simulations inside the bubble column is developed on the Open FOAM platform. The model is validated with experimental data (Hill's 1974) available in the literature. To model the bubble column of Hills (1974), open source code Open FOAM-2.3.1 is used. Grid sensitivity study is carried out for the Hill's bubble column using grid size of 200K, 240K, 280K, and 320K. Euler-Euler Model is used for CFD simulations. Figure-9 shows the typical axial liquid velocity profile and the gas holdup profile at $H/D=4.34$ for 64 mm/s superficial gas velocity. Results are found to be in good agreement with the experimental data. Individual phase mass balance is also established throughout the bubble column. It is evident

from the results that the solver developed in Open FOAM platform is able to capture two phase phenomena inside the bubble column and predict the hold up and liquid velocities well within a close range. Beside this, the model is also validated against the experimental data generated with RPT inside the bubble column with and without internals.

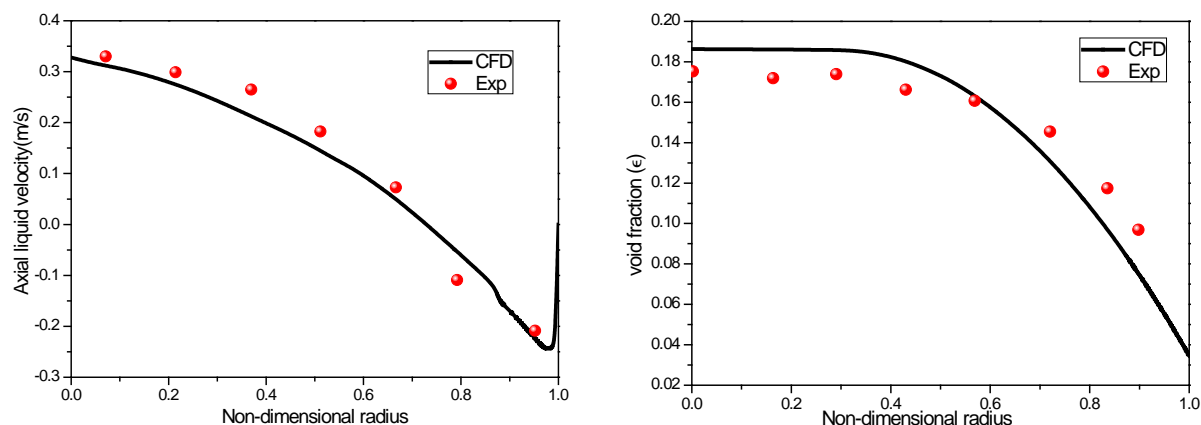


Figure-9 Axial liquid velocity and void distribution as predicted by CFD and compared with experimental data

Experimental and numerical studies of bubble column using RPT:

Experimental studies are carried out in a bubble column of 120mm ID and 1.2 m bubble column with and without internals. RPT method is used for measuring the liquid velocity profiles and turbulent quantities inside the batch bubble column. Figure-10 shows the photograph of the experimental setup used for generating data for liquid velocity and turbulence quantities inside the bubble column.



Figure-10 Photograph of the experimental setup

Two different configurations are chosen for this study (i) without internals and (ii) vertical central rod of 36 mm diameter as an internal. Air volumetric flow rate is varied between from 10 LPM to 150 LPM which corresponds to the range of air superficial velocity from 14 mm/s to 221 mm/s for two percentages of covered cross-sectional area: 0 % (no internals, configuration-A) and 9 % (configuration-B). The experiments are performed in two steps: (i) calibration and (ii) actual experiment. Prior to performing the experiment, the calibration is done. During the RPT experiment, the tracer particle is introduced to move freely inside the vessel. Neutrally buoyant tracer particle is made with small scandium particle embedded in a polypropylene sphere of outer diameter 1.2 mm, along with an air gap. Such a spherical particle having negligibly small terminal velocity in water remains suspended wherever it is left in the column of water. Twelve (2" × 2") NaI scintillation detectors are placed around the bubble column to continuously monitor the γ -rays emitted by the tracer particle. A distance-count relationship is established by calibration of all detectors, which is performed by keeping the particle at several known locations. Once distance-count relationship from the calibration step is obtained, the tracer particle is allowed to freely move in the bubble column. Its position is monitored by the array of detectors for the duration of 15 hrs. The time differencing of the instantaneous positions yields instantaneous velocities and the corresponding ensemble average gives the mean velocities. Further, turbulent quantities are evaluated from the instantaneous data of tracer particle fluctuations. Figures 11 and 12 show time and planer averaged two-dimensional velocity vector plots for the liquid recirculation patterns in a bubble column for configuration-A and B, at superficial gas velocities ranging from 14 to 221 mm/s. The length of the arrow shows the magnitude of the liquid velocity and the orientation shows the direction of liquid flow. CFD simulations are also carried out for the bubble column with and without internal and the CFD model developed for two phase flow is validated against the experimental data generated in RPT experiments.

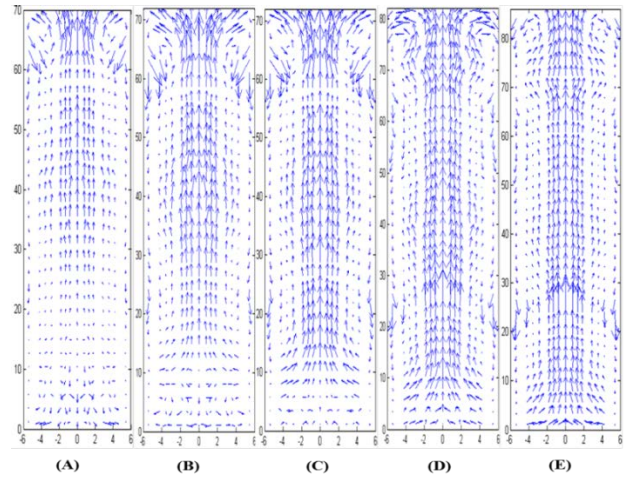
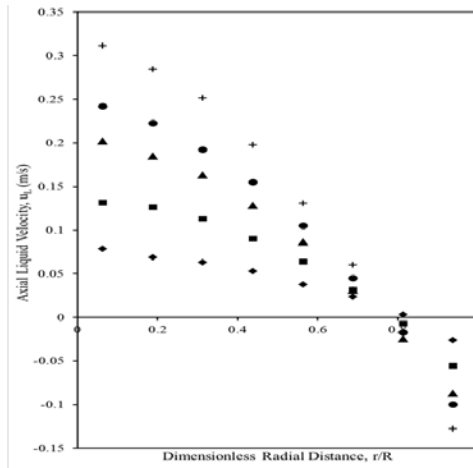


Figure-11 Effect of superficial gas velocity on overall flow patterns for Configuration-A:
(A) 0.014 m/s (♦) (B) 0.044 m/s (■) (C) 0.088 m/s (▲) (D) 0.132 m/s (●) (E) 0.221 m/s (+)

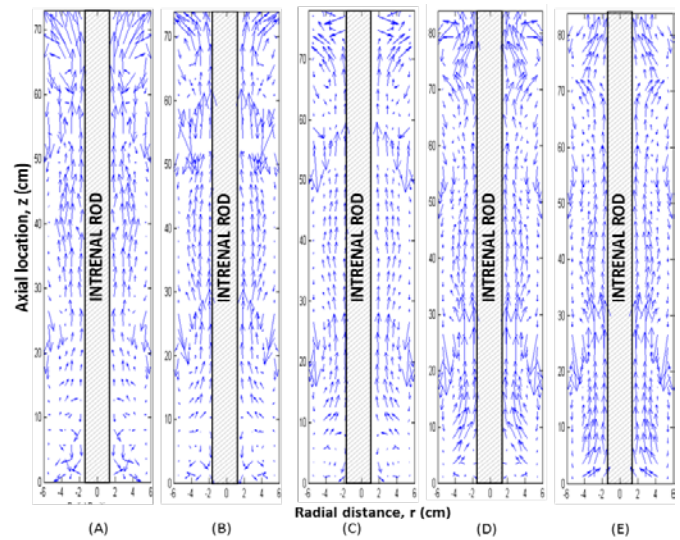
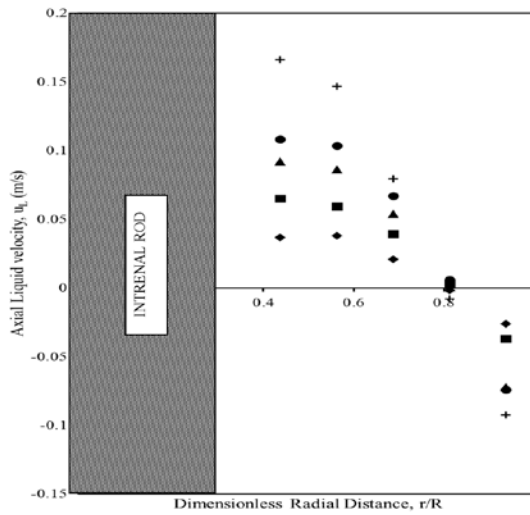


Figure-12 Effect of superficial gas velocity on overall flow patterns for Configuration-B:
(A) 0.014 m/s (♦) (B) 0.044 m/s (■) (C) 0.088 m/s (▲) (D) 0.132 m/s (●) (E) 0.221 m/s (+)

Study-4: Estimation of flow and void distribution inside coolant channel of AHWR during SBO conditions of heat removal

This study includes challenges as modeling of multidimensional two phase boiling flow, subcooled boiling heat transfer, uneven flow area with shading effect inside pressure tube.

While removing decay heat by passive means, it is important to ensure that no hot spot should occur inside fuel rod bundle of the reactor, which may lead to fuel failure. Detailed CFD simulations for multidimensional boiling flow over fuel rod cluster (heated rod bundle)

of AHWR channel is carried out to understand the flow behavior inside the complex geometry of the rod bundle. The simulations are carried out for void and flow distribution inside the rod bundle for four instances during decay heat removal. The maximum decay heat is 6% during the initial stage of the shut down and it reduces to ~2% in 1 hrs. Following a SBO, hot stand by conditions of the reactor is maintained at 7.6 MPa for 30 minutes using hot shut down passive valve. During this period the flow through the core remained about 650kg/s (Figure-13), while decay heat is removed by isolation condenser submerged in GDWP. Figure-13 shows the pressure of the MHTS during depressurization phase. Four instances during the depressurization phase are selected for estimations of the detailed flow patterns inside rod bundle for checking the presence of hot spots. 1/6th sector of the rod bundle with full height of 3.5m is simulated.

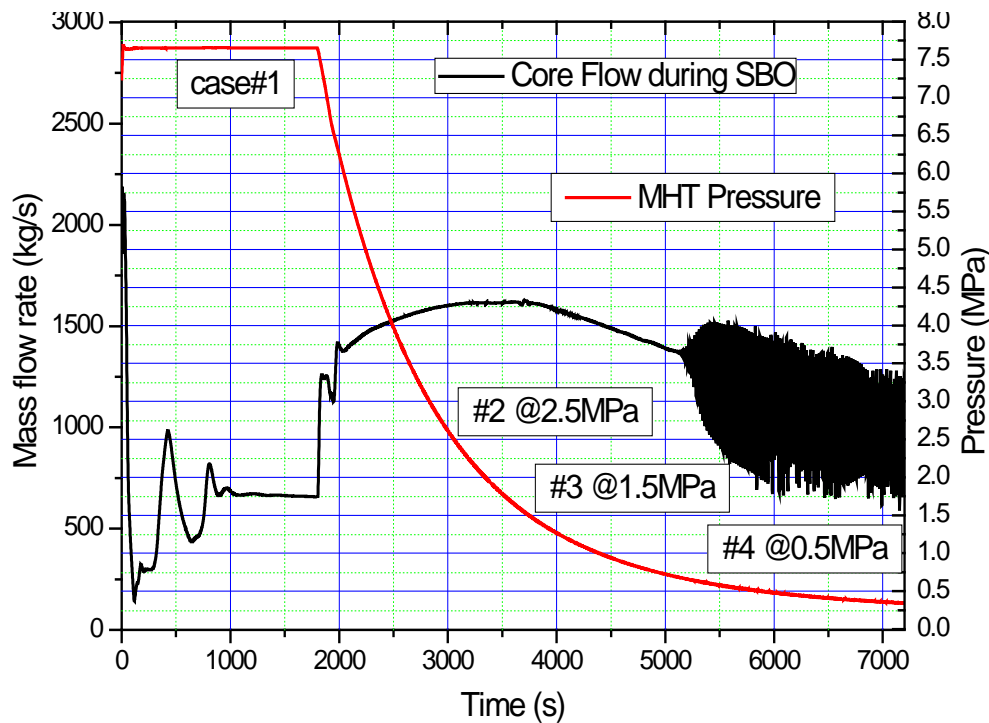


Figure-13 Core flow and MHTS pressure during SBO

It contains 9 full fuel rods of the AHWR 54 fuel pin rod bundle. Figure-14 show the details of the AHWR channel, 1/6th sector of the AHWR rod bundle and mesh generated in top plane. Grid independence study is carried out with 3.2 million, 3.5 million and 3.6 million

cells and the area average void fraction at the channel out is compared. A variation of less than 1% is observed from one grid to another, besides a wall Y plus value of 20 is observed in each case. The CFD model is validated against the experimental data of Bartilomej (1982) before its application to rod bundle. Case#1 resembles a case with two phase flow conditions while other cases fall in a region of single phase flow.

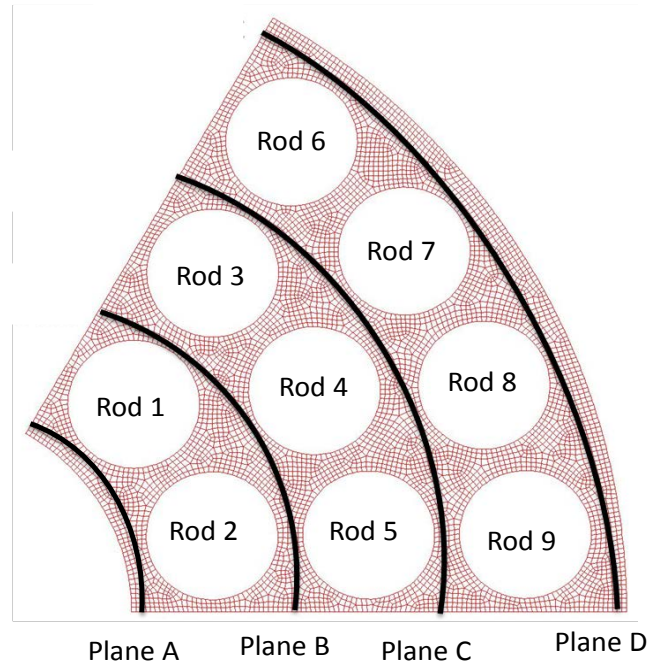


Figure-14 Mesh and Radial planes on which results are presented

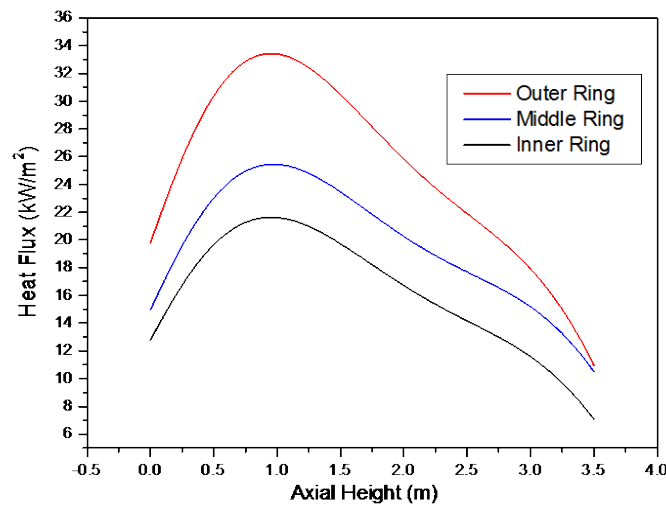


Figure-15 Heat Flux boundary condition as applied to the fuel rods (for Case#1)

Figure-15 shows the heat flux boundary conditions as applied for case#1 and case#4. Typical results for case#1 are presented here. The area average void at the outlet is observed to be ~22% and a flow quality of 4% is seen at the outlet. Maximum void is found to be 0.71, at an axial location ~2.5m from inlet on the outer ring rods, due to a bottom peaking profile of heat flux. Void and temperature distribution at various radial planes (Plane A, B, C and D shown in figure 14) is presented in figure-16. It is observed from temperature contours and 2D angular plots that the fluid temperature rises at angles corresponding to 17.5° and 45° for radial plane-A, 12.5° , 30° and 47.5° for radial plane-B, 10° , 30° and 50° for plane-C and 7.5° , 22.5° , 37.5° and 52.5° for radial plane D as seen in figure-16. It happens due to the presence of fuel rods at these angular locations. This trend continues up to an axial location of ~1.25 m from inlet. After that a phase shift of 180° is observed. This may be attributed to high heat transfer in sub-cooled boiling and void formation after 1.25 m in the vicinity of fuel rods. However, rise in the fluid temperature is observed slightly away from the wall where a reduction in the void is seen. It shows that bubble, after condensing in the bulk of the liquid, transfers its energy to the bulk fluid and raises the temperature of the fluid. Maximum temperature is observed to be saturated temperature and it is observed that boiling started at a height of 0.5 m from inlet. However, area averaged fluid temperature remains sub-cooled till the outlet. Increase in voiding and liquid temperature is observed in the outer sub-channel due to high heat addition in this sub-channel. A high enthalpy zone is observed between the fuel rods 3 & 7 and 5 & 8. However, no hot spot is observed in this case.

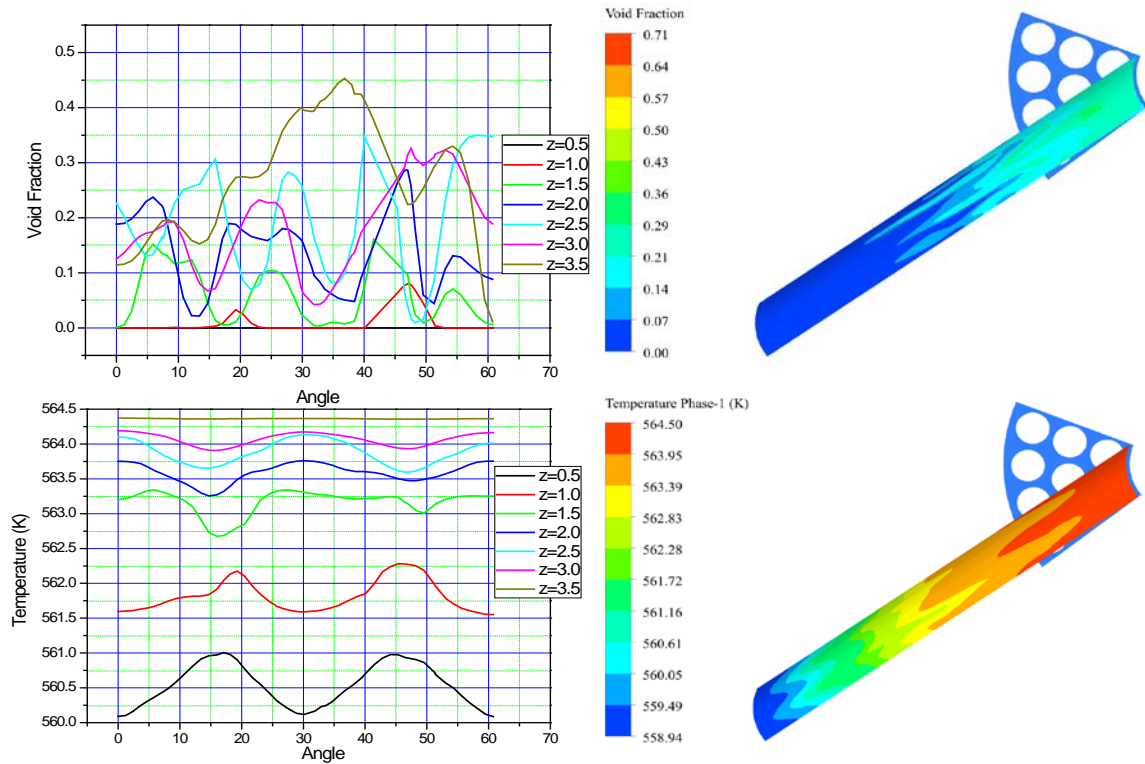


Figure-16a Void and temperature distribution @ radial plane A from inlet to outlet

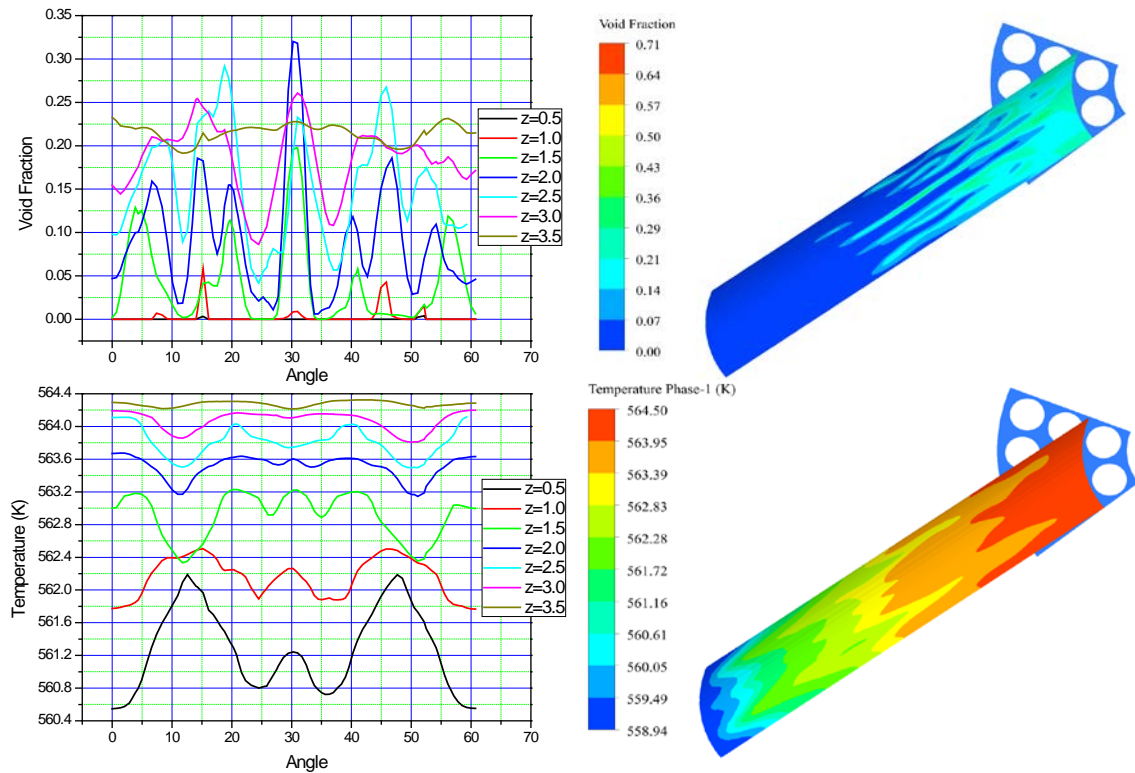


Figure-16b Void and temperature distribution @ radial plane B from inlet to outlet

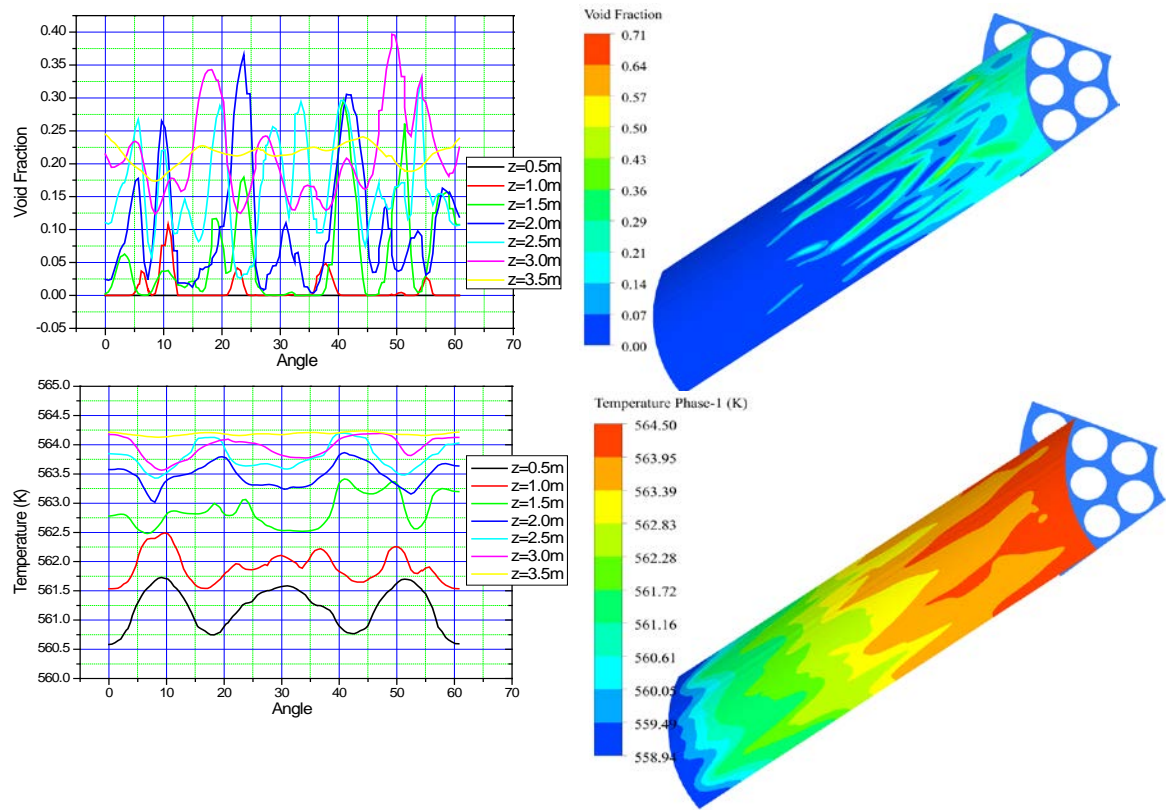


Figure-16c Void and temperature distribution @ radial plane C from inlet to outlet

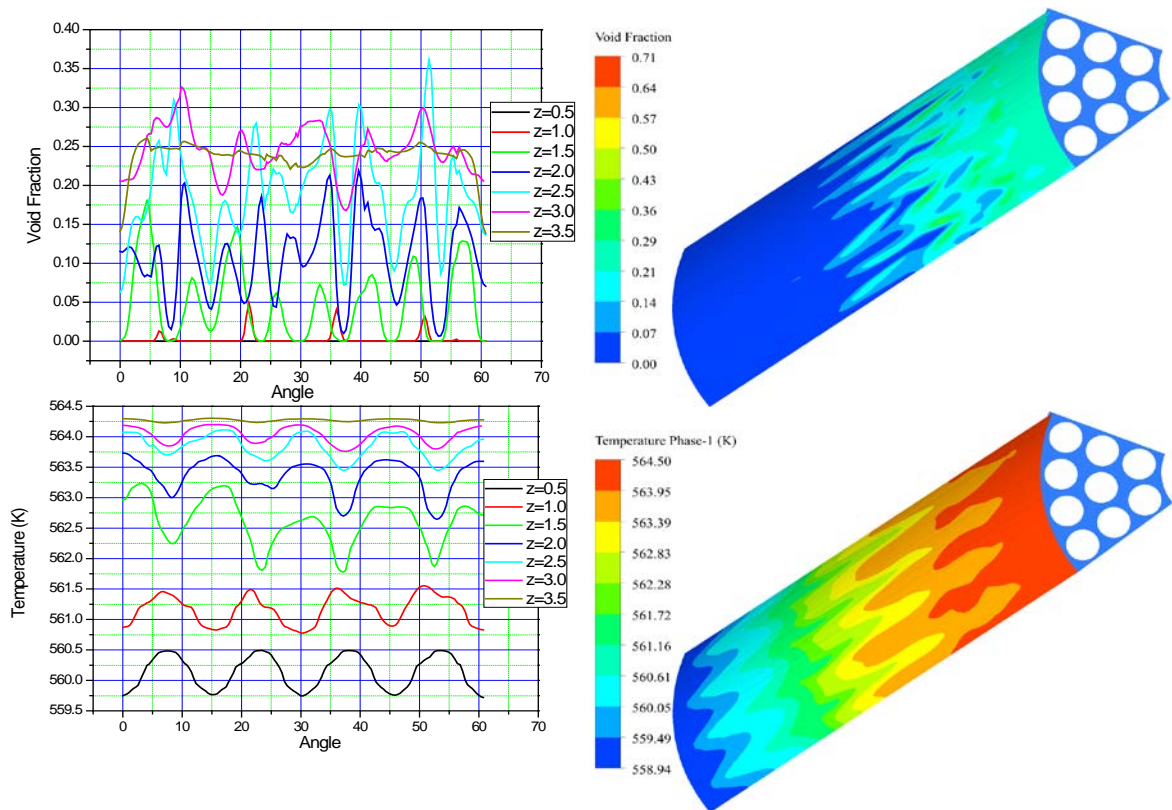


Figure-16d Void and temperature distribution @ radial plane D from inlet to outlet

Figure-16 Radial void and temperature distribution from inlet to outlet for case#1

The research work aimed understanding of the AHWR behavior during decay heat removal in view of Fukushima accident. The work was divided in two parts viz studies of the flow over heated calandria rods (outside the pressure tube) and inside the heated rod bundle. Both experimental as well as numerical studies were carried out for aforementioned two cases. The natural circulation behavior inside the calandria vessel was studied experimentally as well as numerically. It was concluded that reactor is capable of removing decay heat for more than 7 days without any safety implications. However, few new systems were incorporated in the reactor design as a part of post Fukushima design modifications as suggested after these studies.

Seven days grace period during a prolonged SBO was demonstrated in an experimental facility simulating important systems of AHWR. Besides, it was shown that there are no hot pockets in the calandria vessel during decay heat removal by natural circulation. A boiling Eulerian model is developed for estimation of the flow and void behavior inside the AHWR rod bundle during decay heat removal. The model so developed is used to predict the flow behavior at 4 steady state instances during decay heat removal. The area averaged prediction of the model is also compared with the results of the RELAP5 predictions. The results of the two numerical models are found to be in good agreement.

The results indicate that there is no hot spot formulation inside the rod bundle. The research work includes study of the reactor design in experimental test facility, CFD modeling where it is feasible and system scale modeling with RELAP5 and concludes that AHWR design is capable of removing decay heat for more than 7 days without hampering the safety of the reactor.

List of Figures

Figure-2.1	Schematic of AHWR	16
Figure-2.2	Various passive systems of AHWR	17
Figure-2.3	Passive decay heat removal system of AHWR	18
Figure-2.4	GDWP compartments and the Isolation Condensers	18
Figure-2.5	Level of water in tail pipe tower after relocation of all of GDWP water into V1 following LOCA	19
Figure-2.6	Relocation of GDWP water into V1 and V2	19
Figure-2.7	Relocation of GDWP water in V1, V2 and annulus gap	20
Figure-2.8	Decay heat curve for AHWR	30
Figure-2.9	RELAP5 nodalization for AHWR	33
Figure-2.10	RELAP5 nodalization for Case-b	34
Figure-2.11	SBO results with no loss of GDWP water (Case-a)	38
Figure-2.12	SBO results with partial loss of GDWP water (Case-b)	39
Figure-2.13	SBO results with complete loss of GDWP water (Case-c)	41
Figure-2.14	SBO with complete loss of GDWP water and dry containment (Case-d)	42
Figure-3.1	Passive Moderator and Passive Endshield Cooling System	49
Figure-3.2	AHWR general arrangement for Fukushima type of scenario	50
Figure-3.3	Schematic of PAUSE System	51
Figure-3.4	Schematic of Integral test facility simulating Fukushima type scenario	57
Figure-3.5	Scaling adequacy of the test facility	60
Figure-3.6	Fluid temperature at Calandria inlet/outlet and GDWP inlet/outlet	62
Figure-3.7	Fluid temperature variation at Endshield Vessel inlet and outlet	62
Figure-3.8	Temperature distribution inside Calandria Vessel	64
Figure-3.9	Temperature distribution inside Endshield Vessel	65
Figure-4.1	Schematic of heat transfer from fuel to moderator in the Calandria	68
Figure-4.2	Schematic of Pressure and Calandria tube with moderator in Calandria	68
Figure-4.3	Schematic of Passive Moderator Cooling System (PMCS)	69
Figure-4.4	RELAP5 nodalization of AHWR	72
Figure-4.5	MHTS pressure	74

Figure-4.6	MHTS flow rate	74
Figure-4.7	Steam flow rate from MHT to ICs	75
Figure-4.8	Accumulator level	75
Figure-4.9	GDWP water temperature	75
Figure-4.10	Moderator and GDWP side coolant flow	75
Figure-4.11	Moderator temperature	75
Figure-4.12	GDWP side coolant temperature	75
Figure-4.13	Heat balance between moderator primary and secondary side	76
Figure-4.14	Clad surface temperature	76
Figure-4.15	Schematic of PMCS Test Facility	77
Figure-4.16	a: Calandria vessel housing directly heating Calandria tubes, b: Thermocouples arrangement on the Calandria tubes	78
Figure-4.17	Process and instrumentation diagram of PMCS Test Facility	79
Figure-4.18	Temperature variation during 1 st phase of experiment	81
Figure-4.19	Temperature distribution inside Calandria Vessel @ 15 minutes	84
Figure-4.20	Temperature distribution inside Calandria Vessel @ 45 minutes	84
Figure-4.21	Temperature distribution inside Calandria Vessel @ 3 hrs	85
Figure-4.22	Temperature distribution inside Calandria Vessel @ t=0 day	85
Figure-4.23	Temperature distribution inside Calandria Vessel @ t= 1 day	86
Figure-4.24	Temperature distribution inside Calandria Vessel @ t= 7 day	86
Figure-4.25	Fluid temperature variation at Calandria inlet/outlet and GDWP inlet/outlet (Experiment and RELAP predictions)	87
Figure-4.26	RELAP5 nodalization of PMCS Test Facility	89
Figure-4.27	Variation of mass flow rate (RELAP simulation)	89
Figure-4.28	(a) Temperature difference between the outlet and inlet of the Calandria for grid sizes: (1) 0.33 million cells, (2) 0.82 million cells and (3) 2.05 million cells and (b) variation of temperature along the axial height of the Calandria at a location 3mm away from the surface of the central tube	95
Figure-4.29	CFD model and mesh of Calandria Vessel	97

Figure-4.30	Temperature distribution inside Calandria Vessel wall at various inlet temperatures (a) 54 ⁰ C (0 day instance) (b) 57 ⁰ C (0.5 day instance) as predicted by CFD	98
Figure-4.31	Temperature distribution at outlet plane for various inlet temperatures (Comparison of CFD predictions and experiments)	99
Figure-4.32	Velocity distribution at Inlet plane for various inlet temperatures (a) 54 ⁰ C (0 day instance) (b) 57 ⁰ C (0.5 day instance) as predicted by CFD	99
Figure-4.33	Velocity distribution at outlet plane for various inlet temperatures (a) 54 ⁰ C (0 day instance) (b) 57 ⁰ C (0.5 day instance) as predicted by CFD	100
Figure-5.1	Various methods for simulation of two phase flow	107
Figure-5.2	Variation of drag coefficient with particle Reynolds number	123
Figure-5.3	Illustration of subcooled boiling in a channel	128
Figure-5.4	Wall heat flux partitioning	129
Figure-5.5	Variation of correction factor for non-equilibrium boiling	130
Figure-6.1	Photograph of the experimental set-up	155
Figure-6.2	Schematic of column and detector arrangement	157
Figure-6.3.	(a) Schematic diagram of the experimental set-up for RPT (b) Flow diagram for the RPT method with typical Eulerian grid and particle details	159
Figure-6.4.	Top view of the internal configurations: (a) Empty column (Configuration-A), (b) Configuration-B	160
Figure-6.5	Effect of superficial gas velocity on overall flow patterns for Configuration-A	166
Figure-6.6	Effect of superficial gas velocity on axial liquid velocity for Configuration-A	167
Figure-6.7	Effect of superficial gas velocity on axial liquid velocity for configuration-B	167
Figure-6.8	Effect of superficial gas velocity on overall flow patterns for Configuration-B	168
Figure-6.9	Effect of superficial gas velocity on axial turbulent kinetic energy for configuration-A	169

Figure-6.10	Effect of superficial gas velocity on axial turbulent kinetic energy for configuration-B	170
Figure-6.11	Mesh for Hill's case	172
Figure-6.12	Grid sensitivity for Hills (1974) at $V_G=0.038$ m/s	174
Figure-6.13	Grid sensitivity for Hills (1974) at $V_G=0.064$ m/s	174
Figure-6.14	Grid sensitivity for Hills (1974) at $V_G=0.095$ m/s	174
Figure-6.15	Effect of grid sensitivity	175
Figure-6.16	Overview of OpenFOAM structure	175
Figure-6.17	PIMPLE algorithm for twophase Euler Foam	176
Figure-6.18	CFD validations for Hills (1974) experimental data for axial liquid velocity by using OpenFOAM	182
Figure-6.19	CFD validations for Hills (1974) experimental data for gas hold-up by using OpenFOAM	183
Figure-6.20	Typical holdup and liquid velocity profile @ 64mm/s	184
Figure-6.21	Gas Mass balance (Axial variation of superficial gas velocity)	184
Figure-6.22	Liquid mass balance (Axial variation of liquid velocity)	185
Figure-6.23	Grid size used for simulations (a) Configuration A (b) Configuration B	186
Figure-6.24	Variation of axial liquid velocity profiles for Configuration (A)	187
Figure-6.25	Variation of holdup profiles for Configuration (A)	187
Figure-6.26	Variation of axial liquid velocity profiles for Configuration (B)	189
Figure-6.27	Variation of holdup profiles for Configuration (B)	189
Figure-6.28	Turbulent kinetic energy for Configuration (A) and (B)	190
Figure-7.1	Bartolomei experiment details	200
Figure-7.2	Grid for the base case	203
Figure-7.3	Grid independence (a) axial void distribution (b) axial liquid temperature distribution with varying grid points	203
Figure-7.4	Comparison of calculated and measured (a) steam void fraction values and (b) bulk liquid temperature along the axial length of the column	204
Figure-7.5	Radial variation of void and temperature	204
Figure-7.6	Effect of different turbulence models on flow field	206

Figure-7.7	Effect of different bubble induced turbulence models on flow field	209
Figure-7.8	Effect of different drag models on flow field	211
Figure-7.9	Effect of different wall lubrication models on flow field	212
Figure-7.10	Effect of different turbulent dispersion models on flow field	213
Figure-7.11	Effect of different boiling parameters model on flow field	216
Figure-7.12	Effect of different interfacial models on flow field	218
Figure-7.13	Axial void and Temperature predictions by RELAP and CFD	219
Figure-7.14	Axial and radial void distribution	220
Figure-7.15	Axial temperature distribution	220
Figure-7.16	Coolant channel with 54 Rod Bundle	222
Figure-7.17	1/6th Symmetric sector of the rod bundle	222
Figure-7.18	Core flow and MHTS pressure during SBO	223
Figure 7.19	Heat flux boundary conditions	224
Figure-7.20	Top view of mesh for the 1/6th sector of the 54 rod bundle	226
Figure-7.21	Axially averaged void distribution (Grid independence)	227
Figure-7.22	Wall y plus for heater rods	228
Figure-7.23	Various axial and radial planes for CFD data presentation	228
Figure-7.24	Void distribution at various axial planes for Case#1	232
Figure-7.25	Void distribution at various radial planes for Case#1	233
Figure-7.26	Temperature distribution at various axial planes for Case#1	234
Figure-7.27	Temperature distribution at various radial planes for Case#1	235
Figure-7.28	Angular temperature and void distribution on radial planes A, B, C and D for Case#1	237
Figure-7.29	Angular velocity on radial planes A, B, C and D	238
Figure-7.30	Axial phasic velocities and void distribution for Case#1	239
Figure-7.31	Average liquid temperature for Case#1	239
Figure-7.32	Various axial heat fluxes for Case#1	239
Figure-7.33	Bulk bubble diameter from inlet to outlet for Case#1	240
Figure-7.34	Average axial flow quality for Case#1	240
Figure-7.35	Average axial mass transfer rate for Case#1	240

Figure-7.36	Details of the RELAP5 model for Case#1	241
Figure-7.37	Average axial void distribution RELAP and CFD	242
Figure-7.38	Average void fraction from inlet to outlet with Set#2 models	244
Figure-7.39	Angular void and temperature distribution from inlet to outlet for Case#1 with Set#2 models	246
Figure-5.40	Radial temperature distribution at various axial planes	248
Figure-5.41	Radial velocity distribution at various axial planes	248
Figure-7.42	Liquid temperature distribution at various radial planes for Case#2	249
Figure-7.43	Liquid velocity distribution at various radial planes for Case#2	250
Figure-7.44	Angular temperature and velocity distribution on radial planes A, B, C and D for Case#2	252
Figure-7.45	Void variation from inlet to outlet at two radial planes for Case#4	254
Figure-7.46	Temperature distribution at various axial planes for Case#4	254
Figure-7.47	velocity distribution for liquid phase at various axial planes for Case#4	255
Figure-7.48	Temperature and velocity distribution for liquid phase at plane-A	255
Figure-7.49	Temperature and velocity distribution for liquid phase at plane-B	256
Figure-7.50	Temperature and velocity distribution for liquid phase at plane-C	256
Figure-7.51	Temperature and velocity distribution for liquid phase at plane-D	257

List of Tables

Table-1.1	Summary of the research work	8
Table-2.1	Important Design Parameters of AHWR	20
Table-2.2	Various Models in RELAP & Associated Uncertainties	29
Table-2.3	Important Parameters of Isolation Condenser	30
Table-2.4	Initial Operating Conditions for Various Systems of the Reactor	32
Table-3.1	Ratio of scaled parameters in Passive Moderator and Passive Endshield Cooling System Test Facility	56
Table-4.1	Initial Operating Conditions for Various Systems of the Reactor	71
Table-4.2	Geometrical details of the scaled model	77
Table-4.3	Details of CFD cases studied	90
Table-5.1	Characterization of two-phase flow governing equations (1-D)	108
Table-5.2	Various Drag Models for Bubbly Flows	121
Table-5.3	Models for Wall lubrication force	126
Table-5.4	Nucleation site density models	135
Table-5.5	Bubble departure frequency models	137
Table-5.6	Bubble departure diameter models	138
Table-5.7	Models for interfacial heat transfer	140
Table-6.1	Set of experiments performed	156
Table-6.2	Phase interaction models used for simulation for Hill's and RPT experiment	171
Table-6.3	Details of Hill's experimental setup	171
Table-6.4	Boundary conditions used in the simulations	180
Table-7.1	Boundary conditions for Bartolomei experiment	201
Table-7.2	Phase interaction models used for simulation of Bartolomei experiment	201
Table-7.3	Wall y^+ for various grid densities	203
Table-7.4	Heater wall y^+ with different turbulent models	206
Table-7.5	RMS error for different BIT models	208
Table-7.6	RMS error for different Drag models	210
Table-7.7	Combination of boiling parameters models for performance study	214
Table-7.8	Experiment details simulated using CFD	220
Table-7.9	Cases studied with CFD for local level thermal hydraulics	223
Table-7.10	Details of CFD model	226

Abbreviations

AHWR	Advanced Heavy Water Reactor
ATWS	Anticipated Transients Without Scram
BARC	Bhabha Atomic Research Centre
BDBE	Beyond Design Basis Event
CAMP	Code Applications and Maintenance Program
CARPT	Computer-Automated Radioactive Particle Tracking
CFD	Computational Fluid Dynamics
CFVS	Containment Filtered Venting System
CT	Computed Tomography
DBE	Design Basis Event
ECCS	Emergency Core Cooling System
GDWP	Gravity Driven Water Pool
HPA	High Pressure Accumulators
ICAAP	International Code Assessment and Applications Program
ICs	Isolation Condensers system
ICW	Inner Containment Wall
INL	Idaho National Laboratory
IRUG	International RELAP5 Users Group
LDA	Laser Doppler Anemometry
LOCA	Loss of Coolant Accident
MHTS	Main Heat Transport System
NPP	Nuclear Power Plant
OCW	Outer Containment Wall
Open FOAM	Open source Field Operation And Manipulation
PAUSE	Passive Union of V1 and V2 volumes of Containment
PCCS	Passive Containment Cooling System
PCIS	Passive Containment Isolation System
PCRD	Passive Catalytic Recombiner Device
PECS	Passive Endshield Cooling System
PECSTF	Passive Endshield Cooling System Test Facility
PFBR	Prototype Fast Breeder Reactor
PHWR	Pressurized Heavy Water Reactor
PIV	Particle Image Velocity
PMCS	Passive Moderator Cooling System
PMCSTF	Passive Moderator Cooling System Test Facility
PPIS	Passive Poison Injection System
RELAP	Reactor Excursion and Leak Analysis Program
RPT	Radioactive Particle Tracking
ROPS	Relocation of Passive Sink
SBO	Station BlackOut
SPND	Self-Powered Neutron Detectors
VOF	Volume of Fluid

Nomenclature

A, a	Area (m^2)
C_D	Drag coefficient
C_L	Lift coefficient
C_{pL}	Specific heat capacity of liquid (J/kg K)
C_{VM}	Virtual mass coefficient
C_{TD}	Turbulent dispersion coefficient
C_t	Turbulence parameter
$C_{\varepsilon 1}, C_{\varepsilon 2}, C_{\varepsilon 3}$	Constants in epsilon equation
D, d	Diameter (m)
E_o	Eotvos Number
F	Friction/Orifice Number
F_D	Drag force (N)
F_L	Lift force (N)
F_{VM}	Virtual mass force (N)
F_{TD}	Turbulent dispersion force (N)
F_W	Wall lubrication force (N)
f	Frequency of bubble departure (Sec^{-1})
f	Friction factor
f_D	Drag force on single bubble (N)
f_p	Fraction of the heat flux
G_k, G_b	Generation of TKE due to shear and buoyancy
g	Gravitational field (m/sec^2)
H	Enthalpy (kJ/kg)
h_{fg}	Latent heat of vapourisation (kJ/kg)
h_{if}	Interfacial heat transfer coefficient ($\text{W/m}^2\text{K}$)
h_{CL}	single phase heat transfer coefficient for liquid phase ($\text{W/m}^2\text{K}$)
h_{CG}	single phase heat transfer coefficient for gas phase ($\text{W/m}^2\text{K}$)
Ja	Jacob Number
j	Superficial velocity (m/s)

K	Local loss coefficient
k	Turbulent kinetic energy (m^2/sec^2 or J/kg)
k_L	Thermal conductivity of liquid (W/mK)
l	Length (m)
M	Interfacial momentum transfer term (N)
Nu	Nusselt Number
N_w	Nucleation site density
\vec{n}	Normal vector
P	Pressure (Pa)
Pe	Peclet Number
P_m	Production in turbulent kinetic energy
Pr	Prandtl Number
V	Velocity (m/s)
q'''	Heat flux (W/m^2)
Q	Conductive heat flux (W/m^2)
Q	Heat source Number
Q_G	Gas volumetric flux (m^3/s)
Re	Reynolds Number
Ri	Richardson Number
St	Stanton Number
\mathbf{u}	Velocity vector (m/sec)
V	Volume (m^3)
S_k, S_M	Source term
T	Temperature (K)
y^+	Wall y plus
y_w	Distance of first cell center from wall
β	Thermal Expansion Coefficient (K^{-1})
ρ	Density (kg/m^3)
ϵ	Fractional gas hold-up, void fraction
Γ	Mass transfer due to phase change (kg)
ϵ	Rate of turbulent kinetic energy dissipation (m^2/sec^3)

μ	Viscosity (Pa-sec)
ν	Kinematic viscosity (m^2/s)
ω	Specific rate of dissipation
\emptyset	Contact Angle (degree)
σ	Surface tension force (N/m)
θ	Angle (degree)
$\tau_{k,ij}$	viscous stress tensor (N/m^2)
$\tau_{k,ij}^t$	Turbulent stress tensor (N/m^2)

Subscripts

b	Bubble
BIT	Bubble Induced turbulence
E	Evaporative
G	Vapour
gj	Drift
h	Hydraulic
i	Interfacial
i, k	i^{th} or k^{th} Phase or component
if	Interface to liquid
L	Liquid
Lift	For Lift force
m	Mixture
Q	Quenching
Sat	Saturation
Sup	Superheat
TD	Turbulent Dispersion
ν	vapour
w	wall
WL	Wall Lubrication
G-L	Vapour to Liquid
L-G	Liquid to Vapour

Superscripts

t	Turbulent
Re	Reynolds stresses

CHAPTER-1

Introduction

1.1 Background.....	2
1.2 Motivation.....	4
1.3 Objectives and methodology	6
1.4 Outline of Thesis.....	9

1.1 Background

Nuclear being a clean and green option of energy has always attracted the attention of mankind for fulfilling the need of energy since its discovery. Design and development of the nuclear reactors were started soon after the discovery of fission. The first commercial NPP was setup at Obninsk, USSR in 1956. The usage of nuclear energy was accelerated from 1960s onward and a large number of nuclear reactors were deployed across the globe after sufficient experience of design and operation obtained in very early reactors, known as research reactors. Installed nuclear capacity initially rose quickly from less than 1 GW in 1960 to 100 GW in late 1970s, and 300 GW in late 1980s. This was the golden age for the expansion of nuclear power and related technologies. Presently, nuclear is having an installed capacity of ~400GWe in the world with operation of around 450 NPPs, mostly by water cooled nuclear reactors, and also it has the potential to meet large fraction of global energy requirements without carbon footprints.

India also flagged its nuclear power programme with Asia's First Nuclear Reactor "APSARA" at Bhabha Atomic Research Centre (BARC). This was built entirely by Indian engineers and made critical on August 4, 1956. Dr. Homi J. Bhabha conceptualized India's three stage nuclear power programme considering the natural resources available in the country. With large reserves of thorium in the country, it is apparent that only thorium can bridge the big gap in electricity production and demand. India's nuclear power program was designed based upon the natural resources of heavy material available in the country. This long term energy sustainability envisages in three stages viz. Stage-I, II and III.

- Stage-I includes utilization of natural uranium using PHWRs. Reprocessing of the spent fuel from this stage will produce plutonium to be used in stage-II, which will help in attaining closed fuel cycle strategy.
- Stage-II includes utilization of plutonium in fast breeder reactors to produce uranium-233 from thorium. This uranium-233 will be used in stage-III power generation.

Prototype Fast Breeder Reactor (PFBR) is one such reactor, under commissioning at Kalpakkam, which will produce the fuel for stage-III using the spent fuel of stage-I.

- Stage-III will be the self-sustaining power generation stage, as it will use the uranium-233 produced in previous stage from India's vast thorium reserves. Advanced Heavy Water Reactor (AHWR) is the prime example of such an innovation.

In addition to indigenously developed PHWRs, currently, India is having operating experiences of almost all kind of reactors right from first kind of BWRs to current generation PWRs.

Besides, many countries across the globe chose nuclear as their prime power generation asset and nuclear grown with many success stories. However, the success and growth story of nuclear power suffered due to the accidents at TMI-2 and Chernobyl reactors, and recently at Fukushima. These affected the public perception of safety of nuclear power plants even though the risks due to these plants are much less than other industrial hazards. The accidents happened in the history of nuclear has put a question mark on its safe disposition hence the development got hampered. On March, 11, 2011, the Tsunami followed by earthquake had triggered severe accidental conditions in Fukushima Daiichi Nuclear Power Plant. The accident had its effect on nuclear power industry and reliability of the safety systems become questionable. After Fukushima accident, the design criteria for newly developed and existing reactors against natural disaster accidents are being reviewed across the globe and new criteria are being established. Carefully, if we observed the Fukushima accident, it is essentially an extended Station Blackout (SBO), that posed a need to have a decay heat removal system that can provide longer grace period without operator intervention which can only be achieved by passive systems.

Worldwide, reactor systems, almost all operating and new designs were analyzed in view of Fukushima accident and necessary modifications in the reactor as well at the NPP site are suggested and incorporated. Addressing the issues of the Fukushima type accident is the need

of the hour and hence it was taken as the research work for one of the tube type BWR developed in India.

1.2 Motivation

BARC, India has designed an innovative reactor Advanced Heavy Water Reactor (AHWR) (Sinha and Kakodkar, 2006), which is a 920 MW_{th}, pressure tube type boiling light water cooled and heavy water moderated reactor. It is equipped with many passive features for safety. AHWR design was also need to be analyzed for addressing the Fukushima scenario and establishment of the safe decay heat removal for prolonged period. Looking at the features of AHWR, the reactor includes many passive features in its design and one of the important features of the reactor is fission heat removal by natural circulation mode of cooling. Some more new passive systems have also been incorporated in reactor design to achieve absolute safe decay heat removal during postulated Fukushima kind of accident.

Historical development of Nuclear reactor shows that advanced reactor design developed after Chernobyl accident includes more and more passive features in their design viz. VVER, ESBWR, AP-1000, APR1400, APR+, AHWR etc. Few of them also employed natural circulation as the mode of heat removal from the core even during normal operation like AHWR and ESBWR. Natural circulation systems are having many advantages over conventional pump systems. In a natural circulation system, the driving buoyancy force is generated by the thermally induced density difference. Larger density differences are possible to achieve in two-phase flow systems compared to single-phase flow systems so two phase flow system becomes the choice of the designers. The main advantage of natural circulation is that the fluid circulation is achieved naturally without any fluid moving machinery. The absence of pumps simplifies the system, reduces operation and maintenance cost and eliminates all postulated initiated events associated with pump failure and operator intervention thereby enhancing safety and reliability. Steady state flow prevails in a natural

circulation loop when the driving buoyancy force is balanced by the retarding frictional forces. In a natural circulation system, flow automatically gets established according to the channel power.

Despite the certain advantages, natural circulation systems have their own challenges. One of the drawbacks of natural circulation systems is that their driving force is low. The simplest way to increase the driving force is to increase the loop height, which may be uneconomic. In addition, use of tall risers can make natural circulation systems slender in structure and may raise seismic concerns. Low driving force results in low mass flux in natural circulation systems compared to the forced circulation systems. Operating with low mass fluxes, maximum channel power is also lower which leads to a larger core volume compared to a forced circulation system of the same rating.

While instability is common to both forced and natural circulation systems, the natural circulation based system is inherently less stable than forced circulation systems. This may be attributable to the regenerative feedback inherent in the natural circulation phenomenon, where any change in the driving force affects the flow which, in turn, affects the driving force that may lead to sustained oscillatory behavior for certain operating conditions.

Natural circulation systems need to be started up from rest at low pressure which makes important to understand the thermo hydraulic relationships applicable to low pressure and low flow conditions of natural circulation systems. The presence of instability at low pressure conditions requires special startup procedures for natural circulation systems. The phenomena involved in natural circulation systems may have considerable three dimensional effects. Under these conditions, the conventional 1-D models used for the thermo hydraulic design and safety analysis may not be adequate for natural circulation systems. Hence, the tools used for the analysis of such systems need to be separately developed and validated.

AHWR also incorporate many passive safety systems in its design. Though there are many unresolved issues and challenges associated with natural circulation based system, here, an effort has been made to demonstration of the safety of AHWR for Fukushima type of scenario.

1.3 Objectives and methodology

The objectives of the research work include:

1. Estimation of decay heat removal capabilities of AHWR design for prolonged SBO
2. Setting up a scaled test facility and experimentation demonstrating the safe decay heat removal for prolonged period
3. Validation of system code for natural circulation operations and validation of the CFD code for multidimensional flow inside scaled Calandria Vessel and AHWR rod bundle. It includes:
 - a. Development of 3D CFD model for Calandria Vessel for detailed flow and temperature distribution inside it on Open FOAM platform
 - b. Development of CFD model for adiabatic two phase flow simulations inside a Bubble Column
 - c. Validation of the model with the experimental data available in literature
 - d. Radioactive Particle Tracking (RPT) experiments for flow distribution inside a batch Bubble Column and CFD code validation
 - e. Development of the frame work for boiling flows and multidimensional CFD simulations for boiling flows over AHWR fuel rod bundle

Table-1.1 gives the brief summary of the research work and objectives as discussed above.

The objectives are achieved by making use of system code RELAP5 for integral behavior studies, experiments in the scaled test facility of AHWR and finally CFD simulations for multidimensional behavior of flow over heated Calandria tubes and fuel rod bundle.

Integral analysis of the reactor systems is carried out using system code RELAP5 mod 3.2, which confirms the reactor design capability of removing decay heat for more than 7 days. Though, it has been established by analysis with system code, still there is a requirement to demonstrate it in an integral scaled test facility. For this purpose, an integral test facility

incorporating simulated Isolation Condensers (ICs) heaters submerged in Gravity Driven Water Pool (GDWP) along Passive Moderator and Endshield Cooling system (PMCS and PECS) has been designed and built. Experimental demonstration for a grace period of 7 days is established in the test facility.

Besides, system codes are not capable to estimate the local flow behavior at component level of the reactor system such as inside the Calandria Vessel and the rod bundle in the core. The decay heat removal is ensured as predicted by the system code; still there exists a finite possibility of local hot spot inside fuel rod bundle, which may lead to fuel failure and moderator leakages losing the reactor integrity. This may happen because of the multidimensional local circulation phenomena inside the big vessels and flow scarcity at local level inside the fuel rod cluster of the nuclear reactor. The thesis focuses on the estimation of decay heat removal capabilities of AHWR design for prolonged period with inclusion of studies for any hot spot or local excursions inside rod bundle and Calandria Vessel.

Table-1.1 Summary of the research work

	Gap area & Challenges	Objectives	Results
Numerical Studies	<ul style="list-style-type: none"> Heat removal from coolant channel and Calandria Vessel with natural circulation mode of cooling Complex geometry of the rod bundle , very tight pitch between fuel rods (2-3 mm), shading effect of rods inside the bundle, uneven area inside pressure tube, Modelling of two phase flow Multidimensional phenomena, Complexity in modelling of two phase flow 	<ul style="list-style-type: none"> To estimate decay heat removal capability of reactor from fuel bundle using system code RELAP5 Development and validation of CFD model for flow inside Calandria Vessel. To develop CFD model for two phase flow to study the local effects To estimate the 3-D distribution of void, temperature and velocity inside AHWR rod bundle Assessment of hot spot inside the fuel bundle. 	<ul style="list-style-type: none"> Successful Decay heat removal from fuel bundle without hot spot for pronged SBO conditions. CFD model developed and validated with experimental data. Void, temperature and velocity 3-D distribution estimated System code RELAP5 also validated with experimental data.
Experimental Studies	<ul style="list-style-type: none"> Heat removal from moderator and Endshield Multidimensional flow, natural circulation startup, flow distribution inside big vessel: local circulation issues 	<ul style="list-style-type: none"> System design to ensure coolability of moderator and Endshield during decay heat removal. Demonstration of decay heat removal for prolonged period by experiments in integral scaled test facility (PMCS, PECS and ICs). Experimental validation of bubble column CFD model by RPT technique. 	<ul style="list-style-type: none"> Passive moderator and Endshield cooling system maintains the temperature of moderator and Endshield coolant < 100°C Heat removed effectively by PMCS and PECS for >7 days Extensive validation of 2 fluid model for open bubble column

The thesis encompasses CFD code development, validations and simulations for the component level hydrodynamics inside the reactor components viz. Calandria Vessel and fuel rod bundle. CFD simulations give insights for the flow, temperature and void distributions inside the AHWR rod bundle and Calandria Vessel.

In nutshell, the thesis deliberates estimation of AHWR design against Fukushima type of accidents by simulating the reactor systems in integral manner with system code, by experimental demonstration in a scaled test facility of AHWR and also embraces CFD simulations at component scale for Calandria Vessel and boiling two phase simulations for fuel rod bundle for local hot spots.

1.4 Outline of Thesis

The research work is planned to elucidate in the thesis in eight chapters. The essence of the chapters is as follows:

Chapter-1 discusses the background, motivation, objectives and methodology adopted for the research work.

Chapter-2 presents the numerical studies carried out for AHWR for decay heat removal in case of Beyond Design basis Events (BDBEs) similar to Fukushima. Study has been carried out with system code in integral manner. This concluded the robustness of the reactor design against Fukushima type scenarios.

Chapter-3 includes post Fukushima design modification in AHWR as a part of recommendations coming out from the integral behavior study of the reactor, presented in previous chapter. This chapter also includes scaling and designing of the experimental facility for studying the integral behavior of the reactor in scaled facility. Experimental studies are presented for integral behaviour of the reactor in scaled test facility after incorporation of the new systems in the design.

Chapter-4 presents the detailed 3-D flow field investigations for natural convection and circulations inside Calandria Vessel. Taking the output from the studies carried out previously (discussed in Chapter-2 and 3), it will be difficult to conclude the safety of the reactor; 3-D studies are carried out for moderator flow distribution inside Calandria Vessel during prolonged SBO scenario to evaluate the flow patterns inside Calandria Vessel for any dead zone.

For ensuring the safety of the reactor, it is very important to study the flow behavior inside the fuel rod bundle during such accident. Since, it is boiling water reactor so possess two phase flow in its Main Heat Transport (MHT) system. Rest of the chapters covers the study of the flow field for two phase flows. The study has been divided in two steps; one aims the developments of CFD model for adiabatic two phase flow and other is to study the boiling flows inside rod bundle. Targeting this, various models and methods for simulation of the two phase flow are presented in Chapter-5.

Chapter-6 elaborates the studies for adiabatic two phase flows inside bubble column. It incorporates development of CFD model on Open FOAM platform and its validation against the experimental data available in the literature as well as generated by experiments using RPT technique. This chapter also includes experimental studies for RPT inside an open Bubble Column and validation of CFD model with RPT data.

Gaining experience from the CFD developments discussed in Chapter-5 and 6, a frame work has been developed for boiling flows. Chapter-7 brings out the development of boiling frame work. It includes the validation of the framework so developed with literature data (two cases are studied for validations) and its application for the rod bundle of AHWR during SBO.

Finally, Chapter-8 presents the conclusions and summary of research work undertaken. It also incorporates the future directions for further research.

CHAPTER-2

Numerical Studies for Decay Heat Removal in AHWR

2.1	Introduction.....	12
2.2	Brief description of the Fukushima event.....	13
2.1	AHWR system description	15
2.2	Description of relevant postulated Fukushima scenarios for AHWR.....	21
2.2.1	Case-a: Prolonged SBO with no loss of GDWP water.....	21
2.2.2	Case-b: Prolonged SBO with partial loss of GDWP water	21
2.2.3	Case-c: Prolonged SBO with complete loss of GDWP water	22
2.2.4	Case-d: Prolonged SBO with loss of GDWP water and dry containment.....	22
2.3	Analysis methodology	23
2.3.1	Description of system code RELAP5	24
2.3.2	Analysis for Case-a: Prolonged SBO with no loss of GDWP water	29
2.3.3	Analysis for Case-b: Prolonged SBO with partial loss of GDWP water.....	32
2.3.4	Analysis for Case-c: Prolonged SBO with complete loss of GDWP water	34
2.3.5	Analysis for Case-d: Prolonged SBO with loss of GDWP & dry containment.....	35
2.4	Results and discussions.....	36
2.5	Closure	42

2.1 Introduction

Fukushima accident was triggered by the earthquake and the resulting Tsunami had shaken the nuclear community to have a relook at the beyond design basis events (BDBE) and their consequences. Aftermath of Fukushima, capabilities of the reactor designs across the globe were evaluated against such accidental conditions. It is evident from Fukushima accident that removal of the decay heat for prolonged period is a significant reactor safety concern, especially after an accident like SBO. Failure to remove decay heat may cause the fuel temperature to rise to unacceptable levels and can cause core melt accidents like Three Mile Island and Fukushima. In such a scenario, passive systems play important roles. The new generation reactors are being designed keeping this aspect in mind. AHWR is an innovative reactor, designed for thorium utilization with special emphasis on use of passive systems for normal operation and accidents. AHWR employs natural circulation as the mode for removing the fission heat from the reactor core during normal operation as well as during accidental conditions. Besides, AHWR design incorporates various passive safety systems which include Isolation Condensers system (ICs) (Vijayan et al, 2013, Jain et al, 2008) for removal of decay heat; Passive Containment Cooling System (PCCS) (Kumar et al, 2014) for containment cooling and depressurization; Passive Emergency Core Cooling System (ECCS) injection (Dasgupta et al, 2017) into the channels directly in case of Loss of Coolant Accident (LOCA); Passive Poison Injection System (PPIS) (Vijayan et al, 2013) to shut down the reactor passively in case of non-availability of wired shut down system; Passive submergence of the core and feeders in subcooled water pool in case of LOCA using the water from GDWP; and a Passive Containment Isolation System (PCIS) (Vijayan et al, 2013) for isolating the containment from external atmosphere during LOCA. The Passive systems in AHWR are based on simpler designs employing natural physical laws for their actuation and

operation without external source of energy. This enables to avoid human intervention in their operation and hence enhances their reliability.

In view of Fukushima event, the response of the Advanced Heavy Water Reactor (AHWR) for various postulated Fukushima type scenarios was studied. At Fukushima, the reactor meltdown was triggered by long term SBO followed by unavailability of emergency equipment to pump cooling water. Therefore, several scenarios relevant to Fukushima type event were postulated for AHWR and analysis performed. The scenarios considered are more severe than that occurred at Fukushima. The results of the analysis demonstrated the robustness of AHWR design.

2.2 Brief description of the Fukushima event

The Fukushima event (Holt et al. 2012) was triggered by a beyond design basis Great East Japan earthquake of magnitude 9 on the Richter scale (4th largest magnitude recorded on earth) on March 11, 2011 at 2:46 pm. At the time of earthquake struck, Units 1, 2 and 3 were operating and Units 4, 5 and 6 were shut down for maintenance with the full core of Unit 4 offloaded to the spent fuel pool. Due to the earthquake, the power pylons collapsed resulting in loss of external AC power. All operating reactor units were shut down as intended and core cooling continued as per design intent. About an hour later a beyond design basis Tsunami struck the plant, which inundated Units 1-4 up to a level of 11.5 – 15.5m submerging all emergency diesel generators (as these were installed in the basement of the turbine building) resulting in a prolonged station blackout. There were several openings at ground level as well as trenches through which water could flow into the buildings. The emergency batteries were also submerged and damaged rendering all motor operated pumps including ECCS pumps inoperable. All safety and non-safety systems driven by electricity were unavailable. No lights were available in the control room, reactor and turbine buildings. Important instrument indications like reactor water level, reactor, drywell and wet well pressures, were unavailable

for units 1 & 2 due to loss of AC power and batteries making operators totally blind. Instrumentation of Unit-3 was available for 30 hours. Almost no communication existed between emergency response room and field workers. All the sea water pumps were also damaged resulting in the loss of the ultimate heat sink. This resulted in degraded core cooling leading to fuel overheating and melting. The core meltdown in Unit 1 occurred in about three to four hours as its isolation condenser valve was closed and inactive. In Unit-3, sufficient core cooling was provided by the RCIC (Reactor Core Isolation Cooling) and high pressure core injection systems till 2:42 on 13th March 2011. However, core meltdown could not be prevented as adequate counter measures could not be taken at that time. In the Unit-2, RCIC could inject water into its core till 07:30 on 14th March 2011. However, core meltdown also occurred in Unit-2 as adequate countermeasures could not be taken at that time. In Units 1 and 3, hydrogen explosions occurred releasing large amount of radioactive materials into the environment. Fortunately, almost all of the release was towards the sea due to the west wind blowing at that time. In Unit-2, the safety valve inside reactor vessel was opened at 21:00 on March 14 and impact noise occurred near the suppression chamber inside the reactor containment vessel at 0600 hrs on March 15. The containment vessel vent valve was opened at around midnight on March 15 resulting in release of radioactive materials. Due to the south-west wind blowing at that time, led to the spread of radioactive materials around Kanto area including Tokyo. Hydrogen explosion also occurred near the spent fuel pool of Unit-4 presumably due to the metal-water reaction caused by the overheating of the spent fuel in the pool. Besides, hydrogen explosion also occurred in Unit-4 which was produced by the hydrogen flowing into it from Unit-3 through the common stack. The station blackout continued for about four days leading to core meltdown in Fukushima units 1, 2 and 3.

2.1 AHWR system description

Aftermath of Fukushima, AHWR design was assessed for such kind of accidents. AHWR (Figure-2.1) is a 300 MWe vertical pressure tube type reactor cooled by boiling light water and moderated by heavy water fuelled by dual MOX consisting of (PU-Th) O₂ and (U-233-Th)O₂ with a 100 year lifetime (Sinha and Kakodkar, 2006). Natural circulation as mode of coolant circulation is adopted during normal operation, transient and accident conditions which eliminate all accident scenarios resulting from pump failure besides reducing capital and operating costs. One of the design objectives of AHWR is to produce about two-thirds of the power from thorium thus contributing to the sustainability issue in India. Other design objectives include a grace period of three days following a LOCA. Besides, the reactor is being designed to eliminate the requirement of off-site emergency measures so that it can be sited near population centres. The reactor is designed with a core damage frequency which is an order of magnitude lower than the existing units.

The safety features for reactivity control include negative void coefficient of reactivity, two diverse and independent shutdown systems, reactivity insertion limits and a passive poison injection system which ensures reactor shutdown in case of wired shutdown system failures.

The safety objective of AHWR is 'Long term passive (LTP) defence-in-depth' so that the reactor returns to a safe shutdown state without operator intervention. To facilitate this, AHWR employs passive safety features extensively. Figure-2.2 shows various passive systems of the reactor. Apart from natural circulation in Main Heat Transport System, passive safety systems in AHWR include isolation condenser system for decay heat removal in case of unavailability of main condenser as seen in Figure-2.3, emergency core cooling (includes both high pressure and low pressure ECCS) system and containment cooling system. Besides, a vapour suppression pool is provided to limit the maximum containment pressure. Passive systems for containment isolation and automatic depressurization are also

provided. Several passive components like one way rupture disc, passive valves, passive instrumentation and passive control systems are also being developed to achieve completely passive operation independent of operator intervention. Incorporation of acoustic trip, provides protection against stagnation channel breaks (Kumar et al., 2018). In addition special provisions are made to detect and suppress instability. This include use of SPNDs signals to detect and suppress instability and a reactor trip on quadrant core power to limit power rise in case of out-of-phase instability.

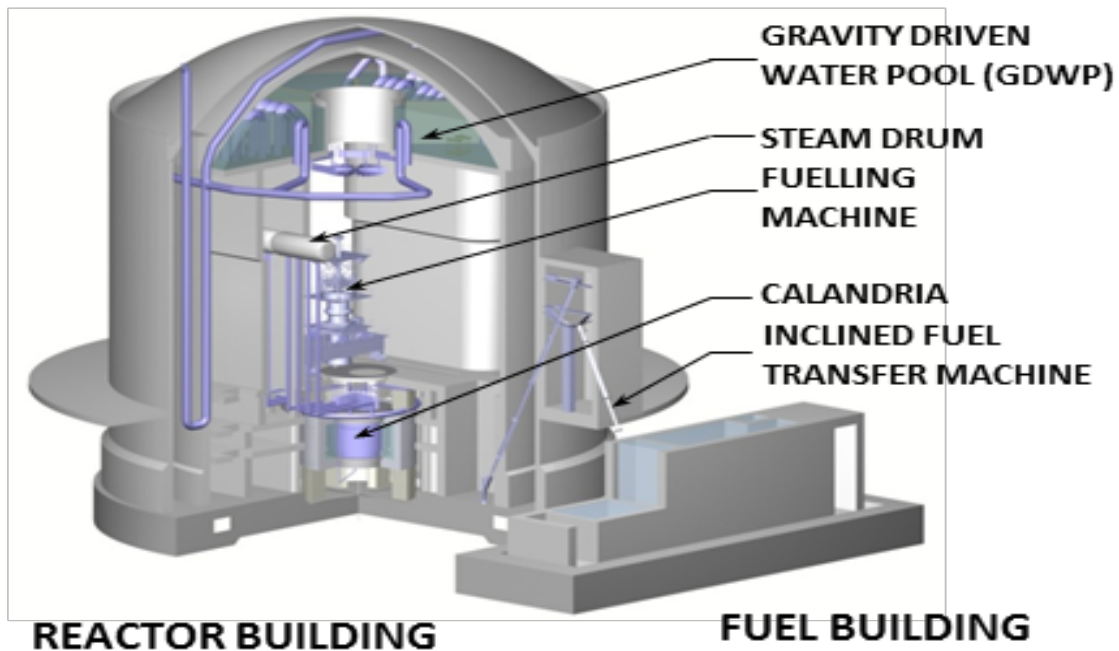


Figure-2.1 Schematic of AHWR

Double containment philosophy is followed in AHWR design. The primary containment is designed for design basis accident LOCA. This is divided into two volumes (V1 and V2) based upon the energy content (High and low enthalpy zones). V1 volume houses Main Heat Transport (MHT) system. The in-containment Gravity Driven Water Pool (Figure-2.2) is a major heat sink for several passive cooling systems of AHWR such as ICs, PCCS. GDWP inventory also acts as vapour suppression system besides acting as a long term low pressure ECC coolant. The total inventory of water in the GDWP is 8000 m³ which is divided into

eight equal and independent compartments as shown in Figure-2.4. Each compartment holds two vertical isolation condensers (Figure-2.4) which are surrounded by shrouds to prevent thermal stratification and to promote full utilization of the GDWP inventory during ICs operation. About 6000 m³ of the GDWP water gets injected into the core following a LOCA and is adequate to provide cooling for three days.

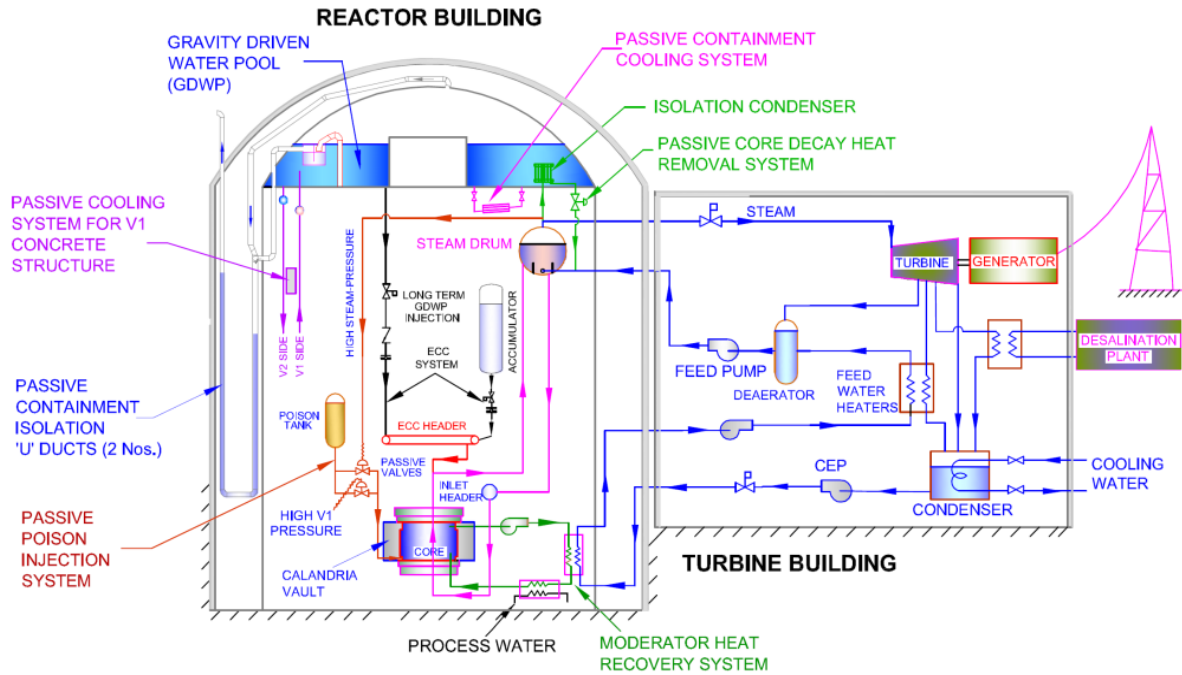


Figure-2.2 Various Passive Systems of AHWR

Since all the primary piping is located in V1 volume, the discharging primary coolant from the break accumulates in V1 eventually submerging the bare primary system piping (Figure-2.5) providing adequate passive cooling for a long time (~ three months) by the ‘boil-off’ mechanism. The total inventory in the MHTS and ECCS can submerge more than one-third of the tail pipe tower. An interesting feature of LOCA in AHWR is that the discharging coolant is not lost, but is passively relocated into the tail pipe tower where it continues to cool the MHTS. In other words LOCA eventually leads to ROPS (Relocation of Passive Sink) without impairing cooling.

Also, in the unlikely event of a beyond design basis earthquake, significant amount of GDWP inventory could be lost due to sloshing to V2 volume. Apart from this, cracks could appear in

the GDWP structure, spilling its inventory mostly into V2 and partly into V1 volumes. Drain pipes from V2 to V1 volume is provided (PAUSE system) so that the level of water in V2 and V1 will equalize eventually enabling prolonged passive cooling through the submerged primary piping (Figure-2.6).

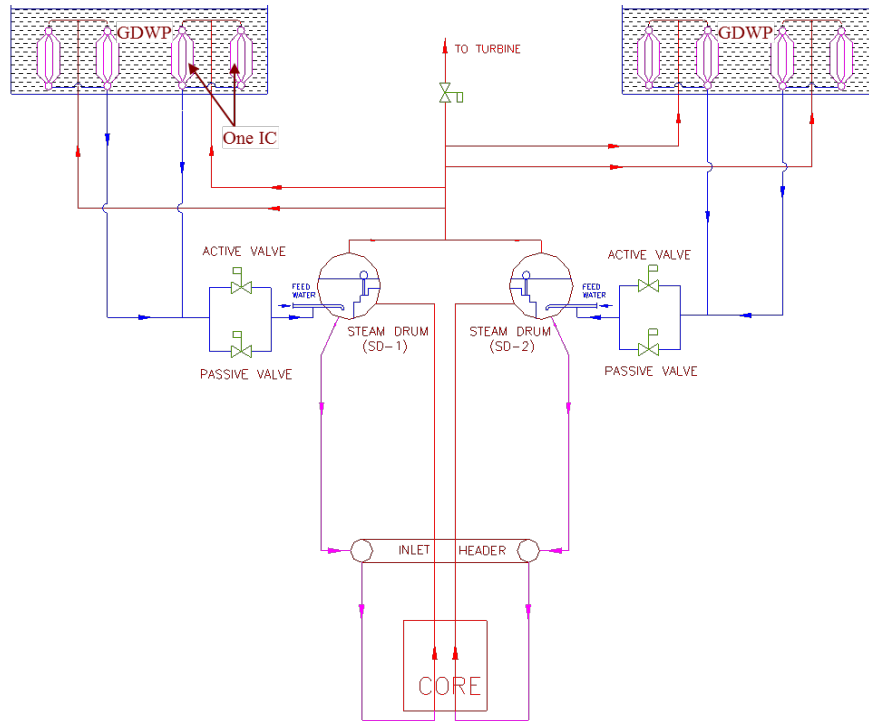


Figure-2.3 Passive Decay Heat Removal System of AHWR

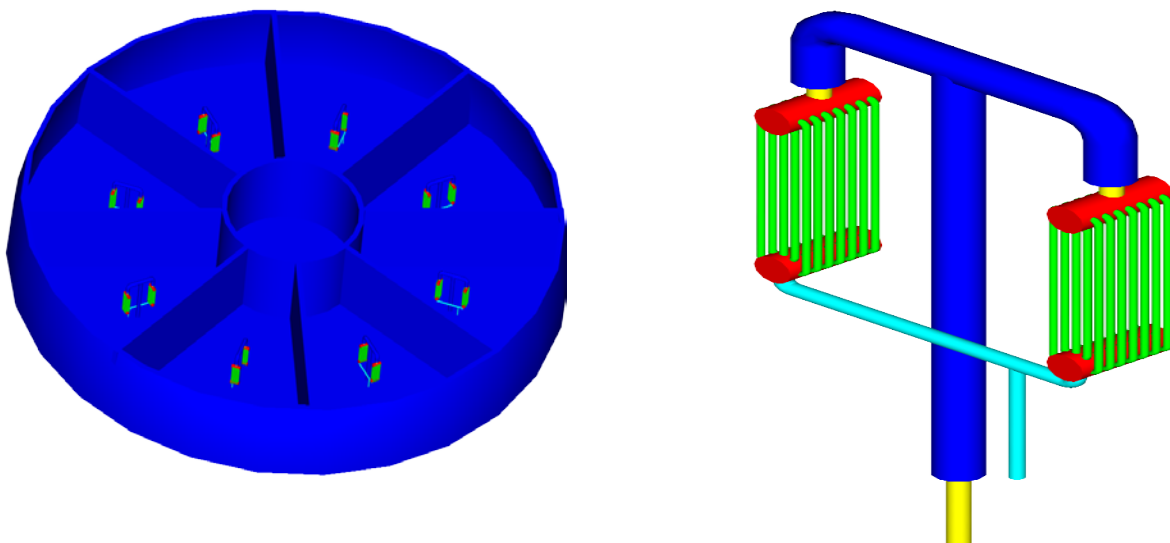


Figure-2.4 GDWP compartments and the Isolation condenser

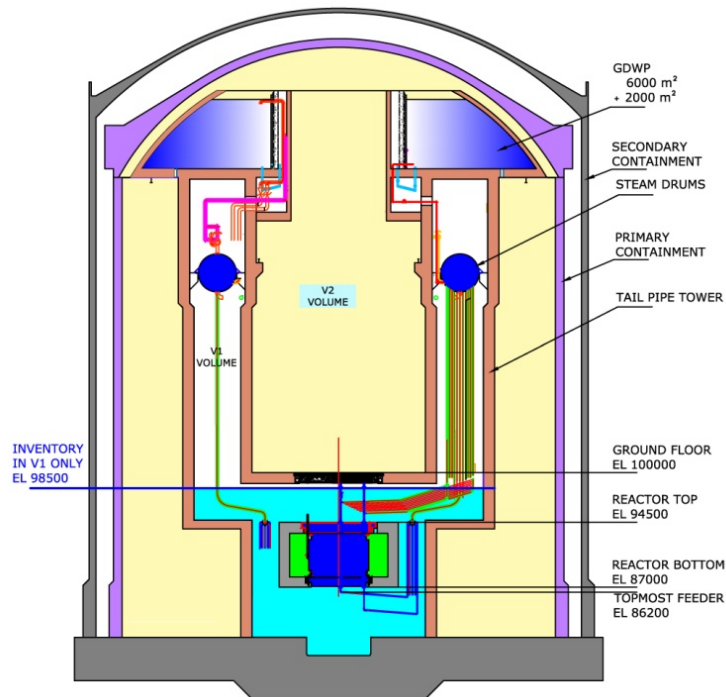


Figure-2.5 Level of water in tail pipe tower after relocation of all of GDWP water into V1 following LOCA

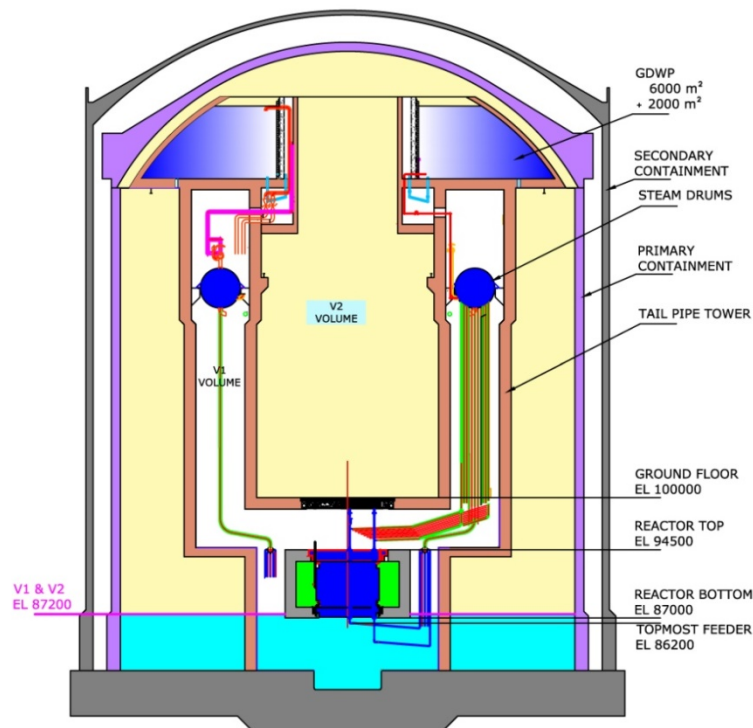


Figure-2.6 Relocation of GDWP water into V1 and V2

If the entire GDWP inventory spills into V2, the equilibrium level established is ~ 1 m above the topmost horizontal feeder providing passive heat sink for several days. In the event of cracks appearing in the primary containment wall in addition to the cracks in GDWP, then the spilled water level is just sufficient to submerge the topmost feeder as shown in Figure-2.7. In the unlikely event of a core melt, a core catcher has been incorporated in AHWR that will prevent recriticality and terminate the severe accident progression, retain the released radioactivity and the corium in the containment besides providing adequate cooling to the corium. Table-2.1 shows important design details of the reactor.

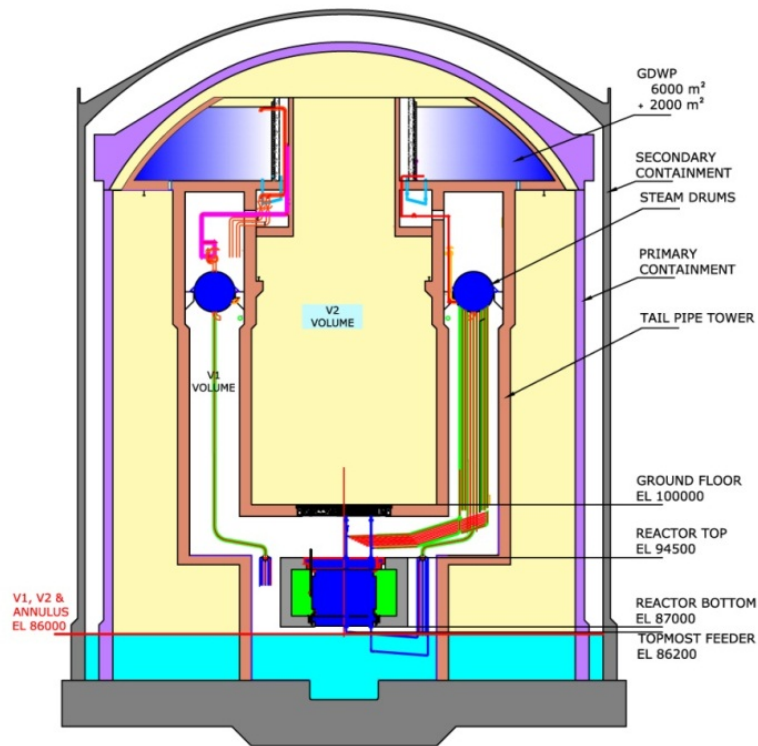


Figure-2.7 Relocation of GDWP water in V1, V2 and annulus gap

Table-2.1 Important Design Parameters of AHWR

Reactor power	920 MW _{th} , 300 MW _e
Core configuration	Vertical, pressure tube type design
Coolant	Boiling light water
Number of coolant channels	452
Pressure tube ID	120 mm
Lattice pitch	225 mm (square pitch)
No. of pins in fuel cluster	54

Active fuel length	3.5 m
Total core flow rate	2141 kg/s
Coolant inlet temperature	259 °C
Feed water temperature	130 °C
Average steam quality	19.1 %
Steam generation rate	408 kg/s
Steam drum pressure	70 bar (abs)
MHT loop height	39 m
No. of Feeders	452
No. of Tail pipes	452
No. of Down comers	16
No. of Steam Drums	4

2.2 Description of relevant postulated Fukushima scenarios for AHWR

Considering the severity of seismic event occurred at Fukushima, several scenarios were postulated for AHWR and are described below:

2.2.1 Case-a: Prolonged SBO with no loss of GDWP water

The rationale for this postulation is that practically no damage occurred to the Main Heat Transport System and the concrete structure during the Fukushima kind of earthquake and the reactor was shut down following a beyond design basis earthquake. Further, the GDWP in AHWR is steel lined and hence cracks in the concrete structure alone will not cause loss of inventory. Here, it may be noted that a reactor trip was incorporated on earthquake signal in all nuclear power plants in India including AHWR following the Fukushima event. In this case ICs are able to remove the decay heat generated after shut down.

2.2.2 Case-b: Prolonged SBO with partial loss of GDWP water

Here, it is postulated that cracks develop both in the GDWP concrete structure and steel lining leading to loss of GDWP water following a beyond design basis earth quake. Since there are eight different compartments in the GDWP, some may survive to provide cooling through the isolation condenser. Therefore, in this case one compartment out of eight GDWP compartments is assumed to survive the earthquake.

2.2.3 Case-c: Prolonged SBO with complete loss of GDWP water

In reality, it is possible to develop cracks in the GDWP concrete structure leading to loss of all GDWP water following a beyond design basis earth quake. Following the development of cracks in the bottom of the GDWP structure, the water can fall in both the V_1 and V_2 volumes of the primary containment. The bottom surface area of GDWP open to V_2 is considerably larger than that of V_1 . Hence leak into V_2 is more probable than V_1 volume. Besides water in V_2 volume can drain into V_1 through the drainpipes provided for this purpose (PAUSE system). Water falling in V_1 volume (tail pipe tower) of the primary containment progressively submerges the feeders, header and tailpipes providing prolonged cooling. Therefore, in this postulation 100% of GDWP water is postulated to fall in the V_2 volume and through the floor drains eventually finds its way to V_1 volume ultimately attaining an equilibrium level which is ~ 1m above the topmost feeder and decay heat can be removed by submerged feeders

2.2.4 Case-d: Prolonged SBO with loss of GDWP water and dry containment

Following the beyond design basis earth quake, the cracks are also developed on the Inner Containment Wall (ICW) causing water level to rise in the annulus. Under this condition, the water drained into the V_1 volume is much lower than that in Case-c. Also, cracks can develop in the Outer Containment Wall (OCW), such that the most of the GDWP water is drained to the outside of the containment. A small fraction could find its way to the primary containment but is unable to wet the feeders or any of the MHTS piping. Under this scenario, the heat sink is assumed lost immediately after the earth quake eventually leading to core meltdown. Following core meltdown, the corium finds its way to the core catcher and coolability of the corium in the core catcher is the issue to be addressed. Besides, the integrity of the tail pipe tower (part of the primary containment, and the last barrier standing) shall be

ensured to prevent release of radioactivity to the environment along with the safe disposal of the hydrogen produced within the containment.

2.3 Analysis methodology

The first three of the postulated scenarios, could be entirely addressed by present day system codes. Here in this study, RELAP5 Mod3.2 was used for system scale analysis. RELAP5 code is extensively used for SBO simulations and decay heat removal by natural model of cooling. Zhou and Novog (2017), Hidayat (2017), Trivedi et al (2016), and Gencheva et al (2015) have demonstrated the decay heat removal capability of pool type reactor, CANDU-900, AP-1000 and VVER-100 respectively with system scale code RELAP5. Considering the established capability of RELAP5 simulating the natural circulation/convection behavior for decay heat removal, it has been used for prolonged SBO simulations in AHWR. The model has been validated against the experimental data generated in integral test facilities. Large number of natural circulation test facilities has been built worldwide and capability of RELAP5 was established by various researchers. Takeda et al (2016) validated the RELAP5 for prediction of the natural circulation during decay heat removal in ROSA and LSTF test facilities. These test facilities are integral test facility of PWR. Mangal et. al (2012) and Hou et al (2017) has investigated the natural circulation behavior using RELAP5 based on their experiment test section data. Zou et.al (2014) have estimated the PRHRS cooling capability in core under design basis accidents and beyond design basis accidents using RELAP5. Their results showed that the PRHRS has good performance to remove heat generation from primary coolant system under accident condition.

For Case-d above, system codes can be used to analyze the scenario till the core melt. After the core melt, as the corium relocates into the core catcher, special codes are required to track the melt coolability.

2.3.1 Description of system code RELAP5

The RELAP5 (Reactor Excursion and Leak Analysis Program) series of codes has been developed at the Idaho National Laboratory (INL) under sponsorship of the U.S. Department of Energy, the U.S. Nuclear Regulatory Commission, members of the International Code Assessment and Applications Program (ICAAP), members of the Code Applications and Maintenance Program (CAMP), and members of the International RELAP5 Users Group (IRUG). Specific applications of the code include simulations of transients in light water reactor (LWR) systems such as loss of coolant, anticipated transients without scram (ATWS), and operational transients such as loss of feed-water, loss of offsite power, station blackout, and turbine trip.

RELAP5 is a highly generic code that, in addition to calculating the behavior of a reactor coolant system during a transient, can be used for simulation of a wide variety of hydraulic and thermal transients in both nuclear and non-nuclear systems involving mixtures of vapour, liquid, non-condensable gases, and non-volatile solute (RELAP5/Mod3.2 Code Manual, 1995). It is based on a non-homogeneous and non-equilibrium model for the two-phase system that is solved by a fast, partially implicit numerical scheme to permit economical calculation of system transients.

The code includes many generic component models from which general systems can be simulated. The component models include pumps, valves, pipes, heat releasing or absorbing structures, reactor kinetics, electric heaters, jet pumps, turbines, compressors, separators, annuli, pressurizers, feed-water heaters, ECC mixers, accumulators, and control system components. In addition, special process models are included for effects such as form loss, flow at an abrupt area change, branching, choked flow, boron tracking, and non-condensable gas transport.

The RELAP5/Mod 3.2 hydrodynamic model is a one-dimensional, transient, two-fluid model for flow of a two-phase steam-water mixture that can contain non-condensable components in the steam phase and/or a soluble component in the water phase. The RELAP5/Mod 3.2 thermal-hydraulic model solves eight field equations for eight primary dependent variables. The primary dependent variables are pressure (p), phasic specific enthalpy (h_G , h_L), vapor volume fraction (void fraction) (ϵ), phasic velocities (v_G , v_L), non-condensable quality (X_n), and boron density (ρ_b). The independent variables are time (t) and distance (x). The mathematical model was developed in late 70s by Ishii (1979). This is generally a four equation model for adiabatic flows and six equation model for diabatic flows. In this case, equations for mass, momentum and energy conservations are solved for each phase. While, the governing conservation equations are simple, the closure equations required for closing the mathematical model are quite complex and no universal agreement exists for closure laws. The mass balance for each phase per unit volume around an arbitrary point in the flow domain are given by Eq (2.1 and 2.2)

$$\frac{\partial}{\partial t}(\epsilon_G \rho_G) + \frac{\partial}{\partial x}(\epsilon_G \rho_G v_G) = \Gamma_G \quad \dots \dots \dots (2.1)$$

$$\frac{\partial}{\partial t}(\epsilon_L \rho_L) + \frac{\partial}{\partial x}(\epsilon_L \rho_L v_L) = \Gamma_L \quad \dots \dots \dots (2.2)$$

In the above equations, Γ_G and Γ_L are the mass source of vapour and liquid per unit volume of the pipe. As the interface can store no mass, the interface conditions would demand,

$$\Gamma_G = -\Gamma_L \quad \dots \dots \dots (2.3)$$

Similarly, the momentum equations for the two-phases are given by Eq. (2.4 and 2.5)

$$\begin{aligned} \frac{\partial}{\partial t}(\epsilon_G \rho_G v_G) + \frac{\partial}{\partial x}(\epsilon_G \rho_G v_G v_G) \\ = -\epsilon_G \frac{\partial p}{\partial x} - \Delta p \frac{\partial \epsilon_G}{\partial x} + \epsilon_G \rho_G g + F_G^i + F_G^W + \Gamma_G v_G \quad \dots \dots \dots (2.4) \end{aligned}$$

$$\begin{aligned} \frac{\partial}{\partial t}(\epsilon_L \rho_L v_L) + \frac{\partial}{\partial x}(\epsilon_L \rho_L v_L v_L) \\ = -\epsilon_L \frac{\partial p}{\partial x} - \Delta p \frac{\partial \epsilon_L}{\partial x} + \epsilon_L \rho_L g + F_L^i + F_L^W + \Gamma_L v_L \quad \dots \dots \dots (2.5) \end{aligned}$$

In the above equations, the convective term on the left hand side has been written after simplifying to the primitive form and taking the velocity inside the derivative. On the right hand side, the force terms sequentially are, the pressure term, body force term, interfacial friction term, wall friction term and interfacial momentum transfer term due to mass transfer.

Energy equation for gas and liquid phases can be written by Eq. (2.6 and 2.7)

$$\begin{aligned} \frac{\partial}{\partial t}(\epsilon_G \rho_G h_G) + \frac{\partial}{\partial x}(\epsilon_G \rho_G v_G h_G) \\ = -\epsilon_G \left(\frac{\partial p}{\partial t} + v_G \frac{\partial p}{\partial x} \right) + Q_G^W + Q_G^i + \Gamma_G h_G^* \quad \dots \dots \dots (2.6) \end{aligned}$$

$$\begin{aligned} \frac{\partial}{\partial t}(\epsilon_L \rho_L h_L) + \frac{\partial}{\partial x}(\epsilon_L \rho_L v_L h_L) \\ = -\epsilon_L \left(\frac{\partial p}{\partial t} + v_L \frac{\partial p}{\partial x} \right) + Q_L^W + Q_L^i + \Gamma_L h_L^* \quad \dots \dots \dots (2.7) \end{aligned}$$

The first and second term on LHS is accumulation and convective term which is has been written after simplifying to the primitive form and taking the velocity inside the derivative. On the right hand side, the energy terms sequentially are, the work done by pressure, wall heat transfer, interfacial energy transfer term and heat transfer due to mass transfer. Here in this mathematical formulation the numbers of unknowns are 7 while equations are 6 in

numbers, so we have to solve one additional equation that establishes the relation between density and pressure (equation of state). Besides it requires number of closures for modeling the interaction terms like momentum and energy interaction between the phases and the conduit wall.

The difference equations in RELAP5/Mod 3.2 are based on the concept of a control volume (or mesh cell) in which mass and energy are conserved by equating accumulation to the rate of mass and energy in through the cell boundaries minus the rate of mass and energy out through the cell boundaries plus the source terms. This model results in defining mass and energy volume average properties and requiring knowledge of velocities at the volume boundaries. The velocities at boundaries are most conveniently defined through the use of momentum control volumes (cells) centered on the mass and energy cell boundaries. This approach results in a numerical scheme having a staggered spatial mesh. The scalar properties (pressure, energies, and void fraction) of the flow are defined at cell centers, and vector quantities (velocities) are defined on the cell boundaries.

A semi-implicit numerical solution scheme is employed, based on replacing the system of differential equations with a system of finite difference equations partially implicit in time. For prolonged SBO simulations maximum and minimum time step specified are 0.25 sec and 1e-8 sec. The semi-implicit numerical solution scheme uses a direct sparse matrix solution technique for time step advancement. The method has a material Courant time step stability limit.

The constitutive relations in RELAP5/Mod 3.2 include models for defining flow regimes and flow-regime related models for interphase drag and shear, the coefficient of virtual mass, wall friction, wall heat transfer, interphase heat and mass transfer.

The phasic interfacial friction force calculations in RELAP5/Mod 3.2 are done using two different models; the drift flux method and the drag coefficient method. The constitutive

models are flow regime dependent. The drift flux approach is used in the bubbly and slug flow regimes for vertical flow. It specifies the distribution coefficient and the vapor drift velocity. The drag coefficient method is used in all flow regimes except for bubbly and slug flows in vertical components. This model uses correlations for drag coefficients and for the computation of the interfacial area density.

The wall friction calculations are based on a two-phase multiplier approach, in which the two-phase multiplier is calculated from the Heat Transfer and Fluid Flow Service (HTFS)-modified Baroczy correlation (Baroczy, 1968). The individual phasic wall friction components are calculated by apportioning the two-phase friction between the phases using a technique derived by Chisholm (Chisholm, 1967) from the Lockhart- Martinelli model (Lockhart and Martinelli, 1949). The partitioning model is based on the assumption that the frictional pressure drop may be calculated using a quasi-steady form of the momentum equation. Table-2.2 shows various empirical models incorporated in RELAP-5 and uncertainty associated with the models. Model uncertainty plays important role in the performance analysis of the safety systems. Such study is essential while doing Reliability assessment of the passive systems. Kumar et al (2014) have considered the effect of model uncertainties on the performance of the PCCS of AHWR during LOCA. They concluded that model parameters have significant effect on the performance of the passive systems and hence reliability, but, no safety issue was observed during LOCA (peak containment pressure was below containment design pressure). In an another study carried out by Nayak et al (2009), reliability of ICs of AHWR was assessed using APSRA (Assessment of Passive System ReliAbility) methodology. The failure probability of ICs to maintain the hot shut down has been calculated by them. They have considered the variation in the important operating and model parameters for reliability calculations.

Table-2.2 Various Models in RELAP & Associated Uncertainties

Sl.No.	Model	Uncertainty
1.	Heat Transfer I. Dittus-Boelter Correlation (Dittus and Boelter, 1930) II. Sellars-Tribus-Klein Correlation (Sellars et al., 1956) III. Churchill-Chu Correlation (Churchill and Chu, 1975) IV. Nusselt Correlation, (Nusselt, 1916) V. Shah Correlation (Shah, 1976) VI. Chato Correlation (Chato, 1961) VII. Chen Correlation (Chen, 1966)	$\pm 25\%$ $\pm 10\%$ $\pm 12.5\%$ $\pm 7.2\%$ $\pm 25.1\%$ $\pm 16\%$ $\pm 11.6\%$
2.	Wall Friction I. Colebrook-White Correlation with Zigrang-Sylvester Approximation II. Lockhart-Martinelli Correlation (Lockhart and Martinelli, 1949) III. HTFS modified-Baroczy Correlation (Baroczy, 1968)	$\pm 0.5\%$ $\pm 25.61\%$ $\pm 21.2\%$
3.	Interphase Friction I. Chexal-Lellouche Correlation (Drift Flux Model) II. Drag Coefficient Method	$\pm 15.25\%$ $\pm 30\%$
4.	Choking Flow	$\pm 5\%$
5.	Abrupt Area Change	N/A
6.	Counter Current Flow Limitation	$\pm 8.7\%$
7.	Modified Energy Term	N/A
8.	Stratification	$\pm 20\%$
9.	Thermal Front Tracking	$\pm 13-19\%$

2.3.2 Analysis for Case-a: Prolonged SBO with no loss of GDWP water

Scenario considered: Reactor trips at $t=0$ on earthquake signal and decay heat is now required to be removed. Figure-2.8 shows the decay heat curve for the reactor. The station blackout occurs at $t=0$, leading to the closure of Main Steam Isolation Valve (MSIV) thus boxing up the MHTS. The MHTS is intact along with the Isolation Condensers (ICs) and Emergency Core Cooling System (ECCS). The ECCS consisting of high pressure accumulators (HPA) and low pressure GDWP are assumed to be available. Following the boxing up of MHTS, the MHT pressure increases and when it reaches the set point of the passive valve, it opens and closes maintaining the MHTS in hot shutdown state by transferring heat to the GDWP water through Isolation condensers (Figure-2.3). At $t=30$

minutes, the active valve opens and remains open thereafter for the remainder of the transient and thus dumping the decay heat into GDWP through ICs and MHTS gets depressurized.

These Active valves are pneumatic control valves which actuates with the fail safe open logic. Once, the air supply to the valves stops, these valves opens. However, if these valves do not open, though the decay heat can also be removed by ICs with operation of passive valves only. Only MHTS will remain pressurized in that condition.

Details of ICs are depicted in Table-2.3. When the MHTS pressure falls below the set point (5 MPa) of the Accumulator isolation passive valve, then high pressure Accumulator cuts in.

During this transient, the heat is rejected to the GDWP water raising its temperature.

Table-2.3 Important Parameters of Isolation Condenser

Number of ICs	8
Heat Transfer Area/IC	27.28 m ²
Number of Pipes/IC	90
Pitch	100 mm
Header Length	1.2 m
Header Size	300 mm NB SCH 80 (324 mm OD X 25.4 mm WT)
Tube Length	1.6 m
Pipe Size	50 mm NB SCH 80 (60.3 mm OD X 5.5 mm WT)
Overall Size	
Length	4 m
Width	1.2 m
Height	2.2 m
Level of GDWP when ICs start uncovering	3.0 m (GDWP total Level is 6.67m)

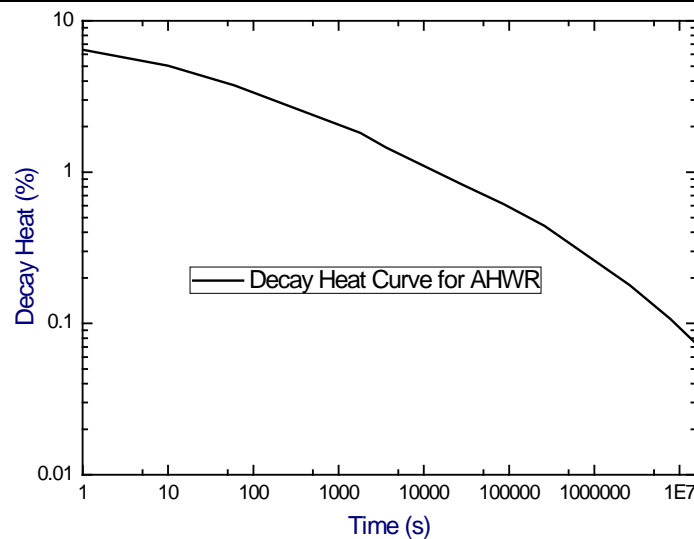


Figure-2.8: Decay Heat Curve for AHWR (Log-Log Plot)

Nodalisation Details: Figure-2.9 shows RELAP5 nodalisation adopted. Various systems of the reactor viz Main Heat Transport System (MHTS), Isolation Condensers (ICs); Emergency Core Cooling System (ECCS), Passive Containment Cooling System (PCCS) and Primary Containment volumes i.e. V1 and V2 are integrally simulated with the system code RELAP5 Mod3.2. Initially, steady state is obtained for MHTS and the containment volumes V1, V2 and ECCS are initialized as per the initial conditions given in Table-2.4.

In RELAP5 Nodalisation, all the channels in the MHTS are grouped as a single equivalent channel having the total flow area and heat transfer area, generating the full power. This channel is connected to a single equivalent feeder of the 452 feeders of the reactor and a single equivalent tail pipe of the 452 tail pipes of the reactor. The four steam drums are combined into an equivalent steam drum. Similarly all the downcomers are modelled as an equivalent downcomer which is connected between the header and steam drum. All the tubes in the ICs are combined into an equivalent tube connected between the headers of the ICs. Five axial nodes are taken for IC tubes, which are associated with heat structure. The GDWP is connected to the containment volume V2 since GDWP is situated at the top of the containment. The two containment volumes are initially isolated from each other and filled with the air at the normal operating condition as shown in Table-2.4. The containment volume V1 is modeled without heat absorbing capacity, while volume V2 is modeled with heat absorbing capacity. In order to estimate the heat transfer to the containment wall during condensation, the heat structure associated with the containment volume V2 is divided in 21 radial mesh points. The first 5 mesh points are 5 mm width and next 5 mesh points are of 10 mm width. This is followed by 5 numbers of 25 mm width and 6 numbers of 322.5mm. Since concrete is having poor thermal conductivity and high heat capacity, the nodalisation considered in the radial direction gives more accurate prediction of condensation on V2 volume wall than considering an average one, so to account the realistic rate of heat of heat

transfer relatively fine nodalisation is taken. It may be noted that thermal stratification in the large pool is a 3-D phenomenon requiring special attention. It is difficult to model with system codes. It requires 3-D CFD treatment for modeling and experimental demonstration and itself is topic of research. However, this problem can be modeled to some extent by a suitable nodalisation in RELAP5. In case of AHWR, GDWP has been equipped with 3 shrouds which facilitate channelizing the flow in GDWP so as to suppress thermal stratification problem. RELAP nodalisation has been prepared with the shroud arrangement to avoid thermal stratification and optimum utilization of the pool.

Table-2.4 Initial Operating Conditions for Various Systems of the Reactor

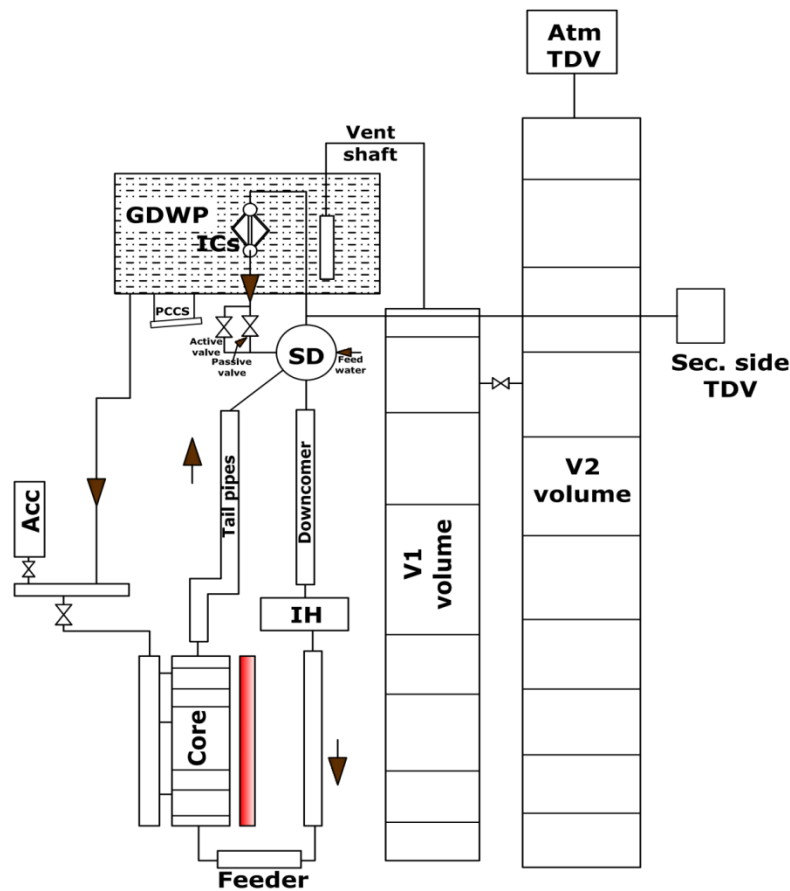
	Pressure	Temperature	Power
MHTS	70bar (abs)	Core Inlet = 260 ⁰ C Core Outlet = 285 ⁰ C	920MW (Full Power)
V1 Volume	1.0056 bar (abs)	285 ⁰ C	
V2 Volume	1.0046172 bar (abs)	30 ⁰ C	
Advanced Accumulator (ECCS)	55bar (abs)	40 ⁰ C	
GDWP (ECCS)	4 bar (abs)	40 ⁰ C	
Passive Valve	Start opening at 76.5 bar and fully opens at 79.5 bar of MHTS		
Active Valve	Opens at 79.5 bar of MHTS or 30 minutes after SBO (due to loss of pneumatic supply)		

2.3.3 Analysis for Case-b: Prolonged SBO with partial loss of GDWP water

Scenario considered: Reactor trips at t=0 on earthquake signal. The effect of earthquake is assumed to be so severe that only one out of the eight compartments survives. The MHTS is assumed intact along with the Isolation Condensers (ICs) whereas GDWP water is lost in all due to cracks triggered by the earthquake but one of the compartments survives. SBO occurs

at $t=0$, leading to the closure of MSIV thus boxing up the MHTS. The GDWP water lost eventually accumulates in V1 volume providing passive cooling through the submerged primary piping.

However, no credit is given to this heat removal. The seven uncovered isolation condenser lose heat by natural convection to the containment atmosphere increasing its pressure and temperature. This is accounted in the analysis so as to ensure that the concrete temperature remains within safe limits. Heat loss from the concrete is neglected in this analysis.



Acc: Accumulator
 Atm TDV: Atmospheric Time dependent Volume
 GDWP: Gravity Driven Water Pool
 IH: Inlet Header
 ICs: Isolation Condensers
 SD: Steam Drum
 Sec. Side TDV: TDV simulating secondary side conditions (7MPa)

Figure-2.9 RELAP5 Nodalisation for AHWR

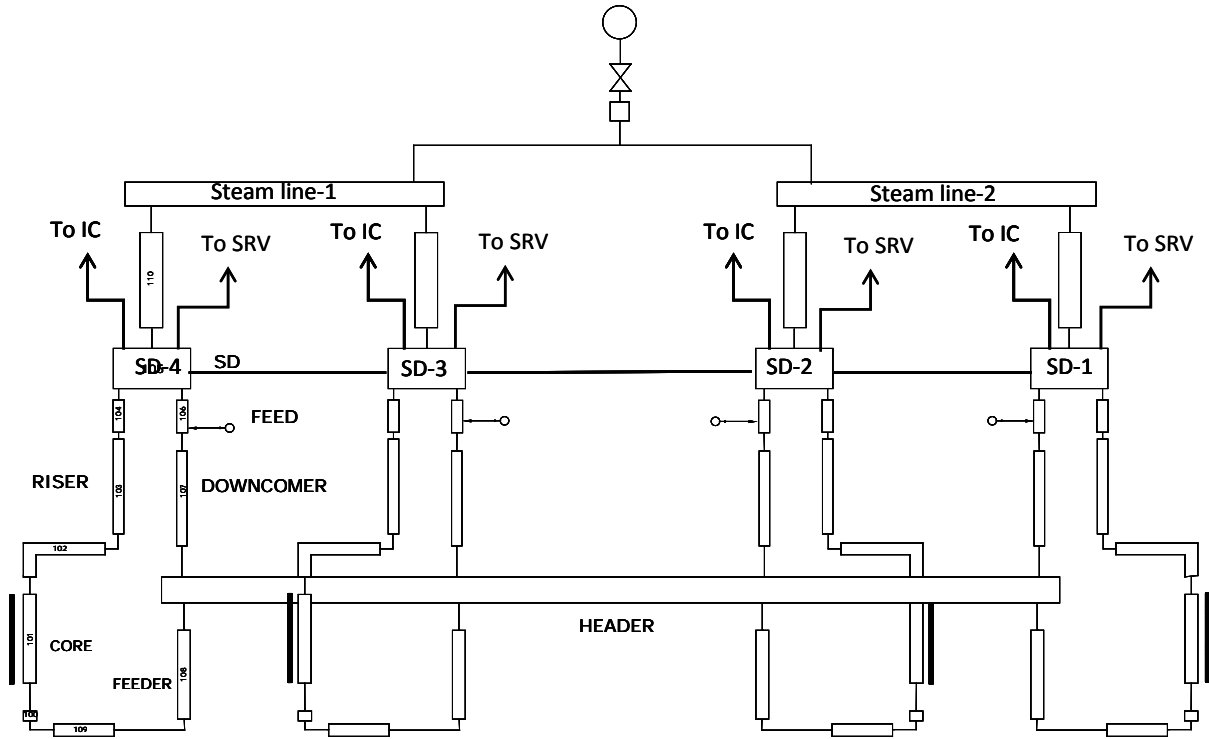


Figure-2.10 RELAP5 Nodalization of MHTS for Case-b

Nodalisation considered: Figure-2.10 shows MHTS the nodalisation for Case-b, rest of the nodalisation remains same as shown in Figure-2.9. In this case, the MHTS is modeled as four independent loops. The interconnections of the steam drum water space as well as steam space are considered.

2.3.4 Analysis for Case-c: Prolonged SBO with complete loss of GDWP water

Scenario considered: Under this condition, GDWP as a heat sink is assumed being lost completely. However, there will be heat rejection from the exposed ICs by natural convection to the GDWP atmosphere. The main heat sink under this condition will be the accumulated water in the V1 volume of the primary containment. Part of the ECCS consisting of high pressure accumulators (HPA) is assumed to be available. Following the boxing up of MHTS, the MHT feeders and other exposed pipes reject heat to the accumulated water in the primary containment (i.e. volume V1). At t=30 minutes, the active valve opens and remains open thereafter for the remainder of the transient. If the MHTS pressure falls below the set point (5

MPa) of the accumulator isolation passive valve, it opens and high pressure Accumulator valves in. Containment heating and pressurization occurs due to the heat rejection through the ICs (by natural convection of air) as well as through the MHT piping (by natural convection of water and boil-off).

Nodalisation adopted: In this case, the nodalisation considered is same as that for Case-a.

2.3.5 Analysis for Case-d: Prolonged SBO with loss of GDWP & dry containment

Scenario considered: Reactor trips at time $t=0$ on earthquake signal. The station blackout occurs at $t=0$, leading to the closure of MSIV thus boxing up the MHTS. The MHTS is intact along with the Isolation Condensers (ICs) whereas GDWP water is lost almost completely to the outside of containment. Even if some water finds its way into the primary containment (i.e. volume V1), the level of water in the primary containment is below the feeder pipes, so that no heat transfer from MHTS feeders or tail pipes to this water takes place. Part of the ECCS, consisting of high pressure accumulators (HPA) is assumed to be available. Following the boxing up of MHTS, the MHT pressure increases and when it reaches the set point of the passive valve, it opens and closes periodically, maintaining the MHTS in hot shutdown state. At $t=30$ minutes, the active valve opens and remains open thereafter for the remainder of the transient. If the MHTS pressure falls below the set point (5 MPa) of the accumulator isolation passive valve, it opens and HPA valves in. During this transient, heat is rejected to the containment through ICs by natural convection of air as well as by the relief valves. This heat rejection to the containment leads to rising containment pressure and temperature. The heat rejection from MHTS takes place initially by the available inventory in MHTS and accumulator and inventory of MHTS boils off. As the MHTS inventory loss by boil-off (through the relief valves) continues, eventual core uncover and heat up results leading to core meltdown. RELAP nodalisation adopted is same as that shown in Figure- 2.9.

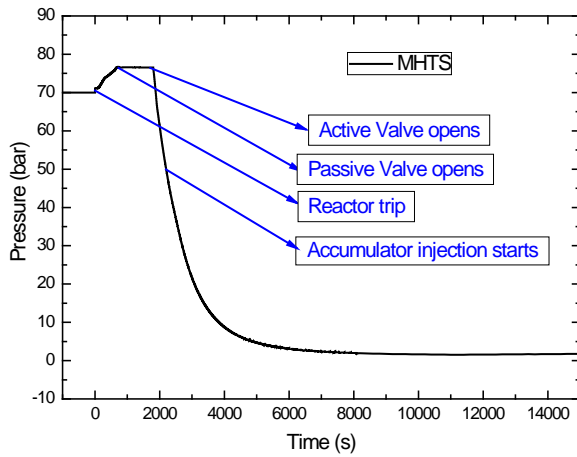
2.4 Results and discussions

Case a: In this case, the MHTS pressure starts rising following the boxing up of MHTS. The isolation condenser system is valved in periodically by the action of the HSPV (Hot Shutdown Passive Valve) when the pressure reaches 76.5 bar. After 30 minutes, the active valve opens and there after remains open, which leads to the large reduction rate in pressure as shown in Figure-2.11a. As the pressure falls below the set point of the accumulators, it valves in and low level isolation occurs at about 2.5 hours. However, the pressure remains well above the set point of the low pressure injection system. Passive core cooling continues by rejection of heat into the GDWP through ICs.

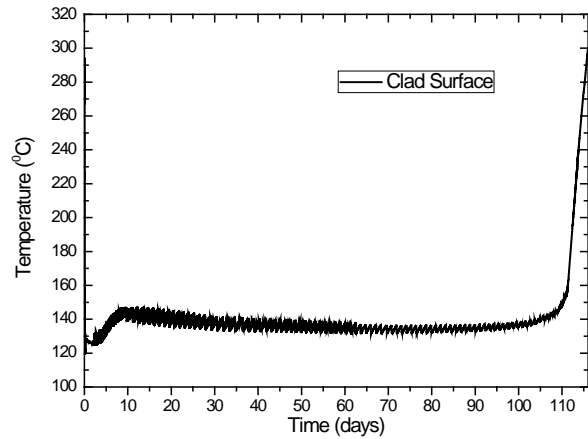
With GDWP available, AHWR can withstand very long periods (exceeding three months) of station blackout without clad temperature rise as shown in Figure-2.11b. However, long periods of station blackout leads to containment pressure rise beyond the design pressure, once the GDWP water starts boiling (Figure-2.11c). The GDWP water starts boiling after about seven days. Although the pressure is well below the design pressure even after 7 days, approximately 500 m³ of GDWP water evaporates during this time. Hence, credit for station black out can be taken for only that duration for which containment pressure equals its design pressure (approx. 7 days) in case of AHWR. However, with the incorporation of a filtered and vented system, the station blackout can be taken for very long duration as shown in Figure-2.11c. The GDWP water can serve the purpose for nearly 110 days, in which the GDWP water completely boils off (Figure-2.11d). Figure-2.11e shows that the MHTS pressure rises after 110 days after complete boiling off of the GDWP water. After 105 days, the GDWP water level falls below 1.2 m and the ICs got exposed to the surrounding atmosphere of the containment eventually heat transfer become poor due to unavailability of water around the IC tubes. In that case, the ICs are no longer able to remove decay heat generated in the core and MHTS pressure starts rising. Once the MHTS pressure reaches to

92 bar safety relief valve opens and resets at 88 bar and continue. Thus decay heat is removed by losing the primary inventory. After around 27 hrs, core uncover (water level starts falling below active core) starts and clad surface temperature rises in uncontrollable manner which is reflected in the Fig-2a after 100 days.

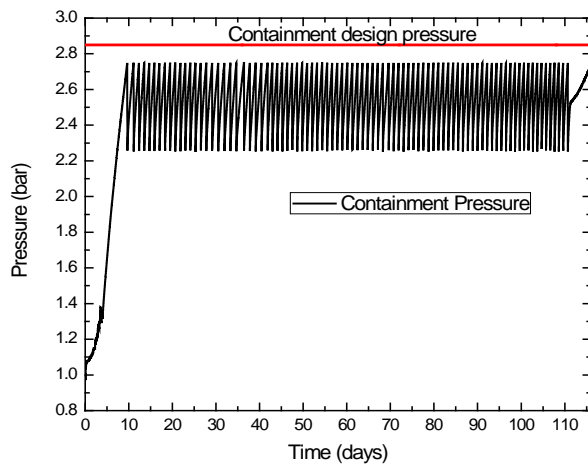
Case b: In this case, the MHTS pressure continues to rise even after valving in of the only remaining ICs (Figure-2.12a). After half an hour, although the active valve opens, this is unable to bring down the pressure. The pressure continues to rise, but the peak value reached is below the set point of the safety relief valves.



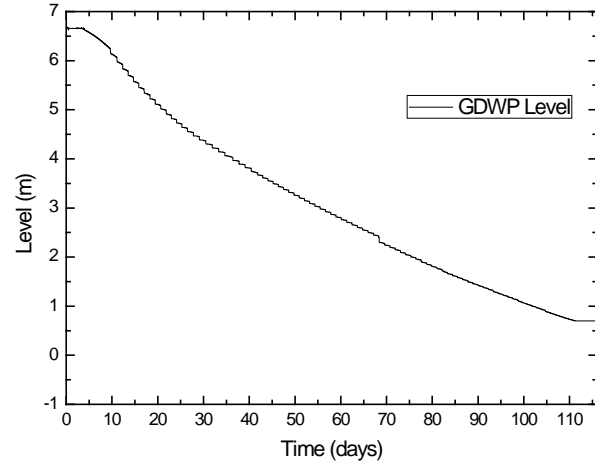
(a) MHTS Pressure



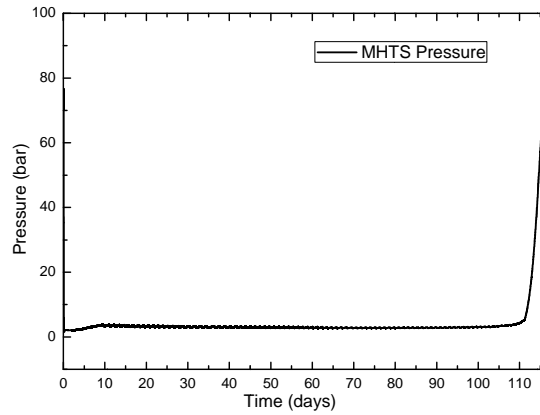
(b) Clad temperature



(c) Containment Pressure



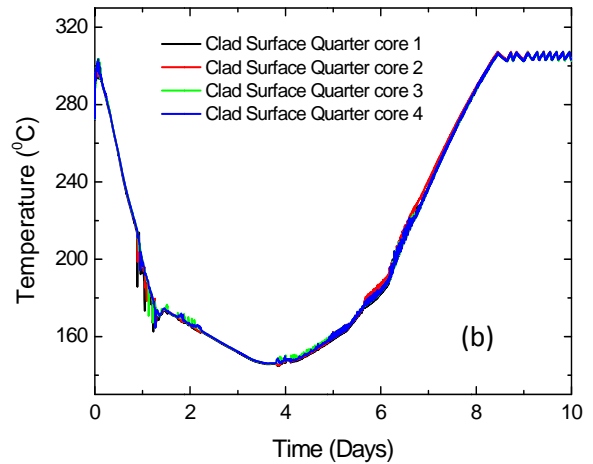
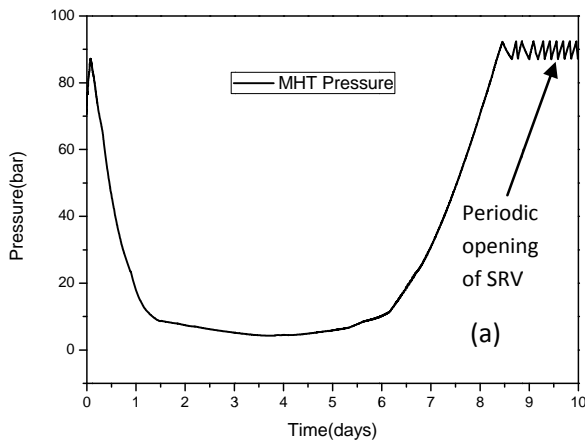
(d) GDWP level



(e) MHTS pressure for long term

Figure-2.11 SBO results with no loss of GDWP water (Case-a)

Beyond about 2 hours, the pressure begins to fall reaching the accumulator set point at about 11.5 hours. The peak clad temperature reached is about 10°C more than the normal operating value (Figure-2.12b). After ~4 days available ICs performance degraded due to lesser water available in GDWP tank and pressure of MHTS starts building. The Containment pressure and level are given in Figure-2.12c and d respectively. At the end of sixth days, the GDWP level attains a constant value indicating the complete exposure of IC tubes. As the exposure of IC tubes progresses, MHTS temperature increases. After about 8 days, MHTS pressure is maintained by the periodic opening of SRVs (Safety Relief Valves).



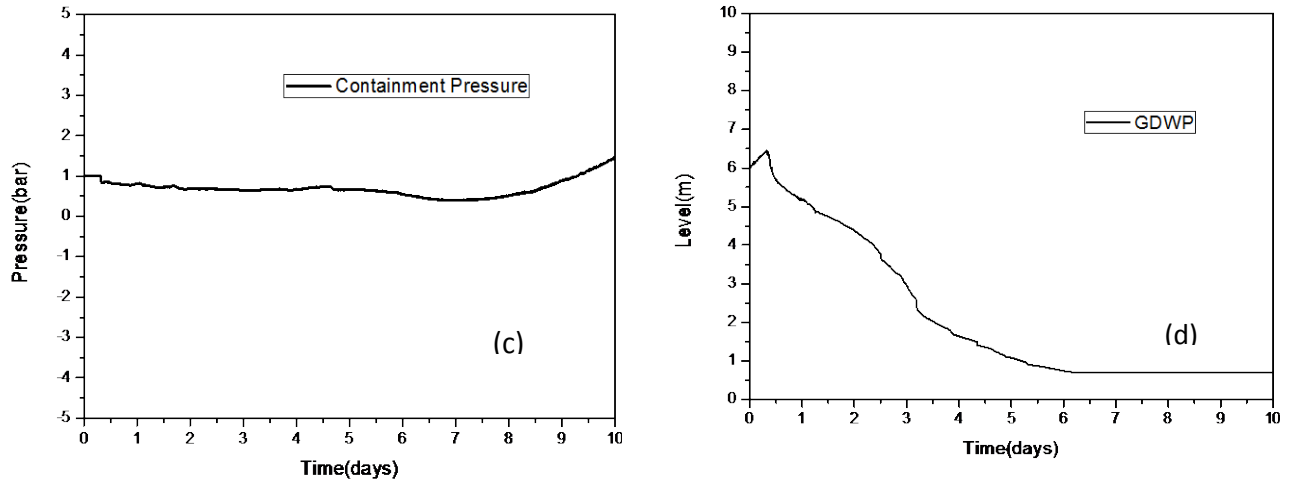
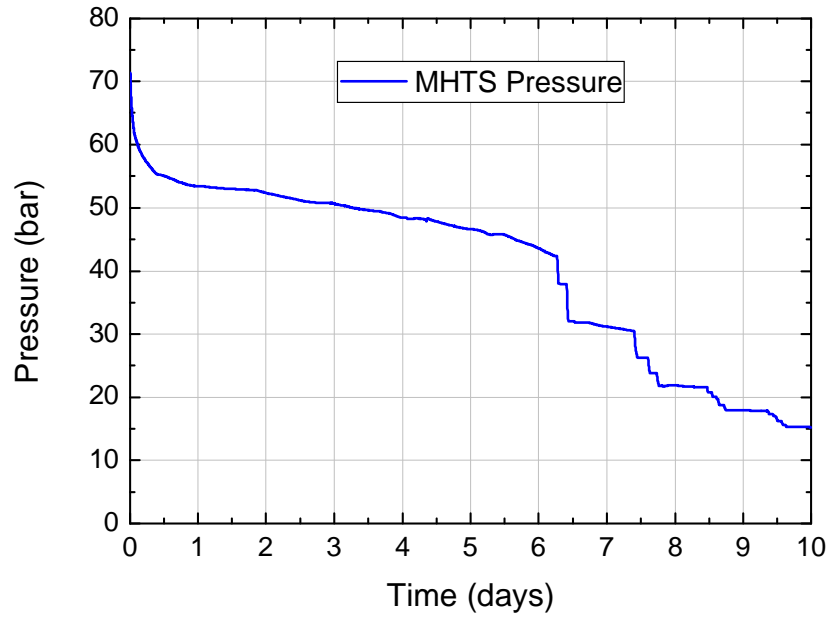
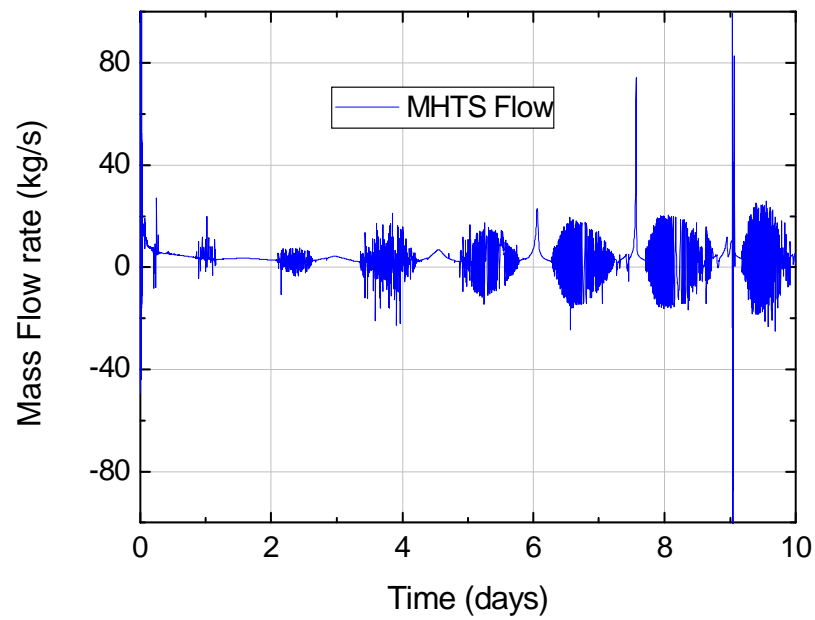


Figure-2.12 SBO results with partial loss of GDWP water (Case-b)

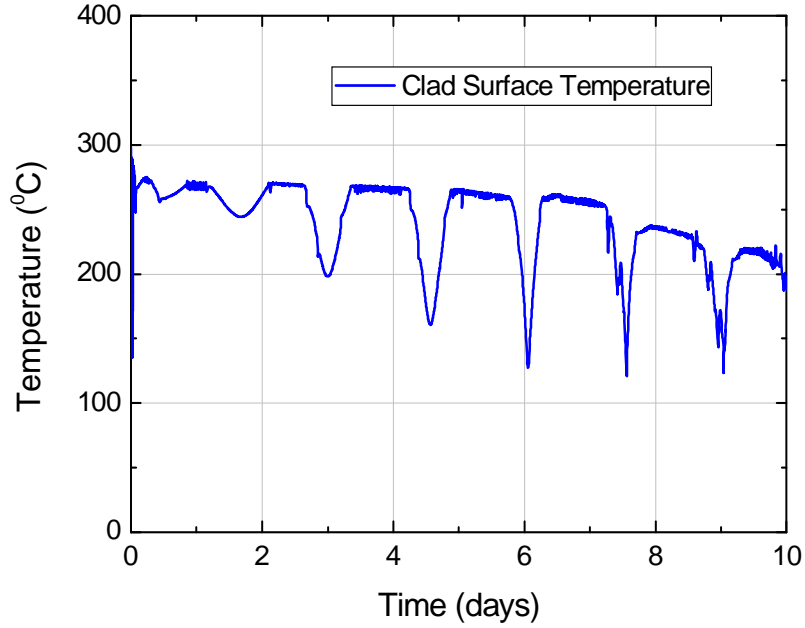
Case-c: It may be noted that this calculation assumes instantaneous relocation of the GDWP inventory to V1 volume. This assumption is conservative as water in the GDWP tends to cool down the MHTS much faster. As shown in this case, pressure does not even rise to the set point of HSPV (Figure-2.13a) and the opening of the active valve after 30 minutes does not cause crash cooling as all the GDWP water is assumed lost at $t=0$. The MHTS pressure gradually reduces to the set point of accumulator passive valve in about 3.5 days. The mass flow rate is found to be oscillating around the zero value (Figure-2.13b) since the heat sink of the MHTS is now located at the bottom most elevation. Under near stagnant flow conditions, the core fluid temperature keeps on rising, and it is able to overcome the negative buoyant effect of the heat sink at the lowermost elevation of the MHT loop resulting in periodic flow. The periodic flow is sufficient to maintain the clad surface temperature below the normal operating point (Figure-2.13c).



(a) MHTS Pressure for Case-c



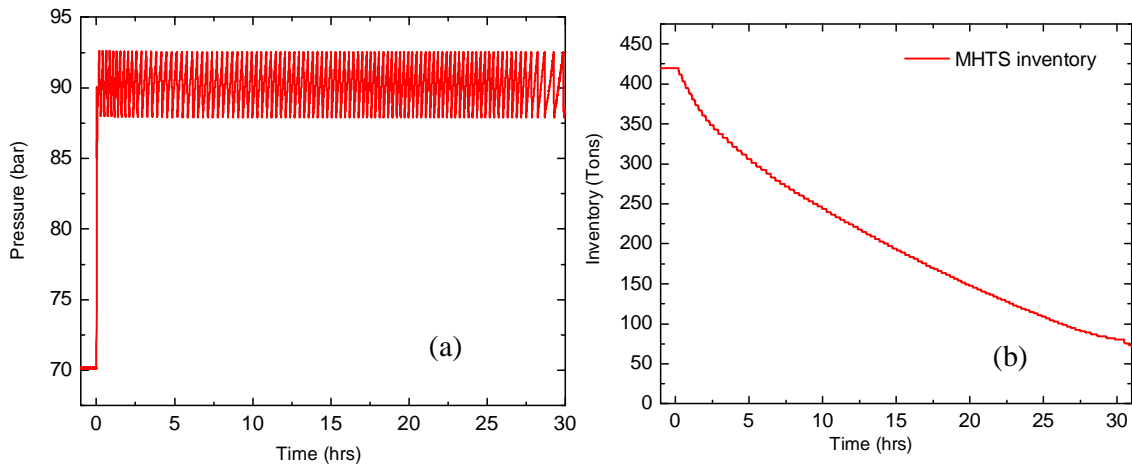
(b) MHT flow for Case-c



(c) Clad temperature for Case-c

Figure-2.13 SBO results with complete loss of GDWP water (Case-c)

Case d: Even under this condition, no clad over heating takes place for slightly more than a day (~27 hours). The heat removal is maintained by boil-off through the safety relief valve (Figure-2.14a). The initial inventory of 420 tons reduces gradually (Figure-2.14b) and significant fuel heat up occurs only after 27 hours (Figure-2.14c). Significant amount of hydrogen generation starts at about 32.5 hours (Figure-2.14d) and the total hydrogen released is about 440 kg.



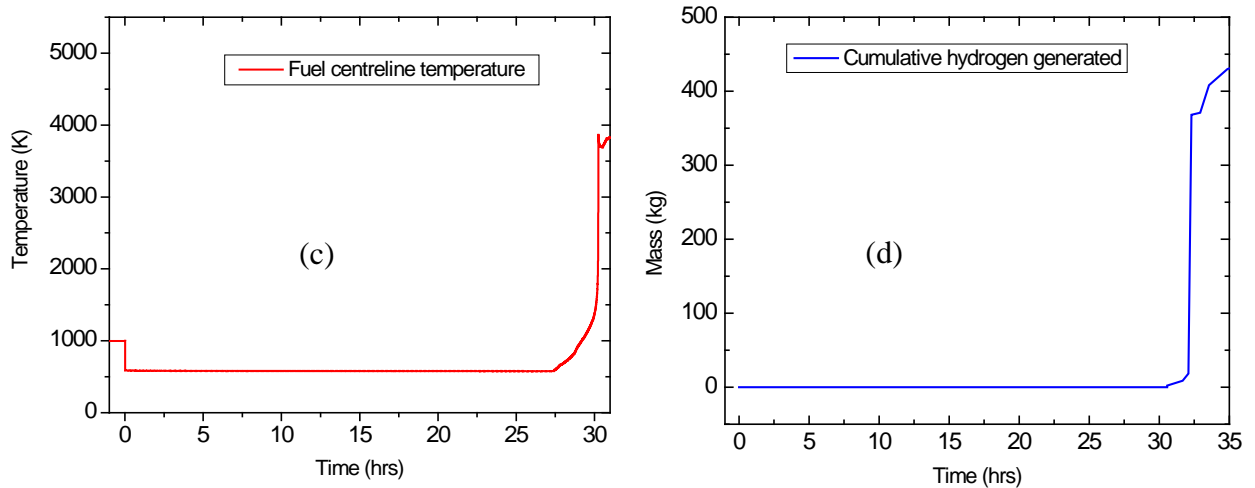


Figure-2.14 SBO with complete loss of GDWP water and dry containment (Case-d)

2.5 Closure

The Analysis was carried out for various cases postulated for AHWR. Integral system behavior of the reactor in Fukushima type of accident is studied by simulating with RELAP5. Various systems of the reactor viz. MHTS, ICs, Containment (V1 and V2 volume) and GDWP are simulated for a postulated initializing event (Fukushima type) causing prolonged SBO in the reactor.

The analysis confirmed that reactor design is capable of removing decay heat for more than 100 days. The results indicate that the reactor, after being shut down safely on seismic signal similar to that in Fukushima, can remove the decay heat by passive means using ICs which dissipate the heat into the Gravity Driven Water Pool (GDWP). The GDWP holds a large amount of water of about 8000 m^3 , which is located at a relatively higher elevation from the steam drum of the reactor in order to promote natural circulation. The large pool of water i.e. GDWP ($\sim 8000 \text{ m}^3$) can absorb the decay heat for more than 100 days. The steam so generated by boil-off of the water in GDWP, can condense passively on the walls of containment and on tubes of PCCS without exceeding the containment design pressure for 7 days. If venting is carried out beyond this period, the decay heat can be removed passively even for longer period.

However, with isolation condensers it is ensured that decay heat can be removed for more than 100 days but the cooling of Moderator and Endshield could not be maintained and containment pressurizes to its design limits after 7 days. It is important to maintain the temperature of Moderator and Endshield within design safe limits (below 100⁰C) to ensure the reactor integrity. If the temperature of Moderator and Endshield is not maintained the moderator gets leak out in the containment due to pressurization of the Calandria Vessel (~4 hrs) and radioactivity will be released inside the containment. A need for few new passive systems is established for ensuring the safe decay heat removal for prolonged period. To cater the issues, new passive systems called PMCS and PECS are incorporated in the design. Details of these systems are discussed in Chapter-3. Performance studies after incorporation of new systems are also discussed in next chapters.

Besides, RELAP being a one-D code is not capable to capture the initiation of the natural circulation flow in the big vessels or pools due to highly 3-D nature of the phenomena. RELAP solves the flow field equations in flow direction only and uses empirical closures for interactions at the transverse directions in the flow domain. RELAP is able to capture the gross/global circulation flows in the loops once the flow gets established in the natural circulation system. However, thermal stratification problem was handled to some extent by a proper nodalisation scheme with parallel pipes connected in transverse direction, but, sometimes it gives more mixing than the realistic situations (Verma et al, 2013). Thermal stratification and simulation of initial phase of natural circulation cannot be addressed by RELAP, so 3-D CFD simulations need to be performed for stratification studies.

CHAPTER-3

Post Fukushima Design Modifications: Experimental Studies

3.1 Introduction.....	45
3.2 Post Fukushima design modifications in AHWR	46
3.2.1 Passive Moderator Cooling System (PMCS)	47
3.2.2 Passive End-shield Cooling System (PECS)	48
3.2.3 Passive Union of V1 & V2 volumes of primary containment (PAUSE)	50
3.2.4 Core catcher	51
3.2.5 Hydrogen mitigation system.....	52
3.2.6 Containment Filtered Venting System (CFVS).....	52
3.3 Experimental studies.....	52
3.3.1 Scaling methodology	52
3.3.2 Integrated Scaled Test Facility	56
<i>Scaled Passive Moderator Cooling System</i>	56
<i>Scaled Passive Endshield Cooling System</i>	57
<i>Scaled GDWP tank with simulated Isolation condenser heaters</i>	58
3.3.3 Instrumentation for the Test Facility	58
3.3.4 Scaling adequacy and distortion	59
3.3.5 Experiment conducted	60
3.3.6 Experimental results	61
3.4 Closure	65

3.1 Introduction

The recent Fukushima accident raised strong concern and apprehensions about the safety of reactors in case of a prolonged SBO continuing for several days. Design of the new and existing reactors are being assessed considering Fukushima type of accident and even for much more low probable events. It resulted in more and more use of passive systems in the reactor design for performing safety function. Considering this, passive systems are increasingly playing a prominent role in the advanced nuclear reactor designs and are being utilized for normal operations as well as in safety systems of the nuclear reactors. A passive system essentially removes dependency on external sources of energy and operates solely based on natural physical principles. Also, it reduces dependency on human actions for operation. Passive systems are credited with a higher reliability as compared to active systems, because of reduced unavailability due to hardware failure and human error.

Besides, in existing NPPs a number of safety provisions are incorporated at the site as Fukushima safety measures after learning the lessons from this event. Some of the important lessons that can be learned from Fukushima accident includes:

- a. Requirement of longer grace period (~7 days) for safety systems
- b. Need of operator independence for prolonged period
- c. Prevention of containment over pressurization
- d. Provision of Hydrogen mitigation measures
- e. Provision of Core melt stabilization technique
- f. Prevention of fission product release into environment
- g. Protection of electrical and I&C system from floods/Tsunamis
- h. Enhancement of the seismic safety

3.2 Post Fukushima design modifications in AHWR

A detailed study has been performed simulating low probable events like Fukushima in AHWR. In such scenario, it is found that the decay heat can be safely removed for more than 100 days with the help of isolation condensers through natural circulation being the mode of cooling. Various cases addressing Fukushima kind of events and even more severe cases have been studied as discussed in Chapter-2. However, in those cases, the moderator and Endshield temperature and pressure may rise due to non-availability of their cooling in prolonged SBO conditions.

To cope with such issues and maintaining the conditions for moderator and Endshield within safe limits for at least 7 days, a noble concept of moderator and endshield cooling has been incorporated in the reactor design. A new passive safety system for maintaining the moderator conditions called Passive Moderator Cooling System (PMCS) has been envisaged and incorporated in the reactor along with Passive Endshield Cooling System (PECS) that maintains the conditions in the Endshields. The reactor design after incorporation of PMCS and PECS is assessed in view of Fukushima scenario.

Learning from Fukushima accident, following systems/design provisions have been incorporated in the AHWR design to minimize the impact to public in the event of design extension conditions.

1. Passive moderator cooling system (PMCS)
2. Passive End-shield cooling system (PECS)
3. Passive Union of V1 and V2 volumes of Containment (PAUSE)
4. Core catcher
5. Hydrogen management system
6. Containment Filtered Venting System (CFVS)

3.2.1 Passive Moderator Cooling System (PMCS)

In thermal reactors, purpose of moderator is to maintain criticality in the reactor core by slowing down the high-energy neutrons to low energy thermal neutrons where their probability for fission capture is greater. Heavy water used as moderator inside the calandria gets heated up due to neutron moderation and capture, attenuation of gamma radiation as well as due to transfer of heat from Main Heat Transport System (MHTS) by radiation being the mode of heat transfer. The total heat generated in the moderator at full power is estimated to be about 48.5 MW. This heat is removed by main moderator circulation system which maintains equilibrium moderator temperature in the core, by providing sufficient cooling. Heat removal is accomplished by circulating the moderator through heat exchangers where the heat is transferred to process water. In case of SBO, only heat that comes to the moderator is from MHTS through radiation, which is about 2MW at full power condition. As soon as SBO occurs and reactor gets tripped and decay heat mode starts, now this load (2MW) drastically reduces.

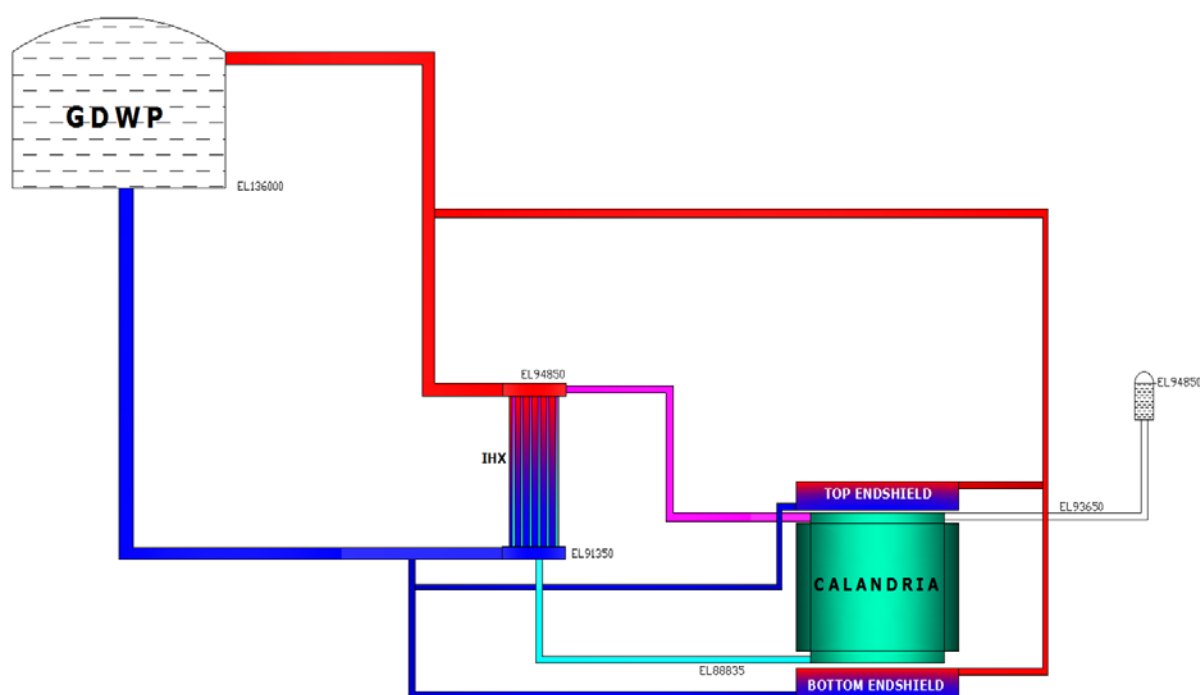
The PMCS is designed with an objective to remove the heat from the moderator in case of SBO and maintaining its safe conditions for at least 7 days. For 7 days duration, the flow rates and the heat removed should be sufficient to ensure that the temperatures inside the Calandria remain within the permissible safe limits (100°C) because if temperature rises above 100°C there may be moderator leakages from Calandria through Calandria Tube Endshield joints (Rolled joint designed for 100°C). This passive design provides a grace period of 7 days, during which no operator intervention is required to maintain moderator temperature.

In AHWR, main moderator cooling system maintains the equilibrium moderator temperature in the Calandria Vessel, while PMCS performs the same function during accidental scenarios like SBO. PMCS serves to cool the heavy water moderator that fills the Calandria up to 100%

level during accidental conditions, when main moderator circulation system is unavailable. Figure-3.1 shows the simplified flow sheet for Passive Moderator Cooling System. Heavy water is drawn from the top of Calandria at about 80°C. This heavy water goes into a heat exchanger, where it exchanges heat with shell side GDWP water. The cold moderator returns back to the Calandria after joining the main moderator circulation system in the same way as at the exit. The heat exchanger is vertical shell and tube type having capacity of 2 MW. Heavy water is kept at tube side so as to reduce the heavy water inventory. Shell side of the heat exchanger is GDWP water, which on heated up by heavy water moderator moves towards the GDWP. The relatively cold water enters at the bottom of the heat exchanger shell side. Isolation condenser will cause thermal stratification in the pool and upper portion of the GDWP will become hotter as compared to the lower portion. Hence, PMCS lines supplying cold water have been connected at the lower elevation in the GDWP and return line with hot fluid has been connected at higher elevation. This system always remains in operation. During normal operation of the reactor it adds 2 MW heat to GDWP continuously which is removed by GDWP heat removal system during normal operations. During accident conditions when main moderator circulation system is unavailable, the heat from moderator is removed by GDWP water passively through the heat exchanger. The heat load to the GDWP decreases continuously from the initial 2MW due to shut down of the reactor since moderator nuclear heat is negligible after reactor shut down. The heat load to GDWP is mostly the heat transfer from MHTS to moderator, which gradually reduces due to cooling down of the MHTS from initial 285°C. GDWP water starts boiling in 7 days; hence this system maintains the moderator conditions within safe limit for maximum 7 days of SBO.

3.2.2 Passive End-shield Cooling System (PECS)

The end shields are provided at both the ends of the Calandria. The two end shields, Top Endshield and Bottom Endshield, together with Calandria and Calandria tubes form an



The passive union system for V1 (tail pipe towers) and V2 (outside tail pipe towers) volumes is designed to meet following functions:

- a. To maintain complete isolation and maintain pressure boundary between V1 and V2 volumes of AHWR under normal plant operating conditions.
- b. To hold water inside V1 volume in case of GDWP failure in V1 area.
- c. To create union of V2 and V1 volume and allow water to pass from V2 to V1 in case of GDWP failure in V2 area alone or both V1 & V2 areas.

Figure-3.3 shows the schematic of the PAUSE system connecting the V1 and V2 volumes of the primary containment.

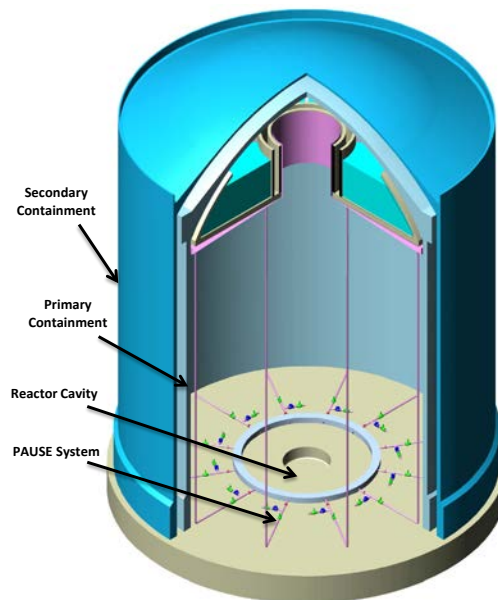


Figure-3.3 Schematic of PAUSE System

3.2.4 Core catcher

In a very low probability event of a core melt, a core catcher has been incorporated in AHWR that will prevent recriticality and terminate the severe accident progression, and retains the corium in the containment besides providing adequate cooling to the corium for prolonged period.

3.2.5 Hydrogen mitigation system

The objective of hydrogen mitigation system is to limit the hydrogen concentration inside containment below the flammability limit by controlled combustion of hydrogen using catalysts. In AHWR, Passive Catalytic Recombiner Device (PCRD) developed in-house will be used for hydrogen mitigation system.

3.2.6 Containment Filtered Venting System (CFVS)

Following the post-Fukushima measures, the Containment Filtered Vent System (CFVS) finds its need in AHWR. Under some postulated severe accident conditions involving multiple system failures in AHWR, the primary containment pressure may increase beyond the design pressure limit and must therefore be depressurized at high pressure to maintain the containment integrity. In addition, the radioactivity released must be retained so as not to release beyond allowable limit at the public domain. These functions are carried out by a filtered hardened vent system. The function of the filtered hardened vent system is to effectively mitigate the consequences of a severe accident by releasing the pressure from primary containment to atmosphere and also to reduce significantly the level of radioactive release to the public.

3.3 Experimental studies

In order to simulate the Fukushima type scenario in AHWR, an integrated test facility comprises of Passive Moderator Cooling System Test Facility (PMCSTF), Passive Endshield Cooling System Test Facility (PECSTF) and GDWP tank with submerged ICs has been built (Figure-3.4). Integrated experiments have been performed for establishing the capability of the decay heat removal of the reactor.

3.3.1 Scaling methodology

For maintaining the geometrical and dynamic similitude in the facility for accurate predictions, reduced height scaling methodology was adopted for the design of the PMCSTF

and PECSTF experimental facility and power to volume philosophy is used for designing the GDWP tank with ICs. The three-level scaling methodology of Ishii has been applied in the scaling of the PMCSTF and PECSTF facility (Ishii et al., 1983, Ishii et al., 1998). The three-level scaling methodology consists of the integral system scaling (global scaling or top down approach), the control volume and boundary flow scaling, and local phenomena scaling.

For the single phase flow in the present case, one dimensional area averaged mass, momentum and energy balance equations were used. Using boundary conditions for these equations, similarity groups were identified and finally the important dimensionless numbers characterizing the geometric, kinematic, dynamic and energetic similarity parameters were derived. The present analysis considers the following assumptions:

- a. The viscous heating is negligible.
- b. Heat losses to ambience are negligible.
- c. Boussinesq approximation is valid, i.e. fluid properties can be considered to be constant in the governing equations except for the density in the buoyancy force term which is assumed to vary linearly with temperature as

$$\rho = \rho_o \{1 - \beta(T - T_o)\} \quad \dots \dots \dots (3.1)$$

- d. Since the analysis is for single phase liquid conditions, the fluid is assumed to be incompressible.

The governing equations for a one-dimensional flow around a loop compose of several sections can be given as follows:

Continuity equation:

$$u_i = \frac{a_o}{a_i} u_r \quad \dots \dots \dots (3.2)$$

Integral momentum equation:

$$\rho \frac{du_r}{dt} \sum_i \frac{a_o}{a_i} l_i = \beta g \Delta T l_h - \frac{\rho u_r^2}{2} \sum_i \left(\frac{f l}{d} + K \right) \left(\frac{a_o}{a_i} \right)^2 \quad \dots \dots \dots (3.3)$$

where u_i is the velocity in the i_{th} section, u_r is the velocity in the core, a_o is the core flow area and l_h is the vertical separation between the hot and the cold thermal center in the loop. u_r is a function of time, but during a steady-state natural circulation it is denoted by u_o and it is the reference velocity used in non-dimensionalization.

Integral energy equation:

$$\rho C_p \left(\frac{\partial T_i}{\partial t} + u_i \frac{\partial T_i}{\partial x} \right) = q_i''' \quad \dots \dots \dots (3.4)$$

The non-dimensionless parameters are defined as follows:

$$u_i^* = \frac{u_i}{u_o}, \quad u_r^* = \frac{u_r}{u_o}, \quad a_i^* = \frac{a_i}{a_o}, \quad x_i^* = \frac{x_i}{l_o}, \quad l_i^* = \frac{l_i}{l_o}, \quad l_h^* = \frac{l_h}{l_o}$$

$$t^* = \frac{t u_o}{l_o}, \quad T^* = \frac{T}{\Delta T_o} \text{ and } \Delta T^* = \frac{\Delta T}{\Delta T_o} \quad \dots \dots \dots (3.5)$$

where ΔT_o is the maximum temperature difference in the loop during steady state natural circulation.

$$u_i^* = \frac{u_r^*}{a_i^*} \quad \dots \dots \dots (3.6)$$

Integral momentum equation:

$$\frac{du_r^*}{dt^*} \sum_i \frac{l_i^*}{a_i^*} = \frac{\beta g \rho \Delta T_o l_o}{u_o^2} \Delta T^* l_h^* - \frac{u_r^{*2}}{2} \sum_i \frac{\left(\frac{f l}{d} + K \right)_i}{a_i^{*2}} \quad \dots \dots \dots (3.7)$$

Integral energy equation:

$$\frac{\partial T_i^*}{\partial t^*} + u_i^* \frac{\partial T_i^*}{\partial x^*} = \frac{q_i''' l_o}{\rho C_p u_o \Delta T_o} \quad \dots \dots \dots (3.8)$$

Here the coefficients in nondimensional equations are the non dimensional group need to be same for both model as well for prototype.

These non dimensional coefficients are:

$$\text{Richardson number, } Ri = \frac{\beta g \rho \Delta T_o l_o}{u_o^2} \quad \dots \dots \dots (3.9)$$

$$\text{Friction/Orifice number, } F = \left(\frac{f l}{d} + K \right)_i \quad \dots \dots \dots (3.10)$$

$$\text{Heat source number, } Q = \frac{q_i''' l_o}{\rho C_p u_o \Delta T_o} \quad \dots \dots \dots (3.11)$$

The integrated test facility operates with same fluid as that in prototype along with same pressure and temperature conditions. With these assumptions we have:

$$\rho_R = \beta_R = C_{PR} = 1$$

To achieve geometrical and dynamic similitude, the ratio of various dimensionless parameters in the prototype and the model must be equal. For any dimensionless parameter ψ :

$$\psi_R = \frac{\psi_{Model}}{\psi_{Prototype}} = 1 \quad \dots \dots \dots (3.12)$$

This yields

$$\left. \begin{aligned} a_{iR}^* &= 1, \quad l_{iR}^* = l_{hR}^* = x_{iR}^* = 1, \quad T_R^* = 1, \\ \text{Richardson Number ratio } Ri_R &= 1 \Rightarrow \left(\Delta T_{oR} = \frac{u_{oR}^2}{l_{oR}} = 1 \right) \Rightarrow u_{oR} = \sqrt{l_{oR}} \\ t_R^* &= 1 \text{ and } t_R = \frac{l_{oR}}{u_{oR}} \Rightarrow t_R = \sqrt{l_{oR}} \\ \text{Also Friction Number ratio } F_R &= 1 \\ \text{Heat Source Number ratio } Q_R &= 1 \Rightarrow q_R''' = \frac{u_{oR}^3}{l_{oR}} \Rightarrow q_R''' = 1 / \sqrt{l_{oR}} \end{aligned} \right\} \dots \dots (3.13)$$

The length and area ratio of the various component dimensions in the scaling of PMCSTF and PECSTF was kept as 1/10 and 1/100.

The various ratios of the scaled facility parameters are listed in Table-3.1. This scaling is based on three-level scaling philosophy, which consists of the integral system scaling (global scaling or top down approach), the control volume and boundary flow scaling, and local phenomena scaling. The integral system scaling ensures the preservation of the transient response of various variables in single and two-phase flows and also ensures that steady-state and transient conditions are well simulated within each component. The control volume and boundary flow scaling ensure preservation of inter-component mass and energy flows as well as the mass and energy inventories in each component. Local phenomena scaling ensure the preservation of local conditions inside the components of the model same as prototypic

conditions. Reduced height scaling was adopted for the test facility mainly because of space constraint for 45 m of height. The reduced height scaling philosophy facilitates the reduction in height of the natural circulation loop which has been brought down to 4.5 heights from 45 meters. The scaling preserves and ensures the thermal hydraulic phenomena occurring in the prototype conditions well in the model.

Table-3.1 Ratio of scaled parameters in PMCS and PECS Test Facility

Parameter	Scaling Law	Design
Length	l_R	1/10
Diameter	d_R	1/10
Area	a_R	1/100
Volume	$a_R l_R$	1/1000
Temperature	l	1
Time	$\sqrt{I_R}$	1/3.16
Velocity	$\sqrt{I_R}$	1/3.16
Power/Volume	$1/\sqrt{I_R}$	3.16
Power	$a_R \sqrt{I_R}$	1/316
Mass Flow rate	$a_R \sqrt{I_R}$	1/316
Heat Flux	$1/\sqrt{I_R}$	3.16
Pressure drop	l_R	1/10
Aspect ratio	$l_R \sqrt{a_R}$	1

3.3.2 Integrated Scaled Test Facility

The integral facility including scaled model of PMCS, PECS and GDWP with submerged ICs heaters has been built and shown in Figure-3.4. Description of scaled models of various passive systems of the reactor is as follows:

Scaled Passive Moderator Cooling System

The PMCS in test facility comprises of simulated Calandria Vessel, Intermediate heat exchanger, piping and GDWP tank. The simulated Calandria Vessel is a 0.6 m ID and 0.6 m long SS304 cylindrical tank with 19 electrical heater tubes (in two rings with PCD of 0.24 m

and 0.48 m) that simulate the Calandria tubes of the reactor. These are arranged in two circular rings. The heat exchanger (IHx) in Figure-3.4 is a shell and tube type heat exchanger designed to remove 10 kW. The shell inner diameter is 52.5 mm housing 40 tubes of 6 mm ID. The pipes connecting Calandria and heat exchanger are of 50 Nominal Bore sch40. The shell side of the heat exchanger is connected to the GDWP tank. The GDWP tank is a large 0.8 m × 1.2 m × 1 m steel tank, which is open from the top. An expansion tank (height 0.5 m and 0.3 m diameter) is connected to the top of the Calandria Vessel and located at the highest elevation of the primary loop. Figure-3.4 shows the Calandria Vessel, heat exchanger, piping, expansion tank and GDWP tank of the experimental facility.

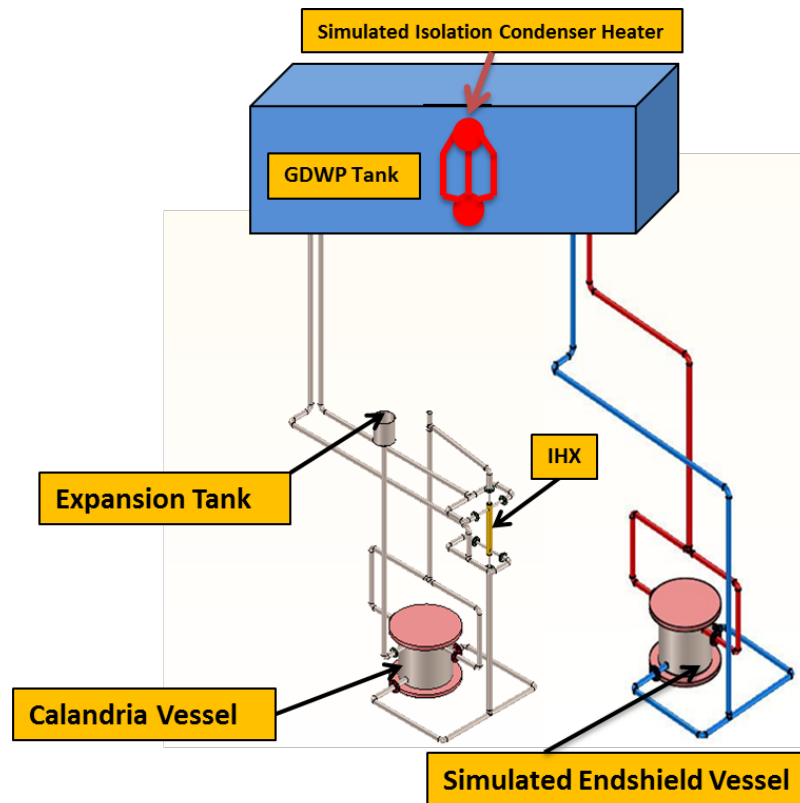


Figure-3.4 Schematic of Integral Test Facility simulating Fukushima type scenario

Scaled Passive Endshield Cooling System

The PECS in the test facility comprises of Endshield Vessel, piping and GDWP tank. The simulated Endshield Vessel is 0.6 m ID and 0.5 m long SS304 cylindrical tank. It houses 14 Lattice tubes, five immersion heaters for uniform heating and it is filled with 5 mm SS balls

having a ratio of 60:40 with water. The Endshield Vessel is connected to the GDWP tank by 50 nominal bore sch 40 pipes directly. The vessel is designed with two outlet and two inlet nozzles for leaving hot water from the top of the Endshield vessel after absorbing heat from Endshield and entering cold water at the bottom of the Endshield vessel respectively. A common water tank called GDWP tank is used for the three facilities. Figure-3.4 shows the Endshield Vessel, piping and GDWP tank of the experimental facility.

Scaled GDWP tank with simulated Isolation condenser heaters

GDWP tank is provided with immersion heaters simulating ICs of the reactor. The decay heat of the reactor that is being removed by ICs is supplied to these scaled immersion heaters for evaluating the decay heat removal capability of the reactor. The GDWP tank has dimensions as $0.8\text{ m} \times 1.2\text{ m} \times 1\text{ m}$, which is open from the top. Figure-3.4 also shows GDWP tank with submerged heaters simulating ICs of the reactor in experimental facility.

3.3.3 Instrumentation for the Test Facility

Test facility is provided with extensive instrumentation. Fifty seven thermocouples are placed on nineteen Calandria tubes for fluid temperature measurement inside the Calandria vessel, while 45 thermocouples are placed inside Endshield vessel. These thermocouples are distributed uniformly inside the vessels. This gives a 3D temperature profile inside the Calandria and the Endshield vessel at all times. Further, thermocouples are also placed each at the inlet and outlet of the Calandria, Endshield Vessel, tube side of the heat exchanger and shell side of the heat exchanger. These are mineral insulated 0.5 mm diameter chromel-alumel thermocouples (K-type). Thermocouples were calibrated in the range of 0-150°C and are having measuring accuracy of 0.4 % or $\pm 1.1^\circ\text{C}$, whichever is less, here maximum measuring error will be 1.1°C . Heater power could be controlled using dimmerstat and measured with the help of Wattmeter having an accuracy of 0.5 % of the span (0-10kW). All temperature data were recorded at a time interval of 10 seconds and fed to a data logger,

however, the data logger possess frequency of 4 MHz. For flow measurements, differential pressure across heat exchanger shell side and Calandria Vessel was measured using capacitance type differential pressure smart transmitters. Differential pressure transmitters have been installed with the three way manifold valves. Six hybrid recorders (Yokogawa make) were used for data acquisition. The integral test facility has been insulated with ceramic wool to minimize the heat loss to the environment.

3.3.4 Scaling adequacy and distortion

It is important to establish the scaling adequacy and differences in the test results due to scaling distortions. Considering this, the scaling adequacy analysis of the test facility along with that of the reactor has been carried out. Figure-3.5 shows normalized mass flow rate variation with time for prototype as compared with the test facility during SBO conditions. Initial flow rates were under predicted in the model as compared to the prototype. But at later stage, normalized flow rates were comparable. Besides, there exist some distortions in simulated test facility. Difference between the prototypic conditions in IC and the experimental facility can be regarded as physical distortion; IC has been simulated as the immersion heater with scaled power in the test facility whereas condensation takes place at elevated temperatures in the reactor. This distortion will have substantial effect in terms of local conditions in the pool since the condensation occurs at higher temperature in the prototype (285°C). Though, the heat added to the pool is in a scaled ratio but the local temperatures (heat flux) will be very low. In long term, the conditions of the prototype will prevail in the test facility. Various non-dimensional numbers discussed in section 3.3.1 were simulated for the model. Heat flux at reduced height is higher for the model as compared to the prototype. However, the facility operates in single phase flow zone, so the effect of increased heat flux is not substantial in this case.

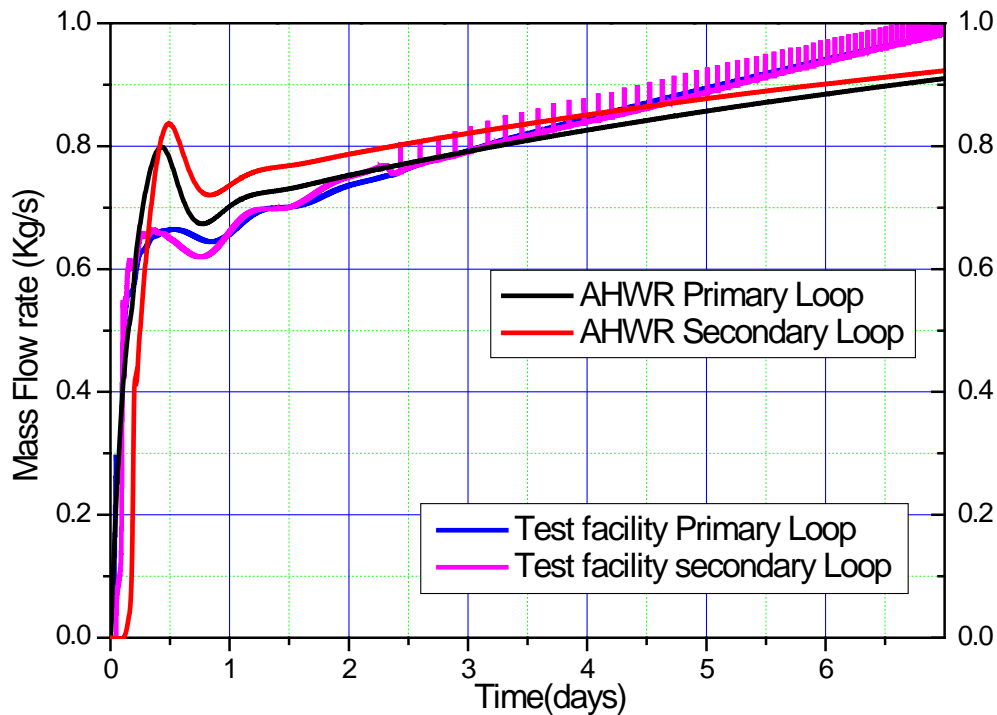


Figure-3.5 Scaling adequacy of the test facility

3.3.5 Experiment conducted

The primary loop of the scaled PMCS was filled with water through the expansion tank as seen in Figure-3.4. In this process, trapped air in the loop was vented through a nozzle present at the top horizontal section of the primary loop. The level in the expansion tank was filled upto 0.55 m. The secondary loop of scaled PMCS and the scaled PECS were then filled through the GDWP tank, which was filled from the top till the overflow line, 0.05 m below the top surface of GDWP (Figure-3.4). Any air trapped in the Endshield vessel was vented through a vent line provided at the top of the Endshield vessel. Once all three scaled systems (PMCS, PECS and GDWP tank with ICs) were filled, the power was switched ON and maintained at 1.5 kW (corresponding to average radiation heat transfer from MHTS to moderator for 7 days) in moderator as well as in Endshield system. Alongside, the power of the GDWP immersion heaters that simulates the ICs was also switched ON and maintained at 1.2 kW (corresponding to average decay heat for 7 days) for 7 days.

3.3.6 Experimental results

Experiment has been conducted for 7 days without operator intervention with 1.5 kW power level in each scaled PMCS and PECS and 1.5 kW power in simulated ICs heaters. Experiment showed successful decay heat removal by GDWP water for a prolonged period. Figure-3.6 shows the temperature variation of the moderator and GDWP water for 7 days. The temperature at Calandria outlet rises to 60°C after 1 day and reaches to 70°C in 7 days. Figure-3.7 shows the temperature variation in the Passive Endshield Cooling System Test Facility. During the initial phase of experiment the temperature at the outlet of the Endshield Vessel rises to 56°C and then drops to 41°C before it starts rising further. This is observed due to delay in establishing the natural circulation flow in the loop.

The initial condition of temperature inside Moderator and Endshield Vessel in the reactor, when PMCS and PECS called upon is ~50-55°C. Here, the experiment was started with initial conditions as atmospheric temperature (32°C) in both the vessels and GDWP tank. The pool temperature is maintained as 40°C in the reactor. A dedicated GDWP recirculation system has been employed for maintaining the temperature of GDWP water. Actual SBO simulation is starts only after achieving the initial conditions of the prototype in the test facility. It can be seen from Figure-3.6 and Figure-3.7 that initial conditions of temperature for the reactor was realized in 17 hrs in the test facilities after starting the experiment with 1% decay heat. This time is termed as negative time as it was taken for achieving the initial conditions of moderator and Endshield in the reactor when passive systems will be invoked in the reactor during SBO conditions. The temperature at the outlet of the Calandria Vessel and Endshield Vessel remains well with safe limits of 100°C.

The phenomena observed during the experiment conducted can be divided into two phases; initial phase when natural circulation was not started only local convection currents were generated and a phase with established natural circulation flow in the loop.

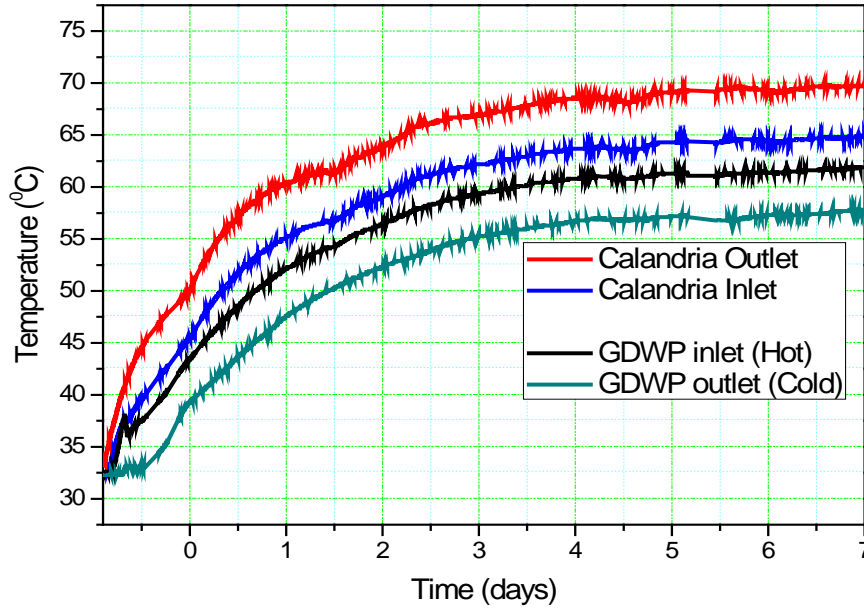


Figure-3.6 Fluid temperature variation at Calandria inlet/outlet and GDWP inlet/outlet

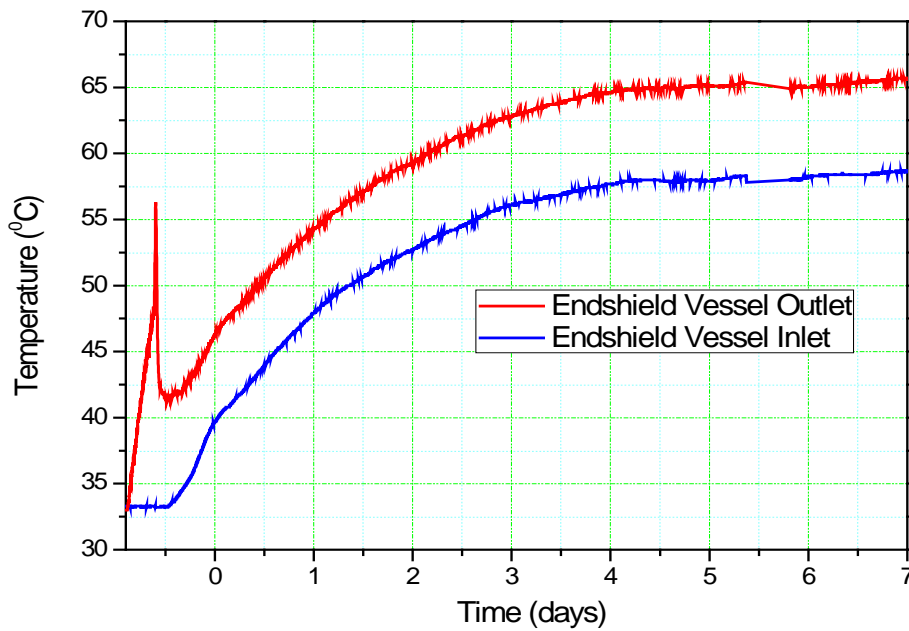


Figure-3.7 Fluid temperature variation at Endshield Vessel inlet and outlet

During the initial phase the fluid temperature inside the vessels increases because of no or very low circulation flow in the loop. Once temperature inside the vessels crosses the threshold of gravity because of increasing buoyant forces due to increasing density difference at inlet and outlet of the vessel; there was gross natural circulation flow in the loops.

Figure-3.8 shows the temperature distribution inside Calandria Vessel of PMCSTF during various stages of the experiment. Figure-3.8a shows the temperature profile inside Calandria

Vessel after 1800 s of the experiment at outlet plane; two outlets are placed at 525 mm height of the vessel at 180° apart. After 1800 s the maximum temperature observed inside vessel is 36.7°C and temperature difference of 3°C is observed inside the vessel. It can be concluded from the contours that the cold water current rises from the center of the vessel and the hot fluid gets accumulated at the top. Similar behavior can be depicted from Figure-3.8b after 1 hr of experiment; however, more developed temperature profiles are observed as compared to 1800 s of experiment. After 10 h of experiment, developed temperature profiles are observed inside Calandria Vessel and a gross circulation flow gets developed. This can be observed from Figure-3.6 around 17 h of experiment ($t=0.7$ days), the GDWP water temperature decreases from 38°C to 36°C due to the natural circulation flow in the secondary loop. Figure-3.8d shows the temperature distribution inside Calandria Vessel after 7 days, the maximum temperature observed inside vessel is 72°C , conforming to no local boiling inside vessel without any safety implications.

Figure-3.9 shows the temperature distribution inside Endshield Vessel of PECSTF from 1800s to 7 days during various important phases of the experiment. The maximum temperature found inside Endshield Vessel is 42°C after 1800 s. This temperature is slightly higher than that observed in Calandria Vessel of PMCTF after 1800 s, due to less thermal inertia in the Endshield Vessel (filled with SS balls and water; thermal inertia of SS balls and water mixture is less as compared to water only in the same volume). Local convection currents are observed inside the vessel till 7 h without any gross natural circulation in the loop (Figure-3.7). As the circulation flow starts, the temperature of the fluid coming out of the Endshield Vessel drops down to 42°C from 56°C as seen from Figure-3.7. More temperature gradients are observed in the Endshield Vessel conforming less circulation flow as compared to PMCSTF, which is very much obvious due to high pressure drop across the

Endshield Vessel containing SS balls and water mixture. The maximum temperature after 7 days is found to be 68°C inside the vessel, in compliance with the safety margins.

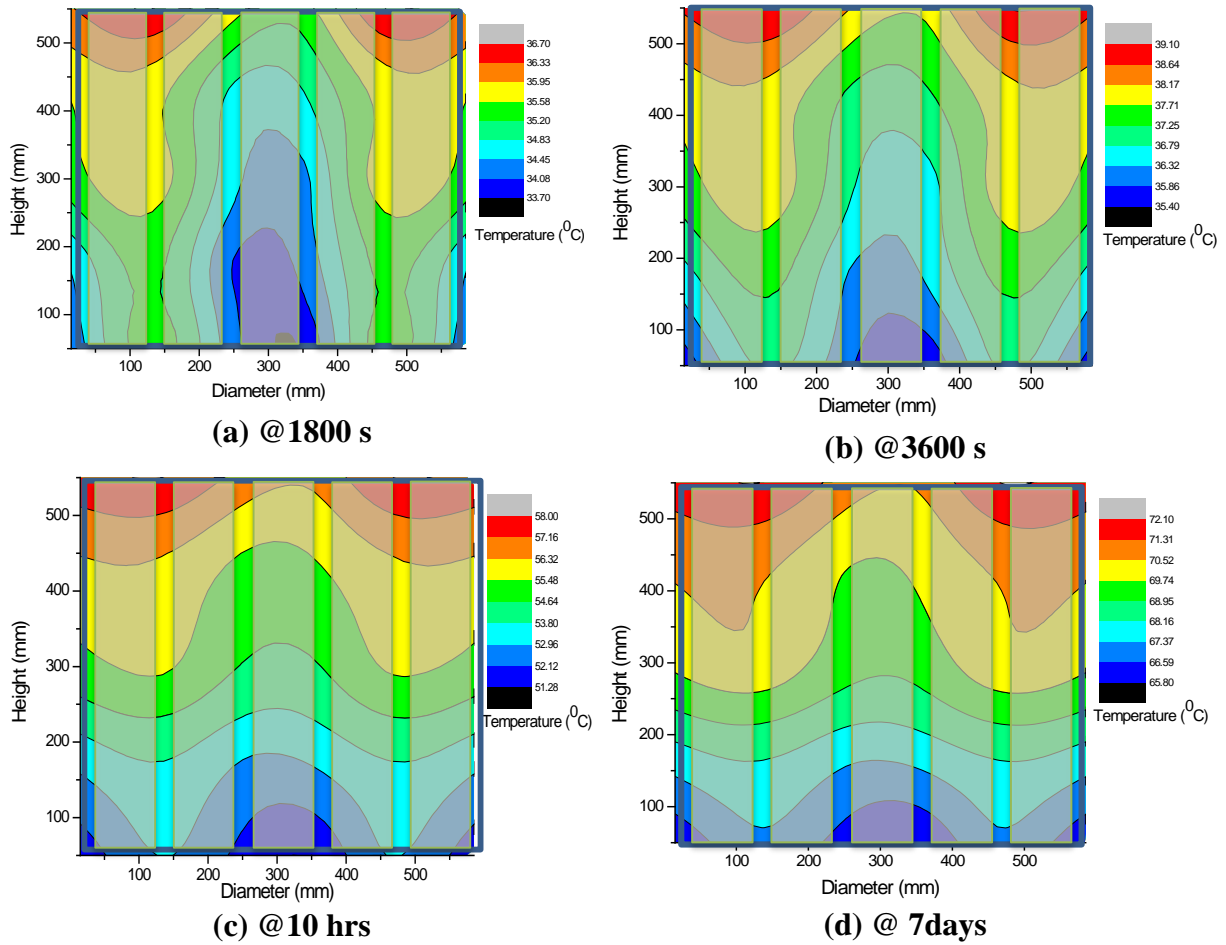
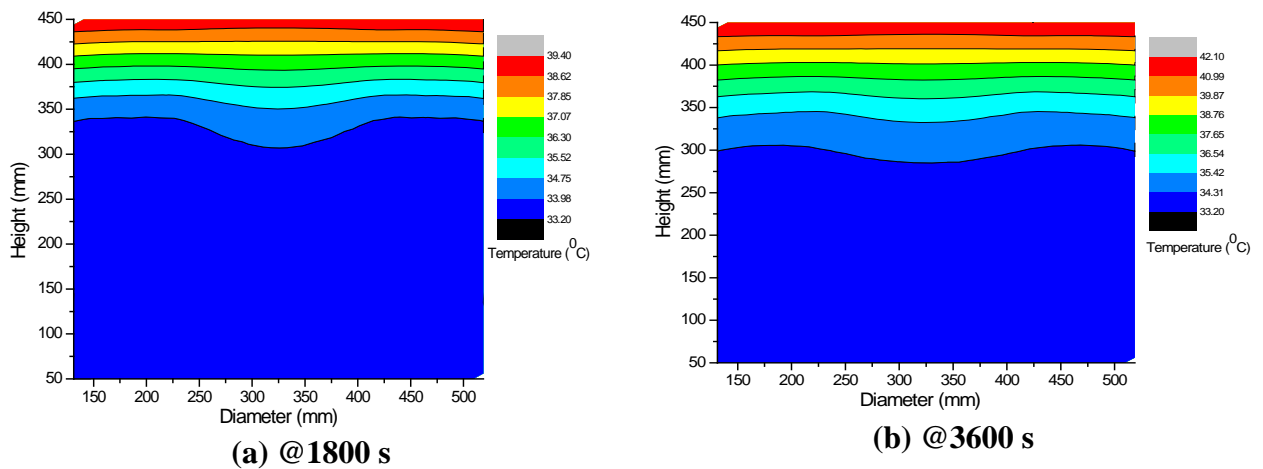


Figure-3.8 Temperature distribution inside Calandria Vessel



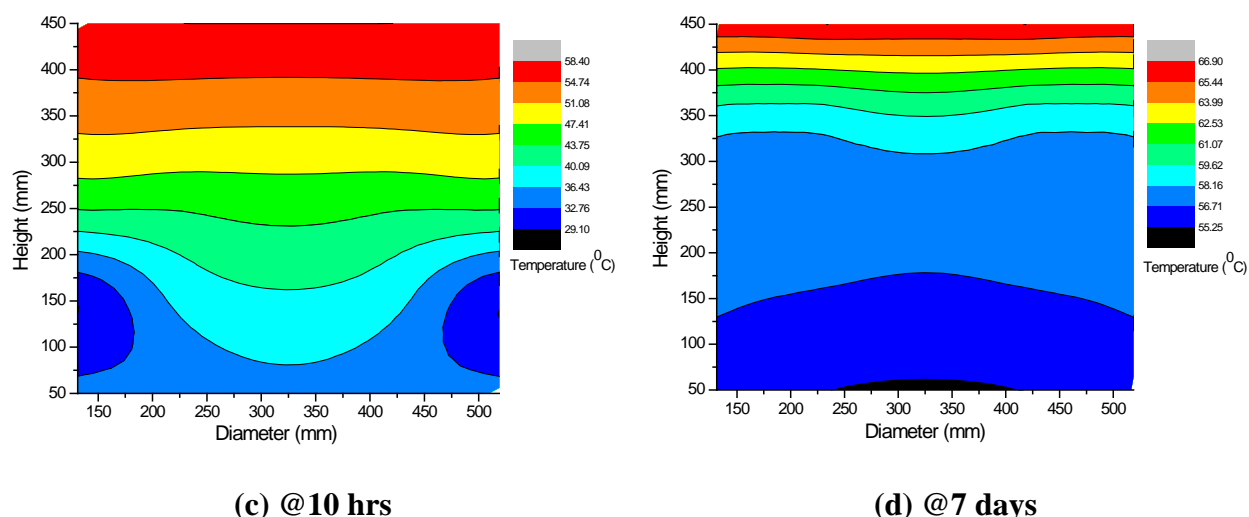


Figure-3.9 Temperature distribution inside Endshield Vessel during SBO

3.4 Closure

Fukushima accident was an extreme event with no restoration of power supply to the nuclear power plant for several days. In such a situation, no active system can work and assure the safety of the reactor. Only passive systems will be available during such conditions to remove decay heat for minimum grace period for which they are designed. AHWR design has been evaluated in view of Fukushima scenario and some design modifications have been made; few new systems have been incorporated in the design. The decay heat removal capability of AHWR is experimentally demonstrated at least for 7 days without operator intervention. In addition to this, this study brought out the development of natural circulation flow inside coupled loops and parallel loops.

CHAPTER-4

Investigations of Natural Circulation and Convection in PMCS Test Facility

4.1	Introduction.....	67
4.2	PMCS: Calandria and moderator heat generation	67
4.3	Integral analysis of reactor during prolonged SBO with PMCS	70
4.3.1	Performance evaluation of AHWR with PMCS	70
4.3.2	Scenarios considered	71
4.3.3	Results and discussions.....	73
4.4	Experimental studies.....	76
4.4.1	Facility description	76
4.4.2	Instrumentations	78
4.4.3	Experimental methodology.....	79
4.5	Experiment results	80
4.5.1	Obtaining the initial conditions of moderator in the Test Facility.....	80
4.5.2	Decay heat removal in a scaled test facility for prolonged period	83
4.6	RELAP simulation of the test performed in the scaled Facility	87
4.6.1	Nodalisation scheme	87
4.6.2	RELAP and experimental data comparison.....	88
4.7	CFD simulation of simulated Calandria Vessel for steady states	90
4.7.1	Governing equations.....	90
4.7.2	Turbulence modeling	91
4.7.3	Boundary conditions for modeling	92
	<i>Inlet</i>	92
	<i>Outlet</i>	93
	<i>Wall</i>	93
4.7.4	Methodology for analysis	94
	<i>Residual for the simulations</i>	96
4.8	CFD predictions and experimental data comparison.....	97
4.9	Closure	100

4.1 Introduction

The new nuclear reactor designs that are being developed incorporates passive systems extensively especially after Fukushima accident. These systems use entirely passive components or active components in a limited manner (IAEA-TECDOC-1624, 2009). The driving forces in these systems are natural forces such as gravity. These are highly useful in the conditions like station blackout, where an external energy such as pump/electricity is not available for circulating the coolant. In addition, these systems eliminate costs of installation, operation and regular maintenance of the active systems. Here in this chapter detail studies of one such system of AHWR known as Passive Moderator Cooling system (PMCS) has been discussed. Firstly, performance assessment of the system followed by experiments in the test facility built for PMCS is discussed. This chapter also includes CFD simulations for flow over heated Calandria rods, thus giving insights for the fluid flow behavior inside the Calandria Vessel in the scaled test facility.

4.2 PMCS: Calandria and moderator heat generation

The Calandria Vessel of the reactor is a vertical cylindrical tank that houses 452 coolant channels surrounded by Calandria tubes, reactor control mechanism and heavy water as moderator. The fuel bundle, which consists of 54 fuel rods, is housed inside a pressure tube/coolant channel (which carries the coolant) which is surrounded by Calandria tube, separated from the pressure tube by an annulus filled with gas (Figure-4.1). The heavy water moderator is filled inside the Calandria Vessel surrounding these Calandria tubes (Figure-4.2). During normal operation of the reactor, heat is continuously generated in the moderator due to neutron moderation and capture, attenuation of gamma radiation as well as due to radiation heat transfer from the Main Heat Transport System (MHT), i.e. the coolant. In this process, a total of approximately 48 MW heat is deposited in the heavy water moderator for a

reactor full power of 920MW_{th} in AHWR. This heat is planned removed through a forced moderator cooling circuit, to maintain the moderator temperature at 60°C .

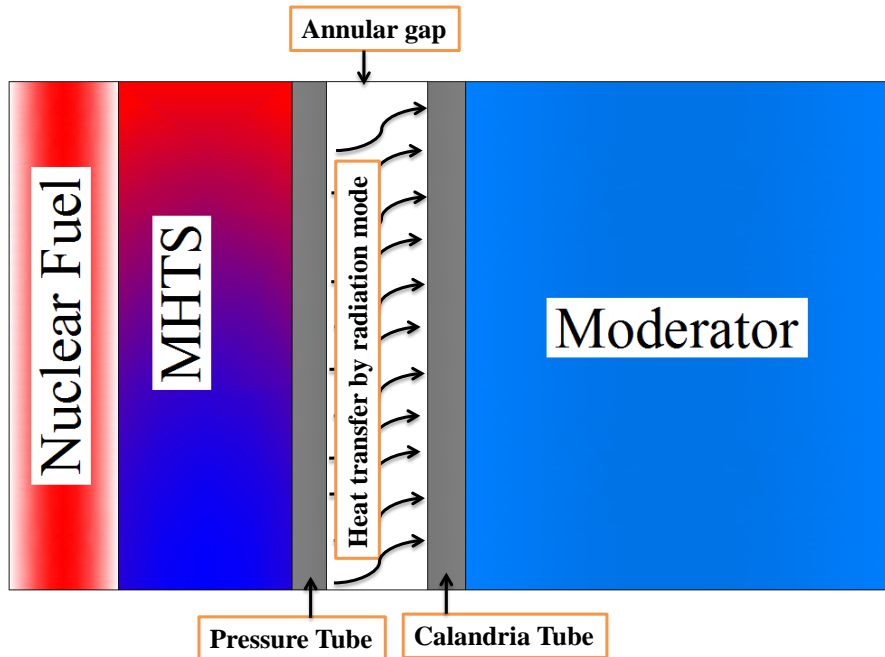


Figure-4.1 Schematic of heat transfer from fuel to moderator in the Calandria (half symmetry from center of fuel channel)

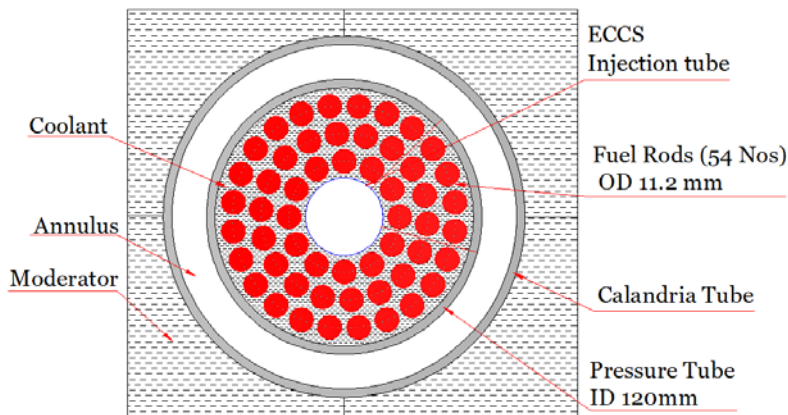


Figure-4.2 Schematic of pressure tube and Calandria tube with moderator in Calandria

In the event of a prolonged SBO, the reactor trips and the nuclear fission stops. As a result, the energy dissipation in the moderator stops. Now, only the heat is transferred from MHTS across the Pressure tube and Calandria tube gap as radiation mode. This heat is estimated to be 2 MW, at the beginning of the reactor trip and reduces as the decay heat generation (hence MHT temperature) reduces. In SBO, the moderator can no longer be cooled by active means

due absence of pump. The Passive Moderator Cooling System (PMCS) (Figure-4.3) is designed to remove this heat, in order to prevent the pressure rise inside the Calandria Vessel beyond permissible safe limits and prevent boiling of moderator & eventually the reactor integrity

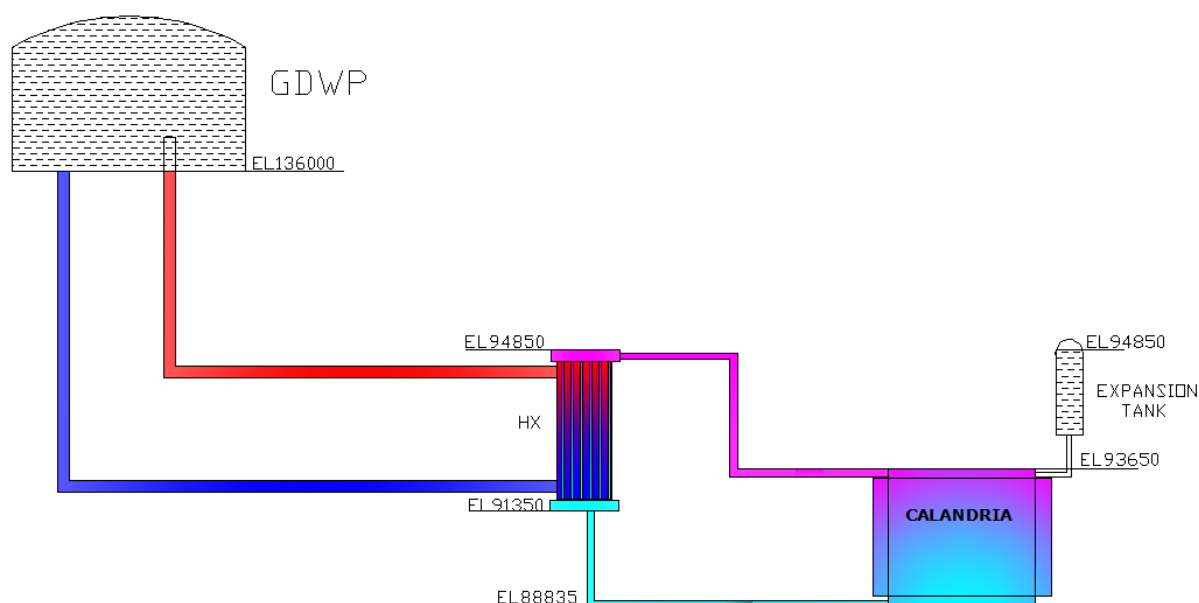


Figure-4.3 Schematic of Passive Moderator Cooling System (PMCS)

Passive cooling of the moderator system is a topic of research for tube type reactors. Several researchers have worked on the problem of moderator cooling. The tube type reactors utilize heavy water as moderator which is separated from the main coolant through pressure tube and Calandria tubes. These reactors like Indian PHWRs and CANDUs have a large inventory of liquid moderator which may act as a heat sink. Thus, the Atomic Energy of Canada Limited (AECL) has also been contemplating to use the moderator as a passive decay heat removal system during a Loss of Coolant Accident (LOCA) with simultaneous loss of emergency core cooling system (Baek and Spinks, 1994; Khartabil and Spinks, 1995; Umar et al., 1999; Umar and Vecchiarelli, 2000). In the event of LOCA, moderator may act as a medium for decay heat removal from the reactor after sagging of the pressure tube and a contact is made between PT/CT. Baek and Spinks (1994) reported that the passive moderator heat rejection system being developed for CANDU reactors will act as a heat sink, in the

event of simultaneous LOCA and loss of emergency coolant injection system. Khartabil and Spinks (1995) carried out experiments and analysis for a flashing-driven Passive Moderator Cooling System for CANDU reactors. In this concept the moderator exits the Calandria Vessel at a temperature close to saturation so that vapor is generated in a riser connecting the Calandria to a heat exchanger. The two phase flow increases the driving force, making it possible to remove moderator heat passively. Also in case of SBO, it is a need to cool the moderator for maintaining the reactor integrity. For that purpose one such system has been developed for AHWR. The system operates on natural mode of heat removal and fulfills the intended functions. The detail of the system is described in the subsequent section.

4.3 Integral analysis of reactor during prolonged SBO with PMCS

Integral behavior of the reactor is studied during prolonged SBO conditions with Passive moderator cooling system. From the earlier analysis, it is evident that decay heat removal is not an issue in AHWR during SBO conditions. However, moderator cooling could not be ensured, as cooling of moderator in Calandria Vessel is maintained by active cooling system, which may not be available during SBO conditions. With incorporation of PMCS in the reactor design, safe condition for moderator could be maintained for prolonged period. Here, performance analysis of the reactor design is carried out for SBO type of accident for prolonged period with PMCS in place.

4.3.1 Performance evaluation of AHWR with PMCS

Various systems of the reactor viz Main Heat Transport System (MHTS), Isolation Condenser System (ICS), Emergency Core Cooling System (ECCS), Passive Containment Cooling System (PCCS), and Primary Containment volumes, i.e. V1 and V2 along with the Passive Moderator Cooling Systems are integrally simulated with the system code RELAP5 Mod3.2. Initially, steady state is obtained for MHTS and the containment volumes V1, V2 and ECCS are initialized as per the initial conditions given in Table-4.1.

Table-4.1 Initial Operating Conditions for Various Systems of the Reactor

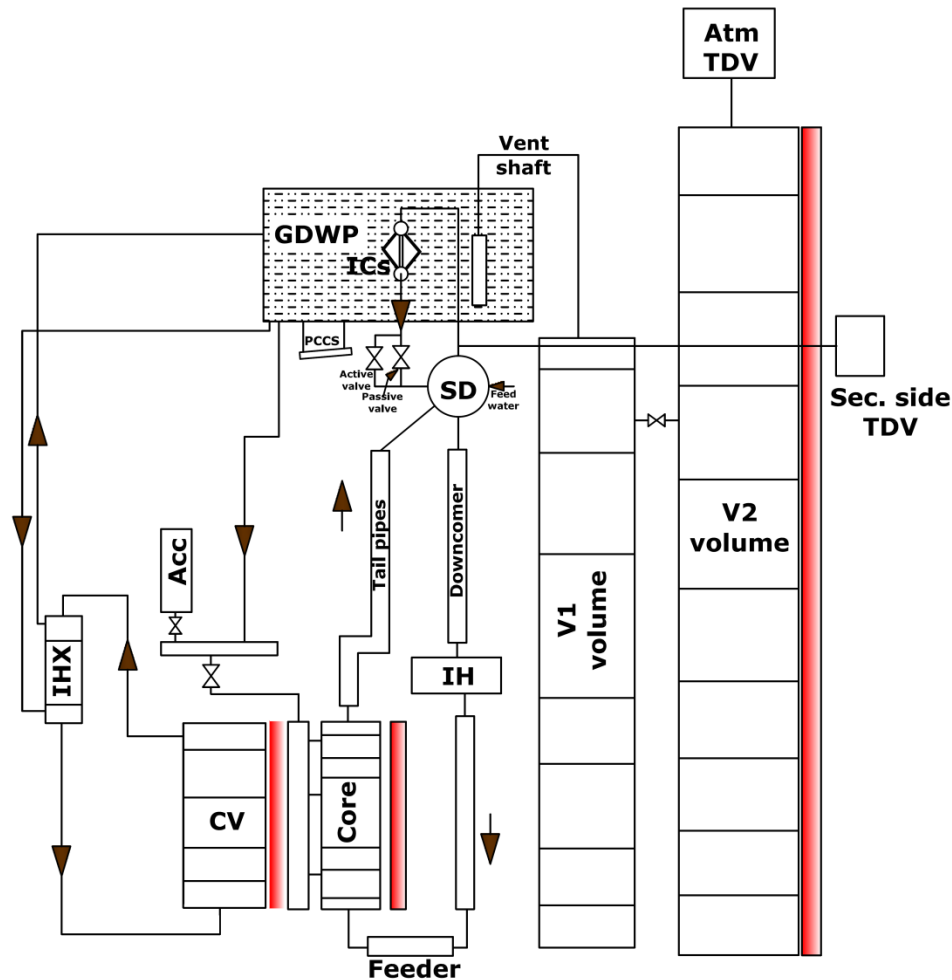
	Pressure	Temperature	Power
MHTS	70bar (abs)	Core Inlet = 260 ⁰ C Core Outlet = 285 ⁰ C	920MW (Full Power)
V1 Volume	1.0056bar (abs)	285 ⁰ C	
V2 Volume	1.0046172bar (abs)	30 ⁰ C	
Advanced Accumulator (ECCS)	55bar (abs)	40 ⁰ C	
GDWP (ECCS)	4 bar (abs)	40 ⁰ C	
Passive Valve	Start opening at 76.5 bar and fully opens at 79.5 bar of MHTS		
Active Valve	Opens at 79.5 bar of MHTS or 30 minutes after SBO (due to loss of pneumatic supply)		

Figure-4.4 shows the RELAP5 Nodalisation of the various systems of the reactor. Same RELAP model that is used for integral analysis (discussed in section 2.3.2) has been used here. Only PMCS is incorporated for integral calculations with PMCS. All the Calandria tubes are lumped in a representative one and heat transfer area of all the tubes are provided for heat removal calculations in heat structure model of RELAP5. Radiation mode of heat transfer is considered between the MHTS pressure tube and Calandria tubes. Calandria tubes are connected to the moderator thermally (as a heat structure), moderator is considered inside the Calandria Vessel. Total 24 axial nodes are considered for the Calandria tubes as well as for the Calandria Vessel. The intermediate heat exchanger shell and tubes are again lumped in a single representative shell and tube.

4.3.2 Scenarios considered

A prolonged SBO condition has been considered for analyzing the decay heat removal capability of the reactor. The cause of the SBO was postulated to be a strong earthquake

followed by a Tsunami which may cause the SBO. With initiation of the earthquake, the reactor gets safely shut down on the seismic signal. The turbine gets tripped which causes closure of CIESV and the feed water supply line isolation at the same time due to unavailability of feed pumps. Thus, the MHTS becomes boxed up, which causes the pressure of the MHTS to start rising.



Acc: Accumulator
Atm TDV: Atmospheric Time dependent Volume
CV: Calandria Vessel
GDWP: Gravity Driven Water Pool
IH: Inlet Header
IHx: Intermediate Heat Exchanger
ICs: Isolation Condensers
SD: Steam Drum
Sec. Side TDV: TDV simulating secondary side conditions (7MPa)

Figure-4.4 RELAP5 nodalization of AHWR

When the pressure of the MHTS reaches the set point of the passive valve of the Isolation Condenser (IC), i.e. 76.5 bar, the ICs gets valved in. Due to unavailability of the power supply, the pneumatic pressure is lost after 30 minutes, which causes the active valve in the ICs to remain continuously open. If the pressure of the MHTS falls below 50 bar, ECCS injection from accumulators starts and continues until the level in the accumulators falls below 75 cms which is a low level isolation of accumulator. If the MHTS pressure does fall below 3 bar then injection from GDWP may start injecting water into the core. The heat from the MHTS is modeled to transfer by radiation mode of heat transfer.

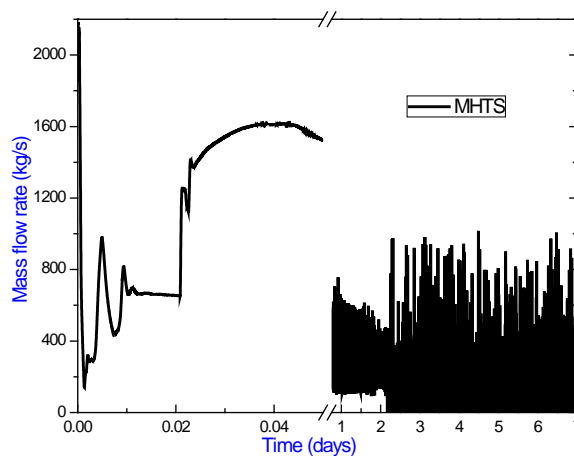
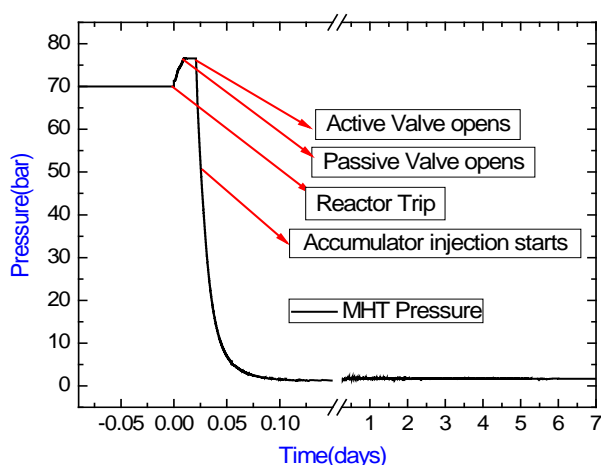
4.3.3 Results and discussions

Figures-4.5 and 4.6 show the variation of MHTS pressure and flow respectively. At time $t=0$ s, the reactor trips on the seismic signal. Due to a rise in pressure, the passive valves open at 76.5 bar after nearly 600 seconds and maintains the hot stand by conditions of 76.5 bar. The steam generated in the MHT system is condensed in the ICs just to maintain MHTS pressure constant. MHTS flow rate decreases instantaneously as the reactor trips due to void collapse and reduction in driving force. As soon as the ICs valve in and steam condense in ICs, the driving head increases and MHTS flow rate increases again. In longer term at decay power $<1\%$, the flow is observed to be fluctuating with net positive flow. Figure-4.7 shows the steam flow rate from the MHT to the ICS. The flow rate is initially higher due to larger decay heat, which reduces continuously due to reduction of decay heat with time. The active valve opens after 30 minutes, which directs a larger flow rate of steam into the ICs. This causes rapid condensation of steam resulting in progressive decrease of MHT pressure. At around 45 minutes, the MHT pressure falls to the set point of the accumulators and cold water is injected into the core passively. At about 2.5 hrs., Accumulator injection stops due to the low level of Accumulators (Figure-4.8). The MHT pressure remains well above the inject set point of GDWP. As a result no injection from GDWP occurs during the whole transient.

GDWP average water temperature is shown in Figure-4.9. It can be seen from Figure-4.9 that there is an initial surge in GDWP water temperature, which is due to the high decay heat just after reactor shutdown. Its average temperature reaches $\sim 95^{\circ}\text{C}$ after 7 days, but locally boiling occurs at atmospheric pressure nearly after 3 days.

Figure-4.10 shows the mass flow rate in the primary and secondary loop of the moderator circuit. It can be observed from this figure that mass flow rates are high during the initial period and decreases subsequently as decay power decreases. However, the temperature of the moderator entering the Calandria Vessel as well as leaving the Calandria Vessel (Figure-4.11 and 4.12) increases with time as the sink (GDWP) temperature rises. Figure-4.13 shows the heat balance between the moderator primary and secondary side of the heat exchanger.

The variation of clad surface temperature is shown in Figure-4.14. The clad surface temperature falls below 125°C after such a long transient, which implies that the passive systems are capable of cooling the fuel with sufficient margins for such a prolonged period. If containment venting is carried out after 7 days of the accident, the decay heat is removed by ICs by boil off of the GDWP water. However, in that case moderator temperature will keep on rising and moderator circuit over pressure rupture disc will burst that causes moderator to leaks out of the Calandria.



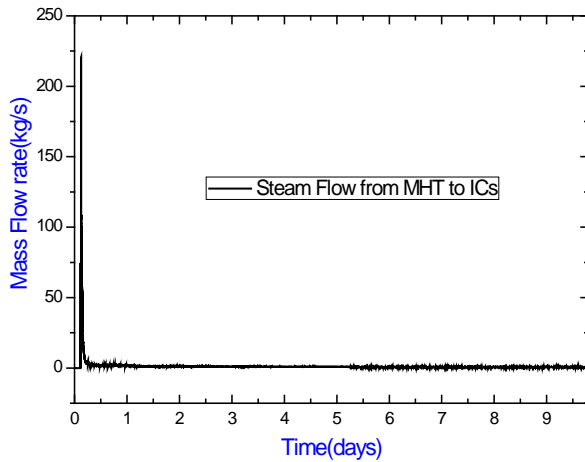


Figure-4.7 Steam flow to ICs

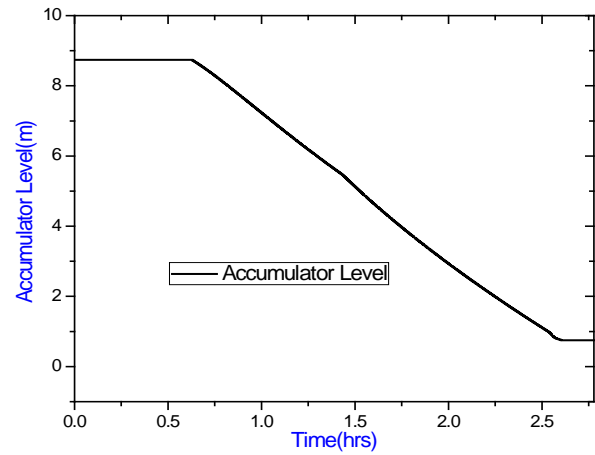


Figure-4.8 Accumulator level

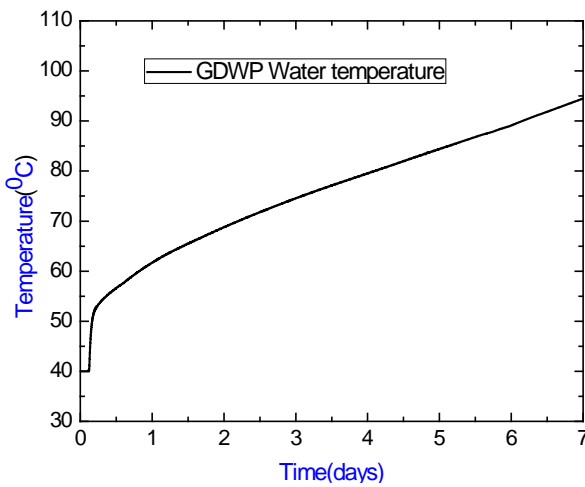


Figure-4.9 GDWP water temperature

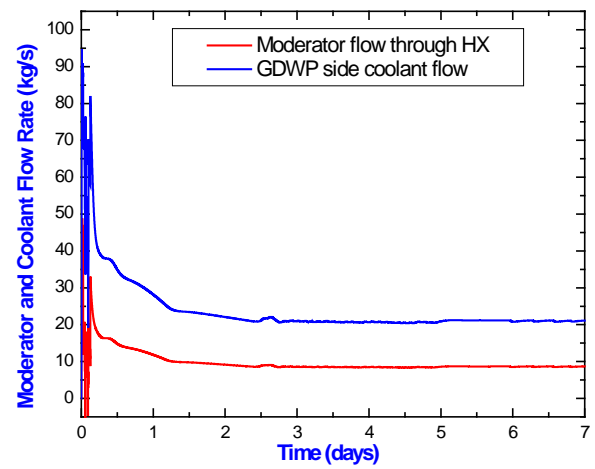


Figure-4.10 Moderator and GDWP side coolant flow

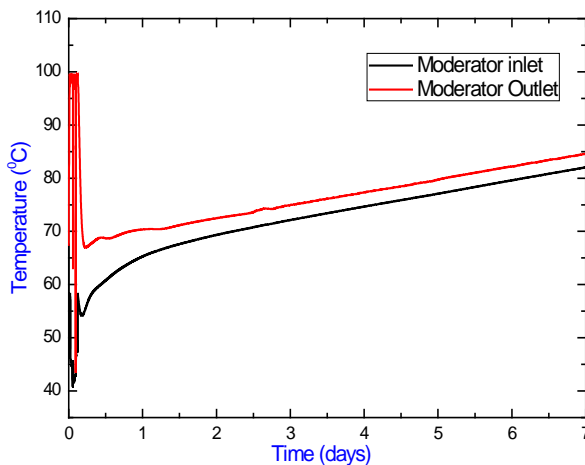


Figure-4.11 Moderator temperature

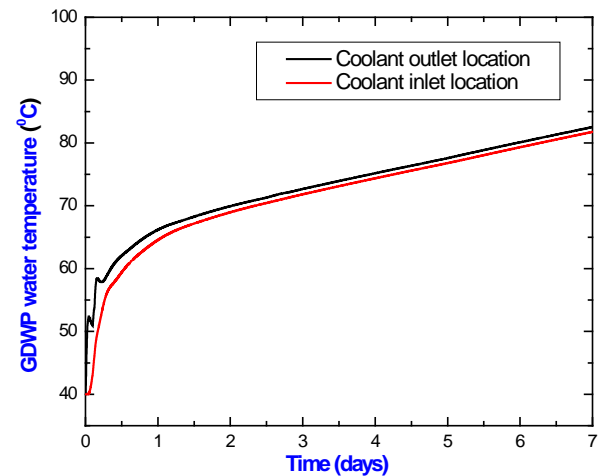


Figure-4.12 GDWP side coolant temperature

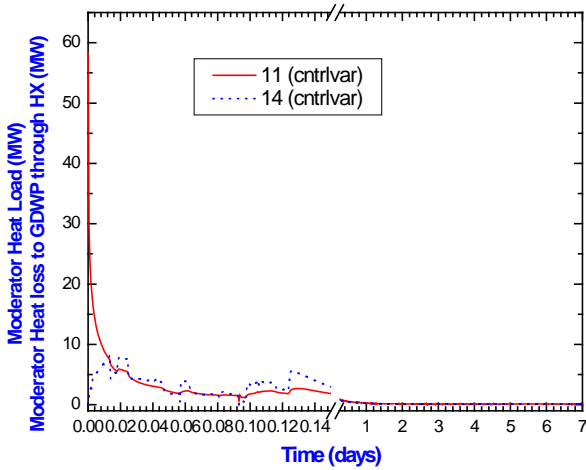


Figure-4.13 Heat balance between moderator primary and secondary side

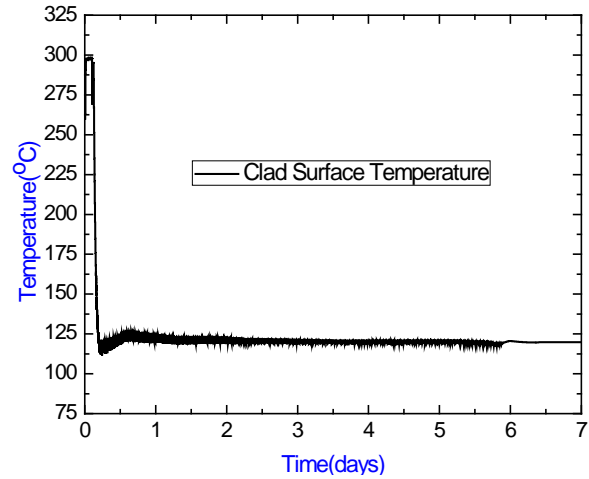


Figure-4.14 Clad surface temperature

4.4 Experimental studies

The test facility for experimental studies was designed based in Ishii three level scaling philosophy. Details of the scaling and ratios have been discussed in chapter-3. The test facility and experiments conducted in PMCS facility only is discussed here in this chapter.

4.4.1 Facility description

The Calandria Vessel (1, Figure-4.15, Figure-4.16a) is a 0.6m ID carbon steel cylindrical tank with 19 electrical heater tubes (in two rings with PCD of 0.24m and 0.48m) that simulate the Calandria tubes of the reactor. These are arranged in two circular rings as shown in Figure-4.16a. The heat exchanger (2), in Figure-4.15, is a shell and tube type heat exchanger designed to remove 10 kW. The shell inner diameter is 0.0525m housing 40 tubes of 0.006m OD. The pipes connecting Calandria and heat exchanger are of 50 NB sch40. The shell side of the heat exchanger is connected to the GDWP tank (4, Figure-4.15). The GDWP tank is a large 0.8m x 1.2m x 1m steel tank, which is open from the top. An expansion tank (height 0.7m and 0.3m diameter) is connected to the top of the Calandria Vessel and is located at the highest elevation of the primary loop to take care of thermal expansion of water. Figure-4.15 shows the Calandria Vessel, heat exchanger, piping, expansion tank and GDWP tank of the

experimental facility. To take care of heat loss to the atmosphere, the loop is insulated with ceramic wool. The geometrical details of the facility are summarized in Table-4.2.

Table-4.2 Geometrical details of the scaled model

Component	Dimensions	Actual PMCS	PMCS Scaled Model
Calandria	Diameter of shell, D_s (m)	6.0	0.6
	Outer diameter of fuel channel, d_t (m)	0.168	0.09
	Length, L (m)	5.3	0.6
	Total no. of tubes, N_t	513	19
Heat Exchanger	Diameter of shell, D_s (m)	1.35	0.0525
	Outer diameter of tube, d_t (mm)	12.7	6
	Length, L (m)	3.5	0.6
	Total no. of tubes, N_t	3431	40
	Thickness of tube, t (mm)	2.5	0.7

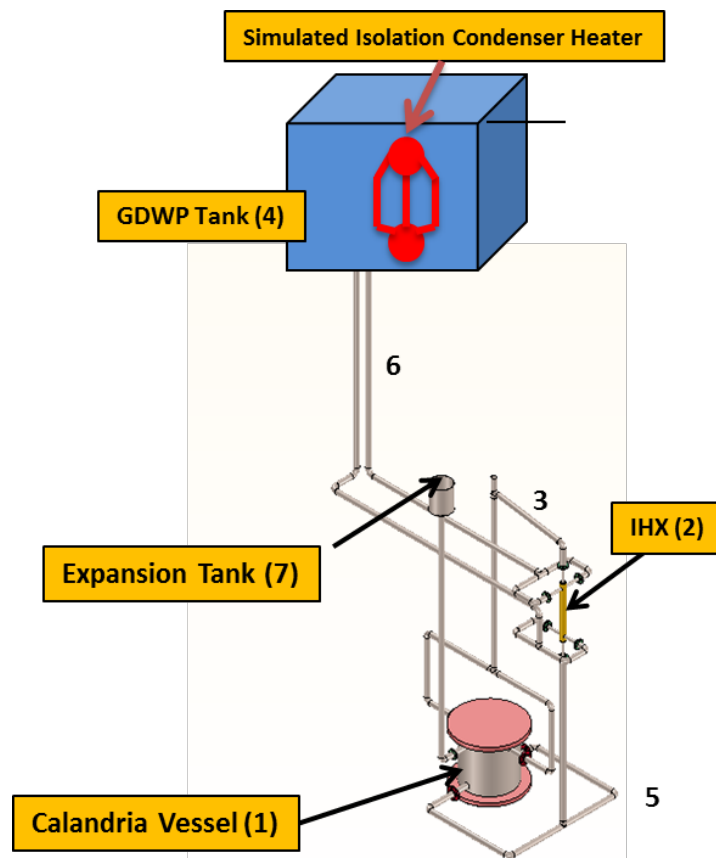


Figure-4.15 Schematic of PMCS test facility

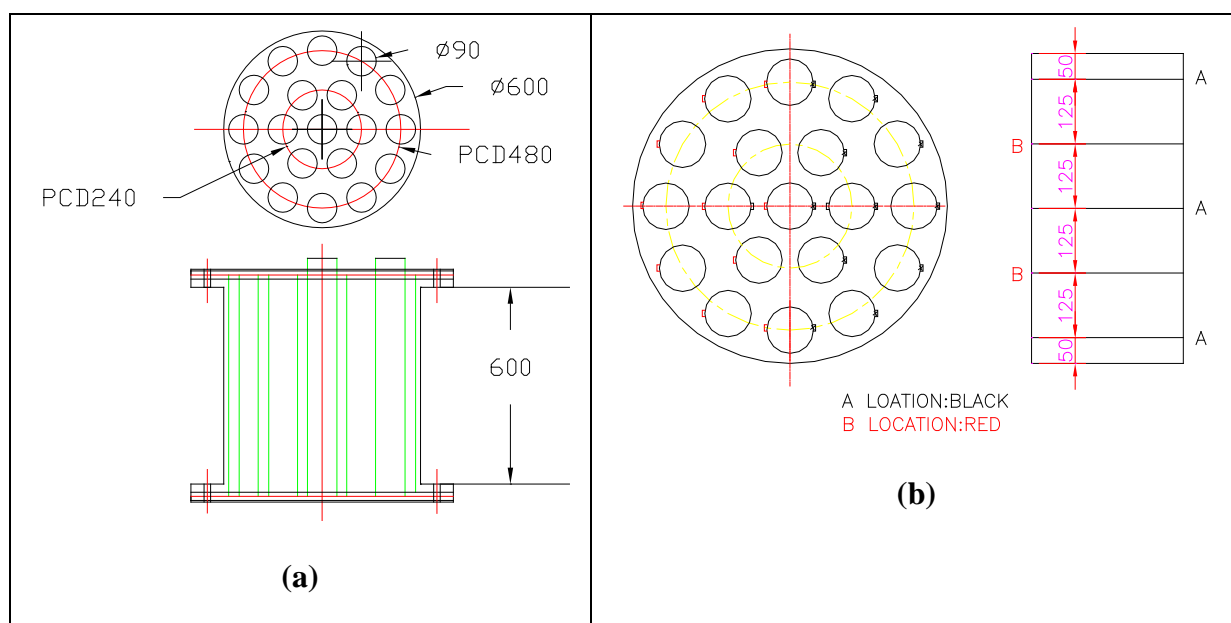


Figure-4.16 Details of simulated Calandria Vessel (a) Calandria Vessel housing directly heated calandria tubes (b) Thermocouples arrangement on the Calandria tubes

4.4.2 Instrumentations

Figure-4.17 shows process and instrumentation diagram of the test facility. Fifty seven thermocouples have been placed on nineteen Calandria tubes for fluid temperature measurement inside the vessel as shown in Figure-4.16b. 8 Calandria tubes contain 3 thermocouples each at various axial locations kept at 125 mm apart (A location in Figure-4.16b, 24 nos of thermocouples) while other 8 contains 2 thermocouples each at complementary locations at 125 mm apart (B location in Figure-4.16b, 16 nos of thermocouples). Remaining 3 Calandria tubes contain 5 thermocouples each at various axial locations as shown in Figure-4.16b (15 nos of thermocouples). Two additional thermocouples are placed for tripping the power supply at over temperature. Thus total 57 thermocouples are distributed uniformly among all the tubes. This gave a 3D temperature profile inside the calandria at all times. Further, thermocouples are also placed each at the inlet and outlet of the calandria, tube side of the heat exchanger and shell side of the heat exchanger. These are mineral insulated 0.5 mm diameter chromel-alumel thermocouples (K-type). Thermocouples

were calibrated in the range of 0-150 °C and are having measuring accuracy of 0.4 % ($\pm 0.6^{\circ}\text{C}$). Heater power could be controlled using dimmerstat and measured with the help of Wattmeter having an accuracy of 0.5 % of the span (0-10kW). All temperature data were recorded at a frequency of 10 seconds and fed to a data logger. For flow measurement differential pressure across heat exchanger shell side and Calandria Vessel was measured using capacitance type differential pressure smart transmitters. Differential pressure transmitters are installed with the three way manifold valves.

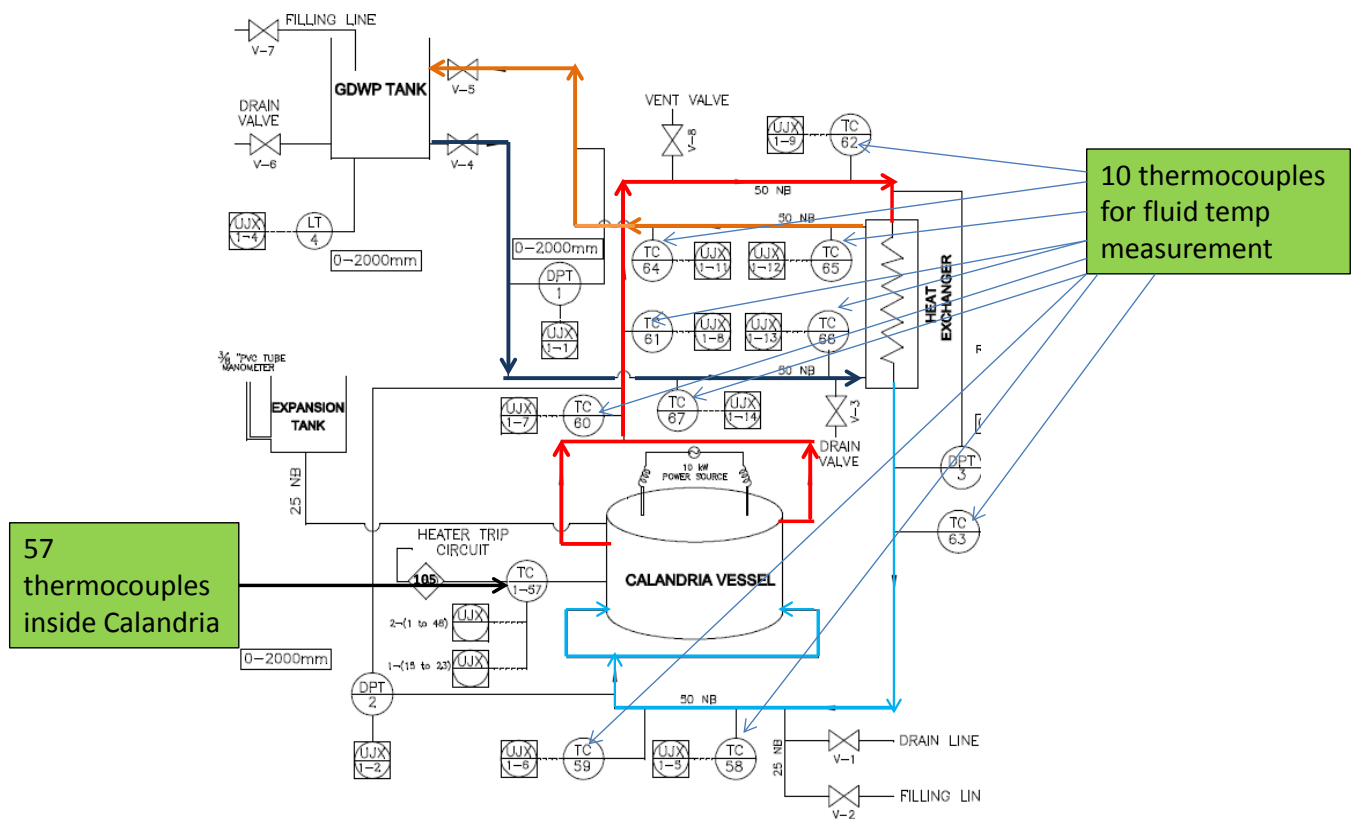


Figure-4.17 Process and instrumentation diagram of PMCS Test Facility

4.4.3 Experimental methodology

The primary loop was filled with water through the top expansion tank (7) in Figure-4.16. In this process, any air trapped in the loop was vented through a nozzle (8 in Figure-4.16) present at the top horizontal section of the primary loop. The level in the expansion tank was filled upto 0.55 m. The secondary loop was then filled through the GDWP tank till the level

in GDWP tank reaches 350 mm below the top surface of GDWP (4 in Figure-4.16), which is calculated based on the scaling for 7 days decay heat. The data recorders were switched on and then the heater power input was switched on. Average power of 1.8 kW was given to the moderator system for 7 days, while 1.2 kW average power corresponding to decay heat of 7 days was supplied to the GDWP heaters simulating isolation condensers. GDWP heaters were switched ON after achieving the initial steady conditions of moderator system. The experiment was conducted at atm pressure condition and only temperatures were measured due to difficulty in measurement of low flow in the loop by conventional differential pressure transmitters (DPTs).

4.5 Experiment results

The experiment performed can be divided in two steps:

4.5.1 Obtaining the initial conditions of moderator in the Test Facility

The Passive moderator cooling system in the reactor operates all the times i.e. during normal operation as well as during SBO conditions that enhances the reliability for the availability of the passive system. In this process the PMCS will transfer 2 MW heat to GDWP water. During the normal operation the moderator leaves the Calandria Vessel at 60⁰C and enters at 52⁰C temperature, while GDWP water temperature was maintained at atmospheric conditions by GDWP cooling system (active system). The GDWP cooling system will not be available during SBO and hence the temperature of GDWP will rise due to removal of decay heat through Isolation condensers and PMCS.

For simulating the prototypic conditions in the scaled test facility, moderator was brought to the initial conditions of temperature and flow in the system. During this phase of experiment, the temperature of water inside the GDWP increases as GDWP water cooling system was not incorporated in the test facility. For meeting the GDWP water temperature requirement as per prototypic conditions, the GDWP tank water was replaced with some fresh stock of water at atmospheric conditions, thus meeting the initial temperature and flow conditions. Figure-

4.18 shows the temperature variation during this phase of experiment. Around 14 hours were taken by the loop to reach the initial prototypic conditions of the moderator system.

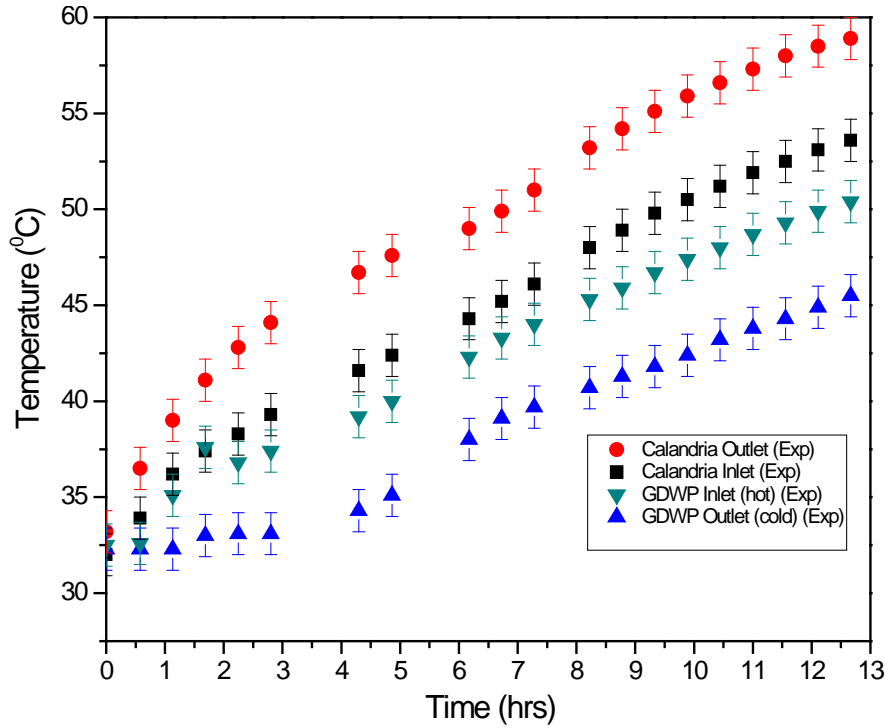


Figure-4.18 Temperature variation during 1st phase of experiment

The phenomena occurring during this initial phase of experiment can be further distinguished into three stages:

Stage I: Stationary primary and secondary loops

When the power is switched on, the fluid near the hot tubes gets heated, rises due to buoyancy and gets piled up at the top of Calandria. Simultaneously, relatively colder fluid is sucked from within the Calandria to replace this hot fluid, thus forming recirculation within the Calandria. As it is observed in the 15 minutes (Figure-4.18) there is hardly any change in the outlet temperature of Calandria and the heat exchanger. This means that the hot fluid is not coming out of the Calandria, i.e. flow is getting stratified inside the Calandria itself. Figure-4.19 shows the temperature distribution (stratified) inside Calandria vessel during this phase. The first contour shows the temperature distribution at vertical outlet plane and second

contour shows the temperature distribution at the mid horizontal plane. It can be regarded as the phase of 3-D natural convection phenomena inside the Calandria Vessel.

Stage2: Circulation in primary and stationary secondary loop

At time $t=30$ minutes, the temperature increases at both the inlet and the outlet of the Calandria, whereas the heat exchanger shell side outlet temperature remains constant. At this instant, the buoyancy head developed in the primary loop is sufficient to overcome the resistance of the loop. However in the second loop still the circulation does not get started. As a result the hot fluid coming out of the Calandria returns back to the Calandria with merely any change in temperature.

Stage3: Circulation in both primary and secondary loops

At $t = 45$ minutes, the buoyancy has risen sufficiently high that the circulation also begins in the secondary loop. This can be observed by the rise in shell outlet temperature. This circulation results in heat transfer from the tube side to the shell side of the heat exchanger. Consequently, the hot fluid exiting the Calandria transfers heat at the heat exchanger, and the cold fluid returns to the Calandria. The extent of heat transfer could be observed by the increase in temperature difference between the inlet and outlet of Calandria. The temperature at the shell side outlet increases sharply to almost equal to the Calandria inlet temperature and then rises smoothly after a small dip as depicted by Figure-4.20. Figure-4.21 shows the temperature distribution inside Calandria Vessel after circulation flow was established in both the loops. It is observed, that, initially the temperature contours are according to the local heat source present, i.e. locations where hot tubes are present have higher temperature, overlapped with a higher temperature zone near the top (i.e. stratification).

4.5.2 Decay heat removal in a scaled test facility for prolonged period

This phase of experiment is envisaged corresponding to the SBO conditions in the reactor. The average simulated decay heat for 7 days was supplied to the submerged heaters inside GDWP and moderator through Calandria tubes. The experiment was run for 7 days to simulate prolonged SBO conditions of the reactor. Figure-4.22 shows the temperature distribution inside Calandria Vessel at day 0 (initial conditions for second phase of experiment) corresponding to the prototypic moderator conditions inside Calandria Vessel.

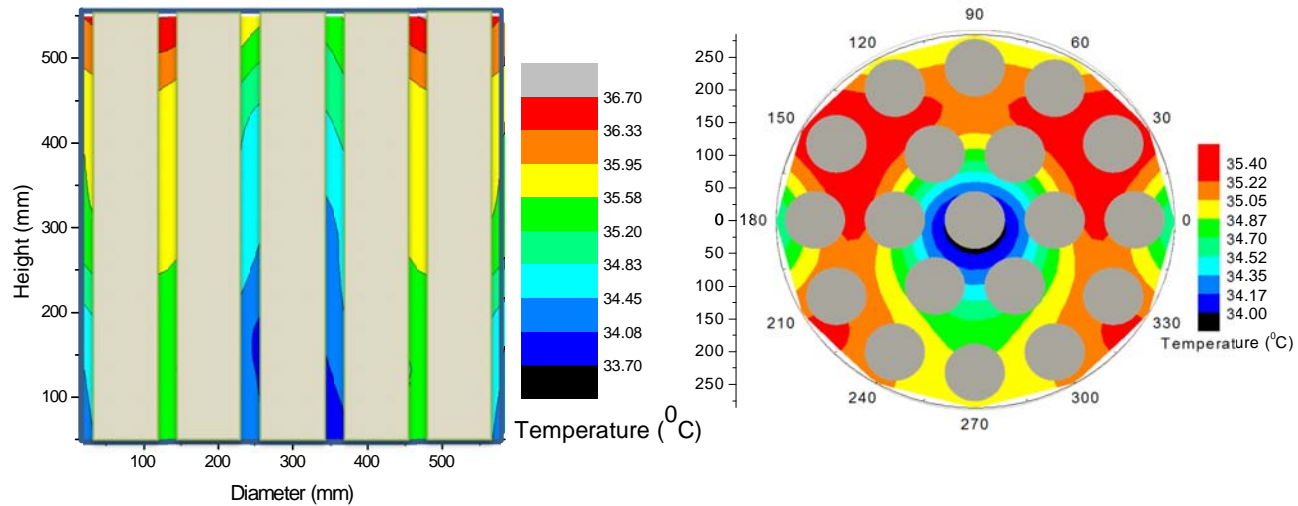


Figure-4.19 Temperature distribution inside Calandria Vessel @ 15 minutes during 1st phase of experiment

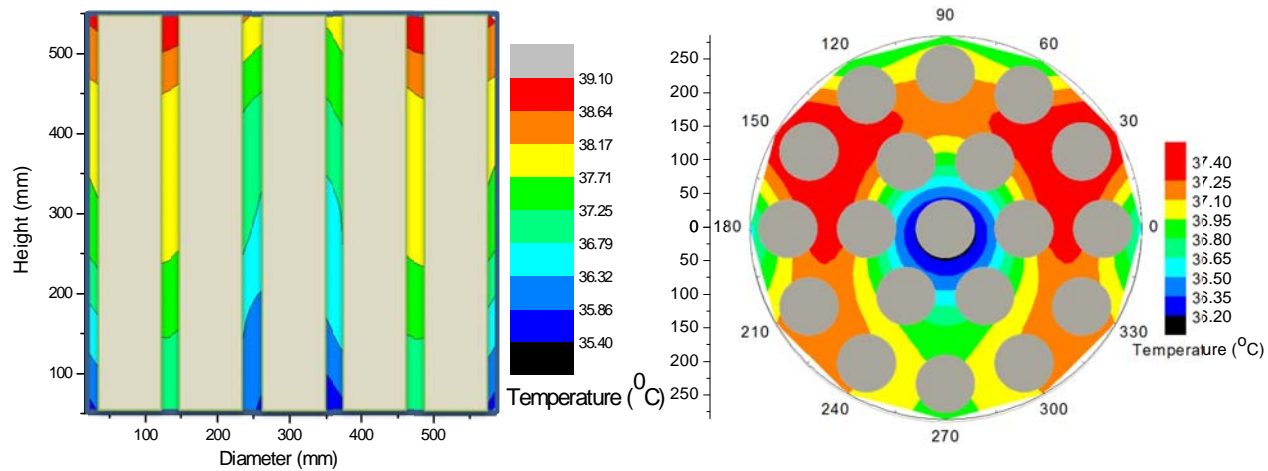


Figure-4.20 Temperature distribution inside Calandria Vessel @ 45 minutes during 1st phase of experiment

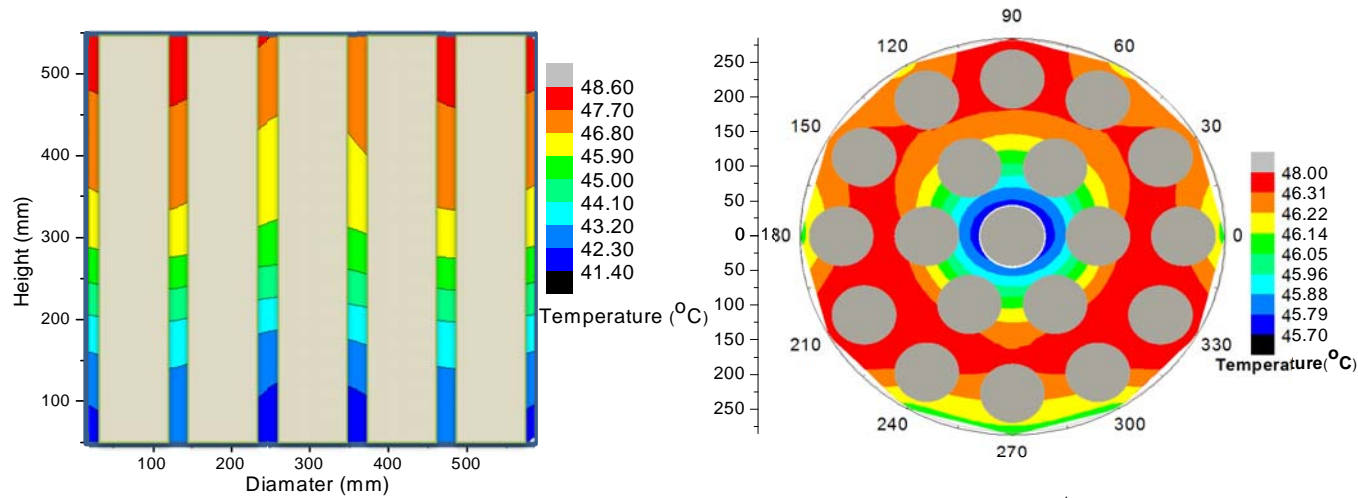


Figure-4.21 Temperature distribution inside Calandria Vessel @ 3 hrs during 1st phase of experiment

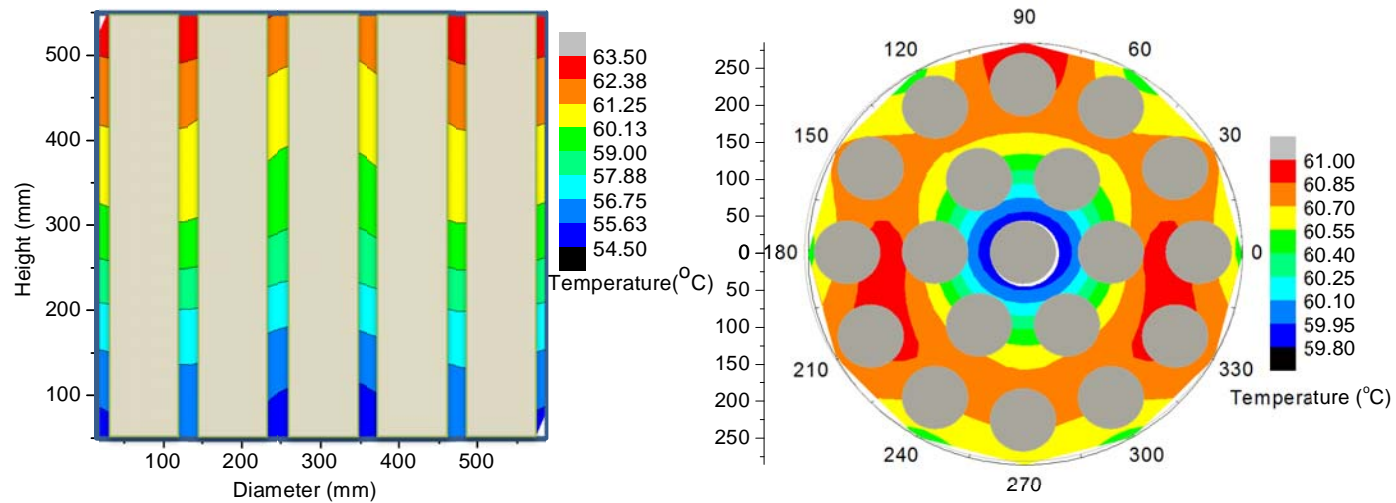


Figure-4.22 Temperature distribution inside Calandria Vessel @ t=0 day during 2nd phase of experiment

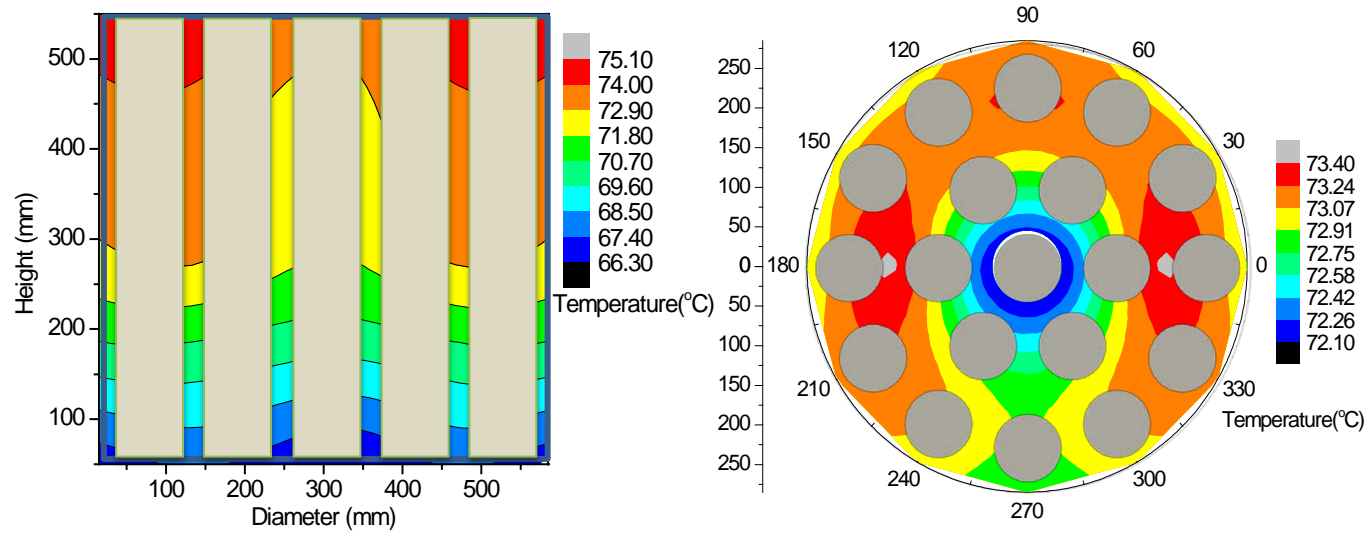


Figure-4.23 Temperature distribution inside Calandria Vessel @ $t = 1$ day during 2nd phase of experiment

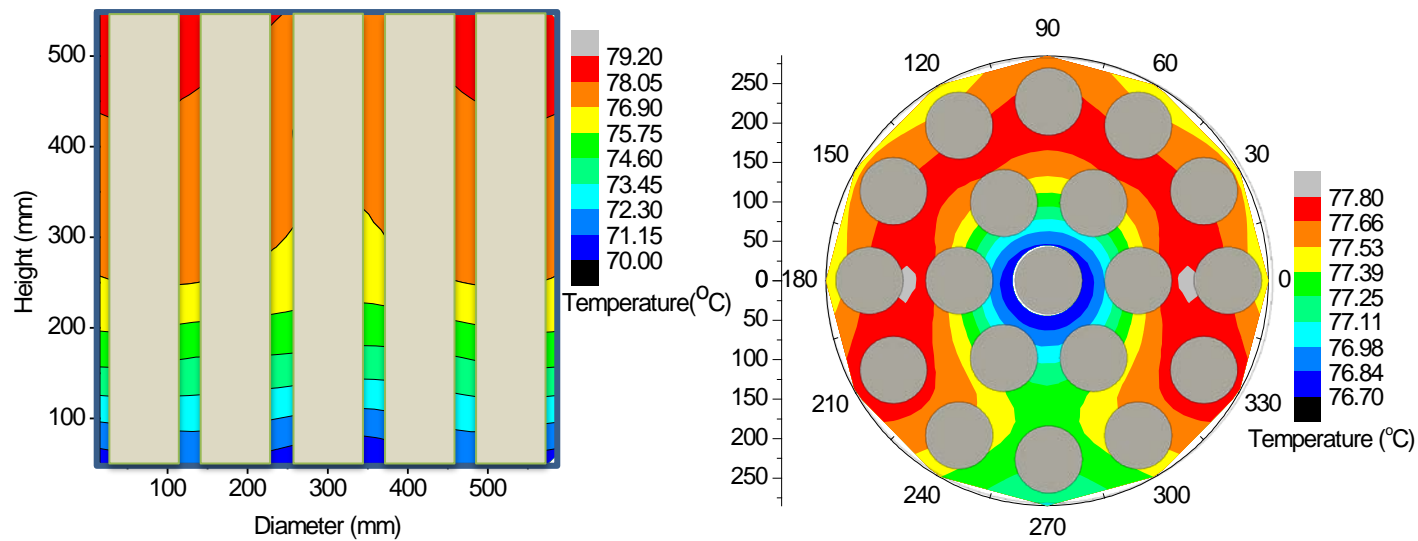


Figure-4.24 Temperature distribution inside Calandria Vessel @ $t = 7$ day during 2nd phase of experiment

Temperature contour for long duration:

Figure-4.23 and Figure-4.24 show the time varying temperature contours for the entire duration of the experiment, taken at day 1 and day 7. It can be observed from these contours that the major flow throughout the entire loop is unable to affect the stratified contour inside Calandria. Figure-4.25 shows the temperature variation of the moderator and cold water entering and leaving the Calandria and GDWP tank respectively. It can be observed from Figure-4.22 that the temperature of the moderator leaving the Calandria vessel does not rise above 80°C for 7 days.

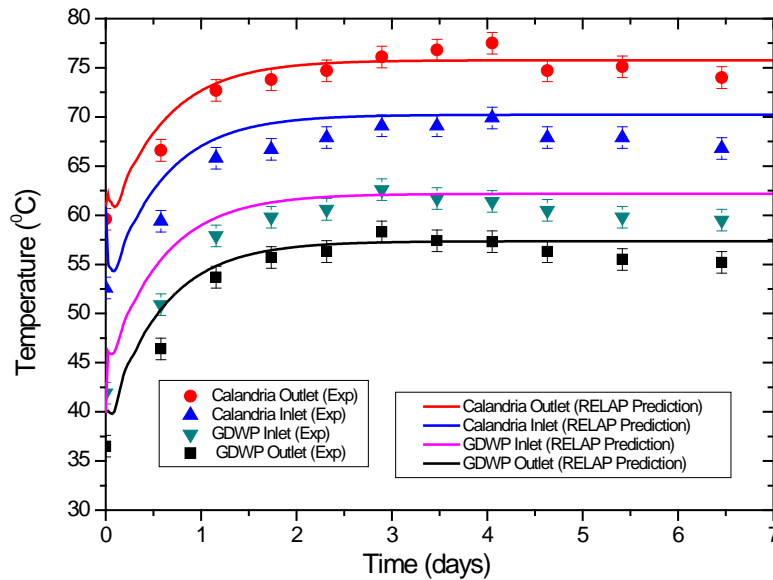


Figure-4.25 Fluid temperature variation at Calandria inlet/outlet and GDWP inlet/outlet (Experiment and RELAP predictions)

4.6 RELAP simulation of the test performed in the scaled Facility

4.6.1 Nodalisation scheme

Both the primary and secondary loops in the PMCS test facility were simulated with heat transfer across the heat exchanger tubes. All the tubes of the heat exchanger were grouped as a single equivalent channel having the equivalent flow area and heat transfer area. Similarly, the Calandria vessel also was simulated as an equivalent channel. All the Calandria tubes were lumped together into one having the same heat transfer area and heater power input as

the actual tubes. Both the Calandria and the heat exchanger length were divided into uniform 20 nodes. The GDWP was simulated as a pipe volume with 20 nodes of water and top 2 nodes with air connected to an atmospheric volume. The isolation condenser heaters were simulated as the heat structure to the GDWP volumes from node 5 to 10. The connecting pipes were nodalised with 0.1m nodes. The heat input to the Calandria tube was given as a constant power corresponding to the average decay heat. The working fluid was light water in both the loops. Figure-4.26 shows the nodalisation of the test facility for RELAP5 Mod 3.2.

4.6.2 RELAP and experimental data comparison

RELAP prediction results are shown in Figure-4.25 and Figure-4.27. Figure-4.25 shows the temperature variation of the moderator and GDWP cold water for 7 days. On comparing with the experimental data with RELAP predictions from Figure-4.25, it can be seen that RELAP was able to predict the behavior in a narrow band. RMS error in predicting the Calandria inlet, outlet and GDWP inlet and outlet are found to be 3.2%, 1.5%, 3.8% and 2.5% respectively. The difference in the predictions and experiment is high at higher GDWP water temperature due to large heat losses at higher temperature which could not be captured by RELAP5 correctly.

RELAP being a 1D code is not able to capture the initial transient in which there are internal recirculatory flows within the Calandria. This is because, in 1-D case, as soon as the heat input to Calandria begins the hot fluid rises due to buoyancy and exits the Calandria, rising further upward through the pipes. In turn, to maintain continuity, the cold fluid gets sucked in through the inlets of the Calandria, completing the flow in the entire loop. Thus, unlike in the real experiment, a temperature difference across the inlet and outlet of Calandria is observed from the beginning.

Also on the shell side a similar phenomenon is seen. The temperature at the shell side inlet, keeps on increasing in the RELAP simulations. However, in this experiment the temperature

remains almost constant till 1h. Figure-4.27 shows the mass flow rate in the primary and secondary loop of the PMCS test facility. As soon the simulation starts due to less temperature difference in the outlet and inlet of the calandria vessel and intermediate heat exchanger, as high flow of 0.068 and 0.060 kg/s is observed in secondary and primary loops respectively as seen in Figure-4.27. But as the moderator and GDWP water temperature increases and temperature difference between inlet and outlet increases, a dip in flow can be observed before it again increases to steady value of 0.074 and 0.068 Kg/s in secondary and primary loop, respectively.

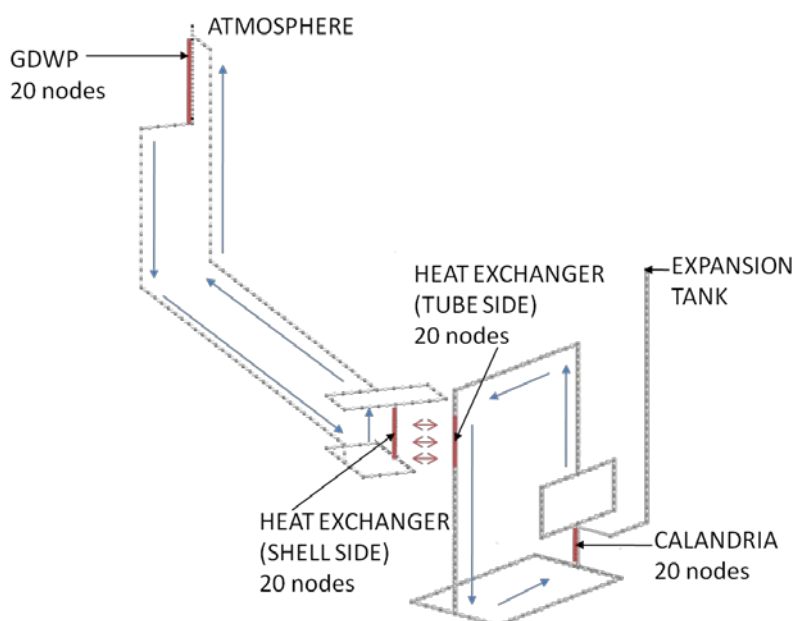


Figure-4.26 RELAP5 Nodalisation of PMCS Test Facility

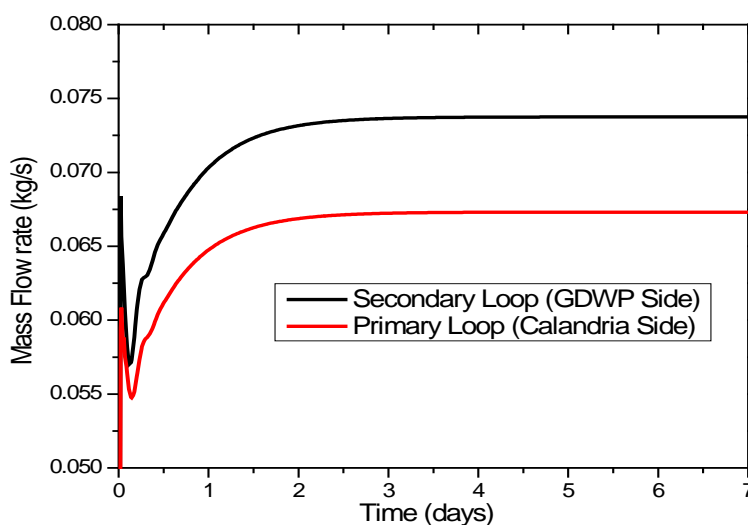


Figure-4.27 Variation of mass flow rate (RELAP Simulation)

4.7 CFD simulation of simulated Calandria Vessel for steady states

In this study, CFD simulation was carried out for the steady state condition of mass in and out to the Calandria Vessel. Only Calandria Vessel has been simulated with Open source Open FOAM 2.3.1 (Open FOAM,2014). The steady state temperature distribution inside the Calandria Vessel was obtained from CFD and results are compared with the steady state experimental data of the temperature distribution inside Calandria Vessel at two time instances during the experiment. The initial and boundary conditions are described in Table-4.3 for the selected CFD cases. The cases (#1 and #2) were selected for the time instances after achieving the initial conditions of the moderator in the Calandria Vessel same as that in the reactor.

Table-4.3 Details of CFD cases studied

Case No.	Time instances during experiment	Initial and boundary conditions for calandria vessel				CFD Solver	Turbulence Model
		Inlet Temperature ($^{\circ}\text{C}$)	Inlet Mass Flow rate (kg/s)	Outlet Conditions	Heater Power (W)		
1	0 day (Initial state achieved)	54	0.065	outflow	1800	bouyantBoussinesq simpleFoam	k- ϵ model
2	0.5 day (After achieving initial state of moderator temperature)	57	0.065	outflow	1800	bouyantBoussinesq simpleFoam	k- ϵ model

4.7.1 Governing equations

The flow is assumed to be steady, incompressible, 3-dimensional and turbulent. Fluid properties are assumed to be constant, i.e. fluid properties are not varying within the

considered temperature range. The governing equations for the Newtonian, incompressible turbulent flow are given by:

Continuity equation:

$$\frac{\partial \bar{u}_j}{\partial x_j} = 0 \quad \dots (4.1)$$

Momentum transport equation:

$$\frac{\partial \bar{u}_i}{\partial t} + \frac{\partial}{\partial x_j} (\bar{u}_j \bar{u}_i) - \frac{\partial}{\partial x_j} \left\{ \nu_{eff} \left[\left(\frac{\partial \bar{u}_i}{\partial x_j} + \frac{\partial \bar{u}_j}{\partial x_i} \right) - \frac{2}{3} \left(\frac{\partial \bar{u}_k}{\partial x_k} \right) \delta_{ij} \right] \right\} = -\frac{1}{\rho} \frac{\partial \bar{p}}{\partial x_i} + S_M \quad \dots (4.2)$$

where $\nu_{eff} = \nu_0 + \nu_T$

The buoyancy effect is modeled by the inclusion of a source term in the momentum equation as follows: $S_M = (\rho - \rho_{ref})g_i$ (4.3)

where ρ is the fluid density and ρ_{ref} is the fluid reference density.

Since the pressure gradient is relatively small in the natural circulation loop and density variations are due to only temperature variations, the Boussinesq approximation was used as follows: $S_M = -\rho_{ref}\beta g_i(T - T_{ref})$ (4.4)

where β is the thermal expansion coefficient $\beta = -(1/\rho) \cdot \partial \rho / \partial T|_p$

The reference temperature is taken equal to the temperature on the heat exchanger tube surface for each simulated case. All the thermal properties are defined at this reference temperature.

Energy conservation equation:

$$\frac{\partial \bar{T}}{\partial t} + \frac{\partial}{\partial x_j} (\bar{T} \bar{u}_j) = \frac{\partial}{\partial x_j} \left[\left(\frac{\nu_t}{Pr_T} + \frac{\nu_0}{Pr} \right) \frac{\partial \bar{T}}{\partial x_k} \right] \quad \dots (4.5)$$

where Pr_T is the turbulent Prandtl number.

4.7.2 Turbulence modeling

The CFD simulations were performed for a pseudo steady state conditions on the Calandria vessel. Uniform flow fields are expected to be generated inside it; hence, considering the

isotropy of turbulence k-ε turbulence model has been selected for simulations. The equations of the models are described below:

The standard k-ε model (Launder and Sharma, 1974)

The eddy viscosity is modeled as follows:

$$\mu_t = C_\mu \frac{k^2}{\varepsilon} \quad \dots (4.6)$$

Turbulent kinetic energy (k) transport equation:

$$\frac{\partial(\rho k)}{\partial t} + \nabla \cdot (\bar{u}_j \rho k) = \nabla \cdot \left[\left(\mu + \frac{\mu_t}{\sigma_k} \right) \nabla k \right] + G_k + G_b - \rho \varepsilon \quad \dots (4.7)$$

Turbulent dissipation rate (ε) transport equation:

$$\frac{\partial(\rho \varepsilon)}{\partial t} + \nabla \cdot (\rho \varepsilon \bar{u}_j) = \nabla \cdot \left[\left(\mu + \frac{\mu_t}{\sigma_\varepsilon} \right) \nabla \varepsilon \right] + C_{1\varepsilon}(G_k + C_{3\varepsilon}G_b) - C_{2\varepsilon}\rho \frac{\varepsilon^2}{k} \quad \dots (4.8)$$

where $G_k = -\rho \overline{u'_i u'_j} \frac{\partial \bar{u}_j}{\partial x_i}$, $G_b = -\beta g \frac{\nu_t}{\sigma_t} \frac{\partial \bar{T}}{\partial z}$ and $\beta = -\frac{1}{\rho} \left(\frac{\partial \rho}{\partial T} \right)_p$

The model constants are given as follows:

$$C_{1\varepsilon}=1.44, C_{2\varepsilon} = 1.92, C_{3\varepsilon} = 0.09, \sigma_k = 1.0, \text{ and } \sigma_\varepsilon = 1.3$$

4.7.3 Boundary conditions for modeling

Inlet

At inlet, the Dirichlet boundary conditions are specified for all the mean velocity components and temperature while homogeneous Neumann boundary conditions are specified for the pressure. For turbulent kinetic energy k, constant value can be prescribed based on the background disturbances usually measured in terms of turbulent intensity (I), defined as:

$$I = \frac{\sqrt{\frac{2k}{3}}}{U_\infty} \quad \dots (4.9)$$

In current analysis inlet intensity of 5% has been used. This gives the value of k at inlet. The inlet value of ε is calculated using the following equation as has been explained in Biswas and Eswaran (2002):

$$\varepsilon = \frac{k^{3/2} C_\mu^{3/4}}{0.07 L_{char}} \quad \dots (4.10)$$

where L_{char} is taken as the hydraulic diameter.

Outlet

At the outlet boundary, homogeneous Neumann boundary condition can be prescribed for all the scalars except the pressure.

$$\frac{\partial f}{\partial x} = 0; \quad f = u, T, k, \varepsilon \quad \dots (4.11)$$

For pressure a constant value equal to zero or ambient pressure is assigned at the outlet.

Wall

At solid no-slip wall boundaries, the standard wall function treatment is applied for all the velocity components and turbulence quantities (k, ε). For the pressure homogeneous Neumann boundary condition ($\partial p / \partial x = 0$) is applied.

Near the wall turbulent fluctuations tend to zero and flow very close to the wall is laminar in the so-called laminar sub-layer. In this sub-layer the velocity gradient is very high compared to the region outside it. Thus to give proper boundary conditions at the wall for the RANS mean velocity equations, the grid-points near the wall have to be very close to be able to properly resolve this high gradient. But an alternative is to assume a fully developed turbulent boundary layer and then apply velocity and scalars boundary values using analytical expressions such as log-law. This approach is termed as wall function approach. The velocity scale near the wall which is also called friction velocity, u_τ , is defined as,

$$u_\tau = \sqrt{\frac{\tau_w}{\rho}} \quad \dots (4.12)$$

where τ_w is the shear stress near the wall. It has been shown in Pope (2000) in the wall region,

$$\begin{aligned} u^+ &= y^+; & \text{for } y^+ \leq 10.9; & \quad \text{viscous sub - layer} \\ u^+ &= \frac{1}{\kappa} \ln(Ey^+); & \text{for } 300 > y^+ & \\ &\geq 10.9; & \text{log - layer} & \quad \dots (4.13) \end{aligned}$$

where κ is the von-Karman constant (=0.42) and $E = 9.0$.

In the logarithmic region, the viscous stresses are low, and the turbulent shear stress is approximately equal to the wall shear stress.

Hence

$$\mu_t \frac{\partial u}{\partial y} \approx \tau_{wall} = \rho u_\tau^2 \quad \dots (4.14)$$

At the wall, $u, v, w \rightarrow 0$ and $k \rightarrow \text{constant}$, so the modelled equation for k (Eq. 4.7) gives

$$0 = \mu_t \left(\frac{\partial u}{\partial y} \right)^2 - \rho \varepsilon \quad \dots (4.15)$$

where log-law gives (Eq. 4.13)

$$\frac{\partial u}{\partial y} = \frac{u_\tau}{\kappa y} \quad \dots (4.16)$$

Substituting this along with the definition of μ_t (Eq. 4.6) we get:

$$k = C_\mu^{-1/2} u_\tau^2 \text{ and } \varepsilon = \frac{u_\tau^3}{\kappa y} \quad \dots (4.17)$$

As k becomes a constant value in the log layer, we can prescribe the homogenous Neumann boundary condition for k at the wall, $(\partial k / \partial y = 0)$.

The ε at wall is computed from Eq. (4.17) as:

$$\varepsilon = \frac{u_\tau^3}{\kappa y} = \frac{C_\mu^{3/4} k_P^{3/2}}{\kappa y_P} \quad \dots (4.18)$$

4.7.4 Methodology for analysis

Grid independence study of the meshing was carried out with three different mesh sizes: (1) 0.33 million, (2) 0.82 million and (3) 2.05 million cells. The mesh size increment was kept at the rate of ~2.5 times. A steady state simulation was performed for a constant heater power of 500W. The results are shown in Figure-4.28a where the temperature difference between the outlet and inlet of the Calandria plot for different mesh sizes; and Figure-4.28b in the form of

axial plot of temperature along the z-axis 3 mm from the central tube inside the Calandria. This variation between point (2) and (3) in temperature difference was approximately 8%, whereas the absolute value of the temperature at the Calandria outlet varied within 0.05%. Thus the calculations are performed for the mesh with 1.13 million elements. Figure-4.29 shows the CFD model and the meshing (total 0.82 million cells) of the simulated Calandria Vessel. Modeling of the convection term in the governing equations was done using the second order upwind scheme. A Semi-Implicit Method for Pressure Linked Equation method (SIMPLE) was used for steady state simulations, which is a pressure-velocity coupling numerical algorithm. All the solutions were considered as fully converged when the average of scaled residuals was below 10^{-4} . All the computations were carried out in a parallel manner on a cluster using 48 cores. Boussinesq approximation is assumed to be valid for the model and considered for the density variations for the calculations as the temperature difference across Calandria Vessel is less ($\sim 4^{\circ}\text{C}$ to max 8°C).

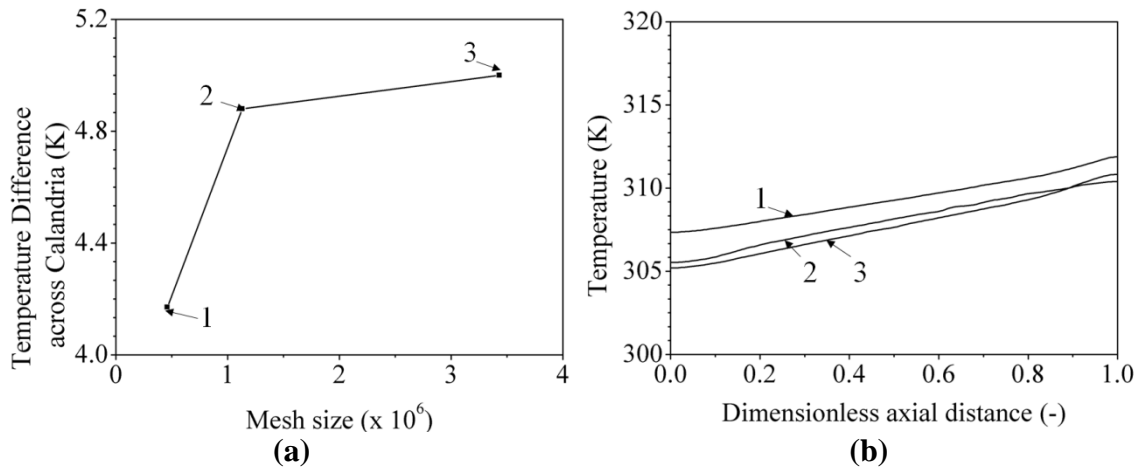


Figure-4.28 (a) Temperature difference between the outlet and inlet of the Calandria for grid sizes: (1) 0.33 million cells, (2) 0.82 million cells and (3) 2.05 million cells and (b) variation of temperature along the axial height of the Calandria at a location 3mm away from the surface of the central tube

For natural convection systems the turbulence is assessed based on Rayleigh number. For the CFD simulation, flow in the system is initially considered stagnant. After application of power, flow is generated in the Calandria. This flow can exist in the form of recirculations

within the Calandria. The flow inside the vessel is similar to natural convection flow in a cavity for which Rayleigh number decides laminar/turbulent regime. The Rayleigh number inside the Calandria vessel is found to be more than 10^9 . The Rayleigh number in the Calandria for the given heat input (1800W) is $\sim 10^{11}$. This lies in the turbulent regime ($Ra > 10^9$) for natural convection. Hence, standard $k-\epsilon$ turbulence model by Launder and Sharma (1974) is used for the CFD simulations.

Figure-4.30 shows the temperature variation on the vessel walls, temperature rising from inlet to the outlet of the vessel after gaining heat from the Calandria tubes. Figure-4.31 shows the fluid temperature distribution inside the vessel at the outlet plane.

Residual for the simulations

CFD codes utilize absolute residual convergence as well as relative tolerance criteria. For a matrix system $Ax = b$, the residual is defined as

$$r = b - Ax \quad \dots (4.19)$$

We then apply residual scaling using the following normalisation procedure:

$$n = \sum (|Ax - A\bar{x}| + |b - A\bar{x}|) \quad \dots (4.20)$$

where \bar{x} is the average of the solution vector. The scaled residual is finally given by:

$$r = \frac{1}{n} \sum |b - Ax| \quad \dots (4.21)$$

This form leads to a normalised residual of 1 for uniform systems, i.e. where $x = \bar{x}$. However, this also shows that if the initial solution changes, e.g. using non-uniform conditions; the normalisation also changes, leading to a different convergence history. Along with the convergence criteria, flux conservation is also important across the boundaries of the domain e.g. mass, heat balances.

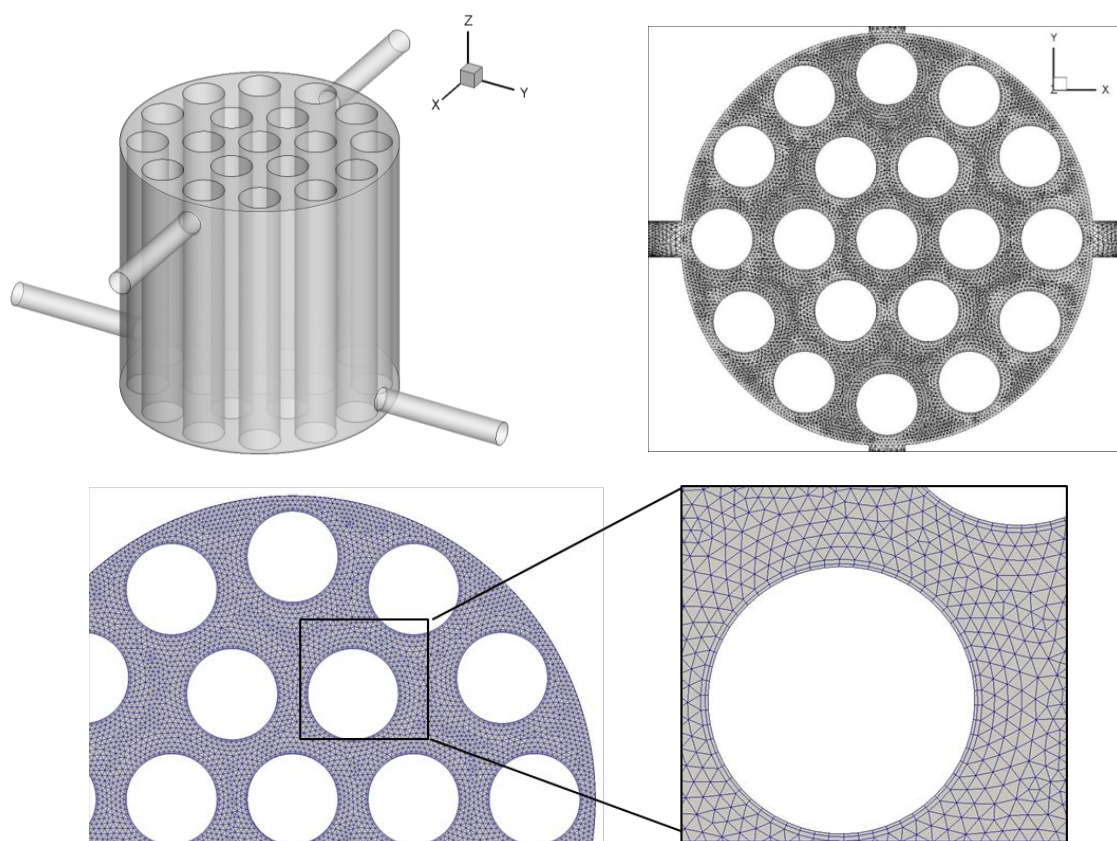


Figure-4.29 CFD Model and Mesh of calandria vessel

4.8 CFD predictions and experimental data comparison

Figure-4.31a shows the fluid temperature distribution as predicted by CFD (i) for case#1 (fluid inlet temperature 54°C at time $t=0$ day; the initial conditions for the experiment conducted) and its comparison with the experimental data (ii), while Figure-4.31b shows the CFD predictions (i) for fluid temperature distribution inside the vessel for case#2 (fluid inlet temperature 57°C at time $t=0.5$ day; a steady condition after achieving the initial conditions) along with the experimental data (ii). A range of temperature from 54.5°C to 63.5°C was observed in both CFD predictions as well as during the experiment for case#1. With almost same average temperature of $\sim 58.5^{\circ}\text{C}$ in CFD and also in experiment for case#1, the temperature contours are also identical (qualitatively) with minor difference. However, for case#2, average temperature is slightly high ($\sim 61.5^{\circ}\text{C}$) for CFD predictions as compared with experimental data ($\sim 60^{\circ}\text{C}$). The temperature contours also shows slight difference in qualitative agreement also. It can be seen from Figure-4.31 that the temperature difference

across the Calandria Vessel as predicted by CFD is comparable and in a close agreement with the experimental data. A RMS error of 0.704 (1.18%) is found at 0 day instance while RMS error of 0.59 (1%) has been observed for 0.5 day instance.

Figure-4.32 and 4.33 shows the velocity distribution at inlet and outlet plane (top view). Velocity is found to be high (80% of maximum velocity of inlet) at the inlet and outlet of the vessel. The velocity is found to be very low ($\sim 0.0025\text{m/s}$) in rest of the vessel, which is expected for a natural driven system operating at low powers.

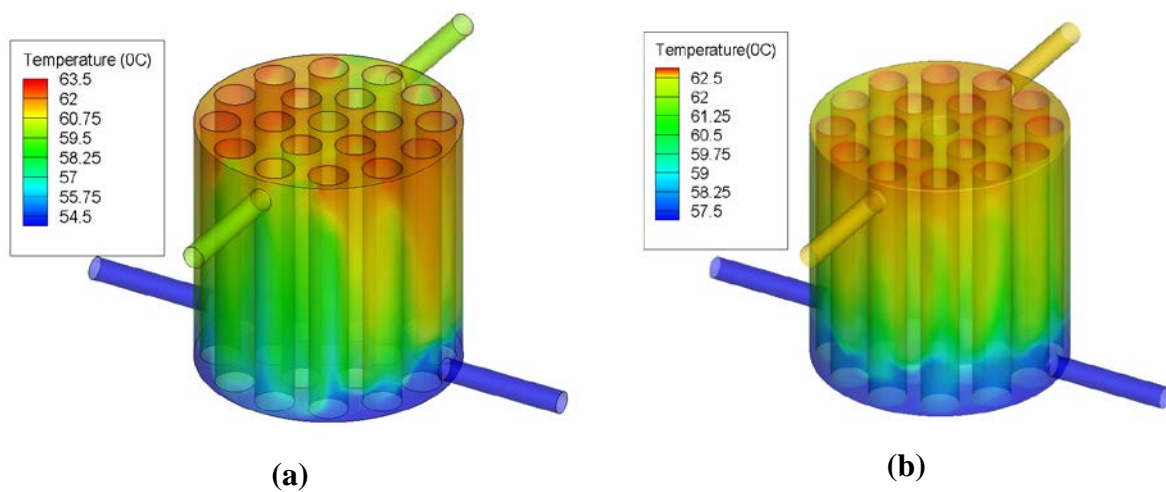
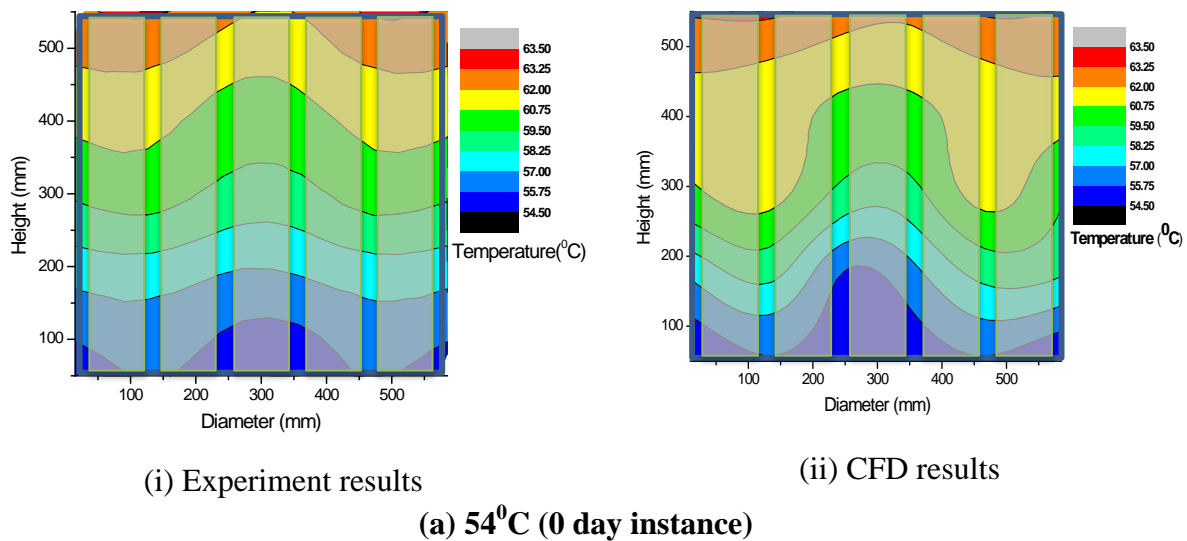
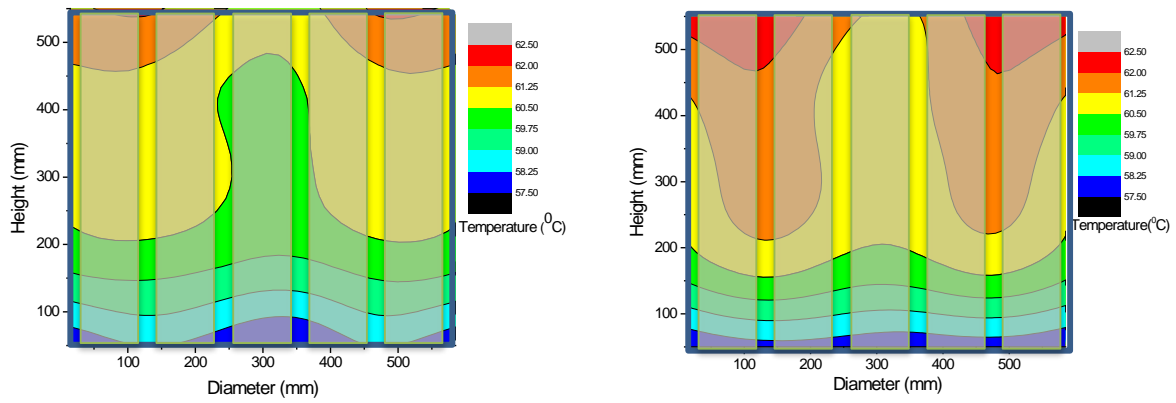


Figure-4.30 Temperature Distribution inside Calandria Vessel wall at various inlet temperatures (a) 54°C (0 day instance) (b) 57°C (0.5 day instance) as predicted by CFD



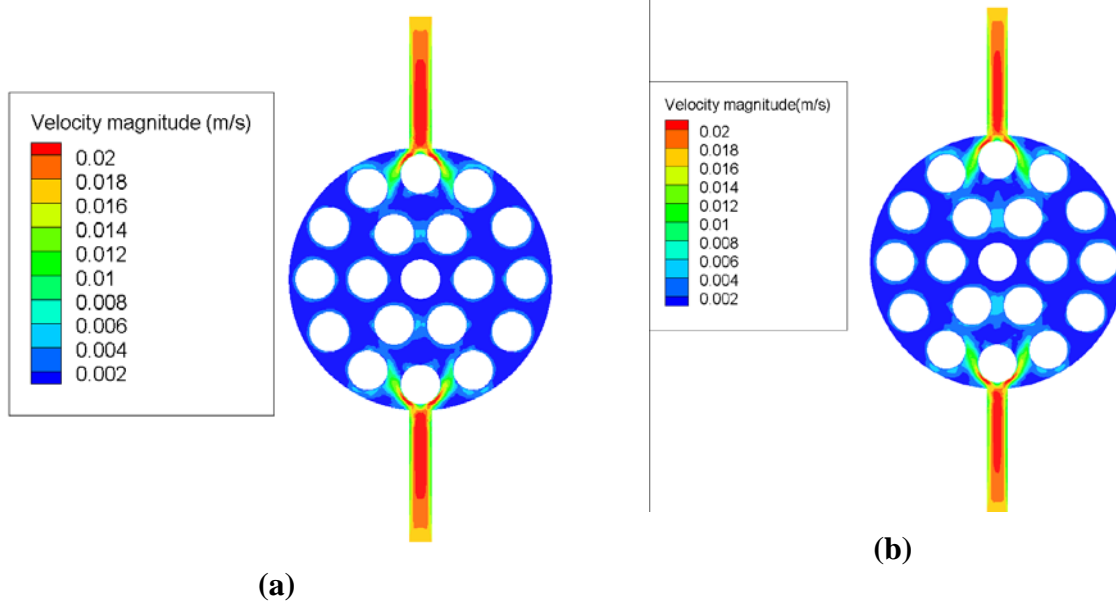


(i) Experiment results

(ii) CFD results

(b) 57°C (0.5 day instance)

Figure-4.31 Temperature Distribution at outlet plane for various inlet temperatures (Comparison of CFD predictions and experiments)



(a)

(b)

Figure-4.32 Velocity Distribution at Inlet plane for various inlet temperatures (a) 54°C (0 day instance) (b) 57°C (0.5 day instance) as predicted by CFD

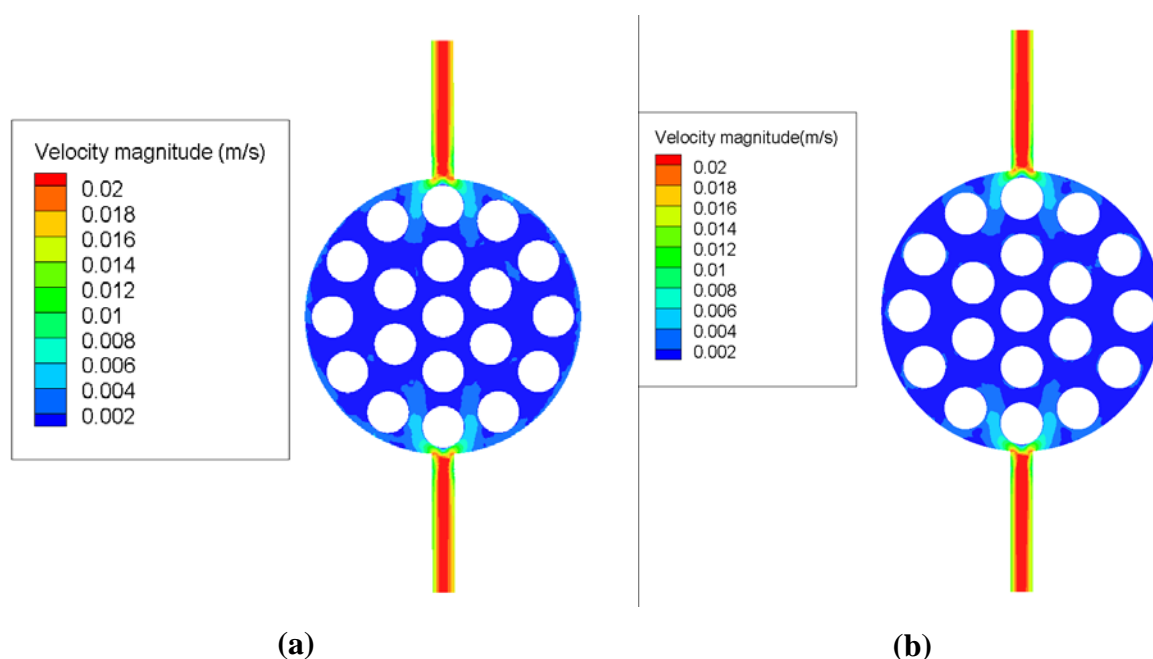


Figure-4.33 Velocity Distribution at outlet plane for various inlet temperatures (a) 54°C (0 day instance) (b) 57°C (0.5 day instance) as predicted by CFD

4.9 Closure

Detailed study for flow inside Calandria Vessel has been discussed in this chapter. Performance assessment of PMCS is carried out with RELAP-5 and a grace period of 7 days is established. Experiment for prolonged SBO conditions in AHWR is carried out in the scaled model of Passive Moderator Cooling Facility to study the natural convection and circulation phenomena in the twin coupled natural circulation loops. The thermal hydraulic behavior of the PMCS loop is understood via these experiments. Furthermore, numerical investigations using 1D numerical code and CFD are also performed. A comparison between the performance of the codes as well as comparison with experimental data is done. The following conclusions can be made based on the studies:

- a. 3-D natural convection inside the Calandria Vessel is observed during the initial phase of the experiment. Both the loops were stationary for initial ~30 minutes. Only local convection currents generated inside the Calandria Vessel. The phenomena could not be captured by RELAP code due to its limitation of 1-D formulations. As the bouncy

force increased due to density/temperature differences between the hot and the cold leg of the primary loop, the flow is observed in the primary loop. However, secondary loop remained stationary for next ~15 minutes.

- b. Gross circulation flow established in 45 minutes after introducing power to the facility. Thus flow was established essentially as 1-D flow like pipe flow. RELAP model is able to capture the gross circulation phenomena during second phase of experiment very well. The RELAP results are found to be in very good agreement with the experimental data as discussed earlier.
- c. CFD simulations carried out for some steady state instances of the test facility for observing the temperature distribution inside Calandria Vessel. CFD predictions for temperature distribution inside vessel for steady state instances are in good agreement with the experimental data.
- d. A well distributed flow field was observed with the CFD predictions and nowhere inside the vessel the temperature raised beyond the permissible limits.
- e. Once gross circulation is established; No recirculating flows inside the vessel were observed in the simulations as well as in the experiments.

CHAPTER-5

CFD of Multi-Phase Flow

5.1 Introduction.....	103
5.2 CFD of two phase flow	104
<i>Complexity in modeling of Two Phase Flow</i>	106
5.3 Mathematical modeling of two phase flow.....	107
5.3.1 Homogeneous flow model.....	110
5.3.2 Drift flux model	111
5.3.3 Separated two fluid model	112
5.4 Two fluid model (Euler-Euler formulations).....	113
5.4.1 Governing equations	113
5.4.2 Principle of determinism and closure relations	116
5.4.3 Closure in continuity equation.....	117
5.4.4 Closure in momentum equation (Interfacial forces).....	118
<i>Drag force</i>	119
<i>Lift force</i>	123
<i>Virtual mass/ Added mass force</i>	124
<i>Turbulent dispersion force</i>	125
<i>Wall lubrication force</i>	126
5.4.5 Closure in energy equation	127
<i>Heat flux partitioning model</i>	128
<i>Nucleation site density</i>	131
<i>Bubble departure frequency</i>	132
<i>Bubble departure diameter</i>	133
<i>Interfacial heat transfer</i>	140
5.5 Turbulence modeling	140
<i>k-ϵ model for two phase flow</i>	142
<i>Reynolds Stress (R_{ij}-ϵ) Model</i>	144
<i>Bubble induced turbulence</i>	145
5.6 Closure	146

5.1 Introduction

Integral analysis of the reactor systems is carried out using system code RELAP5 mod 3.2, which confirms that the reactor design is capable of removing decay heat for more than 7 days. Though it was established by analysis with system code, still there is a requirement to demonstrate it in an integral scaled test facility. For this purpose an integral test facility incorporating simulating ICs heaters submerged in GDWP along Passive Moderator and Endshield Cooling system was designed and built. Experimental demonstration for a grace period of 7 days was also established in the test facility as discussed in Chapter-2 and Chapter-3. Multidimensional phenomenon inside the Calandria Vessel, for checking any maldistribution inside it, was studied in Chapter-4 which confirms the anticipated design conditions of the moderator system.

Besides, system codes are not capable to estimate the local flow behavior at component level of the reactor system such as inside the rod bundle of the core. The decay heat removal is ensured as predicted by the system code; still there exists a finite probability of local hot spot inside fuel rod bundle, which may lead to fuel failure because of flow scarcity inside the fuel rod cluster. Multi-phase flow study under the work undertaken focuses on the estimation of decay heat removal capabilities of AHWR design for prolonged period without any hot spot or local excursions inside rod bundle.

For studying the multidimensional two phase behavior inside the fuel rod bundle of AHWR during decay heat removal, a systematic approach in increasing level of complexity is followed. The approach charts the following steps:

- a. Development of two fluid model for simulation of adiabatic two phase system (bubble column) using Open FOAM 2.3.1 platform
- b. Validation of the CFD model with experimental data available in literature

- c. Experiments for flow distribution inside the bubble column using Radioactive Particle Technique (RPT)
- d. Validation of the CFD model with experimental data obtained from RPT
- e. Development and validation of boiling two fluid frame work and application to the AHWR rod bundle during SBO conditions

The chapter is motivated by the need to understand the two phase flow mathematical modeling with closures. The chapter covers the various methods to describe the two phase flow and their current understanding and limitations.

5.2 CFD of two phase flow

Right from the inception of the nuclear reactors, two phase flow based systems are the choice of reactor designers due to excellent heat removal capability of the boiling fluids over single phase fluids. Boiling water systems are employed in nuclear reactors for many roles; most important ones are the heat removal from the core during normal operations and accidents. In case of PWRs, boiling occurs in secondary side of steam generators. For enhanced safety of the nuclear reactors, more and more passive systems are being introduced in the current and future reactor designs. These systems ensure the safety of the reactor as they work on the natural forces in the absence of active systems for example Passive Decay Heat Removal System (PDHRS) or Passive Containment Cooling System (PCCS). Boiling water systems can be used for such duties with compact sizes since more driving head remains available with two phase flow system as compared to single phase system. Designing of two-phase flow systems is different than the conventional systems as they have topographies which are characteristically different from those found in single-phase problems.

The fluid flowing in the primary loop of a nuclear reactor has to serve two purposes: First, it carries the heat from the nuclear fuel to generate power, and second, in the case of water-cooled reactors, it also performs as neutron moderator. A full understanding of its

thermodynamic and hydrodynamic behavior under the conditions prevailing in reactors is therefore of great importance. Heat transport in the reactor represents a system with imposed heat flux and under conditions of insufficient cooling; the temperature may rise to a level where damage of the reactor core is likely to result. On the other hand, prediction of the moderator effect, the factors of interest are primarily the coolant density and in boiling and two-phase flow, the void fraction present in the reactor core. These functions are ensured by efficient heat transfer from the surface of the fuel elements to the coolant and stable flow conditions at adequately high velocities to ensure safe removal of the heat by the coolant due to heat transfer from the core to a heat sink. It is one of the most important problems of two-phase flow obtaining information on fluid density or steam void and their control along with heat transfer in the core ensuring stable flow conditions. Besides, there exist many two phase flow conditions in nuclear power plant particularly after accidents.

Multi-phase flows are generally categorized by the physical states of the constituent components and by the topology of the interfaces. A two-phase flow can be classified as gas-solid, gas-liquid and liquid-solid combinations or in the case of two immiscible liquids, liquid-liquid. Topologically, the flow can be categorized as separated, dispersed or mixed. Because of the diversity in physical phenomena associated with wide range of multi-phase flows, no one method is used universally in simulating them. Some mathematical descriptions lend themselves in a more straightforward and economical fashion than others for a given flow field. Hence, part of the task of simulating two phase system for validation purposes is choosing the most appropriate mathematical model. Broadly, there exist two mathematical descriptions of two-phase flow. The first is the Lagrangian approach which tracks each discrete particle separately with its trajectory being governed by its own equation of motion within the continuous phase. The second, the Eulerian approach, treats the phases as inter-

penetrating continua and models each phase by averaging the microscopic equations of motion.

Figure-5.1 shows the level of complexity and assumptions involved in the various modeling methods of the two phase flows.

- a. Entity Tracking and Interface Tracking models (Lagrangian Approach)
- b. Field Averaging models (Eulerian Approach)

Field averaging models are further classified as homogeneous model, drift flux model, two fluid model and four field model. Selection of the model for simulation of two phase flow system depends upon the requirements of the information of the flow field. Field averaging models are mostly applicable for the engineering applications owing to their simple and averaged descriptions. Though, Interface tracking models and Entity tracking models are close in simulating the real physical phenomena, yet, application of these models for the engineering problems are limited due to their demand for huge computational resources.

Complexity in modeling of Two Phase Flow

Modeling of two phase flow is more complex than that of single phase flow mainly due to:

- ✓ Approximation in the governing equations because of highly statistical nature of flow (use of RANS); the situation becomes much severe in case of two phase flow
 - ❖ Results in loss of flow field information
- ✓ Presence of more than one phase having vast differences in properties
- ✓ Phase distribution patterns from bubbly flow-to-annular flow, which usually specified empirically
- ✓ Inadequate physical formulation rather than in the numerical approaches for engineering applications
 - ❖ Flow dynamics inside dispersed phase may also have significant effect
- ✓ Lack of understanding of interaction phenomena between phases

- ✓ Complex nature of boiling, particularly bubbles generation and their dynamics.
- ✓ Turbulence of such systems is not understood (turbulence modelling is itself not much understood for even single phase flows)
- ✓ Lack of measurements and instrumentations
- ✓ Inadequate experimental data for validation
- ✓ Geometry of the systems like rod bundle in nuclear reactors adds further complexity for solution methodology

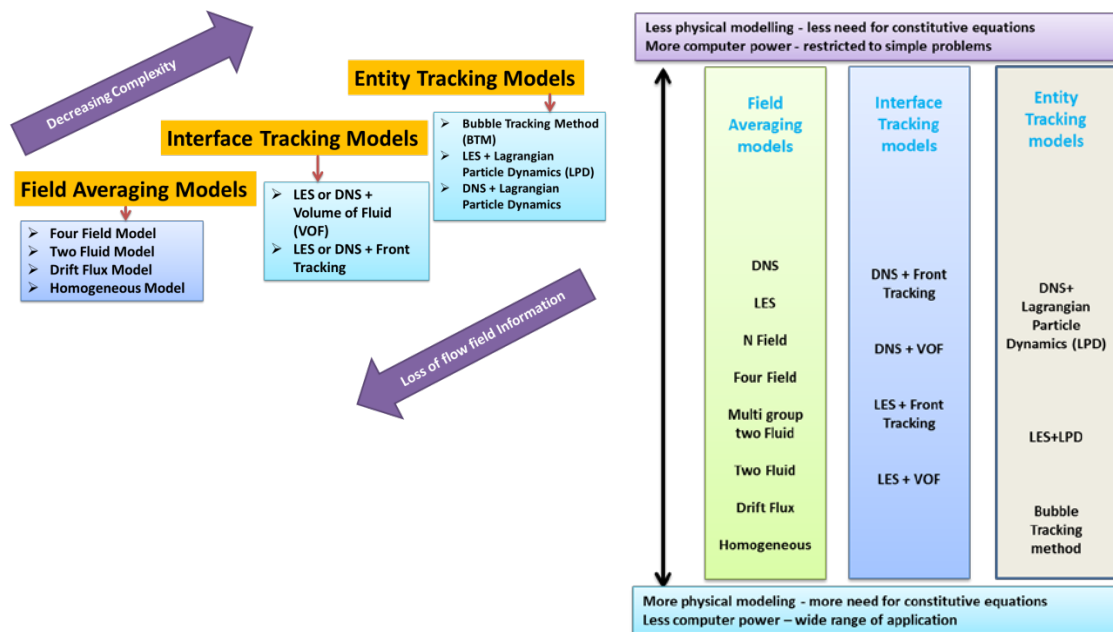


Figure-5.1 various methods for simulation of Two Phase Flow

5.3 Mathematical modeling of two phase flow

The basic design of two phase flow system is complex because of limited understanding of physics and empiricism involved in design. Experiments and computational fluid dynamics (CFD) codes can help to accomplish these important tasks.

Considering the prime importance of two phase flow in many industries, in past, a large number of researchers have devoted a considerable amount of time to develop field equations. In early 1950s to 1960s, numerous studies of boiling heat transfer and two-phase

flow were conducted leading to significant breakthroughs in the modeling of two-phase flow. One of the pioneering efforts was development of the drift flux model by Zuber in the mid-1970s. After that two fluid model was developed by Ishii in 1975 and it was further refined in 1984 by Ishii and Mishima. The model considered each phase separately. Thus the model developed is expressed by two sets of conservation equations governing the balance of mass, momentum and energy for each phase. The success of this model led to major advancements in code development. Table-5.1 shows the various two phase flow models for one dimensional case developed during that time and used as per the requirements.

Table-5.1 Characterization of two-phase flow governing equations (1-D)

6- Equation Model			
Conservation Equations	Restrictions	Constitutive Laws	Calculated Parameters
<i>Two-Fluid Non-equilibrium</i> 2- Mass phase balance 2-Momentum phase balance 2-Energy phase balance	None	2- Phase wall friction 2- Phase heat flux friction 1- Interfacial mass 1- Interfacial momentum 1- Interfacial energy	$\epsilon, p, u_L, u_G, T_L, T_G$
5- Equation Models			
<i>Two-Fluid Partial Non-equilibrium</i> 2- Mass Phase balance 2- Momentum phase balance 1- Mixture Energy balance	$T_L = T_{SAT}$ or $T_G = T_{SAT}$	2- Phase wall friction 1- Mixture heat flux friction 1- Interfacial mass 1- Interfacial momentum	$\epsilon, p, u_L, u_G, T_L$ or T_G
<i>Two-Fluid Partial Non-equilibrium</i> 1- Mixture mass balance 2- Momentum phase balance 2- Energy phase balance	$T_L = T_{SAT}$ or $T_G = T_{SAT}$	2- Phase wall friction 2- Phase heat flux friction 1- Interfacial mass 1- Interfacial momentum 1- Interfacial energy	$\epsilon, p, u_L, u_G, T_L$ or T_G
<i>Slip or Drift Non-equilibrium</i> 2- Mass Phase balance 1- Mixture Momentum balance 2- Energy phase balance	Slip or Drift Velocity	1- Mixture wall friction 2- Phase heat flux friction 1- Interfacial mass 1- Interfacial energy 1- Slip velocity or drift	$\epsilon, p, u_m, T_L, T_G$

		flux	
<i>Homogeneous Non-equilibrium</i> 2- Mass Phase balance 1- Mixture Momentum balance 2- Energy phase balance	Equal velocity $u_L = u_G = u_m$	1- Mixture wall friction 2- Phase heat flux friction 1- Interfacial mass 1- Interfacial energy	$\epsilon, p, u_m, T_L, T_G$
4- Equation Models			
<i>Two- Fluid Equilibrium Model</i> 1- Mixture mass balance 2- Momentum balance 1- Mixture energy balance	$T_L = T_G = T_{SAT}$	2- Phase wall friction 1- Mixture heat flux friction 1- Interfacial mass 1- Interfacial momentum	ϵ, p, u_L, u_G
<i>Drift Partial Non-equilibrium</i> 2- Mass phase balance 1- Mixture momentum balance 1- Mixture Energy balance	Drift velocity $T_G \text{ or } T_L = T_{sat}$	1- Mixture wall friction 1- Mixture wall heat flux 1- Interfacial mass 1- drift flux correlation	$\epsilon, p, u_m, T_L \text{ or } T_G$
<i>Slip Partial Non-equilibrium</i> 1- Mixture Mass balance 1- Mixture Momentum balance 2- Phase energy balance	Slip ratio $T_G \text{ or } T_L = T_{sat}$	1- Mixture wall friction 1- Mixture wall heat flux 1- Interfacial mass 1- Drift flux correlation	$\epsilon, p, u_m, T_L \text{ or } T_G$
<i>Homogeneous, Partial Non-equilibrium</i> 1- Mixture mass balance 1- Mixture momentum balance 2- Phase energy balance	$u_L = u_G = u_m$ $T_G = T_L = T_{SAT}$	1- Mixture wall friction 2- phase wall heat flux 1- Interfacial mass 1- Interfacial energy	$\epsilon, p, u_m, T_L \text{ or } T_G$
3- Equation Models			
<i>Homogeneous Equilibrium (HEM)</i> 1- Mixture mass balance 1- Mixture Momentum balance 1- Mixture Energy balance	$u_L = u_G = u_m$ $T_G = T_L = T_{SAT}$	1- Mixture wall friction 1- Mixture wall heat flux	ϵ, p, u_m
<i>Slip or Drift Equilibrium</i> 1- Mixture mass balance 1- Mixture Momentum balance 1- Mixture Energy balance	Slip or Drift velocity $T_G = T_L = T_{SAT}$	1- Mixture wall friction 1- Mixture wall heat flux 1- Slip velocity or Drift flux	ϵ, p, u_m

The methods used to analyze a two-phase flow are extensions of those already well tried for single-phase flows. The procedure invariably is to write down the basic equations governing the conservation of mass, momentum, and energy, often in a one-dimensional or three-dimensional form and to solve these equations by the use of various simplifying assumptions/methods.

There exists three types of CFD models for simulation of two phase flow viz.:

1. Field averaging Models
 - i. Homogeneous models
 - ii. Drift flux models
 - iii. Two fluid models
 - iv. Four fields models
2. Interface Tracking Models
 - i. LES or DNS + Volume of Fluid (VOF)
 - ii. LES or DNS + Front Tracking
3. Entity Tracking Models
 - i. Bubble Tracking Method (BTM)
 - ii. LES + Lagrangian Particle Dynamics (LPD)
 - iii. DNS + Lagrangian Particle Dynamics

Field averaging models are mostly used for two phase flow simulations. These models are based on Euler-Euler approach. Other type of model like interphase tracking or entity tracking models tracks the individual bubble and hence the model are having limited capabilities due to huge computational capacity requirements. For the current study only field averaging models are considered, which are explained in details.

5.3.1 Homogeneous flow model

In this, two-phase flow is assumed to be a single-phase flow having pseudo-properties arrived at by suitably weighting the properties of the individual phases. The governing equations for one-dimensional area averaged approach are obtained from the classical integral method using the Reynolds Transport Theorem. It begins with the simplest of approaches termed

homogeneous no-slip thermodynamic equilibrium model. In this case, both the phases are assumed to be well distributed in the entire cross section of the duct/pipe so that the mixture of the two-fluids can be assumed to be a single fluid with modified properties. This model inherently assumes no variation of hold-up within a given cross section.

5.3.2 Drift flux model

The next level of complexity starts with the introduction of slip. The motivation comes from the fact that homogeneous model can only be applied to extremely dispersed flows, which are probably valid for dispersed bubble flows with very small bubble diameters. For dense bubbly flows, it would be unreasonable to assume that the bubbles flow at the same velocity as liquid. In commonly occurring two-phase flows, the average gas velocity is higher than that for the liquid. The effect of slip or gas moving faster than the liquid can be accounted in many ways. The most successful procedure to accommodate this is the drift-flux model. The bubble distribution across the cross section need not be uniform there will be a variation of local gas and liquid hold-up in the cross section. The variation of local hold-up necessitates the hold-up or void weighted averages as introduced by Zuber and his co-workers (Zuber and Findlay, 1965). For any general variable F , the void weighted average $\langle\langle F \rangle\rangle$ can be obtained by,

$$\langle\langle F \rangle\rangle = \frac{\int_A F \epsilon_G dA}{\int_A \epsilon_G dA} \quad \dots (5.1)$$

The point values of the void can be measured experimentally by the use of conductance probe and time averaging. The need for void weighting arises from the fact that these can be prescribed by knowing the superficial quantities. For, example, the void weighted gas velocity is nothing but the volumetric flow of gas (Q_g) as shown below,

$$Q_G = \int_A \epsilon_G u_G dA \quad \dots (5.2)$$

A new term using the mean drift velocity, \bar{u}_{gj} , (the relative velocity with which the gas moves faster than the mixture velocity) has been introduced following the work of Zuber and Findlay (1965). The mean drift velocity is defined as,

$$\bar{u}_{Gj} = \bar{u}_G - \bar{j} = \frac{\bar{J}_G}{\epsilon_G} - (\bar{J}_G + \bar{J}_L) \quad \dots (5.3)$$

In the above equation \bar{J}_G and \bar{J}_L are the volume fluxes of gas and liquid respectively. Thus, the mean drift velocity can be measured, if the local void fraction is measured and averaged and the volumetric flow of gas and liquid are known.

At this point, to minimize complicated arguments, it is adequate to point out that in drift flux model, we are introducing the effect of slip, without considering two individual momentum equations. This is possible by employing a drift closure (Zuber and Findlay (1965)), which is just a modified form of Eq. (5.3)

$$\bar{u}_G = \bar{u}_{Gj} + C_0 \bar{j} \quad \dots (5.4)$$

Above, C_0 is the covariance distribution parameter for j , given by,

$$C_0 = \frac{\langle \epsilon_G j \rangle}{\langle \epsilon_G \rangle \langle j \rangle} \quad \dots (5.5)$$

The above parameter can also be experimentally obtained by locally measuring the velocity of the phases and void. Thus, in drift flux model, in addition to the wall shear stress closure in the form of a friction factor f , we need an additional closure that involves two additional empirical parameters. These parameters are not universal and are flow regime dependent. Empirical models are available in literature for these parameters.

5.3.3 Separated two fluid model

In this approach, two phases of the flow are considered to be artificially segregated. Two sets of basic equations are written, one for each phase. Alternatively, the equations can be combined. In either case information must be forthcoming about the area of the channel

occupied by each phase (or alternatively, about the velocities of each phase) and about the frictional interactions with the channel wall. In the former case, additional information concerning the frictional interaction between the phases is also required. This information is inserted into the basic equations, either from separate empirical relationships in which the void fraction and the wall shear stress are related to the primary variables, or on the basis of simplified models of the flow.

5.4 Two fluid model (Euler-Euler formulations)

5.4.1 Governing equations

In Euler-Euler approach, the phases are treated as interpenetrating continua. Interpenetrating continua refers to the presence of both the phases at every location in the domain simultaneously. Both the phases are assumed to be intermingling with each other. The two fluid model was developed with the assumption of interpenetrating continua. The governing equations of the two fluid model contains void fraction (ϵ) with the conservative quantities which assumes presence of void fraction everywhere in the domain. The coordinate system for all the phases is fixed with respect to the geometry in which the flow occurs. Due to the assumption of interpenetrating continua, the mathematical treatment of the governing equations is considerably simplified in Euler-Euler approach. The equations of motion with the Euler-Euler approach are similar to their single phase counterparts (appropriately weighed by phase fraction). The additional source terms due to interfacial momentum exchange arise. For a 3-Dimensional two phase flow, we need to solve 10 conservation equations including 4 equations for the two phases for mass and energy (scalar quantities, one for each phase) and 6 momentum equations (3 velocities for each phase). However, the unknowns in the mathematical model so described are more than 10 in numbers so it becomes a closure problem for this mathematical description.

Following assumptions have been made for the derivation of the conservation equations for two-phase flow:

1. Each phase is treated as a continuum in any size of the domain under consideration.

The phases share this domain and interpenetrate as they move within it.

2. Any small volume of the space in question, at any particular time, can be regarded as containing a volume fraction, ϵ_G of the gas phase and ϵ_L of the liquid phase. The following relation holds:

$$\epsilon_G + \epsilon_L = 1 \quad \dots (5.6)$$

This means there is a sufficiently large number of bubbles in a volume characterized by the macroscopic length of the system.

3. The gas phase is dispersed and consists of bubbles, spherical in shape and uniform in size. The processes of coalescence and breakage are assumed to be absent.
4. When the contents of finite volumes and the flow rates across finite areas are to be computed over finite time intervals, a suitable averaging over space and time is carried out.
5. When any area is occupied by different phases, the pressure has been assumed to be shared by the phases proportional to the fractional area occupied by the phases.
6. In a continuous phase, the shear stress and pressure are continuous in space and time. However, this is not the case at the interface between the two phases. When both the phases are fluids, the interfacial tension keeps the identity of the particle. This also causes the pressure at the interface different from the continuous phase pressure.

Continuity equation

The local continuity equation for any of the two phases is denoted by;

$$\frac{\partial}{\partial t}(\rho) + \nabla \cdot (\rho U) = \Gamma_i \quad \dots (5.7)$$

Conditioning the continuity equation with a phase indicator χ_i and taking the ensemble average gives;

$$\chi_i \frac{\partial}{\partial t}(\rho) + \chi_i \nabla \cdot (\rho \mathbf{u}) = \Gamma_i \quad \dots (5.8)$$

$$\text{From } \bar{\phi} = \frac{\chi_k \bar{\phi}}{\epsilon_k} \quad \dots (5.9)$$

$$\frac{\partial}{\partial t}(\epsilon_k \rho_k) + \nabla \cdot (\epsilon_k \rho_k \mathbf{u}_k) = \Gamma_k \quad \dots (5.10)$$

First term in the Eq. (5.10) represents the accumulation of mass while second one is the convection term (convection or transport of mass). Right hand side term in above equation represents the mass transfer occurring between two phases.

Equation of motion

The momentum conservation for k^{th} (G or L) phase is described by Eq. (5.11)

$$\frac{\partial}{\partial t}(\epsilon_k \rho_k \mathbf{u}_k) + \nabla \cdot (\epsilon_k \rho_k \mathbf{u}_k \mathbf{u}_k) = -\epsilon_k \nabla P + \epsilon_k \rho_k \mathbf{g} + \epsilon_k \nabla \cdot (\tau_{k,ij} + \tau_{k,ij}^t) + \Gamma_k \mathbf{u}_k + M_k \quad \dots \dots \dots (5.11)$$

First term on the right hand side of the Eq. (5.11) represents pressure force term. Second term represents gravity. Third term is a combination of effective viscous stress and turbulent stress term. Fourth term represents gain of momentum due to phase change. Last term represents interfacial forces which include drag force, lift force, wall lubrication force, and turbulent dispersion force.

Energy equation

$$\frac{\partial}{\partial t}(\epsilon_k \rho_k H_k) + \nabla \cdot (\epsilon_k \rho_k \mathbf{u}_k H_k) = \epsilon_k \frac{\partial P}{\partial t} + \nabla \cdot (\epsilon_k \mathbf{Q}_k) + \Gamma_k H_k + q''_{\text{wall},k} \quad \dots \dots \dots (5.12)$$

The first term on the right-hand side of Eq. (5.12) represents the change in enthalpy due to pressure. Second term is a combination of molecular and turbulent heat flux. Third term

represents the change in enthalpy due to mass flux (evaporation and condensation). The last term in Eq. (5.12) is the source term representing wall heat flux, which has been described in detail in section 5.4.5.

5.4.2 Principle of determinism and closure relations

The system of conservation-laws based on average equations cannot cover every aspects of the multiscale, multiphysics flow boiling phenomenon. Many physical interactions are happening at the meso and micro-scales which include: (i) momentum and heat-mass exchanges between phases (at the phase interfaces), e.g. drag, lift, virtual mass forces; bubble deformation, coalescence, and breakup; bubble condensation, (ii) mechanical and thermal interactions on the heating wall, e.g. nucleation, bubble growth and departure, evaporation and wall heat transfer affected by it. Due to the much difference between these physics and average flow in space and time scales and the deficiency/lack of knowledge/understanding about them, the effects of such small-scale physics on the average flow are normally approximated using the so-called closure models, which are commonly derived from separate-effect-test data. The development and application of empirical/semi-empirical closure models and correlations forms an essential part of the modeling.

The governing equations contains terms which require empirical closures for mathematical closing the model. These terms includes interfacial interactions between the two phases like mass jump, momentum jump (interfacial forces) and interfacial energy interactions. These closure relations are dependent on the flow regimes like bubbly flow, slug flow, churn flow, annular flow etc. In this mathematical model (3-dimensional two phase flow) total balanced equations are 10 in number (2 mass conservation, 6 momentum conservation, 2 energy conservation). The total number of unknown variables for which equations to be solved are 11. These variables are void fraction, density, three components of velocities for each phase,

pressure and temperature of each phase. Here total 11 unknowns are needed to be solved using 10 balanced equations and 1 equation of state (relation between pressure and density).

However, here in our simulations state of the fluid (density) is explicitly defined as the function of the field parameters like Temperature in our cases. Also heat transfer is only considered as the mechanism for mass transfer in boiling simulations. Mass transfer due to change in the partial pressure is assumed to be absent owing to highly non equilibrium nature of the boiling phenomenon.

Besides, closure relation are required to express other variables as interface mass, momentum and energy transfer in balance equations in terms of mentioned variables to close the problem.

Closures for various terms can be obtained either from Analytical theory, dedicated experiments or by DNS.

5.4.3 Closure in continuity equation

The continuity equation for the two phase flow contains the term interfacial mass transfer denoted by Γ_k requires closure relation. The inter-phase heat and mass transfer models were obtained by considering the heat transfer from the gas and the liquid to the gas/liquid interface.

- Heat transfer from liquid to interface is

$$Q_L = h_{if} A (T_L - T_{sat}) \quad \dots (5.13)$$

- Heat transfer from gas to interface is

$$Q_G = h_{if} A (T_G - T_{sat}) \quad \dots (5.14)$$

Finally $\Gamma_i = \frac{Q_G + Q_L}{h_{fg}} \quad \dots \dots (5.15)$

Here unclosed terms are h_{if} , which need closure and can be obtained from empirical correlations of interfacial heat transfer coefficient. Modeling of interfacial heat transfer is described in section 5.4.5.

5.4.4 Closure in momentum equation (Interfacial forces)

The interfacial terms in the momentum and energy exchange equation represents the interaction forces between the continuous and the dispersed phase and energy exchange between the two phases.

The interfacial force term M_k in momentum equation represents the interaction forces between the continuous and the dispersed phase. The forces acting on a motionless bubble in a motionless liquid are pressure and gravity. Since there is usually a relative motion between the bubble and liquid, the liquid flow around individual bubbles leads to local variations in pressure and shear stress. A bubble imbedded in a flowing fluid is influenced by a number of forces, which act on it through the traction at the gas–liquid interface. A single particle moving through a fluid experiences forces that affect its motion. If the slip velocity is constant, the force is called as drag. If the motion is non-uniform one needs to extend the concept of drag to include the various non-drag forces such as the so-called virtual mass force and lateral lift force.

Various interfacial forces are categorized as:

- Drag force
- Non Drag forces
 - Virtual mass or added mass force
 - Lift force
 - Turbulent dispersion force
 - Wall lubrication force

Among all interfacial forces drag and lift are very important forces and have significant influence on terminal velocity and hold up distribution in the two phase gas liquid flow. The results predicted by numerical models largely depend upon the formulation of these forces. Lot of efforts has been made by the researchers for bringing out the effect of the interfacial

forces on the simulations. Some of those include Sokolochin and Eigenberger (1994, 2004), Sankaranarayanan and Sundersan (2002), Tomiyama (2004), Zhang (2006), Kulkarni (2008) and many more authors.

Drag force

Drag is the hindering force exerted on a moving body in a fluid medium. It tries to slow down the particle. It is a function of the relative velocity of the particle, its size and shape, and the fluid through which it is moving.

A bubble moving through a liquid flow field, experiences a drag force, which consists of a form drag and a friction drag exerted by the liquid on the moving bubble.

Drag force for a single bubble is given by

$$f_D = \frac{1}{2} C_D \rho_L \frac{\pi}{4} d_B^2 |u_G - u_L| (u_G - u_L) = \frac{V_B}{V} (\rho_L - \rho_G) g \quad \dots \dots \dots (5.16)$$

At steady state this force will be balanced by buoyancy force. Here in this formulation the undisclosed terms are C_D and d_B , known as drag coefficient and diameter of the bubble in the domain, which requires closures. V_B is the volume of the bubbles. Empirical models for these terms are required to close the set of equations. Various models are developed by researchers for drag coefficient and bubble diameters in the flow field. Drag in the presence of many bubbles in vicinity gets modified and need separate attention for modeling.

Drag force for a bubble swarm:

Most expressions for the drag coefficient available in literature are based on empirical data that was measured for single isolated bubbles in an undisturbed liquid flow field. When the gas fraction increases, the forces acting on a bubble are modified by the proximity of other bubbles and this effect is considerable, which can be estimated as:

$$F_D = N f_D = \frac{\pi/4 D^2 H_D \epsilon_g}{\pi/6 d^3} \frac{1}{2} C_D \rho_L \frac{\pi}{4} d_B^2 |u_G - u_L| (u_G - u_L) \quad \dots \dots \dots (5.17)$$

$$F_D = \epsilon_G \rho_L \frac{3 C_D}{4 d_B} (u_G - u_L) |u_G - u_L| \quad \dots \dots \dots (5.18)$$

Here N is the number of bubbles in the domain, H and D are the height and diameter of the column and ϵ_G is the holdup of the column. While estimating F_D using Eq. (5.17), knowledge of d_B (bubble diameter) is needed. Further, the value of C_D in Eq. (5.17) is likely to be different for a single bubble and a bubble swarm. This is because, the shape and size of a bubble in a bubble swarm is much different than that for an isolated bubble. Moreover, the flow structure of liquid surrounding a bubble gets modified when it becomes a part of the swarm. Therefore, the use of Eq. (5.18) is difficult for drag estimation. On the other hand, a simplified estimation of drag force can be made with use RHS of the Eq. (5.17) that yields:

$$f_D = \epsilon_G(\rho_L - \rho_G)g \quad \dots \dots \dots (5.19)$$

In a bubble swarm, there is a possibility that the slip velocity has a range and not a unique value for all the bubbles. This range can be accommodated on the basis of average slip velocity ($|u_G - u_L|$) as,

$$F_D = \epsilon_G(\rho_L - \rho_G)g \frac{(u_G - u_L)}{|u_G - u_L|} \quad \dots \dots \dots (5.20)$$

Further, Eq. (5.20) assumes the drag force to be proportional to the slip velocity. From Eq. (5.17) it can be seen that the drag force is proportional to the square of the slip velocity. Using this relation, Eq. (5.20) can be modified as (Joshi, 2001):

$$F_D = - \frac{\epsilon_G(\rho_G - \rho_L)g(u_G - u_L)|u_G - u_L|}{(u_G - u_L)^2} \quad \dots \dots \dots (5.21)$$

In this formulation, drag is calculated from the field variables itself and requires the estimation of ϵ_G and phasic velocities in the flow domain.

In spite of this approach, the approach of drag coefficient is more popular in current CFD practice due to stability of the solution procedure.

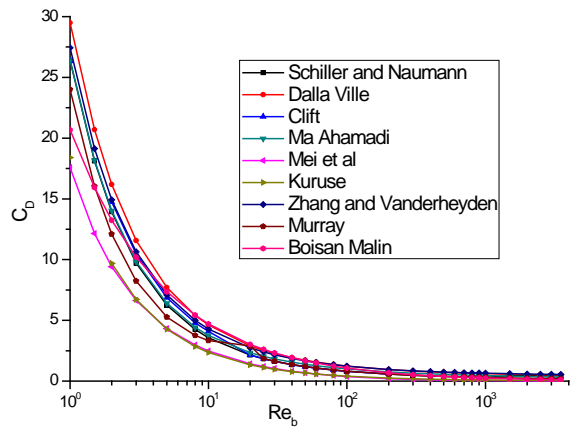
Large numbers of expression are available for C_D in the literature. These expressions were either developed by theoretical analysis or by experiments. Table-5.2 gives various models for the drag coefficients. Starting from the Stokes (1872), these models include Schiller

Naumann (1935), Dalla Ville (1948) and so on as shown in Table-5.2. The value of C_D varies with particle Reynolds number. Figure-5.2a to 5.2d shows the variation of C_D with Reynolds number as evaluated by various expressions of drag coefficient. Large variation in the drag coefficient is seen upto a particle Reynolds number of 200. It is clearly observed from Figure-5.2 that for a particle Reynolds number more than 200, almost all drag models predicts the value of drag coefficient roughly the same. Besides, there are drag models that depends only upon Eotvos number, which is based on fluid properties only and independent of flow properties. These include Ishii and Zuber model (1979), Grevskott (1996) and Tomiyama (2004). Dependency of these models only on fluid properties makes their use skeptical as the flow dynamics is strongly influenced by the flow characteristics particularly the bubble diameter and bubble Reynolds number. However, these models incorporate effect of the shape and size of the bubble in a bubble swarm, which make their use more relevance to the physical world problems.

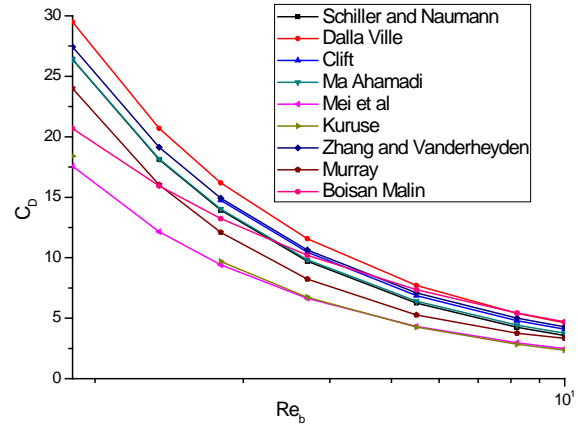
Table-5.2 Various drag models for bubbly flows

Investigators	Drag expression
Stokes (1851)	$C_D = \frac{24}{Re} \quad Re \ll 1$
Hadamard and Rybczynski (1911)	$C_D = \frac{16}{Re} \quad Re \ll 1$
Schiller and Nauman (1935)	$C_D = \begin{cases} \frac{24}{Re}(1 + 0.1Re^{0.687}) & Re \leq 1000 \\ 0.44 & Re > 1000 \end{cases}$
Levich (1949)	$C_D = \frac{48}{Re} \left(1 - \frac{2.21}{\sqrt{Re}}\right) \quad Re \gg 1$
Dalla Ville (1948)	$C_D = (0.63 + \frac{4.8}{\sqrt{Re_b}})^2$
Moore (1963)	$C_D = \frac{48}{Re} \left(1 - \frac{2.21}{\sqrt{Re}}\right) + o(Re_b^{-11/6})$
Clift et al. (1978)	$C_D = \begin{cases} \frac{29}{Re} - \frac{3.8889}{Re^2} + 1.222 & Re \leq 10 \\ \frac{24}{Re}(1 + 0.1Re^{0.687}) & 10 < Re \leq 200 \end{cases}$

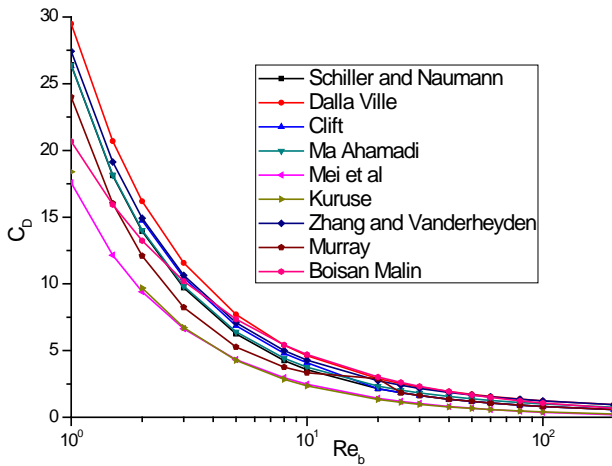
Ishii and Zuber (1979)	$C_D = \frac{2}{3} E_o^{1/2}$
Ma and Ahmadi (1990)	$C_D = \frac{24}{Re} (1 + 0.1 Re^{0.75})$
Mei et al. (1994)	$C_D = \frac{16}{Re} \left(1 + \frac{2}{1 + \frac{16}{Re} + \frac{3.315}{\sqrt{Re}}} \right)$
Grevskott et al. (1996)	$C_D = \frac{5.645}{E_o^{-1} + 2.835}$
Boisson and Malin (1996)	$C_D = \begin{cases} 24/Re & Re \leq 0.49 \\ 20.68/Re^{0.643} & 0.49 < Re \leq 100 \\ 6.3/Re^{0.385} & Re > 100; We \leq 8; Re \leq 2065.1/We^{2.6} \\ We/3 & Re > 100; We \leq 8; Re > 2065.1/We^{2.6} \\ 8/3 & Re > 100; We > 8 \end{cases}$
Kurose et al. (2001)	$C_D = \begin{cases} \frac{16}{Re} & Re < 1 \\ \frac{16}{Re} (1 + 0.1 Re^{0.5}) & 1 \leq Re \end{cases}$
Laín et al. (2002)	$C_D = \begin{cases} \frac{16}{Re} & Re \leq 1.5 \\ \frac{14.9}{Re^{0.78}} & 1.5 \leq Re < 80 \\ \frac{48}{Re} \left(1 - \frac{2.21}{\sqrt{Re}} \right) + (1.86e - 15) Re^{4.756} & 80 \leq Re < 1500 \\ 2.61 & 1500 \leq Re \end{cases}$
Zhang and Vander Heyden (2002)	$C_D = 0.44 + \frac{24}{Re_b} + \frac{6}{1 + \sqrt{Re_b}}$
Tomiyaama (2004)	$C_D = \frac{8}{3} \frac{\ddot{E}_o (1 - E^2)}{E^{2/3} \ddot{E}_o + 16(1 - E^2) E^{4/3}} F(E)^{-2}$ <p>Where</p> $F(E) = \frac{\sin^{-1} \sqrt{1 - E^2} - E \sqrt{1 - E^2}}{1 - E^2}$
Murray et al. (2007)	$C_D = \begin{cases} \frac{24}{Re_b} & Re_b < 1 \\ \left(\frac{24}{Re_b} \right) \left(1 + \frac{3.6}{Re_b^{0.313}} \left(\frac{Re_b - 1}{19} \right)^2 \right) & 1 \leq Re_b \leq 20 \\ \left(\frac{24}{Re_b} \right) (1 + 0.15 Re_b^{0.687}) & Re_b > 20 \end{cases}$



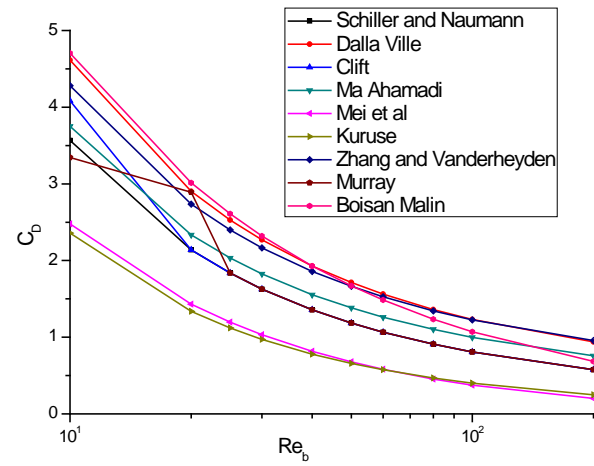
a) Drag Coefficient varying with Re_p at $1 < Re_p < 4000$



b) Drag Coefficient varying with Re_b at $1 < Re_b < 10$



c) Drag Coefficient varying with Re_p at $1 < Re_p < 200$



d) Drag Coefficient varying with Re_b at $10 < Re_b < 200$

Figure-5.2 Variation of drag coefficient with particle Reynolds number

Lift force

Three-dimensional flow past bodies subjected to a uniform shear experience tilting and stretching of their vorticity field parallel to the direction of motion and cause the modification in shear forces. The vortex attached to the body induces a thrust on the fluid and the body experiences a corresponding lift. At the same time bubble in the flow field also experiences Magnus effect force which makes the rotation of the bubble and turns the bubble towards the wall. Magnus force arises out of the gradients in the liquid flow field around the bubble. In such a flow field, the force arising out of rotational effects (Magnus force) and combined effects of shear and strain is known as the lift force. The lift experienced by particles/bubbles

also has an effect of the inertia and the shear rate, which results in the migration of particle/bubble across the streamlines of an undisturbed, laminar flow. The shear-induced lift force, proportional to the vorticity of the liquid phase, is important for phase distributions in two-phase flows. Lift force is the cross product of slip velocity and curl of liquid velocity so it remains perpendicular to both of them. Lift force is given as:

$$F_{Lift} = -C_{Lift}\rho_L\epsilon_G(u_G - u_L) \times (\nabla \times u_L) \quad \dots (5.22)$$

Here, unclosed term is lift coefficient, C_{Lift} , which needs an empirical correlation. For, C_{Lift} a number of correlations are available in literature. Various models available in literature for lift coefficient are Auton (1987), Legendre and Magnaudet (1998), Tomiyama et al.(2002) etc. Auton suggested the value of lift coefficient for rigid spheres as a constant 0.5. The expression for lift coefficient C_L given by Legendre and Magnaudet is given by

$$C_{Lift} = \frac{1 + \frac{16}{Re}}{1 + \frac{29}{Re}} \quad \dots (5.23)$$

Tomiyama et al (2002) described C_L as follows:

$$C_{Lift} = \min(0.288 \tanh(Re), f(Eo)) \quad \dots (5.24)$$

where $f(Eo) = 0.00105Eo^3 - 0.0159Eo^2 - 0.204Eo + 0.474$

$$Eo = \frac{g(\rho_l - \rho_g)d_B^2}{\sigma}$$

Virtual mass/ Added mass force

The virtual mass force is associated with the acceleration of the bubble phase relative to the surrounding continuous phase. The virtual mass force becomes important when a particle accelerates relative to the liquid (continuous) phase such that the inertia of the liquid (continuous) phase mass encountered by the accelerating particles exerts a virtual mass force on the particle. As the “added mass” of the liquid is accelerated, a resistance to the particle acceleration is induced, and the virtual mass force is generated. In most of the simulations

the virtual mass terms is neglected and if considered the coefficient is taken constant value 0.5.

The virtual mass force is given by:

$$F_{VM} = \rho_L C_{VM} \left(\frac{\pi}{6} d_B^3 \right) \left[\frac{Du_G}{Dt} - \frac{Du_L}{Dt} \right] \quad \dots (5.25)$$

This force is effective only when unsteady motion of bubbles. At steady state its value is zero. It is very much important in the stability analysis of the bubble column. In the case of stability analysis, we subject the equations of motion to perturbations and study the response of the system. Since the system under consideration is perturbed, unsteady behavior sets in and virtual mass force becomes important.

Turbulent dispersion force

Bubbles in the turbulent flow field move along a path which may be fluctuating. The fluctuations in the bubble path can disperse the bubbles. The force responsible for the dispersal of bubbles is termed as turbulent dispersion force. The turbulent dispersion force plays a crucial role in movement of the vapor away from the vicinity of the wall towards the center of the domain. This force is taken to be perpendicular to the gradient of dispersed phase hold-up. This force is proportional to gradient of dispersed phase hold-up and the proportionality constant (turbulent dispersion coefficient).

Caricca et al. (1999) represented one such equation given by,

$$F_{TD} = C_{TD} \left[C_D \left(\frac{\pi}{4} d_B^2 \right) \frac{1}{2} \rho_L |u_G - u_L| \right] \frac{\nu_{TB} \nabla \epsilon_G}{\epsilon_G} \quad \dots (5.26)$$

Where, C_{TD} is turbulent dispersion coefficient and ν_{TB} is turbulent kinematic viscosity of the gas phase. Lopez de Bertodano (1991) specifies the formulation of the turbulent dispersion as

$$F_{TD} = C_{TD} \rho_L k_L \nabla \epsilon_G \quad \dots (5.27)$$

Here k_L is turbulent kinetic energy of continuous phase and C_{TD} is turbulent dispersion coefficient.

Burns et al (2004) proposed turbulent dispersion force to be calculated as:

$$F_{TD} = C_{TD} C_D \frac{\nu_{TB}}{0.9} \left(\frac{\nabla \epsilon_L}{\epsilon_L} - \frac{\nabla \epsilon_G}{\epsilon_G} \right) \quad \dots (5.28)$$

Wall lubrication force

The wall lubrication force tends to push the secondary phases away from walls. This force results in the dispersed phase concentrating in a near wall region not immediately adjacent to the wall.

$$F_{wl} = C_{wl} \rho_L \epsilon_G |(\bar{u}_G - \bar{u}_L)|^2 \vec{n} \quad \dots (5.29)$$

Here C_{wl} is wall lubrication coefficient. Various models for this term are presented in Table-5.3.

Table-5.3 Models for wall lubrication force

Author	Model formulation
Antal et al. Model (1991)	$C_{wl} = \max \left(0, \frac{C_{w1}}{d_b} + \frac{C_{w2}}{y_w} \right)$ <p>Where $C_{w1} = -0.01$ and $C_{w2} = 0.05$ are non-dimensional coefficients, d_b is the bubble diameter and y_w is the distance to the nearest wall. Here $C_{wl} > 0$ when $y_w \leq -(C_{w2}/C_{w1})d_b$</p>
Tomiyama Model (1998)	$C_{wl} = C_w \frac{d_b}{2} \left(\frac{1}{y_w^2} - \frac{1}{(D - y_w)^2} \right)$ <p>Where</p> $C_w = \begin{cases} 0.47 & Eo < 1 \\ e^{-0.933Eo+0.179} & 1 \leq Eo \leq 5 \\ 0.00599Eo - 0.0187 & 5 < Eo \leq 33 \\ 0.179 & 33 \leq Eo \end{cases}$ $Eo = \frac{g(\rho_q - \rho_p)d_b^2}{\sigma}$
Frank Model (2004)	$C_{wl} = C_w \max \left[0, \frac{1}{C_{wd}} \cdot \frac{1 - \frac{y_w}{C_{wc}d_b}}{\left(\frac{y_w}{C_{wc}d_b} \right)^{m-1}} \right]$ <p>C_w is calculated same as Tomiyama Model, $C_{wd} = 6.8$ is damping coefficient and $C_{wc} = 10$ is cut-off coefficient and determines the distance to the wall within which the force is active. $m=1.7$ is the power law constant and is recommended to be between 1.5 and 2.</p>

Hosokawa Model (2002)	$C_{wl} = C_w \frac{d_b}{2} \left(\frac{1}{y_w^2} - \frac{1}{(D - y_w)^2} \right)$ <p>Where</p> $C_w = \max \left(\frac{7}{Re_d^{1.9}}, 0.0217Eo \right) \text{ and } y_w \text{ is the distance to the nearest wall.}$
--------------------------	---

5.4.5 Closure in energy equation

During the SBO in AHWR, heat transfer from the core will be in subcooled boiling regime. It is necessary to study the modeling of the subcooled boiling with CFD to capture the flow field inside the channel of the AHWR for any hot spot.

Subcooled flow boiling is also important in the design, operation and thermal–hydraulic safety analysis of a nuclear reactor. This is particularly important where accurate prediction of void fraction is required for the presence of significant voidage in the flow that can affect the core flow rate along with fuel burn up and eventually can lead to boiling inception of two phase flow with fuel failure.

Figure-5.3 shows the schematic of the subcooled boiling inside a pipe flow. During highly subcooled regime, the heat from the wall is transferred through single phase convection process. Further, heater surface temperature rises due to decreasing capability of the liquid to absorb heat with increasing temperature or higher heater power. In this sequence, when heater temperature reaches more than saturation temperature of the liquid, evaporation takes place near wall leaving bulk of the liquid still subcooled. This point is known as onset of nucleate boiling (ONB). The heat removal capacity of the liquid enhances tremendously during this regime. The vapour generated near ONB point immediately condenses and no net vapor is generated. Following ONB, a point reaches in the boiling regime, where a net vapour starts, is known as NVG (Net Vapour Generation) point as shown in Figure-5.3. Heat transfer from the wall during subcooled boiling appears in the energy equation as source term, which again requires modeling and closure correlations for complete solution.

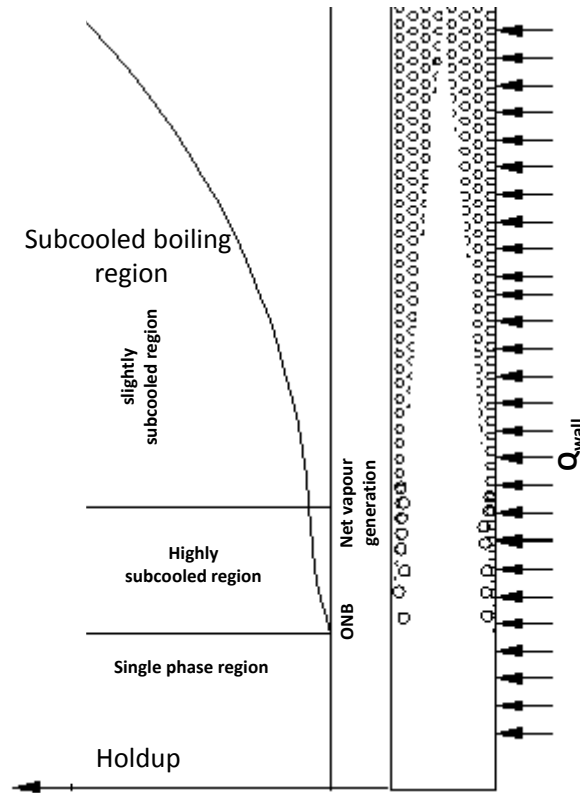


Figure-5.3 Illustration of subcooled boiling in a channel

Heat flux partitioning model

For cases of sub-cooled boiling, the energy is transferred directly from the wall to the liquid. Part of this energy causes the temperature of liquid to rise and part generates vapour. Interphase heat transfer and condensation of saturated vapour also cause the average liquid temperature to increase. Heat flux partitioning model accounts unsteady nature of the physics of subcooled flow boiling. Figure-5.4 presents a description of heat flux components that are taken into consideration in the model. A vapor bubble nucleates at an active nucleation site, and grows to its maximum size at the heated wall. This particular heat transfer rate is referred as microlayer evaporation (\dot{q}_E). As the bubble lifts off from the wall, colder liquid rushes into occupy that area previously occupied by the nucleating bubble. The heat transfer rate to this colder fluid is different from the purely single-phase convection (\dot{q}_C) to a relatively warmer fluid and is accounted as the surface quenching or transient conduction (\dot{q}_Q).

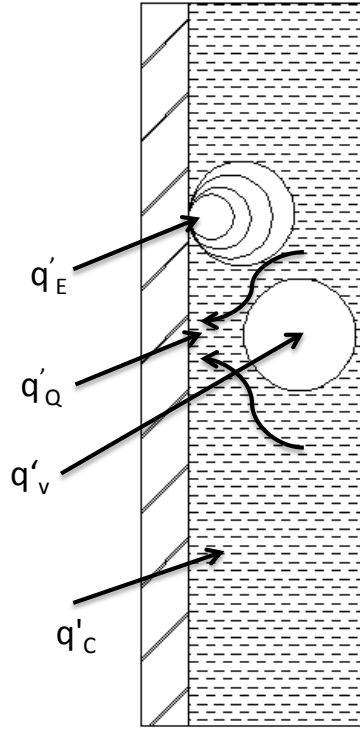


Figure-5.4 Wall heat flux partitioning

The Rensselaer Polytechnic Institute (RPI) model (Kurul & Podowski, 1991) includes these mechanisms to formulate the total wall heat flux in sub-cooled boiling flows as the sum of the convective heat transfer to the bulk liquid, quenching heat transfer after bubble departure and the evaporative heat transfer to vapour phase on the wall surface. In case of non-equilibrium boiling, when void fraction increase more than 20%, voids also accumulates near heater surface and part of heat (fraction $(1 - f_p)$) is also transferred to the vapour phase directly. Then total heat flux of the wall is given by Eq. (5.30).

$$\dot{q}_w = (\dot{q}_c + \dot{q}_Q + \dot{q}_E) f_p + \dot{q}_v (1 - f_p) \quad \dots (5.30)$$

In Eq. (5.30), f_p is the function of liquid phase fraction which is utilized for Non equilibrium boiling case and given by Eq. (5.31) and Figure-5.5 describes the variation of f_p with liquid void fraction.

$$f_p = \begin{cases} 1 - \frac{1}{2} e^{-20(\epsilon_L - \epsilon_{L \text{ critical}})} & \epsilon_L \geq \epsilon_{L \text{ critical}} \\ \frac{1}{2} \left\{ \frac{\epsilon_L}{\epsilon_{L \text{ critical}}} \right\}^{20\epsilon_{L \text{ critical}}} & \epsilon_L < \epsilon_{L \text{ critical}} \end{cases} \quad \dots \dots (5.31)$$

$$\epsilon_{L \text{ critical}} = 20\% \text{ or } \epsilon_{G \text{ critical}} = 80\%$$

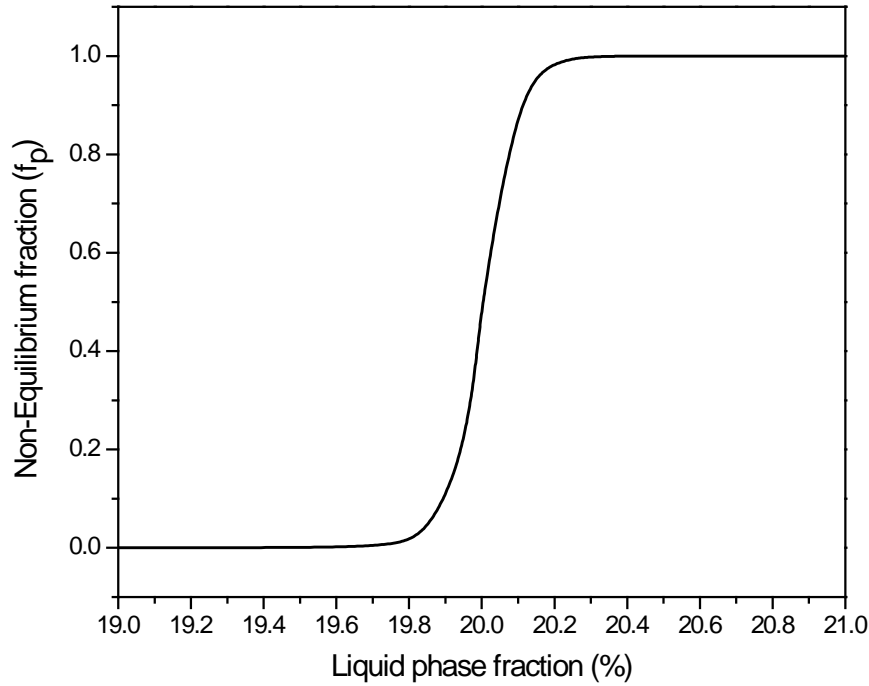


Figure-5.5 variation of correction factor for non-equilibrium boiling

The heated surface is subdivided into area A_b which is covered by nucleating bubbles and a portion $(1-A_b)$ covered by liquid. The convective heat flux \dot{q}_C is expressed by Eq. (5.32) (Kurul & Podowski, 1991)

$$\dot{q}_C = h_C(1 - A_b)(T_w - T_L) \quad \dots (5.32)$$

Where h_C is the single phase heat transfer coefficient and T_w and T_L are the wall and liquid temperatures. The quenching heat flux \dot{q}_Q models the cyclic averaged transient energy transfer (transient conduction) related to liquid filling the wall vicinity after bubble detachment, and is expressed by Eq.(5.33) (Kurul & Podowski, 1991)

$$\dot{q}_Q = \frac{2}{\sqrt{\pi}} \sqrt{k_L \rho_L C_{pL} \cdot f} A_b (T_w - T_L) \quad \dots (5.33)$$

Where k_L is the conductivity of liquid, f is the bubble departure frequency.

The evaporative flux \dot{q}_E is given Eq. (5.34)

$$\dot{q}_E = V_b N_w \rho_G h_{fg} f \quad \dots (5.34)$$

Where V_b is the volume of the bubble based on the bubble departure diameter, N_w is the active nucleate site density, h_{fg} is the latent heat of evaporation and f is the bubble departure frequency. These equations need additional closure for parameters like Area of influence; Frequency of bubble departure; Nucleate site density and bubble departure diameter.

Area of influence (A_b) is based on the departure diameter and the nucleate site density and is given by Eq. (5.35).

$$A_b = \min \left(1, K \frac{N_w \pi D_B^2}{4} \right) \quad \dots (5.35)$$

Where K , is an empirical constant usually set to 4 (Delvalle-Kenning, 1985).

Nucleation site density

Nucleation sites starts become activated as the temperature of the heater surface start rising above the saturation temperature of the liquid at the local pressure. The density of the activation sites depends upon the cavities on the heater wall surface, mutual properties of heater and liquid and contact angle between liquid and the wall. It has been also observed that nucleation site density increases with wall heat flux and mass flux (Zeng and Klausner, 1993). Active nucleation site density governs the evaluation of the heat flux for evaporation as well quenching in wall heat flux partition model. A large number of models have been developed to empirically correlate the active nucleation site density with the aforementioned parameters.

Gaertner and Westwater (1961) carried out boiling experiment for the active nucleation site density with nickel salts dissolved in water and copper-heater surface. They obtained an estimation of the active nucleation site density by counting the number of holes in the deposited nickel layer on the heater surface. They proposed direct proportionality of site density with heat flux. Johov (1969) interrelated the active nucleation site density to the present cavities on the heating surface. Kocamustafaogullari and Ishii (1983) carried out a parametric study to correlate the active nucleation site density for the existing data of pool

boiling in the literature. They also applied the correlation to a few forced convection nucleate boiling data available by using an effective superheat rather than the actual wall superheat. The correlation for system pressures ranging from 1 to 198 bars. Wang and Dhiri (1993) published experimental work showing clearly the effect of the static contact angle on the active nucleation site density as a function of wall superheat. Kolev (1995) summarizes the widespread results of nucleation site density by various researchers and developed a phenomenological model for nucleation site density. Hibiki and Ishii (2003) mechanistically modeled the active nucleation site density by accounting the size and cone angle distributions of cavities existing on the surface. It was shown that the active nucleation site density is a function of the critical cavity size, the contact angle, and the wall superheat. This model gave fairly good predictions over the flow conditions of $0.1 \text{ MPa} < P < 19.8 \text{ MPa}$, $0 \text{ kg/m}^2\text{s} < \text{mass velocity} < 886 \text{ kg/m}^2\text{s}$. Besides, various models along with their application ranges for active nucleation site densities are presented in Table-5.4.

Bubble departure frequency

It is the other important parameter required for heat flux modeling with wall partitioning model. Accurate prediction by the flux partitioning model depends upon the ability of empirical models in prediction the correct physical phenomena. Several investigations were performed by the researchers on the bubble departure frequency. Various models for bubble departure frequency are tabulated in Table-5.5. Cole (1967) investigated boiling photographically in the vicinity of the critical heat flux. His model was based on the basic assumption that when successive bubbles leave the heater surface, touches and coalesces, the bubble frequency multiply by the bubble diameter at lift off will be equal to the rate that bubbles leave the surface. Zuber (1959) assumed that in a gravitational field, the quotient of departure diameter divided by growth time is equal to the bubble rise velocity. He also assumed that bubble waiting time is almost equal to bubble growth time. Ivey (1952)

proposed three correlations, relating the departure frequency with different power of departure diameter, for three different regions as seen in Table-5.5. Most of the data in literature are available for pool boiling heat transfer cases. Kocamustafaogullari and Ishii (1983) considered and boiling channel and formulated a one-dimensional interfacial area transport equation for predicting the average bubble number density. They correlated the bubble departure frequency as the function of fluid properties and bubble departure diameter. Basu, Warrier and Dhir (2005) conducted the experiments for convective boiling over flat plate for bubble generation and waiting time eventually the frequency of departure.

Bubble departure diameter

Size of the bubble diameter at departure is determined either by inertia controlling growth or thermal controlled. It is also an important parameter in heat flux portioning model and requiring closure model. Many models were proposed by the scientist and investigators for bubble departure diameter, some of them are listed in Table-5.6. Most of the developed empirical correlations are functions of bubble contact angle, Jacob number or other thermal hydraulic parameters. Fritz (1935), considered the static equilibrium between adhesive force and buoyancy to predict the bubble departure diameter. Zuber (1963) assumed that a thin superheated thermal layer exists near the surface where the bubble growth occurs. Tolubinsky and Kostanchuk (1970) utilized the local bulk temperature in their correlation for bubble departure diameter. Unal (1976) performed experiments for maximum bubble diameter, maximum bubble-growth time and bubble-growth rate during the subcooled nucleate flow boiling of water up to a pressure of 17.7 MPa for a heat flux variation of 0.47-10.64 MW/m²; and a velocity 0.08-9.15 m/s with subcooling 3 to 86 K. For calculating bubble departure diameter, he used the Rohsenow (1952) superposition method to determine the subcooled nucleate flow boiling heat transfer. Then he applied a similarity method to calculate the heat transfer coefficient. His studies show that the proposed equation for bubble departure

diameter has a good agreement with most of the experiments within $\pm 30\%$ uncertainty. The bubble departure diameter correlation of Kocamustafaogullari and Ishii (1983) has been formulated for boiling systems which has shown good agreement with their experimental data generated for water around atmospheric pressure. This equation was modified for higher pressures with theoretical arguments by them.

Table-5.4 Nucleation site density models

<i>Authors</i>	<i>Model equation</i>	<i>Flow condition</i>	<i>Fluid</i>
Gaertner and Westwater (1961)	$N_w \sim Q_w^{1/m}$ Here $m=0.48$	Pool boiling	Saturated nickel salt based water and copper heater
Mikic & Rohsenow (1969)	$N_w = \left(\frac{D_{c,max}}{D_c} \right)^m, D_c = \frac{4\sigma T_{sat}}{\rho_G h_{fg} \Delta T_{sup}}$	pool boiling, $p \sim 1-13.7$ bar	Saturated water
Lemmert & Chawla (1977)	$N_w = C^n (T_w - T_{sat})^n$ where $C = 210$ and $n = 1.805$	Pool boiling of saturated water	Saturated water
Kocamustafaogullari & Ishii (1983)	$N_w D_B^2 = f(\rho^*) (R_c)^{-4.4}$ where $f(\rho^*) = 2.157e^{-7} \rho^{*-3.2} (1 + 0.0049\rho^*)^{4.13}$ and $\rho^* = \rho_L - \rho_G / \rho_G$ $R_c^2 = \frac{4\sigma T_{sat}}{\rho_G h_{fg} \Delta T_{sup} D_B}$	pool boiling, $p \sim 1-198$ bar	Saturated water
Yang & Kim (1988)	$N_w = \overline{N_w} \phi(\beta) \exp(-K/\Delta T_{sup})$ where $\overline{N_w} \phi(\beta)$ is constant for given liquid and heater surface combination while $K = \frac{2\sigma T_{sat} v_{fg}}{h_{fg}}$		Saturated water
Wang & Dhir (1993)	$N_w = 218.8 \text{Pr}^{1.63} (1/\gamma) \omega^{-0.4} \Delta T_{sup}^3$ where $\gamma = \left(\frac{k_w \rho_w c_{pw}}{k_L \rho_L c_{pL}} \right)^{0.5}$ and	$p \sim 1$ bar Pool boiling on vertical copper surface	Saturated water

	$\omega = 14.5 - 4.5 \left(\frac{Rap}{\sigma} \right) + \left(\frac{Rap}{\sigma} \right)^{0.4}$		
<i>Authors</i>	<i>Models</i>	<i>Flow condition</i>	<i>Fluid</i>
Benjamin and Balakrishnan (1997)	$N_w = 5 \times 10^{-31} (1 - \cos\phi) D_c^{-6}$	P = 0.101 MPa 5 K < ΔT _{sup} < 25K Q up to 3 KW	Water, n-hexane, acetone, and carbon tetrachloride
Basu, Warriar and Dhir (2002)	$N_w = \begin{cases} 3.4 \times 10^3 (1 - \cos\theta) \cdot \Delta T_w^2 & \Delta T_w < 15K \\ 0.34 (1 - \cos\theta) \Delta T_w^{5.3} & \Delta T_w \geq 15K \end{cases}$	convective boiling, low p	
Ishii and Hibiki (2003)	$N_w = \overline{N_w} \left\{ \exp \left(\frac{\lambda' g(\rho^+)}{R_c} \right) - 1 \right\}$ $\text{where } \overline{N_w} = 4.72e5 \left\{ 1 - \exp \left(-\frac{\phi^2}{4.17} \right) \right\}$ $\rho^+ = \log(\rho^*) \text{ where } \rho^* = \rho_L - \rho_G / \rho_G$ $\text{and } \lambda' = 2.5 \times 10^{-6} m$ $g(\rho^+) = -0.01064 + 0.48246\rho^+ - 0.22712\rho^{+2} + 0.05468\rho^{+3}$	pool & convective boiling, p~1-198bar	Saturated water

Table-5.5 Bubble departure frequency models

<i>Authors</i>	<i>Models</i>	<i>Flow condition</i>
Jacob & Fritz (1931)	$f_d D_B = 0.078$	Pool boiling
Pebles & Garber (1953)	$f_d D_B = 1.18 \left(\frac{t_g}{t_g + t_w} \right) \left(\frac{\sigma g \Delta \rho}{\rho_L^3} \right)^{1/4}$	Pool boiling
Zuber (1959)	$f_d D_B = \left(\frac{\sigma g \Delta \rho}{\rho_L^2} \right)^{1/4}$	Pool boiling
Cole (1967)	$f_d = \sqrt{\frac{4g\Delta\rho}{3D_B\rho_L}}$	Pool boiling – Hydrodynamic region (dominated by drag and buoyancy forces)
Ivey (1967)	$f_d = 0.9 \sqrt{g/D_B}$	Pool boiling – Hydrodynamic region
Ivey (1967)	$f_d = \text{Const}/D_B^2$	Pool boiling – Thermodynamic region
Basu, Warriar and Dhir (2005)	$t_w = 139.1(\Delta T_w^{-4.1})$ $t_g = \frac{D_B^2}{45 J_{a \text{ sup}} \exp(-0.02 J_{a \text{ sub}})}$ where $J_{a \text{ sup}} = \frac{\rho_L c_{pL} \Delta T_w}{\rho_G h_{fg}}$ and $J_{a \text{ sub}} = \frac{\rho_L c_{pL} \Delta T_{\text{sub}}}{\rho_G h_{fg}}$	Convective boiling on flat plate heater

Table-5.6 Bubble departure diameter models

Authors	Model equation	Flow conditions
Fritz Correlation (1935)	$D_b = 0.0208\phi \sqrt{\frac{\sigma}{g(\rho_l - \rho_v)}}$ <p>Where $\phi = 80^\circ$</p>	Pool boiling 1 atm pressure
Zuber (1963)	$D_b = \left[\frac{6\sigma}{g(\rho_l - \rho_g)} \frac{k_L T_{sup}}{Q_w} \right]^{1/3}$	
Cole (1967)	$D_b = \phi \sqrt{\frac{\sigma}{g(\rho_l - \rho_v)}} \left(\frac{\rho_l c_{pl} \Delta T_{sup}}{\rho_v h_{fg}} \right)$	P=0.066–1 atm
Tolubinsky and Kostanchuk (1970)	$D_b = \min(0.0014, 0.0006 e^{\frac{-\Delta T_w}{45.0}})$	Stainless steel horizontal plate heating surface Heat flux= 0.47 MW/m ² P=1 atm to 10 atm ΔT_{sub} =5–20 K
Unal (1976)	$D_b = (2.4210)^{-5} p^{0.709} \left(\frac{a}{b\sqrt{\phi}} \right) \text{ where}$ $a = \frac{(T_w - T_{sat})}{2\rho_v h_{fg}} \sqrt{\frac{\rho_s c_{ps} k_s}{\pi}}$	Heat flux= 0.47–10.64 MW/m ² P=1–177 bar ΔT_{sub} =3–86 K

	$b = \begin{cases} \frac{\Delta T_{sub}}{2 \left(1 - \frac{\rho_v}{\rho_l}\right)} \exp\left(\frac{\Delta T_{sub}}{3} - 1\right) & \Delta T_{sub} \leq 3 \\ \frac{\Delta T_{sub}}{2 \left(1 - \frac{\rho_v}{\rho_l}\right)} & \Delta T_{sub} > 3 \end{cases}$ $\varphi = \max\left(\left(\frac{U_b}{U_o}\right)^{0.47}, 1\right)$	
Kocamustafaogullari and Ishii (1983)	$D_b = 0.0012 \left(\frac{\rho_l - \rho_v}{\rho_l}\right)^{0.9} 0.028\phi \sqrt{\frac{\sigma}{g(\rho_l - \rho_v)}}$ <p>where $\phi = \text{contact angle}$</p>	P=1–198 bar Tuned for $\phi \sim 41^\circ$ developed for high pressure conditions

Interfacial heat transfer

The third term in the energy balance Eq. (5.12) contains enthalpy change due to phase change i.e. interfacial mass and heat transfer between two phases. Bubble grows on nucleation sites present on the heated wall. Bubble takes up heat from the wall and gets departed from heated wall. At the time of departure from heated wall, bubble gives heat to the bulk liquid surrounding to it resulting in condensation. Therefore, rate of heat transfer from bubble to bulk liquid is given by:

$$Q_{G-L} = h_{G-L}(T_L - T_G) \quad \dots (5.36)$$

where

$$h_{G-L} = \frac{k_L Nu_i}{d_B} A_i \quad \dots (5.37)$$

Models are developed for Nu_i for interfacial heat transfer. Some of these models are presented in Table-5.7. Ranz Marshall (1952) model gives Nusselt number as

$$Nu_p = 2.0 + 0.6Re_b^{\frac{1}{2}} Pr^{\frac{1}{3}} \quad \dots (5.38)$$

Table-5.7 Models for interfacial heat transfer

Authors	Model Equation	Exp. details
Ranz Marshall (1952)	$Nu_i = 2.0 + 0.6Re_p^{\frac{1}{2}} Pr^{\frac{1}{3}}$	Air water drop with diameter ranging from 0. 6– 1.1 mm in flowing stream of air for $Re_b=0-200$
Hughmark (1967)	$Nu_i =$ $\begin{cases} 2 + 0.15Re_b^{0.5} Pr^{\frac{1}{3}} & (a) \\ 2 + 0.27Re_b^{0.62} Pr^{1/3} & (b) \end{cases}$	Water-Benzonic acid (a) $0 \leq Re_b < 776.06$ and $0 \leq Pr < 250$ (b) $766.06 \leq Re_b$ and $0 \leq Pr < 250$
Tomiyama (1998)	$Nu_i = 2 + 0.15Re_b^{0.8} Pr^{0.5}$	Water-Glycerin

5.5 Turbulence modeling

Turbulence modeling plays a vital role in simulating the flow field. Two phase flows are inherently turbulent and fluctuating, it makes critical the selection of the turbulence model.

Due to the lower density of vapour, it is commonly assumed that, in nucleate boiling flow, the motion of the dispersed vapour phase follows the fluctuations in the continuous liquid phase. Accordingly, the turbulence stresses are modeled only for the liquid phase, whereas the vapour phase is modeled by a simple zero equation model. Turbulence models being utilized for the two phase flow are extension of their single phase counterpart. There exist numerous turbulence models for two phase flows. These include two equations Eddy Viscosity Models (EVM) and Reynolds stresses transport model (RSTM). The majority of industrial CFD applications today are conducted with two-equation eddy viscosity model (EVM), especially the $k-\epsilon$ model, while the Reynolds stresses transport model (RSTM) or Rij- ϵ , remains exceptional. Ikeda et al. (2006) used $k-\epsilon$ model, they confirmed its ability to predict the averaged velocity, but they mentioned that it may be insufficient for narrow channel flow conditions that include non-isotropic effects. Several authors studied the turbulence modeling in the case of water flow with gas bubbles. As an example, a RSTM model adapted to bubbly flows is studied by Chahed (1999) and used to perform simulations of basic bubbly flows. This model is interesting but it requires a doubled computational effort; because it accounts for two scales of turbulence, the first one is the turbulence of the fluid seen in a single phase flow and the second is the pseudo turbulence which considers the fluctuation caused by the motion of the bubble. In Mimouni et al. (2009), the authors proposed a turbulence modeling that takes into account the Reynolds tensor for the continuous phase only, while a more basic modeling is used for the dispersed phase. Also in Mimouni et al. (2009) it is concluded that the use of eddy viscosity models may be sufficient for water bubbly flows in vertical pipes but not for complex geometries especially when swirling flows are involved.

Here in our study, we have two types of problems; one is of bubble column and other is boiling simulations inside rod bundle. The gap between rods in the bundle is very small (2-

3mm), which is essentially an anisotropic problem of turbulence and demands more resolution and hence higher order turbulence model. Considering these requirements for bubble column two equation EVM (k - ε) model is employed, while for rod bundle RSTM is employed. Mathematical formulations of these turbulence models for the two phase flow are as follows:

k - ε model for two phase flow

This model is based on Bousinesq's analogy employing the eddy viscosity as the model parameter. The eddy viscosity assumption transforms the Reynolds stress gradient into a diffusion-like transport term. k - ε model describes energy process in terms of production and dissipation, as well as transport through the mean flow or by turbulent diffusion. The formulation of the standard k - ε modeling concept for the single-phase flow is provided in Jones and Launder (1972). In industrial CFD simulations; the most widely used turbulence model is standard k - ε model with logarithmic wall functions. Standard k - ε model predicts excessive ν_t near the wall as evidenced by Heindel et al. (1994). Further, it over-predicts the near wall heat transfer. Special wall functions and use of damping functions in k and ε equation, to damp the turbulence in the viscous region close to the wall are some remedies for this. In spite of all issues, k - ε model remains the first option/choice as turbulence model due to its reasonable accuracy at low computational cost.

The turbulence in the two-phase is estimated by using mixture k - ε equation given by Behzadi et al. (2004). This model is based on the fact that both gas and liquid phases tend to fluctuate as one entity at high phase fractions and therefore using one set of equations for the mixture. The mixture k - ε equation is based on the summation of the two corresponding phase-averaged (mass-weighted averaging) transport equations for k and ε of the two phases. The set of equations (Behzadi et al. 2004) used in k - ε mixture model is summarized as follows:

k_m -equation

$$\frac{\partial}{\partial t}(\rho_m k_m) + \nabla \cdot (\rho_m u_m k_m) = \nabla \cdot \frac{\mu_m^t}{\sigma_m} \nabla k_m + P_k^m - \rho_m \varepsilon_m + S_k^m \quad \dots (5.39)$$

The source term S_k^m in the above equation arises from the action of interphase forces and hence, it is contributed to interphase energy exchange.

ε_m -equation

$$\begin{aligned} \frac{\partial}{\partial t}(\rho_m \varepsilon_m) + \nabla \cdot (\rho_m u_m \varepsilon_m) \\ = \nabla \cdot \frac{\mu_m^t}{\sigma_m} \nabla \varepsilon_m + \frac{\varepsilon_m}{k_m} (C_{\varepsilon 1} P_k^m - C_{\varepsilon 2} \rho_m \varepsilon_m) + C_{\varepsilon 3} \frac{\varepsilon_m}{k_m} S_k^m \end{aligned} \quad \dots (5.40)$$

The mixture properties appearing in Eqs. (5.39) and (5.40) are related to those of the continuous (liquid) and dispersed (gas) phases are as follows:

$$\rho_m = \epsilon_L \rho_L + \epsilon_G \rho_G \quad \dots (5.41)$$

$$k_m = \left(\epsilon_L \frac{\rho_L}{\rho_m} + \epsilon_G \frac{\rho_G}{\rho_m} C_t^2 \right) k_L \quad \dots (5.42)$$

$$\varepsilon_m = \left(\epsilon_L \frac{\rho_L}{\rho_m} + \epsilon_G \frac{\rho_G}{\rho_m} C_t^2 \right) \varepsilon_L \quad \dots (5.43)$$

$$u_m = \frac{\epsilon_L \rho_L u_L + \epsilon_G \rho_G u_G C_t^2}{\epsilon_L \rho_L + \epsilon_G \rho_G C_t^2} \quad \dots (5.44)$$

$$\mu_m^t = \frac{(\epsilon_L \mu_L^t + \epsilon_G \mu_G^t C_t^2) \rho_m}{\epsilon_L \rho_L + \epsilon_G \rho_G C_t^2} \quad \dots (5.45)$$

$$P_k^m = \epsilon_L P_k^L + \epsilon_G P_k^G \quad \dots (5.46)$$

$$S_k^m = S_k^L + S_k^G = \overline{F_I u_I'} = -A_G (2\epsilon_G (C_t - 1)^2 k_L + \eta_L \nabla \epsilon_G \cdot \bar{u}_r) \quad \dots (5.47)$$

The mixture k - ε model is used in order to solve the turbulence. The value of mixture kinetic energy (k_m) and turbulent energy dissipation rate for mixture (ε_m) are obtained by solving conservation equations of k and ε [Eqs. (5.39) and (5.40), respectively]. The value of k_m is used to find out the turbulent kinetic energy for liquid (k_L) by solving Eq. (5.42), while Eq. (5.43) is used to calculate the value of turbulent energy dissipation rate for liquid (ε_L). By using the individual values of k_L and ε_L , the turbulent viscosity of the liquid (μ_L^t) is

calculated. Similar procedure is followed in order to calculate the turbulent viscosity of the gas (μ_G^t). Thus, the values of μ_L^t and μ_G^t , and hence the value of μ_m^t , are calculated and updated at each iteration.

Reynolds Stress (R_{ij} - ϵ) Model

The rod bundle portrays a complex geometry with wall shear stress giving rise to anisotropy in the flow field. To capture this anisotropic turbulence, Reynolds Stress Model (RSM) is used for the present CFD calculations. RSM, also called the second-order or second-moment closure model is most complex classical turbulence model. Major drawbacks of the two equation models emerge when it is attempted to predict flows with complex strain fields or significant body forces. Under such conditions the individual Reynolds stresses are poorly represented by Boussinesq hypothesis even if the turbulent kinetic energy is computed to reasonable accuracy. The exact Reynolds stress transport equation on the other hand can account for the directional effects of the Reynolds stress field. The exact equation for the transport of 'R', the Reynolds stress takes the following form (Eq. 5.48) for the mixture of the two phase flow.

$$\frac{\partial \rho^m R^m}{\partial t} + C^m = P^m + D^m + G^m - \epsilon^m + \Pi^m + \Omega^m \quad \dots (5.48)$$

where

$$R^m = \frac{\tau_m}{\rho_m}$$

$$R^m = \overline{u_1 u_1}, \overline{u_2 u_2}, \overline{u_3 u_3}, \overline{u_1 u_2}, \overline{u_1 u_3}, \overline{u_2 u_3}$$

Here, the terms $C^m, P^m, D^m, G^m, \epsilon^m, \Pi^m$ and Ω^m consist, respectively, of the rate of advection of R_m , rate of shear stress production tensor of R_m , rate of diffusion of R_m , rate of buoyancy production tensor of R_m , rate of destruction of R_m , transport of R_m due to turbulent pressure-strain interactions and transport of R_m due to rotation. Dissipation rate equation remained unchanged and it is as in k- ϵ model. The details of the RSM employed for two phase flows are given in Launder et al. (1975), Yeoh and Tu, (2010).

Bubble induced turbulence

In single phase flow, the turbulence energy spectrum is considered to follow the Richardson (1922) description. Large scale eddies are generated in regions of high velocity gradients and the mean kinetic energy is converted into turbulent kinetic energy. Thus the energy injection to turbulence is assumed to occur at the highest scale. These large scale eddies are not stable and undergo continuous breakage process (inertial range) till the Kolmogorov length scale is achieved beyond which dissipation of turbulent kinetic energy occurs. There have been various theories of the cascading process, the pioneering contribution has been made by Kolmogorov (1941a and 1941b). Since then, extensive analysis of the inertial range has been performed in the published literature and excellent reviews are available (Frisch, 1995; Pope, 2000). The origin of energy spectrum in gas–liquid two phase flow is different, This is mainly because, though the energy is injected by the introduction of gas phase in the form of bubbles, the observed length scales are in the range of bubble size (or even smaller) to domain size. Thus, the origin of the form of turbulent energy spectrum in two phase flow is different from the single phase flow.

The presence of bubbles in the liquid flow field induces turbulence. While moving in the flow field wake is formed behind the bubble. The bubble imparts its energy to the liquid and induces turbulence in the liquid field.

Two different approaches to account for the turbulence induced by the dispersed phase in the Eulerian framework.

- In first approach, the contribution of bubbles or droplets to the turbulence is simply added to the effective viscosity formulation and the turbulence equations remain unchanged.
- In second approach, the effect of dispersed phase is added as a source term to the primary phase turbulence equations.

The k-ε model can be extended to two-phase flows by assuming that the total Reynolds stress for the continuous liquid is given by

$$\tau_C^{Re} = \tau_{SI}^{Re} + \tau_{BI}^{Re} \quad \dots (5.49)$$

$$\mu_{eff} = \mu_L + \mu_T + \mu_{BIT} \quad \dots (5.50)$$

As per the Sato (1981) model μ_{BIT} is given as

$$\mu_{BIT} = \rho_l C_{\mu BIT} \epsilon_g d_b |\bar{u}_g - \bar{u}_l| \quad \dots (5.51)$$

$$\text{where } C_{\mu BIT} = 0.6$$

5.6 Closure

Till date one dimensional model are widely being used for simulation of the engineering systems due to ease in computational feasibilities and simple models and ability to model the complete systems. However, these models are not able to predict the important 3-D phenomena inside the systems under consideration resulting in conservative system design. For instance, sometimes, it is possibility that in a BWR core simulation the 1-D models may show a design safe but a hot spot may present inside the core causing the failure of the fuel. Such local phenomenon can be captured by detailed CFD modeling. Recent advances have seen increasing use of CFD models for two phase flow simulations for critical applications. Mainly two types of approaches are used for simulating the 3-D two phase flow systems viz. Euler-Euler and Euler-Lagrangian approach. Less expense for computational power for Euler-Euler approach to the real engineering systems makes it more attractive for the engineers. Euler- Lagrangian approach requires huge computational capacity for a system of similar complexity, so its application is limited to the lab scale systems.

Modeling of two phase flow requires a thorough understanding of the two phase phenomena. The averaged governing equations have a number of complex terms, which need to be seen properly for accurate simulation of two phase flow system. A large number of closure relations are available in the literature for various undisclosed terms of the governing

equations, which makes life more complicated. The applicability of closure model for a certain two phase flow system is always questionable. Insight knowledge of the system phenomena is required to choose a right closure relation.

The success of the CFD model depends, to a large extent, on the selection of the appropriate closures for the solution of the mathematical model. A careful observation of the literature shows large variations in the predictions of the phenomena associated with two phase flow.

In spite of large complexities involved in the modeling, efforts have been made to model the complex nature of the two phase flow. Last three decades have seen number of CFD simulations for two phase flow systems. With increasing computational resources, future will see increasing use of CFD methods for critical two phase flow systems. The empirical nature of the models in the Euler-Euler frame works limits its generality in extending boiling flows simulations for complex geometries. Therefore, developments of mechanistic multi-scale models are required for high fidelity simulation. New high fidelity modeling approaches are in development stage for future CFD frame work.

CHAPTER-6

Studies for Adiabatic Two-Phase Flow

6.1 Introduction.....	149
6.2 Experimental studies of bubble column using RPT technique	150
6.2.1 Principle of RPT operations.....	152
6.2.2 Experimental setup	154
6.2.3 Experimental procedure.....	160
6.2.4 Results and discussions.....	161
<i>Liquid velocity profiles</i>	161
<i>Error and uncertainty in the experimental data</i>	163
<i>Turbulent kinetic energy</i>	169
6.3 Bubble column simulation using OpenFOAM	171
6.3.1 CFD code validation with literature data.....	171
<i>Mesh generation and grid sensitivity</i>	172
<i>Method of solution</i>	173
<i>Boundary conditions</i>	177
<i>Results and discussions</i>	180
6.3.2 CFD code validation with RPT data.....	185
<i>Results and discussions</i>	186
<i>Turbulent kinetic energy</i>	188
6.4 Closure.....	191

6.1 Introduction

It is important to have thorough understanding of phenomena associated with turbulent two phase flow systems before designing the system for commercial units. Lot of empiricism is involved in design of such systems. However, increasing trends are being seen in CFD simulations of multiphase flow systems. On the other hand, the CFD for multiphase flow is not very well matured. In view of this, fundamental experimental studies find an important place in Computational Fluid Dynamics (CFD) arena. It is apparent that fundamental studies can be easily conducted in separate effect test facilities and the results can be used for CFD models validations. In this chapter experiments conducted for adiabatic two phase flow inside a bubble column have been discussed and experimental data has been used for the validation of CFD model developed (discussed in Chapter-5) for two phase flow on OpenFOAM platform.

Experiments form the integral part of design and development of any engineering system. The thermal hydraulic performance analysis of engineering systems for simulations of important phenomena are generally performed in either integral test or separate effect test facilities. Experiments targets physical phenomena under consideration, which is further simulated by CFD tools for their predictive abilities.

In multiphase systems, measurement of velocity field of one or more phases under consideration along with void fraction (holdup) are generally the quantities of interest. Broadly, for these measurements, the techniques can be classified to be invasive and non-invasive. Several experimental techniques have been reported in literature to quantify the flow field in multiphase flow systems, with each technique having its own advantages and disadvantages. In an invasive technique a probe is introduced inside the flow field of interest to measure the velocity of one or more phases constituting the system. Some of the widely used invasive techniques for the velocity measurement are Pitot tube measurement, hot wire

or hot film anemometer, optical fiber probes etc. As these techniques includes introduction of probes into the flow field which may in turn alters the flow field. Also, in these measurement techniques, there is a chance of measuring element getting damaged. This is because of the direct contact of measuring elements with the flow field. In non-invasive techniques (for example, Particle Image Velocity (PIV), Laser Doppler Anemometry (LDA), Radioactive Particle Tracking (RPT), Gamma ray densitometry) of velocity and void measurement, one attempts to measure the velocity and void and velocity fluctuations without disturbing the flow. These techniques are indirect measurement techniques, i.e., the acquired data in form of the signals or photographs have to be further processed to get the velocity and velocity fluctuations. Due to the indirect measurement method and the associated hardware and software requirements, the cost of non-invasive techniques is in general higher. In spite of it, non-invasive techniques always remained choice of researchers as these provides more detailed information (3-D flow field) as compared to invasive techniques (point information mostly).

6.2 Experimental studies of bubble column using RPT technique

In literature, lot of citations is available for non-invasive techniques. Work of few researchers using RPT technique is studied here; Devanathan (1990) applied radioactive particle tracking, using a neutrally buoyant particle, to study the liquid phase motion in bubble columns for the first time. Devanathan used sixteen detectors to monitor the motion of liquid in 3D bubble column. Devanathan also estimated higher moments of velocity, such as Reynolds stresses, kinetic energy of turbulence and intensity of turbulence. At that time, such data was scant and Devanathan's work provided new insights into the hydrodynamics of gas-liquid systems like bubble columns, leading to a series of publications that excited both the experimentalists as well as the then fledgling computational fluid dynamics (CFD) community. Yang et al. (1993) found a single recirculation cell pattern, where the gas-liquid co-current upward flow

in the center of the column and the downwards flow of liquid (after getting disengaged from gas) near the wall. Additional recirculation cells may appear in the distributor region at lower gas velocities. Yang et al. also calculated stresses (both axial and radial normal as well as shear stresses) and found to be increased with superficial gas velocity, where the axial normal stresses were significantly higher than the radial normal stresses. The eddy diffusivities were also estimated, assuming isotropic flow, using the relationship of eddy diffusivity with Lagrangian autocorrelation coefficient. The developments brought in the setup and the acquisition protocol described (the way in which the acquired data (photon counts) were stored, through which long acquisition times for the RPT experiment became possible) were so standardized and promising that many of researchers followed their work for the years. After the pioneering work of Devanathan et al. (1990) and Yang et al. (1993), Larachi et al. (1994, 1995, and 1997) brought out some major development in the RPT technique. Larachi et al. (1995) developed a Monte Carlo methodology for predicting the emission, attenuation (transmission) and detection (absorption) of γ -rays from the radioactive source. The developed Monte Carlo model was verified by comparing the counts for eight detectors with those measured by placing the radioactive particle at several locations under actual flow conditions via calibration ports. The inverse operation was used to locate the unknown tracer particle position by using the measured counts in each detector. The accuracy and precision of the model for determining the tracer particle location was increased by increasing the number of detectors, reducing the distance between column wall and detectors and increasing the sampling time. The developments in the knowledge of RPT techniques by Larachi and co-workers set a benchmark for the further developments.

Chen et al. (1999) investigated the hydrodynamics of bubble column (ID=10 cm) by using CARPT, PIV and CT. They made first attempt to compare and validate the CARPT technique with any other standard experimental technique (PIV in this case). The flow field of liquid

phase, as well as the Reynolds stresses, obtained by CARPT and PIV in an air–water system. It was observed that the results obtained by both the techniques are complementary to each other. The CARPT technique used was capable to obtain reliable ensemble averaged quantities of the long-time behavior of liquid flow field in a bubble column. On the other hand, the PIV system has the capability of assessing the coupling effects of the flow field. Also, the time-series information can be obtained to provide valuable characteristics of flow structure. CT can provide the gas hold-up in a system. Thus CARPT, PIV, and CT techniques used together can provide comprehensive insights into the complex flow structure of the turbulent two-phase flow in bubble columns. Cassanello et al. (2001) studied the liquid dynamics by using CARPT. The effect of column diameter (ID=0.1, 0.16, 0.19 and 0.44 m) and pressure (ranging from 0.1 to 0.3 MPa) on the liquid hydrodynamics was studied by applying Lagrangian tool (LT) and qualitative dynamics tools (QDT). It was found to have a drastic effect of increasing pressure on the liquid flow path or chaotic motion.

6.2.1 Principle of RPT operations

RPT uses the γ -radiation emitted by a single radioactive tracer particle to track its motion in the multiphase reactor. The radioactive isotope Sc-46 has been used as tracer particle, which is dynamically similar to the phase of interest, water in the present case, and the tracer particle was introduced into the bubble column. The γ -rays emitted by the tracer particle were recorded by the array of strategically placed NaI Scintillation detectors. The counts (intensity of radiation) recorded by the detector is inversely proportional to the distance between the detector and tracer particle. A distance-count relationship has been established using a prior calibration of all detectors performed by keeping the particle at several known locations. During the actual RPT experiment the tracer particle is introduced to move freely inside the vessel. The counts recorded by each detector are converted into the corresponding instantaneous distance between the tracer and detector using the pre-established distance-

count relationship. Instantaneous position of the tracer particle was calculated from the instantaneous distances obtained for all the detectors using a Monte Carlo method [Larachi et al. (1994), Roy et al. (2002), Upadhyay et al. (2013)]. The time differencing of the instantaneous positions yields instantaneous velocities and the corresponding ensemble average gives mean velocities. Roy et al. (2005) have tabulated nicely how the turbulent parameters can be calculated from the mean and instantaneous velocities.

The radioactive isotope Sc-46 has been used as a tracer in all the experiments performed in this work. It emits γ -ray at 0.889 and 1.13 MeV energy levels (observed as photopeaks), and has a half-life of 84 days. Since Scandium is of high density (2.99 g/cm³), in order to make a tracer particle that is neutrally buoyant, the small scandium particle was embedded in a polypropylene sphere of outer diameter 1.2 mm, along with an air gap, that resulted in a composite (polypropylene, scandium and air) sphere having density very close to that of water (since we have to map flow field of water since we need to make particle neutrally buoyant to with water). For preparing the tracer particle, care was taken to initially make the particle of slightly 'lighter' density than that of the water. For this purpose, a crystal of pure scandium oxide having size of 300 micron (approximately) is, first, irradiated in nuclear reactor to an activity level of 400 μ Ci in BARC, Mumbai. Then the active scandium oxide particle was kept in a hollow polypropylene bead. To match the density of tracer particle, a suitable air gap was maintained in the bead and then sealed with epoxy resin. The sphere was then subjected to a series of tests for measuring terminal settling velocity in a large column of water. When a finite terminal velocity was recorded, the particle was carefully rubbed with some sand paper until the final sphere this formed with density exactly equal to water. Such a sphere particle has a negligibly small terminal velocity in water and would remain suspended wherever it is left in the column of water.

Twelve (2" × 2") NaI (TI) scintillation detectors are strategically placed around the bubble column to continuously monitor the γ -rays emitted by the tracer particle. A versatile experimental rig was fabricated to hold the entire detector assembly firmly. Depending on the expanded liquid height the detectors were arranged at three different axial locations, each axial location holds four detectors and the detector configuration as given in Figure 6.1. The γ -rays striking the detector crystal is converted into electrical pulses. These signals are amplified by suitable electronics and pulses from all detectors are sent to the corresponding single channel analyzer (SCA) to discriminate the energy levels, and to reduce the noise generated by the Compton scattering. The counts recorded by the each detector are saved on personal computer through the interface called MIDAS. The counts (intensity of radiation) recorded by the detector is inversely proportional to the distance between the detector and tracer particle. A distance-count relationship was established using a prior calibration of all detectors, which was performed by keeping the particle at several known locations. Once we got the distance-count relationship from the calibration step, the tracer particle is allowed to freely move in the reactor. Its position is monitored by the array of detectors for sufficient long duration with a sampling rate of 50 Hz to 100 Hz. Instantaneous position of the tracer particle was calculated from the instantaneous distances obtained for all the detectors using a Monte Carlo method. The time differencing of the instantaneous positions yields instantaneous velocities and the corresponding ensemble average gives the mean velocities. Further, turbulent quantities were evaluated from the instantaneous data of tracer particle fluctuations.

6.2.2 Experimental setup

An acrylic column (1), having height 1.2 m and internal diameter of 120 mm, is used as a bubble column as shown in Figure-6.2. The internal (2) is made of acrylic tube having diameter 36 mm and height 1.2 m. Two stainless steel spacers (5) were used to hold the

internal rod tightly at the top and bottom. Two different configurations were used to study the effect of internal, that is, (i) Bubble column without any internal and (ii) bubble column with one vertical central rod of 36 mm diameter as an internal.

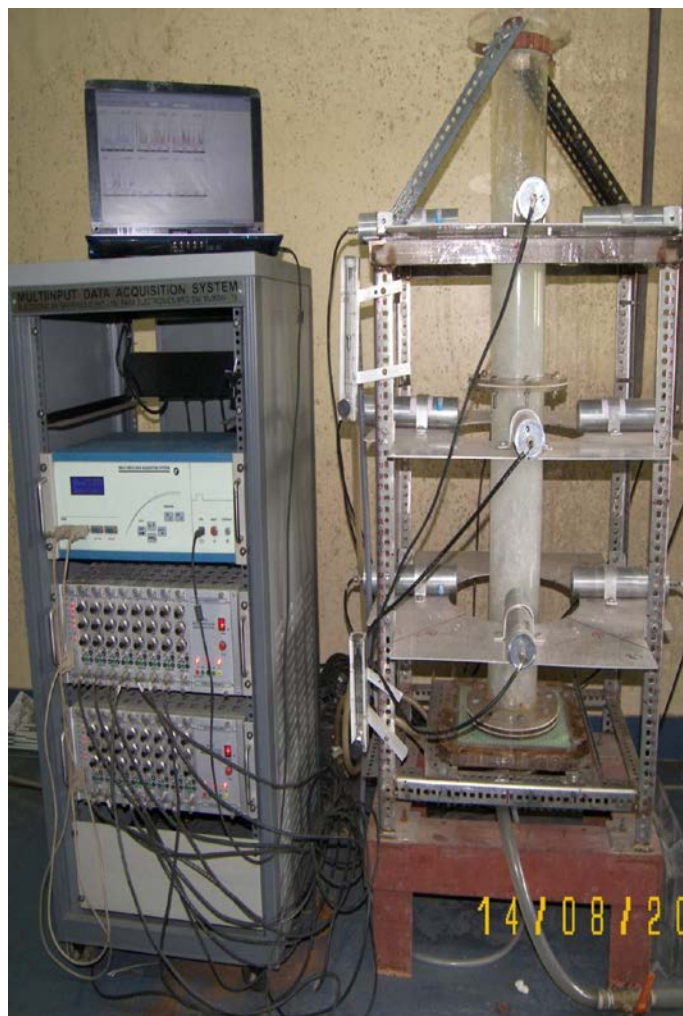


Figure-6.1 Photograph of the experimental set-up

The arrangement of detectors (4) around the column periphery is shown in Figure-6.2. In all the experiments, the initial liquid height is maintained at 655 mm. The experiment is carried out using air as the sparged gas and tap water as the liquid phase. The experiments were performed at an ambient pressure and temperature of 1 atm and 33°C. The properties of water at these conditions were found to be as follows: density (994.7 kg/m³), viscosity (0.00075 Pa.s). Figure-6.3 (a) and (b) show the schematic diagram of the air-water bubble column, with RPT installation and flow diagram of RPT method and typical Eulerian grid with

particle. The compressed air was passed through air and moisture filters (2 and 3, respectively, in Figure-6.3 (a)) to remove dust and oil droplets. The air to the column was sparged through distributor and the flow rate was measured using a series of calibrated rotameters (5, Figure-6.3 (a)). The gas distributor was having 30 apertures, the diameter of each aperture is 2 mm and pitch between two apertures is 10 mm. The air volumetric flow rate is varied between from 10 LPM to 150 LPM which corresponds to the range of air superficial velocity from 14 mm/s to 221 mm/s for two percentages of covered cross-sectional area: 0 % (no internals, configuration-A) and 9 % (configuration-B) as shown in Figure-6.4. Further details of the set of experiments performed are given in Table-6.1.

Table-6.1 Set of experiments performed

Set. No.	S. No	Air volumetric flow rate (LPM)	Air superficial gas velocity (m/s)	Percent area covered by the internals
1	1	10	0.014	0 (configuration-A)
	2	30	0.044	
	3	60	0.088	
	4	90	0.132	
	5	150	0.221	
2	1	10	0.014	9 (configuration-B)
	2	30	0.044	
	3	60	0.088	
	4	90	0.132	
	5	150	0.221	

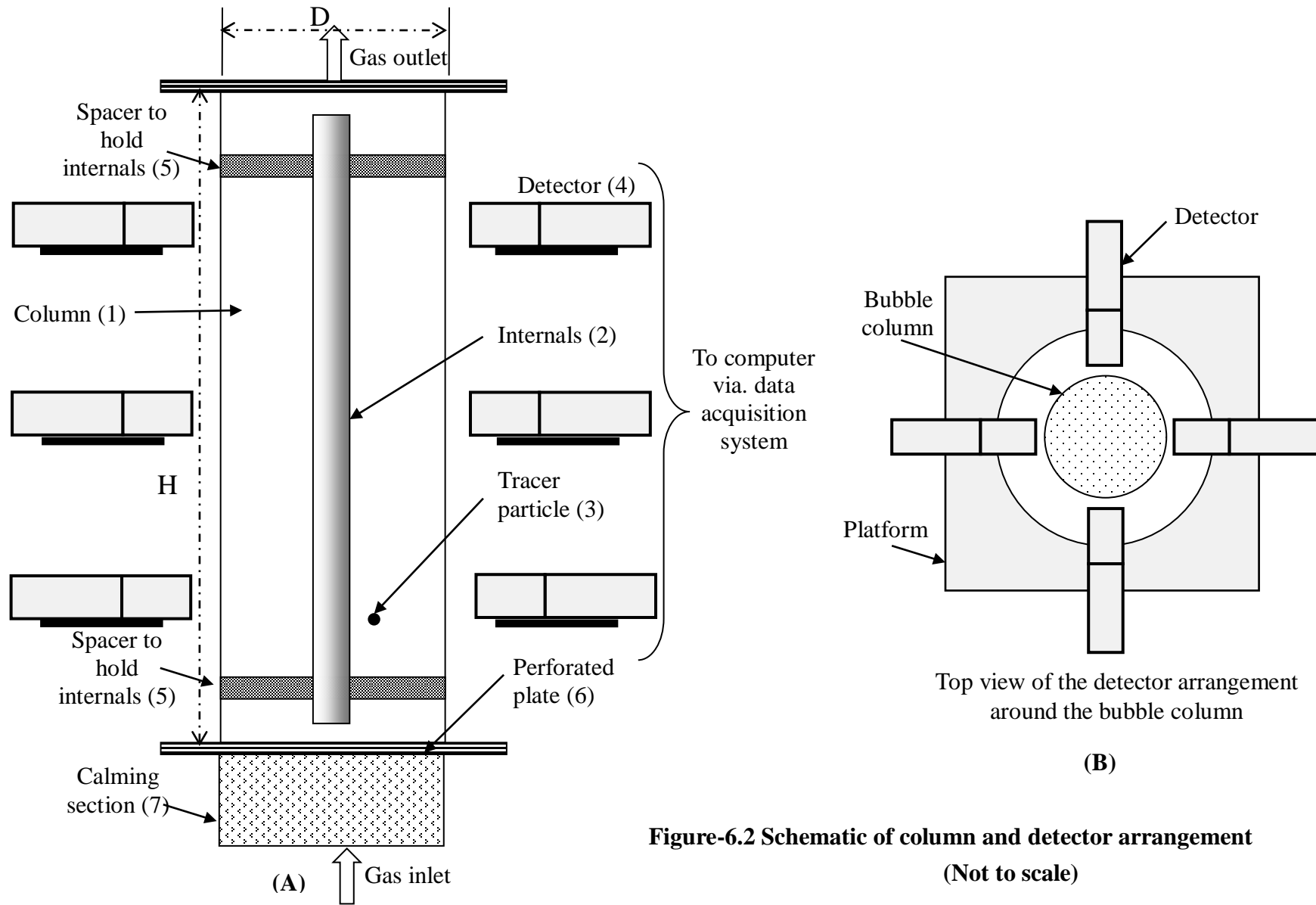
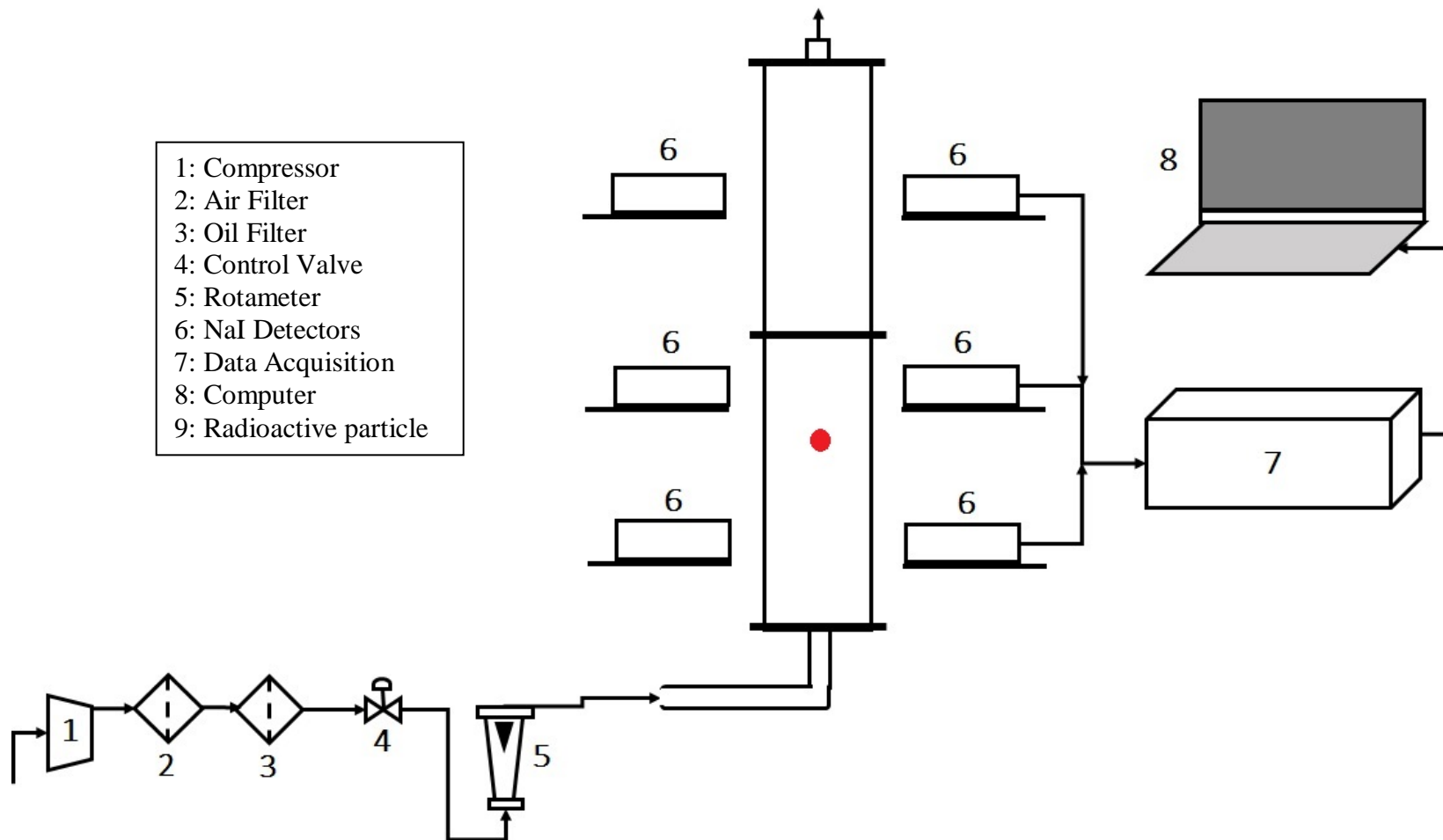


Figure-6.2 Schematic of column and detector arrangement
(Not to scale)



(a)

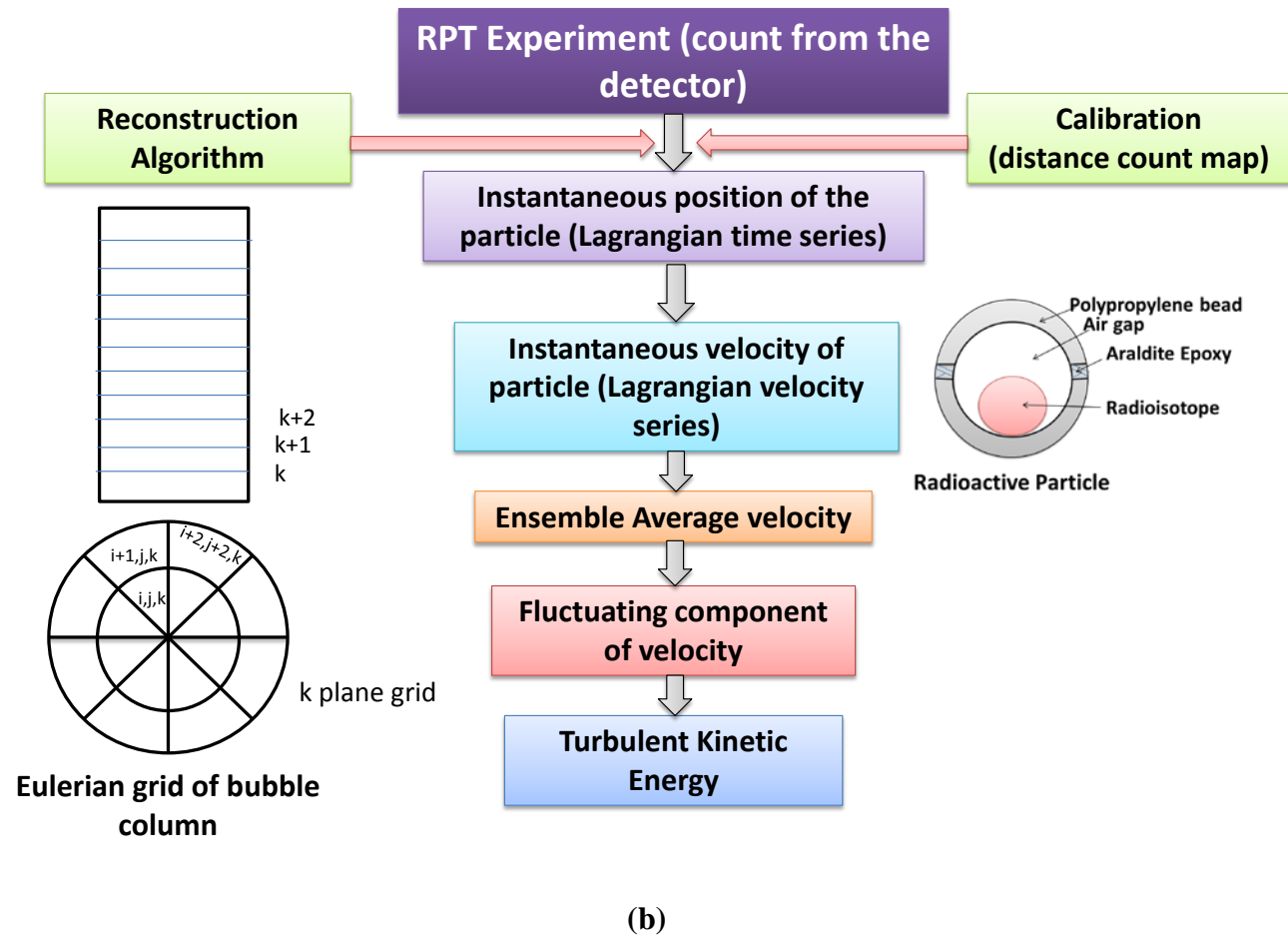


Figure-6.3 (a) Schematic diagram of the experimental set-up for RPT (b) Flow diagram for the RPT method with typical Eulerian grid and particle details

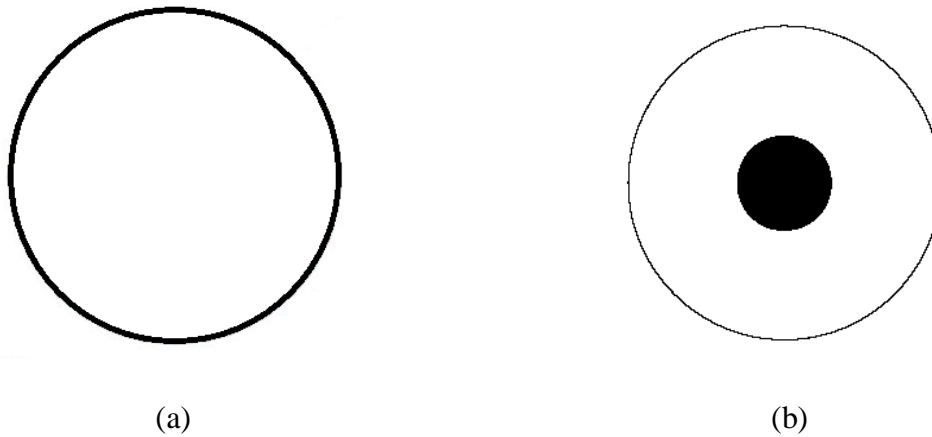


Figure-6.4. Top view of the internal configurations: (a) Empty column (Configuration-A), (b) Configuration-B

6.2.3 Experimental procedure

The experiments are performed in two steps: (i) calibration and (ii) actual experiment. Prior to performing the actual experiment, the calibration of the bubble column was carried out. Figure 6.3 (b) shows the various steps of the RPT along with a typical Eulerian grid of the column and typical particle detail.

6.2.3.1 Calibration of the RPT Experiments:

Calibration is an important step for tracking the particle position precisely. The final results produced by the experiment depend largely on the calibration process accuracy. Calibration method is needed to reconstruct the position of the radioactive particle precisely. The calibration allows relating the intensities calculated by the detector as a function of coordinates of the particle. For calibration whole column was divided into number of small control volumes similar to Eulerian grid as shown in Fig-6.5. In our experiment the whole column was divided into $8 \times 2 \times 20$ volumes (8 X 2 parts in $r-\theta$ plane and 20 in axial plane). A methodology was developed for the calibration of a column by using particle holder (made of acrylic), fishing line and stainless-steel hooks. Provisions were made in the distributor plate to hold the stainless-steel hooks at 15 known coordinate positions in x and y directions. Fishing line has been used to hold the acrylic particle

holder to place the tracer particle in 20 axial locations. The fishing line has been connected to two equal weights on both ends through two pulleys to enable smooth vertical movement. For generating data base for calibration, firstly the particle was fixed at a location in the Eulerian grid discussed above with the help of the aforementioned mechanical arrangement. After that the column was filled with water up to 655 mm height and then the desired air flow was started (the set of the experiment for which calibration is to be done). After that the MIDAS was switched On and gamma counts were recorded for each position in all 12 detectors. With processing of this data, we established the distance count map for the bubble column. This map acts as input for the reconstruction algorithm for generating the Lagrangian position time series.

6.2.3.2 Actual Experiment

During the RPT experiment, the tracer particle was introduced to move freely inside the column. It moves randomly with the liquid phase inside the column since it acts as the liquid phase particle. The experiment was run for approximately 15 hrs duration and the count data was recorded by all 12 detectors with a frequency of 50 Hz.

6.2.4 Results and discussions

Liquid velocity profiles

Figures-6.5 to 6.8 shows the flow patterns in the bubble column at superficial gas velocities ranging from 0.014 to 0.221 m/s for the two studied configurations. Figures-6.5 and 6.8 show time and planer averaged two-dimensional velocity vector plots for the liquid recirculation patterns in a bubble column for configuration-A and B, respectively. The length of the arrow shows the magnitude of the liquid velocity and the orientation shows the direction of liquid flow. On the other hand, Figures-6.6 and 6.7 shows the axial liquid velocity profiles for configurations A and B, respectively.

From Figure-6.5, presence of single circulations cell is clearly seen with liquid moving upwards at the centre and downwards at the wall for all the gas velocities. The centreline rising bubbles carry

some liquid to the top of the column along with them. At the top, the bubbles disengage from the liquid and separated liquid gets pushed towards the column wall by an upcoming jet of the gas-liquid flow at the centre. This liquid then flows down to the bottom of the column along the wall. This liquid flow pattern generates single circulation cell and this observation is in consistent with the behavior of conventional bubble columns as stated in literature [for instance, Hills (1974), Devanathan et al. (1990), Menzel et al. (1990)]. From the Figure-6.5, it is observed that at low superficial gas velocities the flow of the liquid is not fully developed and which indicates the strong entrance effects prevailing at the distributor. As the superficial gas velocity increases the length of the distributor entrance region is gradually reduces and the liquid flow is fully developed right from the distributor plate itself. Further, with increase in the superficial gas velocity the liquid circulation velocity also increases.

The RPT technique gives the information about (time averaged over the duration of 15 hours) the fluid dynamic parameters in all three dimensions on azimuthally averaging. Figure-6.6 shows the radial variation of axial liquid velocity profiles, azimuthally averaged, at all superficial gas velocities given in Table-6.1 for configuration-A. The axial liquid velocity is maximum in the center of the column (Figure-6.5) and shows consistency with the vector diagram plotted in Figure-6.6. With increase in the superficial gas velocity entry region for the establishment of fully developed profiles gradually decreases and the maximum velocity attained by the liquid also increases. Figure-6.6 shows that the upward and downward liquid velocity increases with an increase in the superficial gas velocity which in turn leading to increased liquid circulations.

Figure-6.8 shows the time and azimuthally averaged two-dimensional velocity vector plots for the liquid phase circulations in a bubble column with vertical tube internal (Figure-6.4b, Configuration-B) located at centre of the column for all the superficial gas velocities. From the Figure-6.8, it is observed that for all the gas velocities, there is upflow of the liquid in the centre of the column in the vicinity of internal tube and down flow near the column wall in the annular region of a bubble

column. As observed for simple bubble column, for low gas velocities, the liquid flow is not well developed due to strong entrance effects prevailing at the distributor. Further, increase in the superficial gas velocity enhances the liquid circulation velocity and decreases the length of the distributor region.

Figure-6.7 depicts the variation of the azimuthally averaged axial liquid velocity profiles along with the radial location for the given superficial gas velocities (Table-6.1). The results were found to be in consistent with that of shown in Figure-6.8. It was observed that the entry region for the establishment of fully developed flow reduces with an increase in the superficial gas velocity.

The single cell liquid circulation pattern, liquid upflow in the central region of the column and downflow of the liquid in the vicinity of the wall, is still observed in this case for all the superficial gas velocities (Table-6.1). The centreline liquid velocity as well as the downward liquid velocity found to be increased with an increase in the superficial gas velocity. The effect of presence of the internal is observed in this case. It was found that the presence of internals reduces the flow area available for the incoming gas, which leads to increase in the instantaneous velocities in bubble column. Therefore, the liquid velocity in a column with internal is high as compared to that in the simple bubble column. One of the important finding here is, the magnitude of the mean axial liquid velocities was observed to be very low in the annular region of Configuration-B compared to that of the Configuration-A. Due to the rotating bubble plume around the centred vertical tube the liquid flows upward on one side and flows downward on the other side in the annular region of the bubble column resulting into low mean liquid velocities on time averaging.

Error and uncertainty in the experimental data

Resolution: The technique has been used with a space resolution of 1.2 mm (particle size) and time sampling of 50 Hz (0.02 sec). The time resolution of detector is ~30-40 nSec, but the recording time is 0.02 sec, so we obtained a data of time resolution 0.02 sec. However, with this temporal and space resolution, we can find out the instantaneous velocity and turbulent quantities since we

obtained Lagrangian position vector time series data for very longer duration (15 hrs). From Lagrangian position time series, we find out Lagrangian velocity time series. It gives instantaneous velocity vector with time. After that, average velocity was obtained by ensemble averaging for predefined Eulerian grid volumes. The difference between instantaneous and average velocity for each cell yields the fluctuating component of velocity as a time series. This time series is now used to construct the cross-correlation matrix of fluctuating velocity components, the trace of which gives total kinetic energy per unit volume. The data generated for turbulent quantities will be more accurate for a system divided in relatively larger number of Eulerian grids.

Uncertainty in velocity measurement: Resolution refers to the sphere of uncertainty around the exact particle position. It can also be viewed as the minimum distance between two neighboring positions of the tracer particle that can be discriminated as two different particle positions. It may thus be viewed as the error (or variance) in calculating the mean position of the tracer particle. During the calibration process we have divided our domain with a least count of 1mm while the particle size is 1.2 mm. This yields to a possible error of 1.2 mm in measurement of particle position vector in any direction and any position.

With this spatial and temporal resolution the uncertainty in the instantaneous velocity measurement will be 0.084 m/s which has been calculated as follows:

$$u = \frac{z_2 - z_1}{\Delta t} \quad \dots \dots \dots (6.1)$$

Then the uncertainty in u will be

$$du^2 = \frac{\Delta z_2^2 + \Delta z_1^2}{\Delta t^2} \quad \dots \dots \dots (6.2)$$

$$du = \sqrt{\frac{\Delta z_2^2 + \Delta z_1^2}{\Delta t^2}} \quad \dots \dots \dots (6.3)$$

$$du = 84mm/s$$

Calculation of uncertainty in ensemble average velocity

We run the experiment for 15 hrs with a temporal resolution of 0.02 sec. With this there are 27 lacs population sample of the measurements for the whole domain. We have divided our domain in {(8 X 2 X 20) X 4 (quadrants) =1280} 1280 Eulerian volume, so average number of samples collected for each volume will be 27 lacs/1280=2109.

Then the error in the mean velocity can be calculated as:

$$\overline{du} = \frac{1}{N} \sqrt{\sum_{i=1}^N (du_i)^2} \quad \dots \dots \dots (6.4)$$

Here N= number of samples and $du_i=84\text{mm/s}$ (error in instantaneous velocity)

$$\overline{du} = 1.8 \text{ mm/s}$$

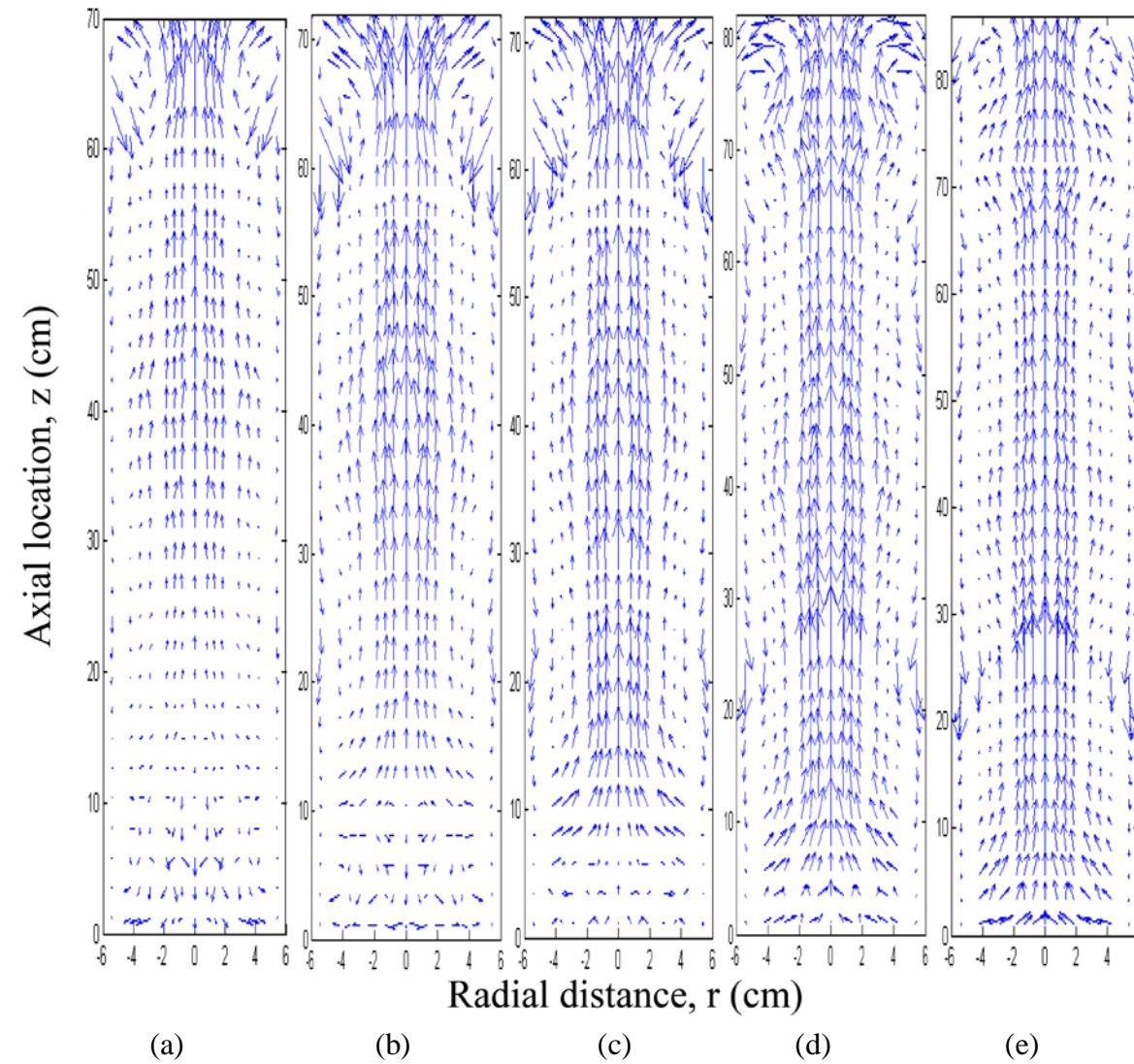


Figure-6.5 Effect of superficial gas velocity on overall flow patterns for Configuration-A:
(a) 0.014 m/s (b) 0.044 m/s (c) 0.088 m/s (d) 0.132 m/s (e) 0.221 m/s

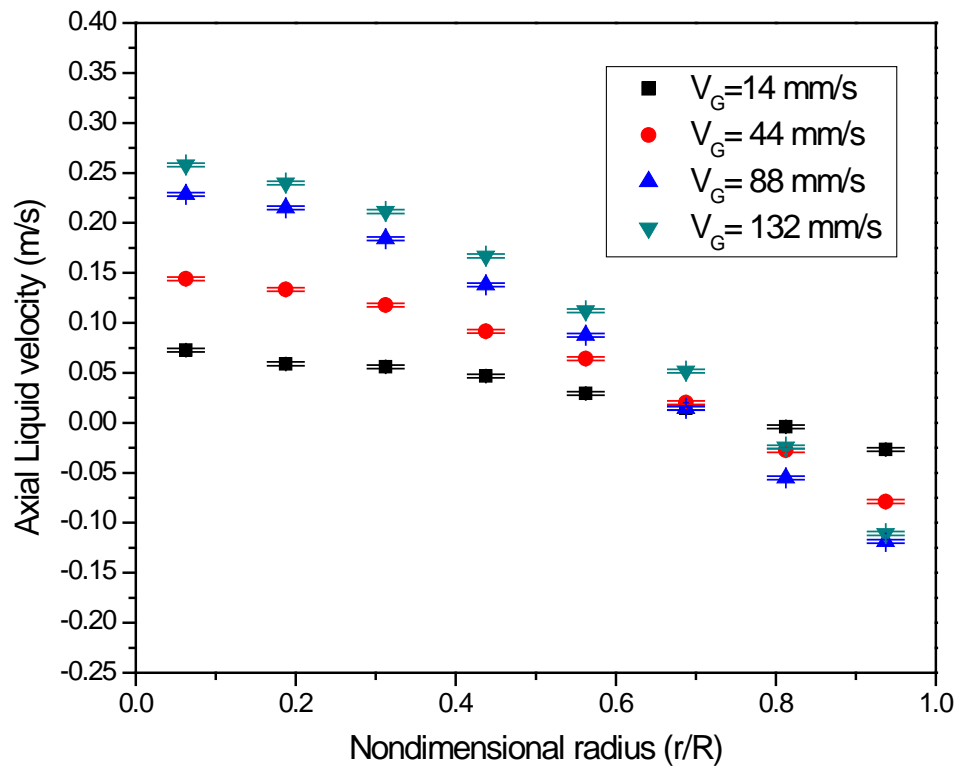


Figure-6.6 Effect of superficial gas on axial liquid velocity for configuration-A

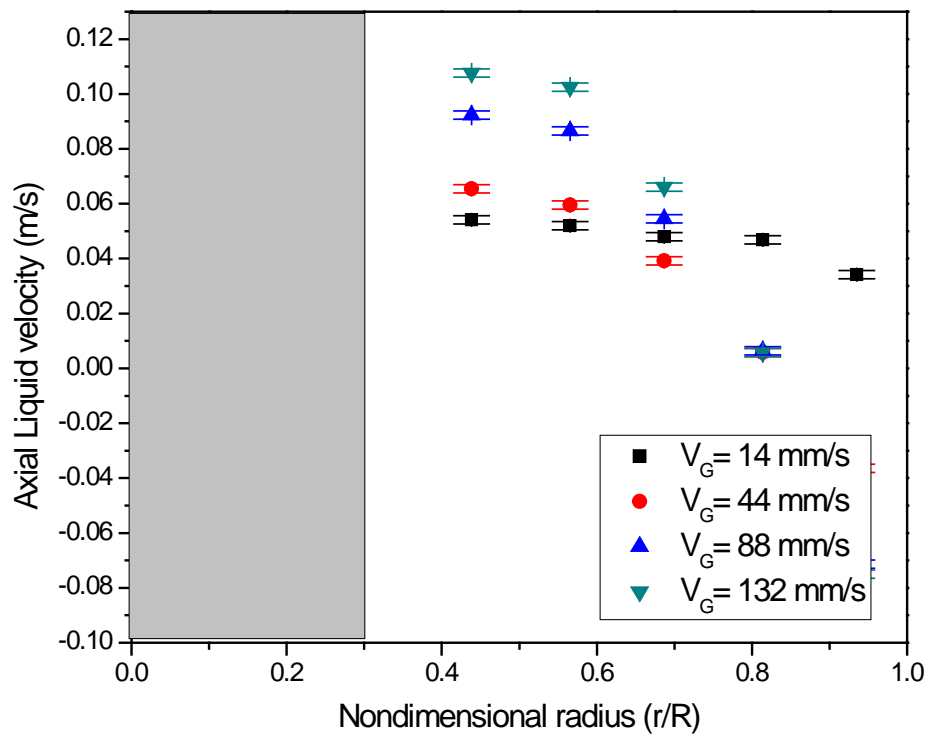


Figure-6.7 Effect of superficial gas velocity on axial liquid velocity for configuration-B

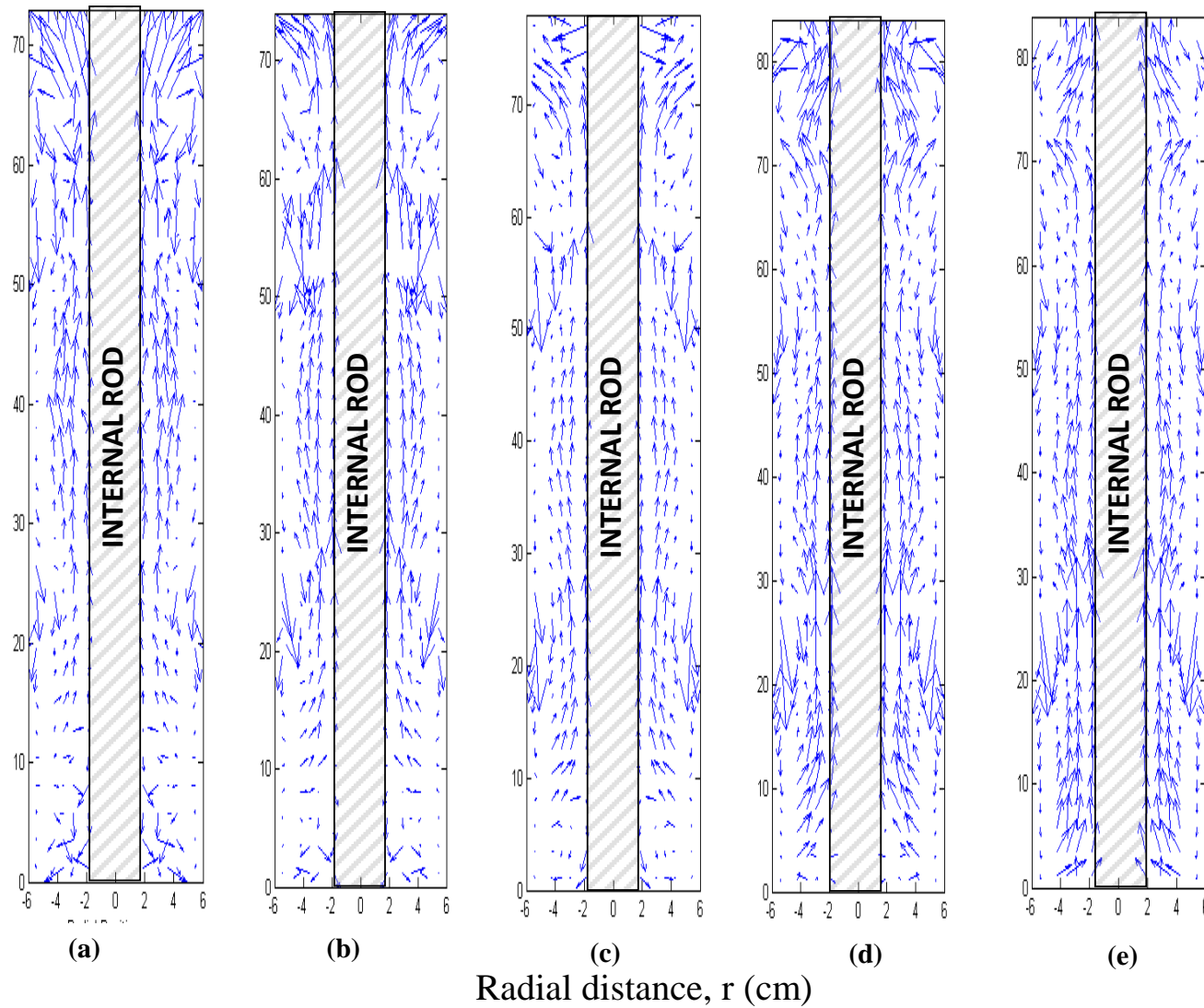


Figure-6.8 Effect of superficial gas velocity on overall flow patterns for Configuration-B:
 (a) 0.014 m/s (b) 0.044 m/s (c) 0.088 m/s (d) 0.132 m/s (e) 0.221 m/s

Turbulent kinetic energy

Figures-6.9 and 6.10 show the turbulent kinetic energy for Configurations- A and B, respectively. In case of Configuration-A, the experimental data shows an increase in the turbulent kinetic energy with an increase in the superficial gas velocity. Turbulent kinetic energy is found to be reasonably increased at lower superficial gas velocities in the column including internals. While the turbulent kinetic energy reduces significantly at higher superficial gas flowrates in the bubble column including internal (Configuration-B).

This is because at higher superficial gas velocities, the bubbles have higher slip velocity and they escape the column rapidly. Thus, the reduction of gas hold-up in a column reduces the turbulent fluctuations or turbulent intensity in the column and hence, at higher superficial gas velocity, the lower turbulent kinetic energies are obtained in the column.

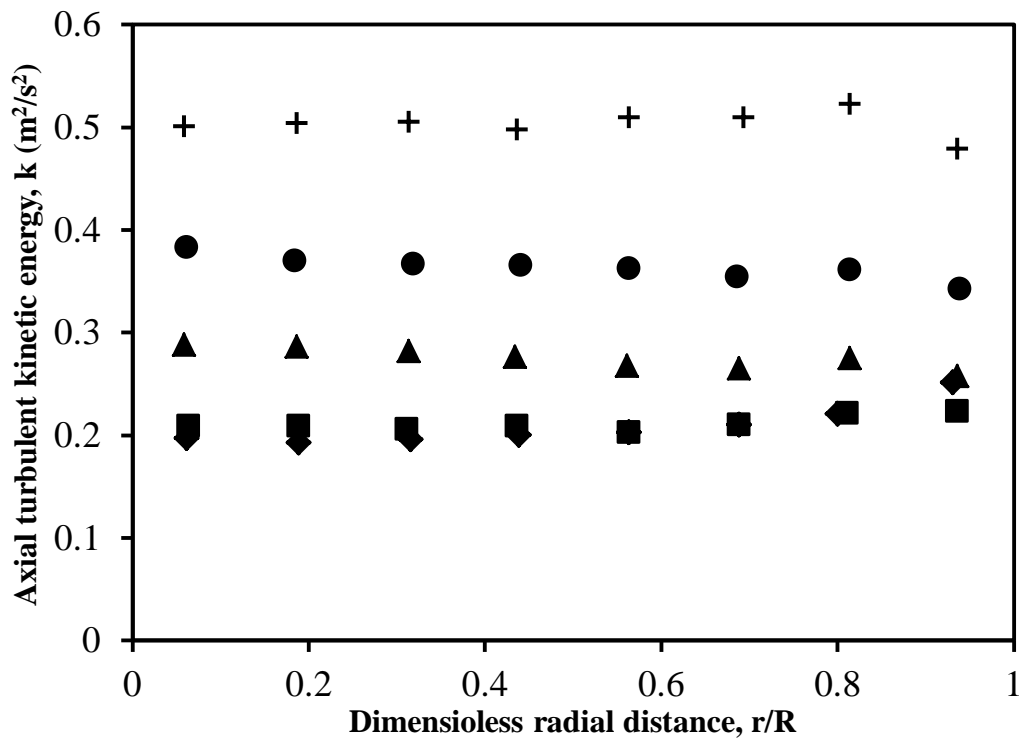


Figure-6.9 Effect of superficial gas velocity [$V_G=0.014$ m/s (♦), $V_G=0.044$ m/s (■), $V_G=0.088$ m/s (▲), $V_G=0.132$ m/s (●), $V_G=0.221$ m/s (+)] on axial turbulent kinetic energy for configuration-A

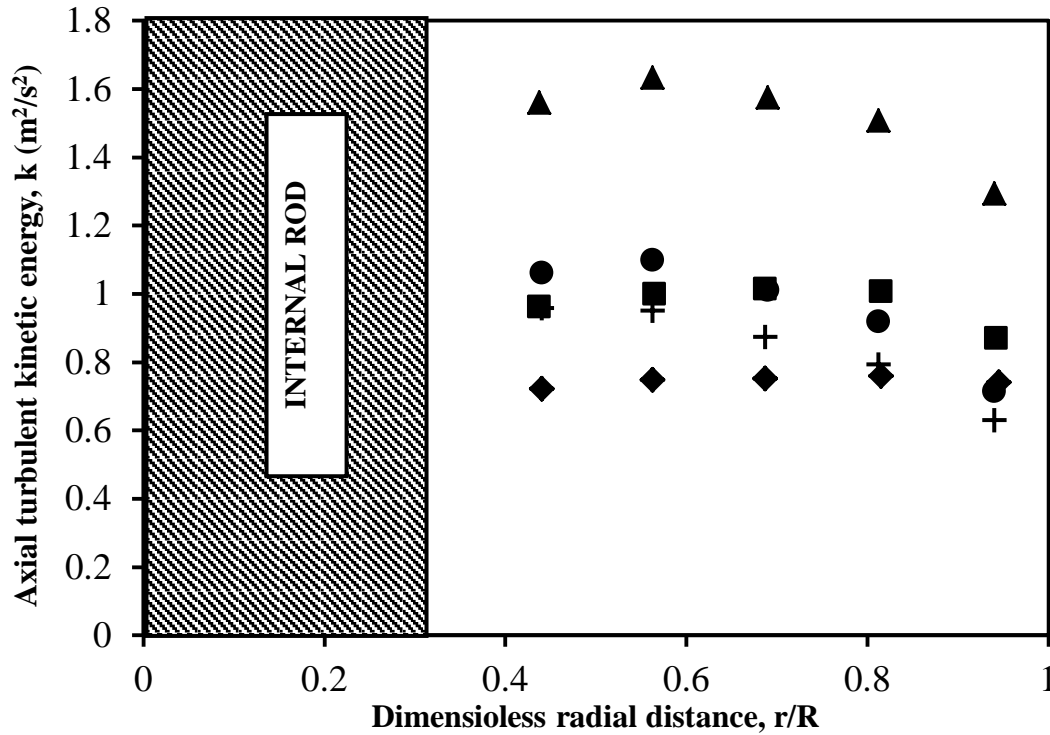


Figure-6.10 Effect of superficial gas velocity [$V_G=0.014$ m/s (♦), $V_G=0.044$ m/s (■), $V_G=0.088$ m/s (▲), $V_G=0.132$ m/s (●), $V_G=0.221$ m/s (+)] on axial turbulent kinetic energy for configuration-B

The turbulent kinetic energy (k) is practically uniform and independent of radial position for all velocities for configuration-A. However, for high velocity flow regime (Figure-6.10) with internals ($V_G > 44$ mm/s), kinetic energy profiles typically exhibit a maximum around the cross-over point for the time-averaged liquid axial velocity, due to the large velocity gradients.

It is observed that the overall flow pattern in the column (i.e., the formation of single circulation cell over the entire length of the column) remains unaffected with the insertion of the internals in the column. It is also observed that the average gas hold-up increases with increase in number of internals. The centerline velocities are found to be decreased with increasing number of internals. The reason behind this is the reduced fluctuations in the column with internals as compared to that of the open column.

6.3 Bubble column simulation using OpenFOAM

CFD model for adiabatic simulations inside the bubble column is developed on the Open FOAM platform. The details of the model are discussed in chapter-5. The model has been validated with experimental data (Hill, 1974) available in the literature and the RPT experiments conducted in open bubble column discussed in section 6.2. Table-6.2 shows the models selected for simulation of the bubble column.

Table-6.2 Phase interaction models used for simulation for Hill's and RPT experiment

Closures	Terms modelled	Empirical model used
Momentum Closure		
	Drag	Schiller Naumann (1935), Ishii Model (1979)
	Turbulent Dispersion	Burns (2004)
	BIT	Sato (1979)
	Lift	$C_L = 0$
	Wall Lubrication	Not Considered
Turbulent Model		k- ϵ for mixture
Solver		Two Phase Euler FOAM

6.3.1 CFD code validation with literature data

To model the bubble column, Hills (1974), the open source code Open FOAM-2.3.1 (Open FOAM, 2014) has been used. Mesh was generated using the open source code g-mesh. Physical dimension of the computational domain is 138 mm x 138 mm x 1370 mm. The diameter of the bubble column under consideration is 138 mm and length is 1370 mm. Experimental data for the void distribution and liquid velocity profile at a plane of $H/D=4.34$ is available for comparison of the CFD results. Details of experimental work are given in Table-6.3:

Table-6.3 Details of Hill's experimental setup

Diameter of column	138mm
Height of column	1.37 m
Sparger	0.4 mm sieve
Measurements	Axial liquid velocity and holdup at $H/D=4.34$
Measurement techniques:	Electro conductivity needle probe for hold up and Pavlov tube for liquid velocity

CFD simulations for superficial gas velocities of 38, 64 and 95 mm/s have been carried out and compared with the experimental data.

Mesh generation and grid sensitivity

Figure-6.11 shows the mesh generated for the bubble column under consideration. The mesh prepared is hexahedral indexed for finer mesh towards wall and inlet/outlet.

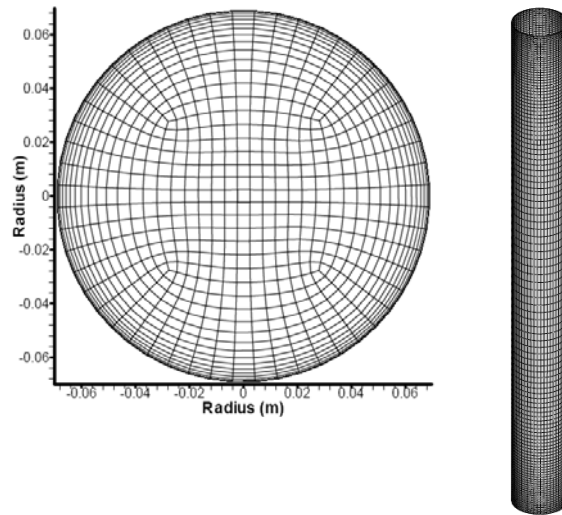


Figure-6.11 Mesh for Hill's case

The quality of the mesh plays a significant role in the accuracy and stability of the numerical computation. In this work, two-fluid Euler-Euler approach is used, which allows to use coarse grid in the core of the flow. Interfacial models selected for the simulations are described in Table-6.2. Here Ishii drag model is assumed for modeling the drag force. Near the wall, it is important to capture wall effects and also to capture minimum liquid velocity point near wall, which is important for accurate estimation of mass balance in the column. In order to capture these effects, the grid size used near the wall is very fine. In this regard the grid sensitivity is studied for the bubble column of Hills (1974). In this work, grid sizes of 200K, 240K, 280K, and 320K are used. In the corresponding mesh core region is set upto radial distance of 0.06 m and wall effects are measured in 0.009 m section between wall and core region. In all of these meshes, grid size in the core region was kept constant and the grid size near the wall was varied (5, 10, 14 and 20 mesh points for 200K, 240K, 280K and 320K respectively). Figure 6.12, 6.13 and 6.14 show the

variation of axial liquid velocity for simulation of the Hill's bubble column for 38mm/s, 64mm/s and 95mm/s respectively. One more grid sensitivity study was carried out for 64mm/s gas velocity with no lift force. In Figure-6.15, lines 1, 2, 3 and 4 represent the predictions of the axial liquid velocity by using grid size of 200K, 240K, 280K, and 320K, respectively with Schiller Naumann drag. The liquid velocity predictions from lines 2 and 3 shows that the velocities are under predicted and hence, there was discrepancy in the gas phase and liquid phase mass balance (discrepancy upto 22% of the central upward volumetric flow rate). While lines 1 and 4 represent very good agreement with the experimental data. In case of line 1, the total mass balance was not satisfied (discrepancy upto 15% of the central upward volumetric flow rate), whereas the discrepancy in gas and liquid phase mass balances was less than 5% then the central upward volumetric flow rate in case of line 4. Hence, the final grid size used for simulation was 320K with Schiller Naumann drag law.

Method of solution

Open FOAM 2.3.1 has been used as the platform for solution and estimation of flow field inside a bubble column. The overall structure of Open FOAM is displayed in Figure-6.16. Details of the modeling are discussed in chapter-5. Two Phase Euler FOAM solver is readily available in Open FOAM 2.3.1 based on the work of Rusche (2002). Here modified two phase Euler foam solver is used which utilizes the PIMPLE (PISO+SIMPLE) algorithm for pressure and velocity linked equations. Finite Volume Method is used for solving the ensemble average equations of mass and momentum conservation. k - ϵ turbulence model for mixture, as discussed in section 5.5 of chapter-5, is selected for the simulations. Figure-6.17 show the details of the solution methodology adopted for simulation.

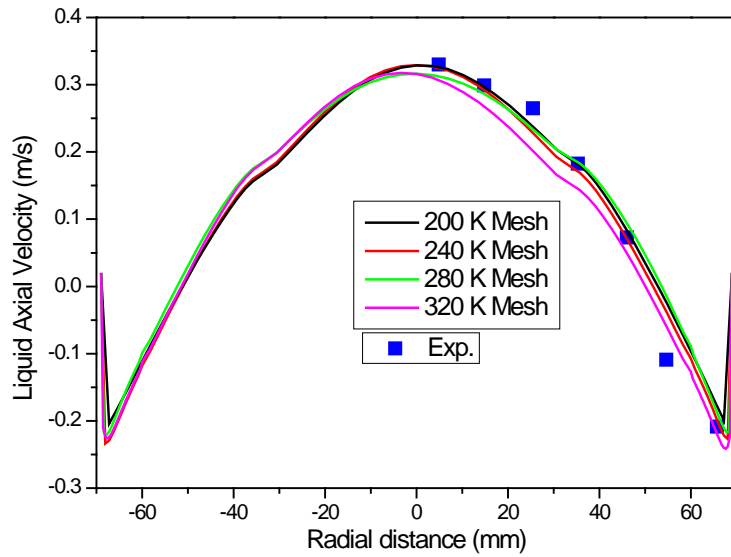


Figure-6.12 Grid sensitivity for Hills (1974) at $V_G=0.038$ m/s

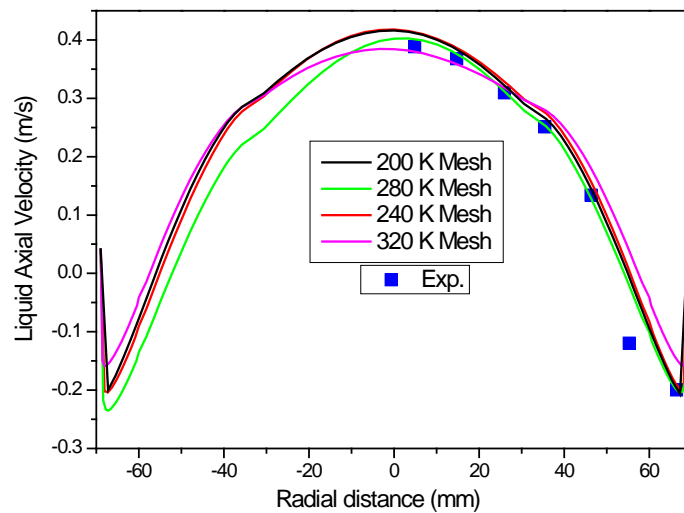


Figure-6.13 Grid sensitivity for Hills (1974) at $V_G=0.064$ m/s

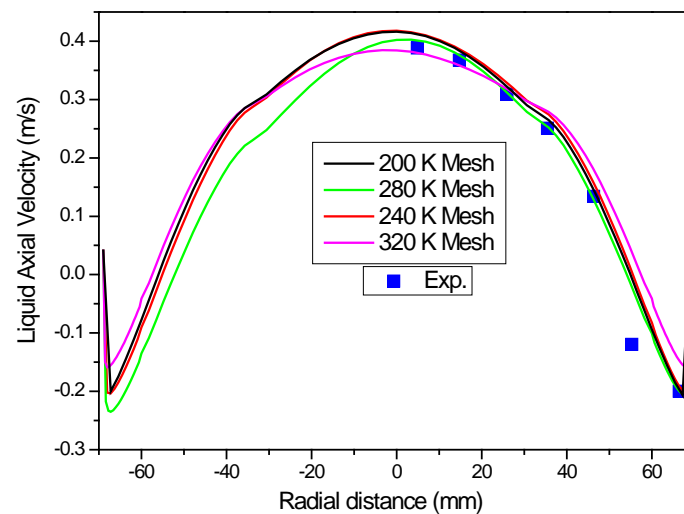


Figure-6.14 Grid sensitivity for Hills (1974) at $V_G=0.095$ m/s

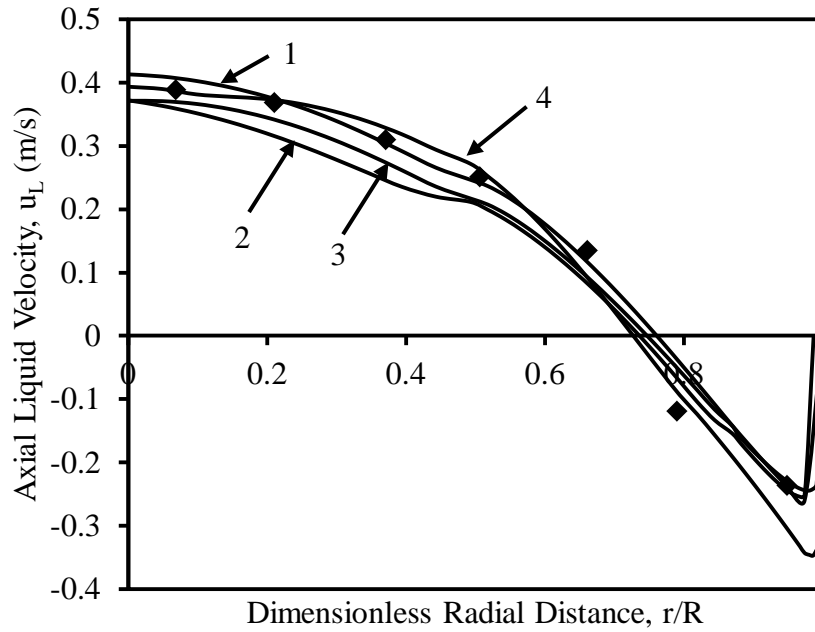


Figure-6.15 Effect of grid sensitivity (64mm/s with Schiller naumann Drag)

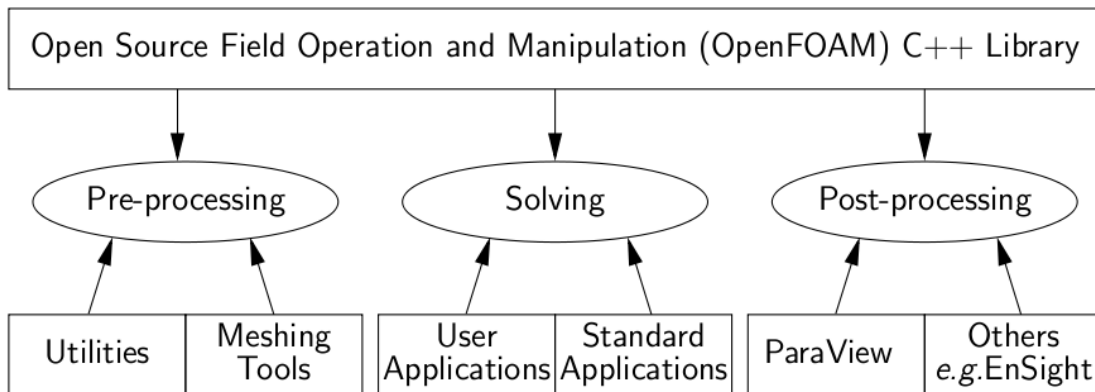


Figure-6.16 Overview of OpenFOAM structure

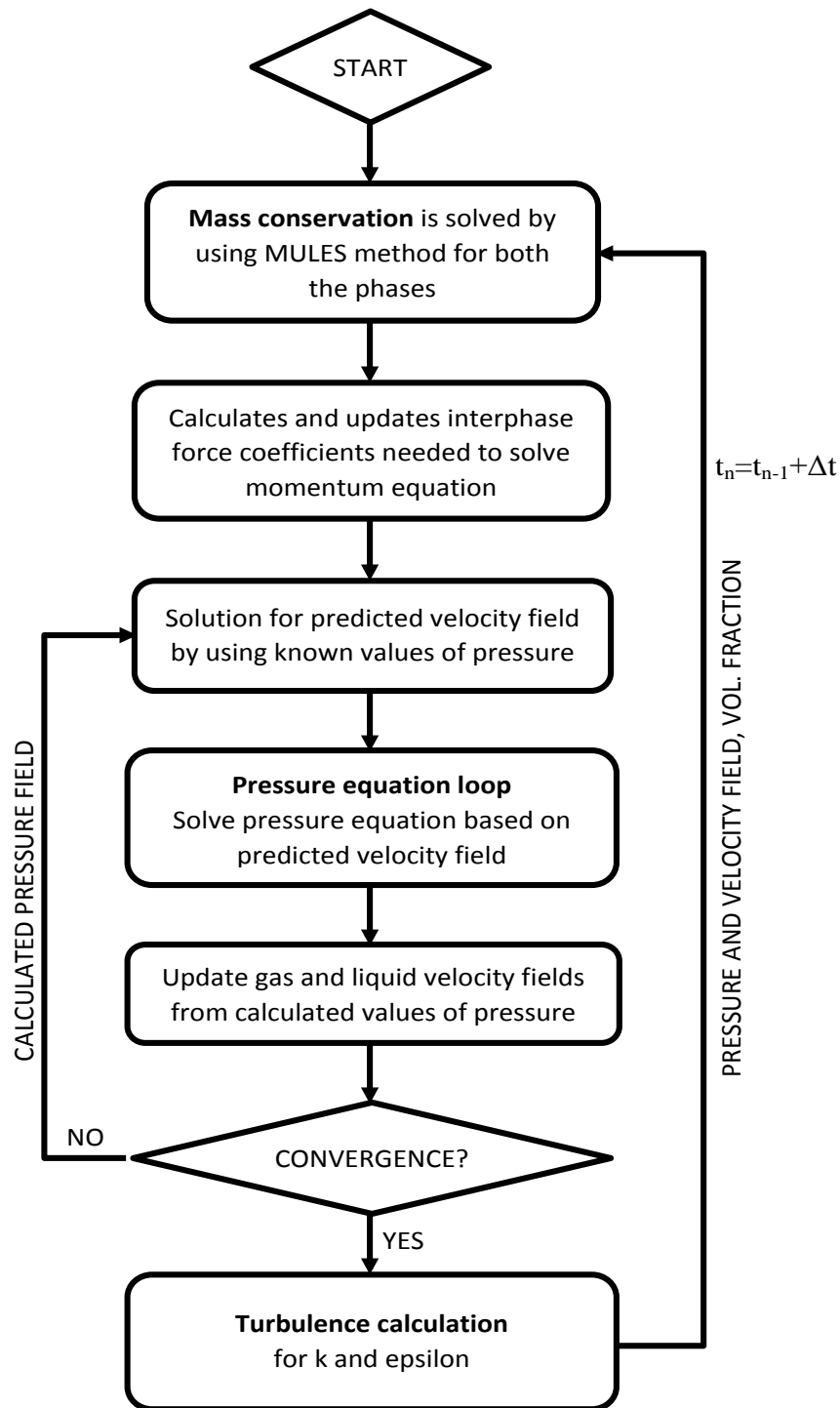


Figure-6.17 PIMPLE algorithm for twophase Euler Foam

Boundary conditions

Inlet boundary conditions

At the inlet, the gas hold-up/void fraction was modeled through non-uniform inlet void fraction. The need for adapting this kind of boundary condition arises due to the elimination of actual sparger design at the inlet. Using non-uniform boundary condition instead of uniform boundary condition at the inlet has advantages, like, (i) Non-uniform inlet hold-up and gas velocity are actual representation of the sparger conditions, which is not the case in uniform inlet hold-up and velocity. Hence, using non-uniform inlet boundary conditions gives us relaxation over making complex sparger geometries. (ii) using simple geometries reduces the overall number of grids used for the simulation and hence, computational time. The expression for the inlet gas hold-up is given by using *groovy* boundary conditions (one of the utility in the OpenFOAM). In order to define the gas hold-up boundary condition at the inlet the correlation proposed by Vitankar and Joshi (2002) was used, which is:

$$\epsilon_G = \frac{m+2}{m} (\bar{\epsilon}_G - \epsilon_W)(1 - \eta^m) + \epsilon_W \quad \dots \dots (6.5)$$

Where, η = dimensionless radial distance

m = the steepness parameter (Luo and Svendsen, 1991)

$$\eta = \frac{r}{R}$$

$$m = 2.188 \times 10^3 \text{Re}_G^{-0.598} \text{Fr}_G^{0.146} \text{Mo}_L^{-0.004}$$

$$\text{where,} \quad \text{Re}_G = DV_G(\rho_L - \rho_G)/\mu_L$$

$$\text{Fr}_G = V_G^2/gD$$

$$\text{Mo}_L = g\mu_L^4/(\rho_L - \rho_G)\sigma_L^3$$

- a. The boundary condition for inlet gas velocity was given as a *fixedValue*. The radial and theta component of gas velocities is given as zero. The axial component was given as a slip velocity

of gas at inlet based on the superficial gas velocity and the averaged gas hold-up at the corresponding gas flow rates.

- b. Since it is a batch type of bubble column, the inlet liquid velocity boundary condition was given as fixed value of zero.
- c. The inlet boundary condition for pressure was *fixedFluxPressure*. This boundary condition adjusts the pressure gradient such that the flux on the boundary was that specified by the velocity boundary condition.
- d. The inlet boundary condition for turbulent kinetic energy (k) for air was given as the *fixedValue*, with the uniform value equal to that of calculated from following equation:

$$k = \frac{3}{2}(u_i I)^2 \quad \dots \dots (6.6)$$

where, u_i is the mean flow velocity of gas at the inlet and I is the turbulent intensity.

- e. In case of turbulent energy dissipation rate (ϵ), at the inlet the values of ϵ are calculated by using following formula:

$$\epsilon = \frac{C_\mu^{3/4} k^{3/2}}{l} \quad \dots \dots (6.7)$$

where, C_μ (=0.09) is the turbulent parameter that relates turbulent viscosity with k and ϵ , l is the turbulent length scale, which is equal to the column diameter for cylindrical columns.

Outlet boundary conditions

- a. At the outlet, *inletOutlet* boundary condition was used for gas hold-up. The *inletOutlet* boundary condition is normally the same as *zeroGradient*, but it switches to *fixedValue* if the velocity vector next to the boundary aims inside the domain (backward flow). The value of that fixed value was inlet value, which is 1 in this case.
- b. For outlet gas velocity, *pressureInletOutletVelocity* boundary condition was used. The *pressureInletOutletVelocity* boundary condition is a blend of *pressureInletVelocity* and *inletOutlet* boundary conditions. The *pressureInletVelocity*, velocity is computed from

difference between total and static pressure where the direction is normal to the patch faces.

This boundary condition can be described as at velocity *inletOutlet* boundary condition patches for where the pressure is specified and *zero-gradient* is applied for outflow (as defined by the flux) and for inflow the velocity is obtained from the patch-face normal component of the internal-cell value.

- c. At the outlet, *fixedValue* pressure boundary condition was used and the value is set to the atmospheric pressure.
- d. The outlet the boundary condition for k given by using Eq. (6.6) at mean flow velocity at outlet.
- e. At the outlet, the values of ϵ is calculated by using Eq. (6.7).

Wall boundary conditions

At the wall, *fixedValue* boundary condition was used for the fractional gas hold-up. The wall hold-up at the wall was taken as zero. For both, the inlet gas velocity and liquid velocity, *fixedValue* boundary condition was used with the value of zero (corresponding to the initial phase fraction of the water at inlet). For pressure *fixedFluxPressure* boundary condition is used. At the wall, the boundary condition for k was given as fixed value of zero, which is in correspondence with the phase velocity at the wall. Near the wall function of type *kqRWallFunction* is used. This works exactly in the same way as that of the zero gradient. Similarly, for ϵ also the fixed value of zero was used as a boundary condition at the wall. Near the wall, the *epsilonWallFunction* was used, where the value of the ϵ is calculated by using following formula:

$$\epsilon = \frac{C_{\mu}^{3/4} k^{3/2}}{\kappa x} \quad \dots \dots (6.8)$$

where, κ is the kappa having value of 0.41 and x is the distance to first node from the wall.

Similar boundary conditions have been employed for liquid phase turbulent kinetic energy also.

Internal field

The initial fields into the internal domain, corresponding to initial liquid height, were set by using *funkySetFields* utility in OpenFOAM. It reads fields from the file *funkySetFieldDict* and after recalculating, writes them back to the boundary file. The initial phase fraction for gas phase was set to the values of the average gas and liquid hold-up in a column upto initial liquid height. Above that the liquid phase fraction was taken to be zero and hence, gas phase fraction was 1. In a similar way, actual velocity based on fractional gas hold-up was set as a gas phase velocity in the region of stable liquid height. The region where gas phase fraction is 1, the superficial velocity was set as a gas velocity for the internal field. Pressure in the internal field of the column was set as a hydrostatic pressure. All the above boundary conditions are summarized in Table-6.4.

Table-6.4 Boundary conditions used in the simulations

Boundary field	Inlet	Outlet	Wall
Gas phase fraction	<i>Groovy BC</i>	<i>inletOutlet</i>	<i>fixedValue</i>
Gas velocity	<i>fixedValue</i>	<i>pressureInletOutletVelocity</i>	<i>fixedValue</i>
Liquid velocity	<i>fixedValue</i>	<i>fixedValue</i>	<i>fixedValue</i>
Pressure	<i>fixedFluxPressure</i>	<i>fixedValue</i>	<i>fixedFluxPressure</i>

Results and discussions

Simulations were performed with an air injection, at the superficial velocities of 38, 64 and 95 mm/s, in the column filled with the water (initial water height of 0.9 m). Comparisons for axial liquid velocities and the gas hold-up profiles between the experimental data and the OpenFOAM predictions shown in Figures-6.18 and 6.19 show very good agreement (standard deviation of less than 2% and 3%, respectively for axial liquid velocity and gas hold-up). From Figure-6.18, it can be observed that the centerline velocity of the liquid phase increases with an increase in the superficial velocity of the gas. Figure-6.19 shows the comparison for gas hold-up at different superficial gas velocities. It is observed that there is maximum gas hold-up in the center of the

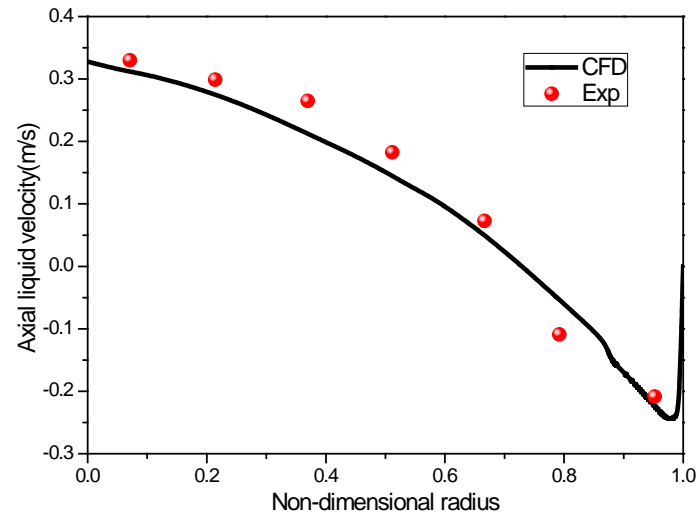
column, while gas hold-up tends to practically zero near the wall. The centerline hold-up increases with an increase in the superficial gas velocity. Figure-6.20 shows the typical void and velocity field inside the bubble column for 64mm/s gas velocity.

It is evident from the results that the solver developed in OpenFOAM platform is able to capture two phase phenomena happening inside the bubble column and predict the hold up and liquid velocities well within $\pm 5\%$ range. After getting CFD predictions, it was thought desirable to establish gas and liquid phase balance. At any cross-section, the following equations hold:

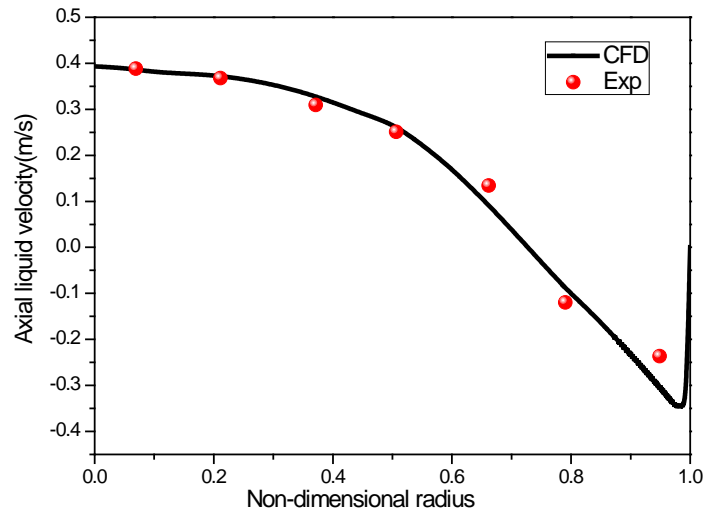
$$Q_G = \int_0^R u_G \epsilon_G 2\pi r dr \quad \dots \dots (6.9)$$

$$Q_L = \int_0^R u_L \epsilon_L 2\pi r dr \quad \dots \dots (6.10)$$

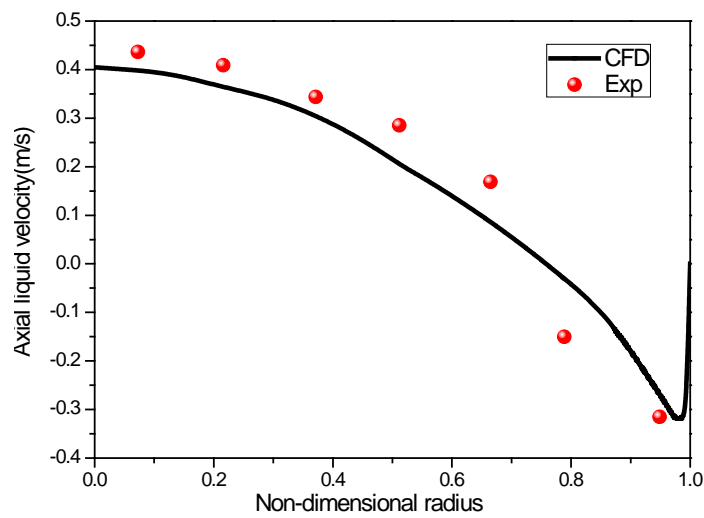
As per Eq. (6.9), the predicted values of Q_G are found to be consistent with corresponding values of superficial gas velocity of 38 mm/s, 64 mm/s and 95 mm/s for which simulations were performed. The value of Q_L (Eq. (6.10)) is found to be practical zero (less than 5% then the central upward volumetric flow rate). It can be observed from Figure-6.21 and 6.22 that the mass of the gas and liquid is conserved during the simulation.



(a)

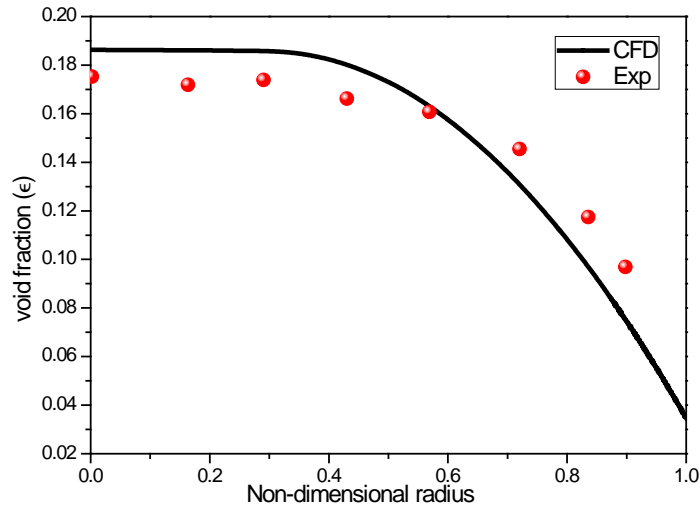


(b)

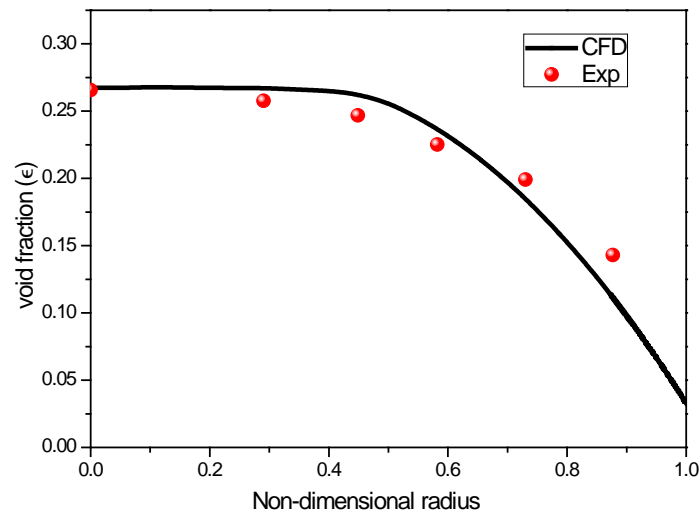


(c)

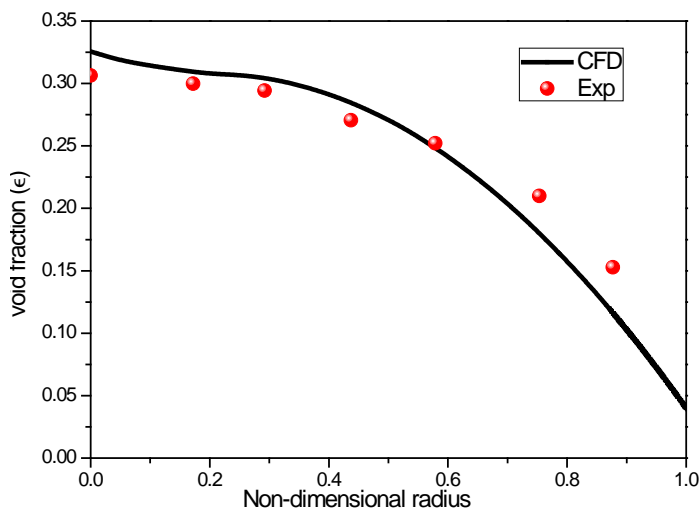
Figure-6.18 CFD validations for Hills (1974) experimental data for axial liquid velocity by using OpenFOAM at (a) 38 mm/s, (b) 64 mm/s and (c) 95 mm/s



(a)



(b)



(c)

Figure-6.19 CFD validations for Hills (1974) experimental data for gas hold-up by using OpenFOAM at (a) 38 mm/s, (b) 64 mm/s and (c) 95 mm/s

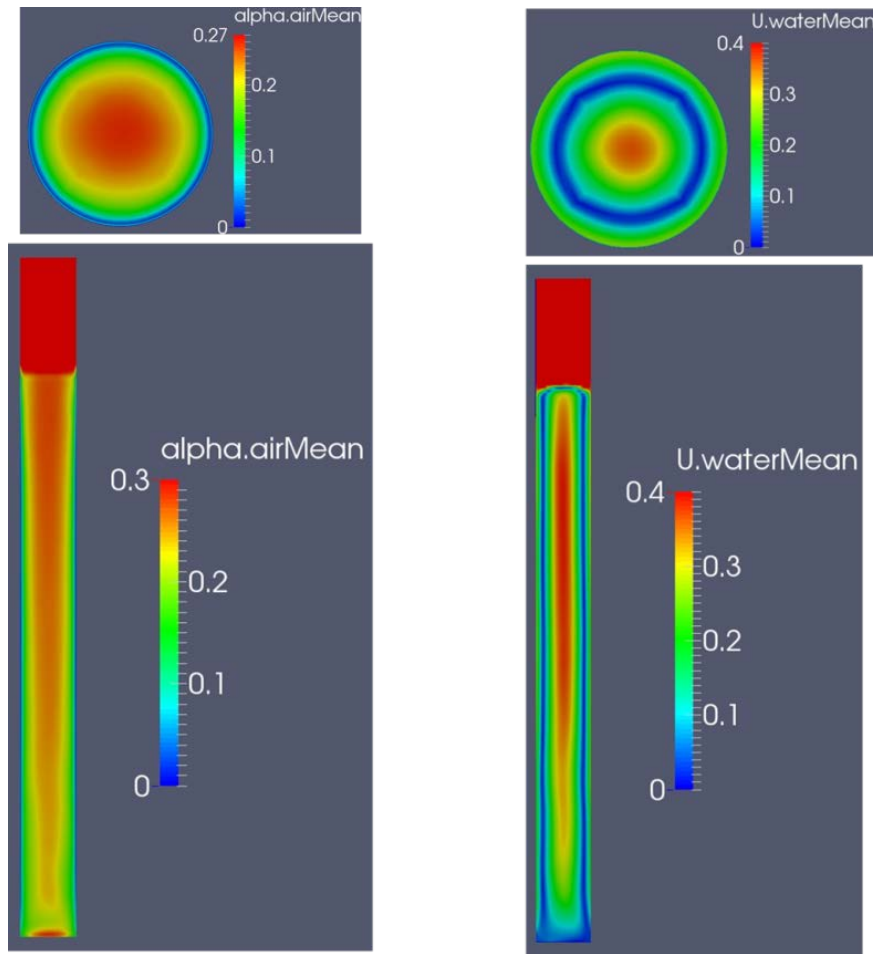


Figure-6.20 Typical holdup and liquid velocity profile @64mm/s

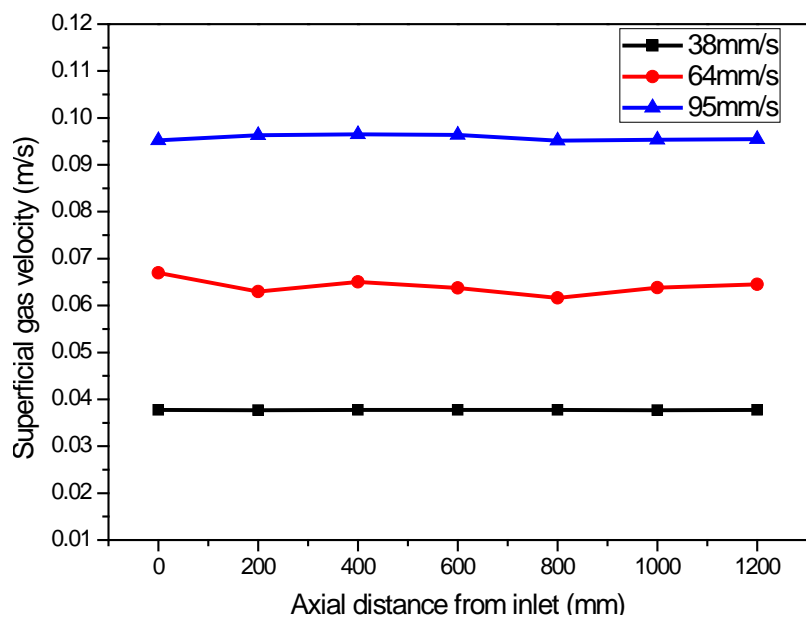


Figure-6.21 Gas Mass balance (Axial variation of superficial gas velocity)

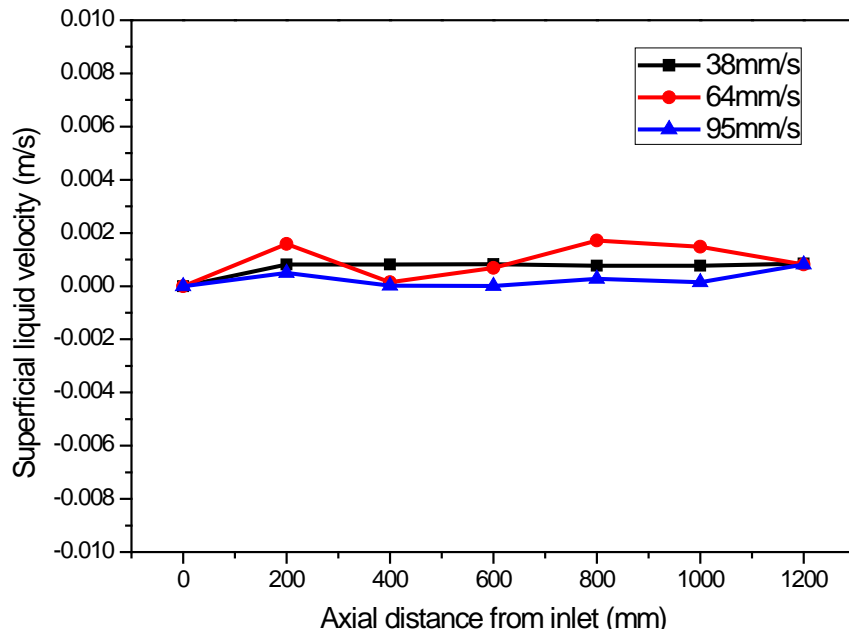


Figure-6.22 Liquid Mass balance (Axial variation of Liquid velocity)

6.3.2 CFD code validation with RPT data

The column under consideration is made of acrylic having height 1.2 m with internal diameter of 120 mm. In the present work, one central rod having outer diameter of 36 mm is considered as internals inside the column. Two different configurations were used in the study viz. Configuration-A column without internal and configuration-B column with one central rod. In these cases, the initial liquid height was maintained at 655 mm. The simulations were performed by using air as the sparged gas and water as the liquid phase. The air volumetric flow rate was set as 10 LPM and 90 LPM which corresponds to the range of superficial air velocity of 14 mm/s to 132 mm/s for two percentages of covered cross sectional area: 0% (no internals, configuration-A) and 9% (configuration-B) as shown in Figures-6.4a and 6.4b, respectively. Figure-6.23 shows the grids used for the simulations of the bubble column two configurations.

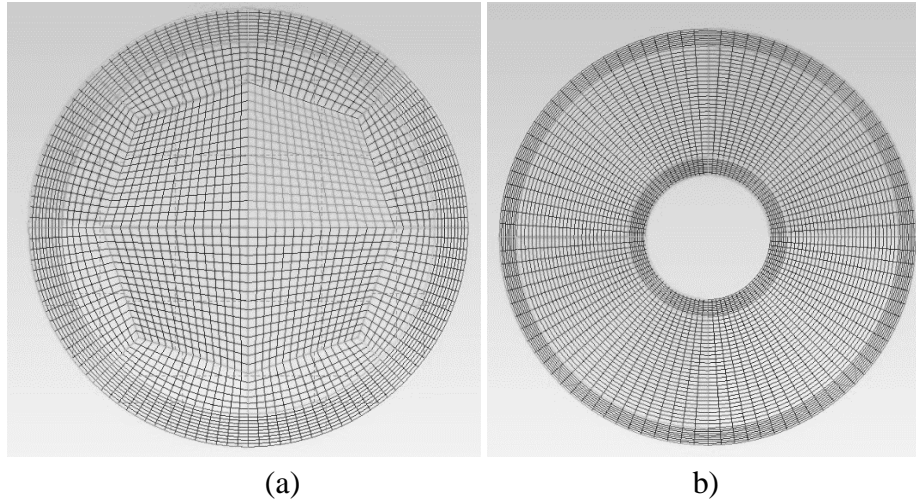


Figure-6.23 Grid size used for simulations (a) Configuration A; (b) Configuration B

Simulations for the two velocities have been performed in the work undertaken. The simulations were performed for gas superficial velocity of 14mm/s and 132mm/s. These were chosen so as to see the predictive ability of CFD for low to higher velocities. Same CFD models and platform as for the Hill's case was chosen for the simulation purposes.

Results and discussions

The results for CFD simulations are compared with the experimental data obtained from Radioactive Particle Tracking (RPT) and are shown in Figure-6.24 and 6.25 for configuration-A. The azimuthally averaged axial liquid velocities (Figure-6.24) and radial gas hold-up (Figure -6.25) profiles are plotted against dimensionless radial distance. It is observed that the OpenFOAM shows good agreement (RMS error for 14 mm/s and 132 mm/s predictions are 0.0037 and 0.055 respectively for Configuration-A in axial liquid velocity) with the experimental data. Magnitude of both the axial liquid velocity and the gas hold-up are maximum in the center of the column. Both centerline axial liquid velocity and gas hold-up in the column increase with increase in superficial velocity of the gas. The radial locations of flow reversal are also adequately (within 5%) predicted. Most importantly, the overall material balance as given by Eqs. (6.1) and (6.2) was satisfied within 7 % in the two cases. The technique of RPT has become a useful tool for the measurement of voidage profiles and the liquid phase flow pattern. The technique provides very good accuracy in

the bulk region; however, has relatively less accuracy in the wall region. This is the reason for some disparity in the model at high superficial gas velocities as shown in Figure-6.24b.

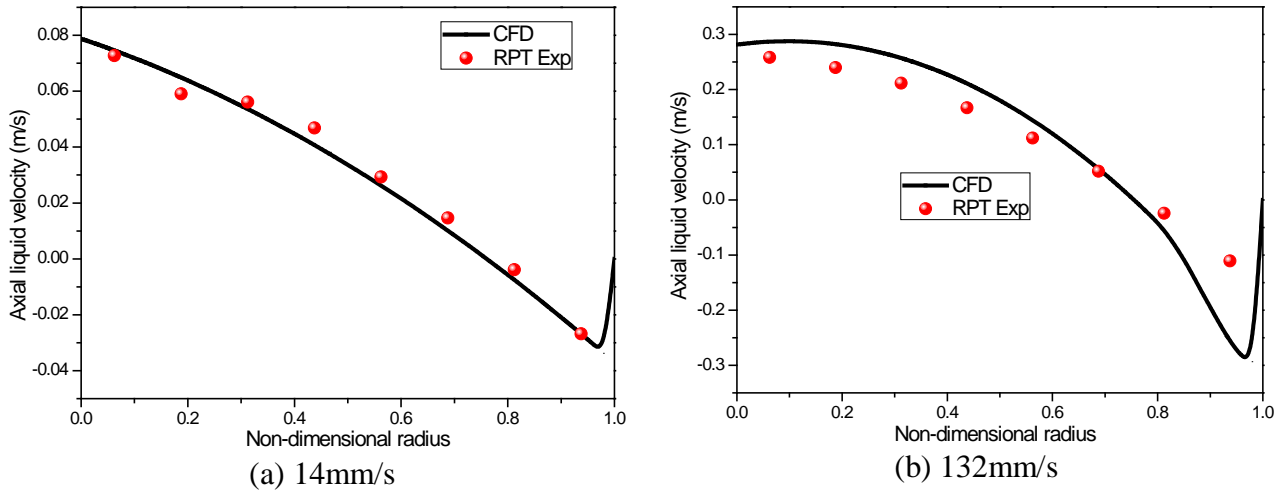


Figure-6.24 Variation of axial liquid velocity profiles for Configuration (A)

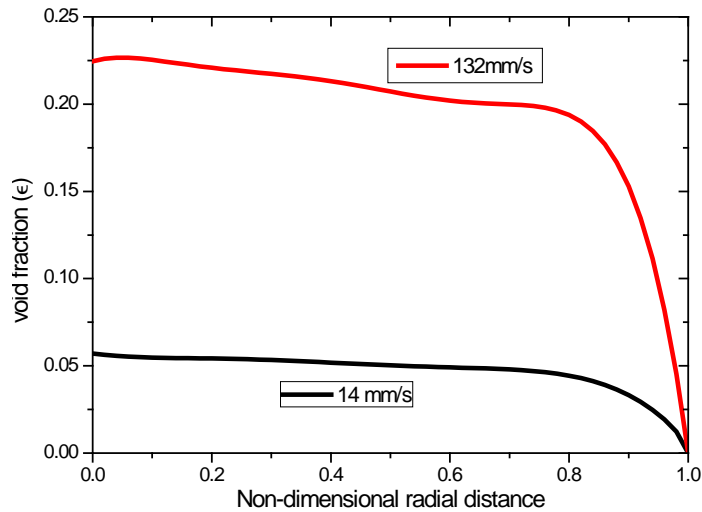


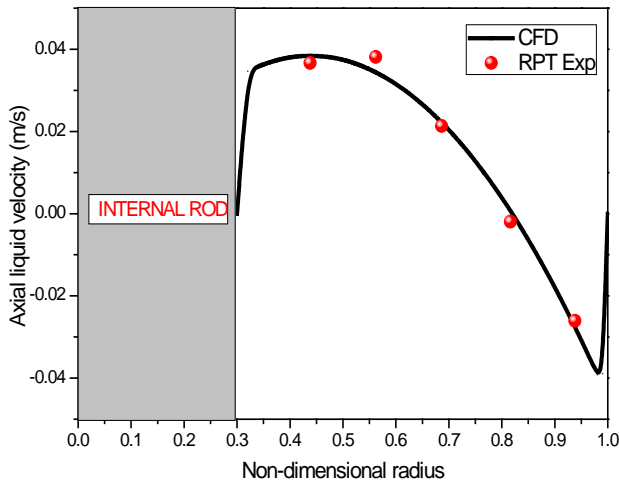
Figure-6.25 Variation of holdup profiles for Configuration (A)

The axial liquid velocity and gas void profiles in the annular space between the column wall and internal tube are plotted in Figure-6.26 and 6.27, respectively. The results were found to be in very good agreement and RMS error for Configuration-B is found to be 0.0018 and 0.0053 for 14 mm/s and 132 mm/s gas velocity predictions. From the profiles of axial liquid velocity, it is observed that the velocity is maximum near the wall of internal tube. The liquid is flowing in the upward

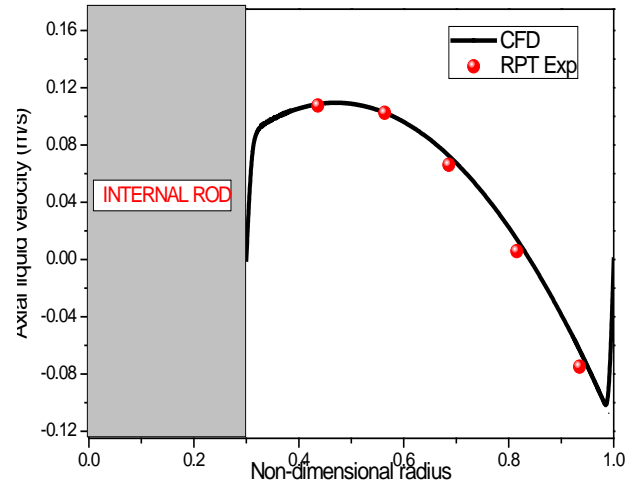
direction in the central region (in the vicinity of internal central tube), while there is a down flow of liquid near the column wall. Thus, the liquid circulation, as observed in the case of Configuration A, still persists even in the presence of central rod. Thus, adding 9% of internals (Configuration- B) in the column does not affect the quality of flow patterns in the bubble column. Similar observations are made in case of gas hold-up also. The gas hold-up is maximum at the central region and decreases with the increase in radial distance in the presence of internals and has no significant effect on overall gas hold-up.

Turbulent kinetic energy

Figure 6.28 shows the comparison of the turbulent kinetic energy for configurations A and B. In both cases, the CFD predictions of k show reasonable deviation (standard deviation of 15-200%) from the experimental data. This is because of the isotropic assumption of the k - ϵ model, which results in a poor representation of the normal stress and hence turbulent kinetic energy. Because only these normal stresses contribute to the total turbulent kinetic energy. The isotropic assumption leads to a limitation to the normal stresses, that all the normal stresses are equal to each other and hence inaccurate predictions of k . The CFD simulations were found to give good prediction of data especially at the lower velocity of the liquid in column without internal. CFD is not able to capture the phenomena at higher velocities with internals. Turbulent kinetic energy obtained from the two-phase k - ϵ formulation arises from the turbulence microscale, while that obtained from RPT experiment arises from relatively larger scales. (For example, it is estimated that the “RPT tracer particle” cannot respond to the turbulence fluctuations above 50 Hz in frequency). It seems that a meaningful comparison of kinetic energy cannot be made as they are not of the same scale at higher gas velocities with internals.



(a) Air velocity 14mm/s



(b) air velocity 132mm/s

Figure-6.26 Variation of axial liquid velocity profiles for Configuration (B)

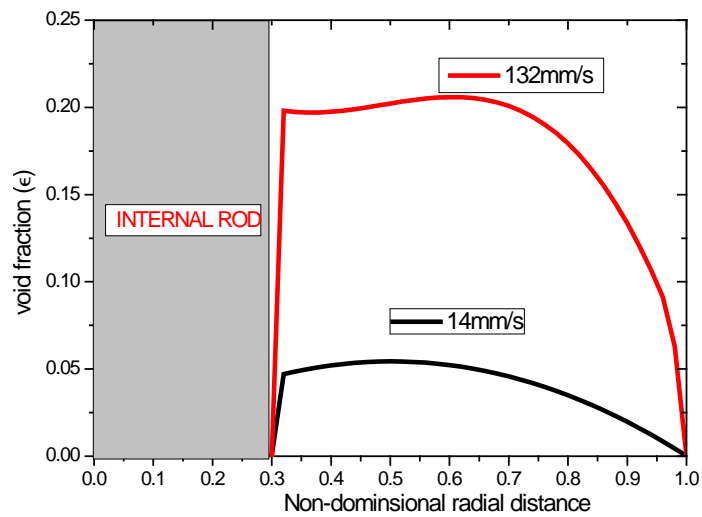


Figure-6.27 Variation of holdup profiles for Configuration (B)

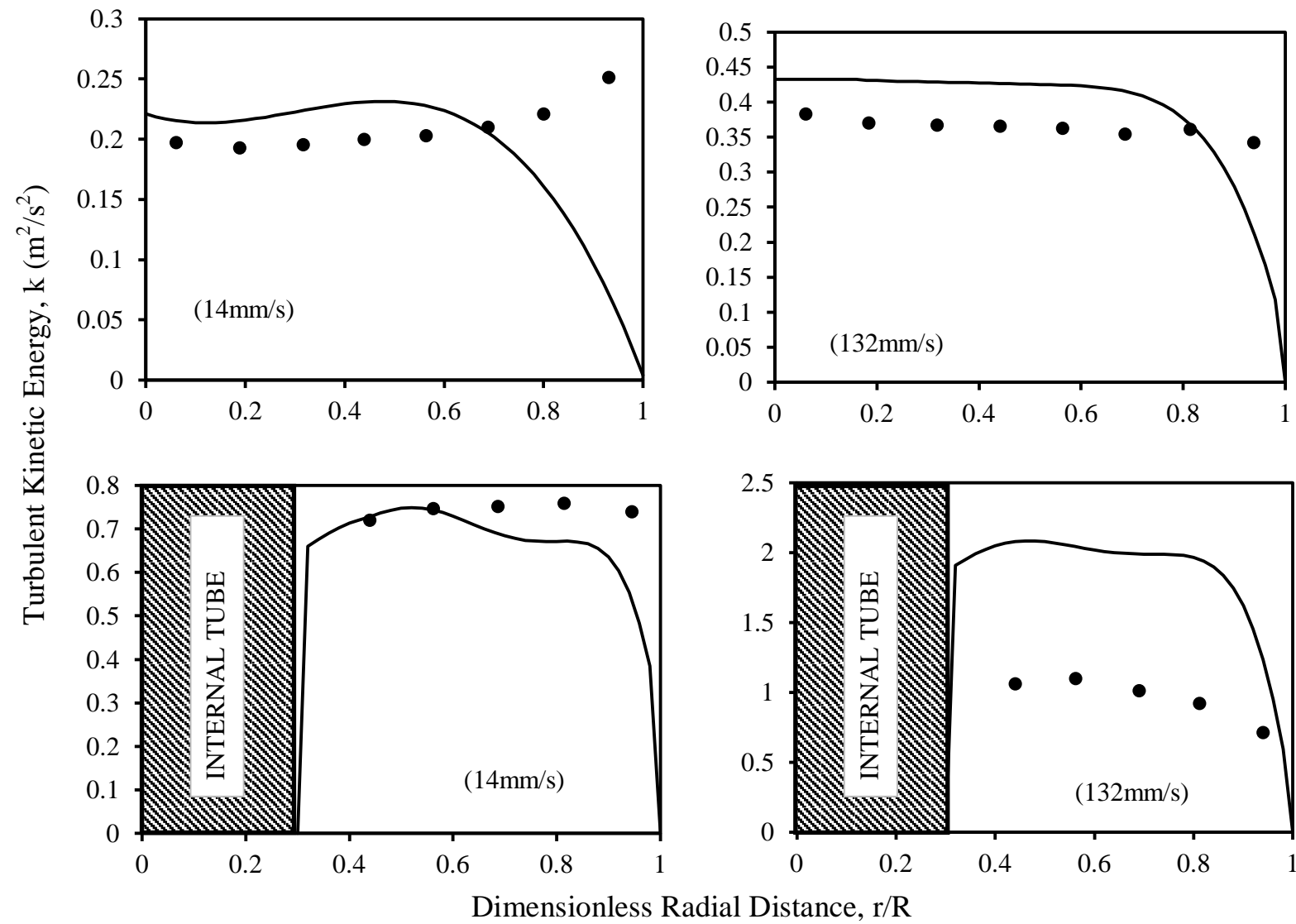


Figure 6.28 Turbulent kinetic energy for Configuration (A) and (B)

6.4 Closure

Experiments have been carried out inside a bubble column of 120mm ID (same size as pressure tube of AHWR) with RPT. Experiments showed that the overall flow pattern in the column (i.e., the formation of single circulation cell over the entire length of the column) remains unaffected with the insertion of the internal in the column. It was also observed that the average gas hold-up increases with increase in number of internals. The centerline velocities are found to be decreased with increasing number of internals. The reason behind this is the reduced fluctuations in the column with internals as compared to that of the open column.

The experiments with RPT were conducted at atmospheric conditions. Bubble dynamics that includes bubble generation, growth, size and detachment depends upon the operating conditions of the system viz. flow velocity, system pressure, temperature etc. Besides, it also depends upon the physical conditions of the bounding surface e.g. heater surface, wall of the conduit and sparger design. Bubble formation and detachment at atmospheric pressure has been experimentally and theoretically studied extensively. This process is assumed to happen in two stages (i) bubble expansion at the crevice or orifice and (ii) bubble detachment due to buoyancy or gas phase momentum. The bubbles generated at atmospheric pressure usually remain spherical in shape. In nuclear reactors, the similar situation is encountered during LOCA or low pressure operations during SBO. The other important point is the rates of coalescence and break-up. These rates are expected to be different for air water system (at atmospheric pressure) as compared with steam water system at elevated pressures. Air-water experiment conducted at low pressure provides insights into the phenomena occurring in reactors at low pressure and data so generated can be useful for validation of the CFD models during such conditions.

At elevated pressures, this process gets modified significantly due to change in properties (surface tension, density of dispersed phase, heat transfer properties, rates of break-up and coalescence of bubbles, etc.) of the fluid and resulting into quite different flow. Relatively thinner (elongated

horizontally in vertical pipe flow) and small diameter bubbles travels in the flow domain at lower velocity at higher pressures. Volume of the bubble at detachment decreases significantly at higher pressures while it increases with higher momentum of the gas phase. For validation of the CFD tool for operations at higher pressure the experimental study is must to be conducted at elevated pressures.

Here in this study, the open-source CFD tool OpenFOAM (v2.3.1) is also standardized and validated for the two-phase bubble columns with literature data as well as RPT experimental data.

It is found that the OpenFOAM simulations are in a good agreement with the experimental data.

It is also observed from the predictions that turbulent kinetic energy is not consistence with that of the experimental results. This is because of the isotropic assumption of the k - ϵ model, which results in a poor representation of the normal stress and hence inaccurate predictions of k . Therefore; it is recommended to use RSM for turbulence in two phase flow cases.

CHAPTER-7

Studies on Boiling Flows through Rod Bundle

7.1 Introduction.....	194
7.2 CFD model for boiling conditions	200
7.2.1 CFD Model details	201
7.2.2 Grid generation and grid independence	202
7.2.3 Sub models performance study	204
<i>Turbulence models</i>	204
<i>Bubble generated turbulent</i>	207
<i>Momentum closures</i>	210
<i>Energy closures</i>	213
7.2.4 RELAP modeling for subcooled boiling.....	218
7.3 Application of the model for high pressure boiling simulation	219
7.4 CFD simulation of thermal hydraulic behavior inside rod bundle	221
7.4.1 CFD Model setup for boiling flows inside rod bundle	225
7.4.2 Results and discussions	228
<i>Case#1 (Set-1 models)</i>	228
<i>RELAP simulation for Case#1</i>	241
<i>Case#1 (Set-2 models)</i>	243
<i>Case#2</i>	247
<i>Case#3</i>	253
<i>Case#4</i>	253
7.5 Closure	257

7.1 Introduction

Rod bundles form the basic geometry of the fuel assembly of any nuclear reactor. These bundles contain fuel rod arranged in a certain pattern and pitch, and coolant flows outside these fuel rods. Nuclear fuel is enveloped by a metallic annulus called clad and thus forming the fuel rod. Coolant removes nuclear heat generated in the fuel rods and exchange heat with heat exchangers to generate steam and eventually electrical power. The heat transport system of any nuclear reactor is designed primarily based on the capacity of the coolant to remove nuclear heat without exceeding the clad surface temperature above safe limits.

Experimental data and empirical correlations based on the specific geometry of the fuel bundle for a particular reactor design are utilized for design and safety calculations of the primary heat transport system. Based on the empirical models established for the nuclear reactor systems, state of the art codes are developed for design and safety calculations. These models are essentially one dimensional in nature due to limited computational resources to handle the complete nuclear system. These models so developed frames best estimate codes, which are non-conservative and able to predict physical events in the boiling systems.

It is apparent that these codes are not able to give the detailed picture inside the rod bundle; the information obtained by these codes is averaged at any axial location. In view of this, there may exist a possibility of hot spots inside the rod bundle which may not be captured by one dimensional system codes. In this series, sub-channel analysis codes were the next in development. These codes utilize an engineered treatment of the rod bundles. The whole rod bundle is subdivided into a number of interacting small sub-channels. These sub-channels are either fuel centered or fluid centered. Relatively better picture of the flow field inside the rod bundle now remained available with the designers and safety engineers. However, sub-channel analysis too is one dimensional only additionally solving one transverse equation in the lateral direction. It is also having similar limitations like one dimensional code.

Looking at the recent computational developments happened in the last decade, it has become feasible to attempt for CFD simulations of complex geometries like rod bundles with, of course, several simplifications made in the modeling.

For example, turbulence modeling for rod bundle kind of geometries with tight pitch to diameter ratio is not matured till date. Many researchers have made extensive effort for rod bundle CFD. Baglietto and Ninokata (2005) gave an insight of the turbulence modeling for rod bundles with tight pitch. Authors brought out the relative performances of various turbulence models for calculation of detailed coolant velocity distribution in a tight lattice fuel bundle. They predicted wall shear stress and velocity field, for a fully developed flow inside a triangular lattice bundle and show the importance of proper modeling of the turbulence-driven secondary flows in subchannels. They concluded that inclusion of adequate anisotropy modeling enables accurate reproduction of wall shear stress distribution and velocity field in tight lattice fuel bundles. Liu et al. (2010, 2012) investigated the effects of different types of meshes on the turbulent mixing and heat transfer characteristics, with numerical issues such as mesh refinement, wall treatment and appropriate definition of boundary conditions. Cui et al. (2012) used CFD to evaluate the effects of mixing vane shape on the flow structure and heat transfer downstream in a sub-channel of fuel assembly by obtaining important parameters like velocity and pressure fields, turbulent intensity, flow mixing factors, heat transfer coefficient, and friction factor. Gan et al. (2013) presented the CFD tool capability to predict the velocity field in a $1/4^{\text{th}}$ sector of 17x17 rod bundle. They also did sensitivity studies for turbulent parameters on 2x2 rods sector of the bundle. Lifante et al. (2013) performed CFD simulations in a 3x3 rod bundle. Different geometry configurations were investigated allowing an analysis of the influence of geometry components like the inlet vessel and the grid spacer. With so many issues in modeling of turbulent single phase flows inside rod bundles, considerable work has also happened for two

phase flow CFD. With one's need and affordability of computational cost, researchers have chosen the methodologies for simulations. It is always a desire of a design engineer to look the detailed 3-D picture of the flow and temperature field of the designed system for its performance for further enrichment. But, it is the computational cost and to some extent the modeling issues which limits his way. Here, modeling issues includes preparation of mathematical model expressing the physical phenomena of the system under consideration and closure models. A tradeoff is made between the need and the availability. Since, most of the engineering systems are large in scale (in meters) with high Reynolds number flows; it is only feasible to handle those with averaged models like Euler-Euler approach for the two phases. Considering all resources and modeling frame works, CFD models are mostly being used to simulate bubbly flows with Euler-Euler methodology. Simulation of plug and slug flows is not possible with this Euler-Euler frame work due to highly fluctuating nature of the slug/plug flows, which presents difficulty in averaging. Also, availability of closure models is limited to only bubbly flows with small void fractions. Through all these years of development, CFD has evolved up to a certain level where it can reliably be used to understand complex flow structures in fluid flows.

On the other hand, experiments are also essential for validations of these CFD models. However, Owing to the complex nature of the boiling, it is also challenging to perform experiment at high pressure with sophisticated instrumentation for generation of meaningful data. Fortunately, some notable work is available in literature to cite, which could be used for validation of the CFD models.

It includes experimental study carried out by Bartolomei and Chanturiya (1967) and Bartolomei et al. (1982) on high pressure subcooled boiling in a vertical tube with water as working fluid. They used gamma ray densitometry for measurement of void fraction. They reported axially averaged void and temperature distribution. Their studies covered pressure

ranging from 1.5 MPa to ~150 MPa with subcooling from 20 to close 160 K. Experimental data of Bartolomei and Chanturiya (1967) and Bartolomei et al. (1982) is extensively used for CFD model validations. Garnier et al. (2001) performed experiments with R-12 refrigerant in a vertical tube of 19 mm ID and 3.5 m long. They have reported axially as well as radial profiles for void and velocity fields. Experiments were performed at 1.4 MPa to 3 MPa pressure range. Lee et al. (2002) did tests for low pressure (0.1 MPa) flow boiling with water as the working fluid. They have also measured void and velocity distribution axially as well as in radial directions. Liu et al. (2010) carried out pressure drop studies for flow boiling in vertical tube of 13.4 m length and inner diameter of 11.6 mm at pressure of 15 MPa.

Besides, some experimental work is also available for two phase flow in rod bundle. Anklaam and Miller (1982) did their experiments under high pressure and low flow conditions in an 8x8 rod bundle of PWRs. They reported axial void, velocity and temperature profiles in the experiment during saturated boiling conditions. Mitsutake (1990) estimated the void inside rod bundle with X-ray tomography in a 4x4 bundle and validated the predictions of three-fluid subchannel analysis code TEMPO. In the recent years, Yun et al. (2008), experimentally assessed flow structure of subcooled boiling water flow in a subchannel of 3x3 rod bundles. They did experiments at atmospheric pressure conditions with a mass flow rate, heat flux, inlet temperature, and subcooled temperature ranges of 250–522 kg/m² s, 25–185 kW/m², 96.6 °C –104.9°C, and 2 °C –11 °C, respectively. Arai et al (2015) developed a subchannel void sensor (SCVS) to measure the cross-sectional distribution of void fraction in a 5×5 heated rod bundle and applied to a boiling two-phase flow experiment under the atmospheric pressure condition assuming at an accident or in a spent fuel pool in a boiling water reactor (BWR). Zhang et al. (2017) performed their experimental studies on a 7 rods bundle for flow boiling heat transfer coefficient. With their data, they developed a new correlation that includes Boiling number, Reynolds number and Martinelli number for prediction of two-

phase flow boiling heat transfer coefficients. Here, it is important to note that due to difference in the geometry of the rod bundles of each reactor; experimental studies for particular bundle are required. Changing the pitch and p/d ratio substantially affect the flow field inside the bundle. Concept of hydraulic diameter is also not much appreciated for rod bundles. Considering the aforementioned fact, it is important to conduct experimental study for AHWR rod bundle also, which is right now not in the scope of the thesis, but, taken as the future work and being conducted in BARC. The reactor operates in saturated boiling flow regime with ~70% voiding at channel outlet during normal operations. However, during SBO conditions, the flow inside the coolant channel will fall in subcooled boiling and single phase liquid flow regime. Considering this, the attention has been focused on the subcooled flow boiling. With development of wall heat flux partitioning model for CFD simulations, substantial work has been carried out for CFD simulations of the subcooled boiling. Koncar et al. (2004), Krepper et al. (2007), Koncar and Krepper (2008), Krepper and Rzehak (2011), Murallidharan et al. (2016), Braz Filho et al. (2016) and Colombo and Fairweather (2016) did extensive work for prediction of the subcooled boiling flow behavior using CFD. Koncar et al. (2004) developed new model for local bubble diameter. This model has been validated against experimental data of Lee et al. (2002) for subcooled nucleate boiling of water in vertical annulus at low pressure. Warrier and Dhir (2006) has summarized the empirical correlations and mechanistic heat transfer models for sub-cooled boiling flows. Murallidharan et al. (2016) as well as Cheung et al. (2014) summarized details of several models for bubble departure diameter, nucleation site density and bubble departure frequency. Zhang et al. (2015) studied the effect of different turbulence models on prediction of subcooled boiling flow in vertical tube boiling. Furthermore, Krepper et al. (2013) has incorporated population balance models for more realistic calculations of the bubble departure diameter and utilized it for estimation of the interfacial forces for better and

realistic predictions. Tentner et al (1996) performed CFD studies for rod bundle, Ikeda et al. (2006), Krepper et al. (2007) successfully demonstrated the capability of the commercial code CFX for prediction of the sub-cooled boiling inside fuel rod assembly of a PWR.

The experimental data available in the literature for boiling two phase flows is available as point information inside the flow field, which puts a limitation on validation part of the CFD models. In such a situation, mechanistically developed models can play a key role and CFD can be helpful for understanding the flow patterns/field during the evolution of the boiling flows. Recent studies conducted by Mazzocco et al (2018) addresses the inconsistent assumptions in force balance models and have proposed a new mechanistic model for bubble departure diameter and wall heat partitioning. Hoang et al. (2017) proposed a mechanistic model for complex behavior of wall heat flux partitioning considering the bubble dynamics governed heat transfer mechanism. They have shown that model has a good predictability against experimental data for nucleate boiling at a variety of flow conditions.

Considering the limitations from modeling as well as from computational view point, an attempt has been made for simulating the flow field inside the rod bundle of an advanced BWR. Aftermath of Fukushima, SBO conditions are simulated in the undergone study.

With this background in mind, the chapter deals with the detailed CFD simulations for multidimensional boiling flow over fuel rod cluster (heated rod bundle) of AHWR channel. The simulations are carried out for void and flow distribution inside the rod bundle for three instances during decay heat removal.

A stepwise procedure is followed for simulation of the rod bundle that includes:

- i. Validation of the CFD for boiling conditions (Bartolomei exp. data @ 4.5MPa).
- ii. Checking the applicability of various sub models for predicting boiling and standardization of the models for high pressure boiling.
- iii. Application of the model for high pressure experiment (Bartolomei data @ 6.89MPa).

- iv. Application of the CFD for rod bundle and prediction of the flow field inside rod bundle.

7.2 CFD model for boiling conditions

A CFD frame work has been developed on Fluent v15.0 for predictions of the boiling two phase flows inside rod bundle of AHWR. Details of the models (governing equations and closures) are discussed in Chapter-5. As a first application, this model is validated against the experimental data of Bartolomei (1982) at 4.5 MPa and then further applied to another experiment carried out by Bartolomei at high pressure 6.89 MPa and subsequently to the AHWR rod bundle during SBO conditions. The experimental setup presented by Bartolomei (1982) consists of a 2 m long heated tube (stainless steel tube; 5 mm thick) with an inner diameter of 15.4 mm (Figure-7.1) operating at a constant wall heat flux of 570 kW/m^2 (one of the case). The mass flow rate of water at a pressure of 4.5 MPa amounts to 900 kg/s.m^2 with inlet sub-cool temperature set at 59 K. Table-7.1 shows boundary conditions for the case under consideration.

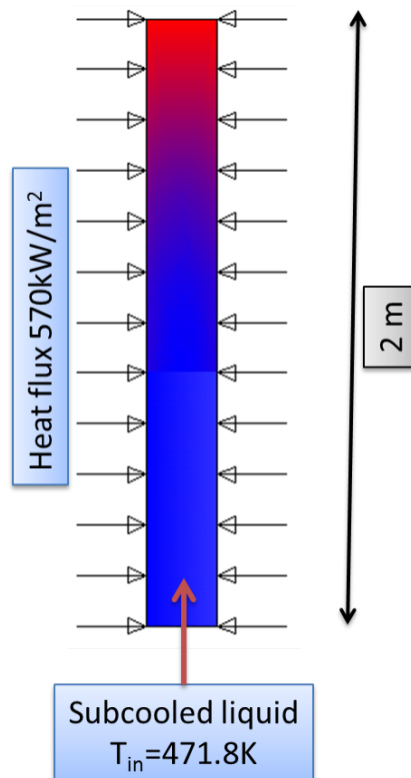


Figure-7.1 Bartolomei (1982) experiment details

Table-7.1 Boundary conditions for Bartolomei experiment

Wall boiling model	Non equilibrium RPI boiling model	
Boundary conditions	Operating Pressure: 4.5 MPa	
Region	Type	Specification
Inlet	Velocity inlet	u-liq = 1m/s ; Liquid Temp = 471.8K
Outlet	Pressure outlet	Backflow void: 0; vapour Temp= 530.55K
Wall-heated	Wall	Heat flux: 570 kW/m ² (uniform)

7.2.1 CFD Model details

For boiling simulations, the tube has been modeled in 2D axisymmetric geometry with 10K, 12K, 15K, 18K and 20K mesh points. For a high pressure operating condition, such as this, the material properties change by a large extent, hence variation in the fluid properties have been accounted during simulation. The solver was run in a transient-implicit-coupled fashion with a QUICK spatial discretization scheme used for void fraction while second order unwind has been used for the momentum and energy formulation. Considering the applicability of each submodel (closures in momentum and energy), the models have been chosen for high pressure boiling conditions as discussed in Chapter-5 in greater details. Summary of phase interaction models are presented in Table-7.2.

Table-7.2 Phase interaction models used for simulation of Bartolomei experiment

Closures	Terms modelled	Empirical model used
Momentum Closure		
	Drag	Ishii Model (1979)
	Turbulent Dispersion	Burns (2004)
	BIT	Sato (1979)
Energy Closure		
	Bubble departure Diameter	Kocamustafaogullari and Ishii (1983)
	Frequency	Cole (1967)
	Nucleation Site	Kocamustafaogullari and Ishii (1983)
	Area Influence Coefficient	Delvalle-Kenning (1985)
	Interfacial Heat transfer	Ranz Marshall (1952)
Turbulent Model		RSM
Solver		Eulerian Multiphase model with wall boiling coupled solver

With all the models shown in Table-7.2, a base line case is formulated and further studies for effect of sub models are performed over base case.

7.2.2 Grid generation and grid independence

The tube has been modeled as 2D axi symmetric problem. For obtaining mesh independence, five grid densities have been used and results for axial void and temperature distributions have been compared with the experiment. Figure 7.2 shows the mesh of 15000 grid density. A minimum size of the cell considered here is 0.3 mm with an incremental ratio of 1.1. Figure-7.3 shows results of CFD for sectional averaged values of the steam volume fraction and the water temperature distribution as predicted by various grid densities and compared with the experimental data. Both, the point of boiling inception and the increasing of the vapor volume fraction over the height show good agreement to the experimental data with almost all grids. Also the calculated temperature averages correspond very well to the experiment. In all cases of varying grid densities, RSM mixture model is used for turbulence modeling. For predictions of two phase flows, it is important to accurately predict the turbulence, with y^+ as an important parameter. Table-7.3 shows y^+ values for all grid points. y^+ values of ~157 is observed for 10K mesh size which decreased continuously upto 20K mesh. It has been observed that for 15K mesh y^+ value persisted as ~71 which remained almost constant for further refinement of the grids. RMS error of 0.0202 is observed for 12K mesh which is minimum among the other meshes results. A RMS error of 0.0241 is observed for 15K mesh.

After doing this study, it is seen that the results are invariable after 15K mesh points, so, a mesh density of 15 K has been chosen for further analyzing the performance of the sub models. Figure-7.4 shows CFD predictions of average void and liquid temperature distribution axially as compared against the experimental data with 15K mesh density. Figure-7.5 a, b shows the radial variation of steam volume fraction and the bulk liquid

temperature at different heights. These curves depict an increased vapor fraction value at the vicinity of the wall which is a direct implication of the boiling at the wall.

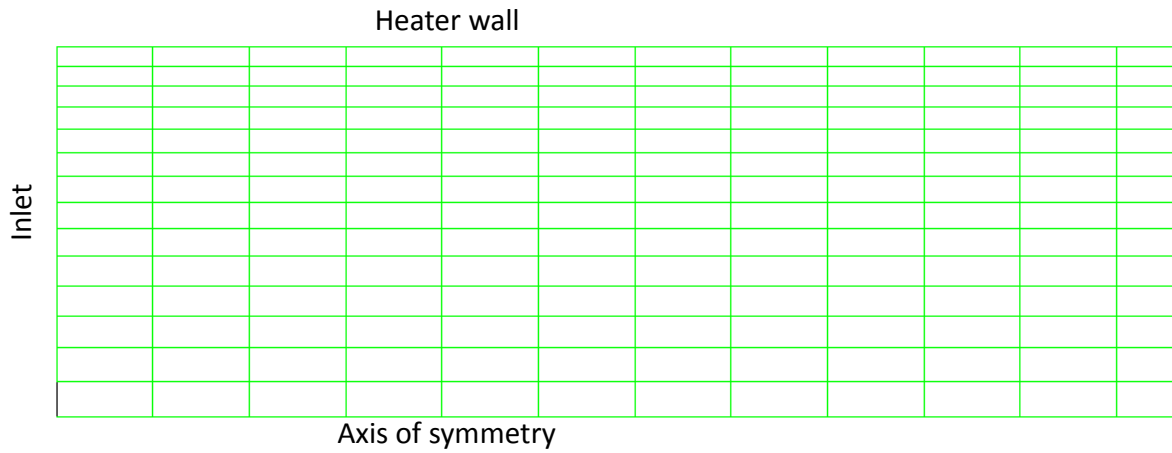


Figure-7.2 Grid for the base case

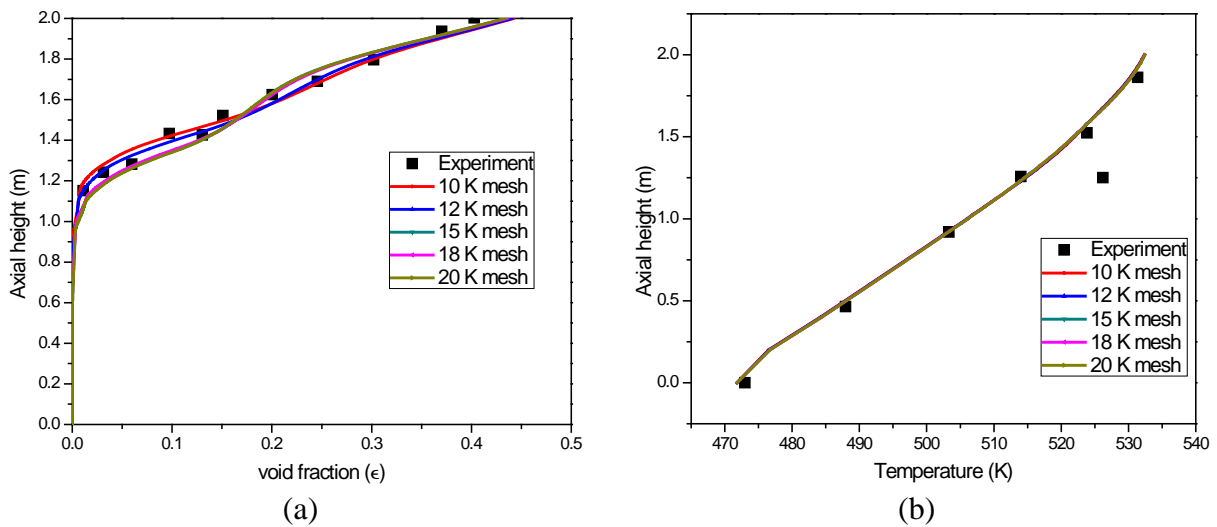


Figure-7.3 Grid independence (a) axial void distribution (b) axial liquid temperature distribution with varying grid points

Table-7.3 Wall y^+ for various grid densities

Grid density	Wall y^+ for liquid phase	Wall y^+ for vapour phase	Void RMS Error
10K	157.8	12.8	0.0209
12K	127.75	10.79	0.0202
15K	71.46	6.73	0.0241
18K	71.31	6.47	0.024
20K	71.12	6.42	0.0235

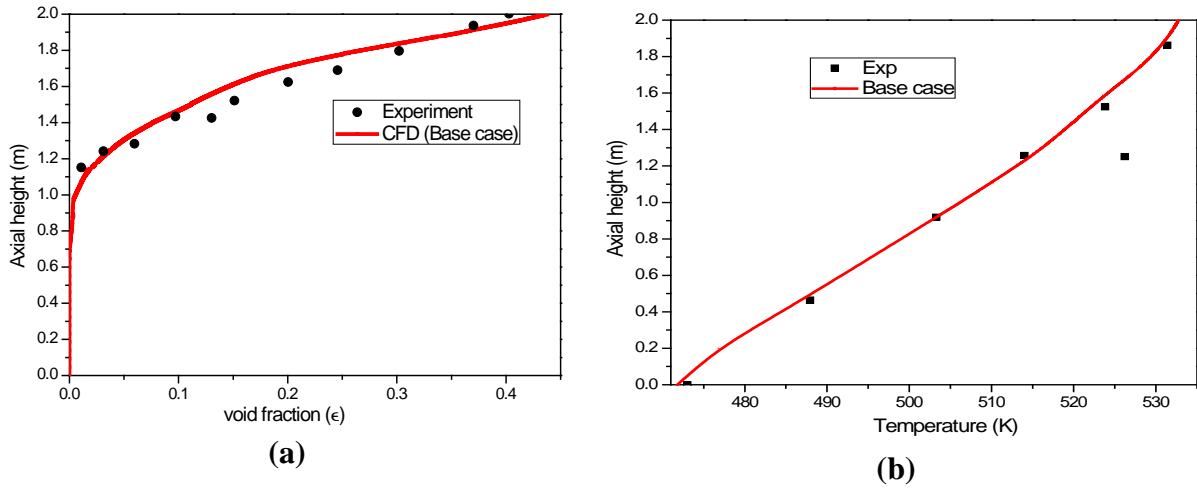


Figure-7.4 Comparison of calculated and measured (a) steam void fraction values and (b) bulk liquid temperature along the axial length of the column

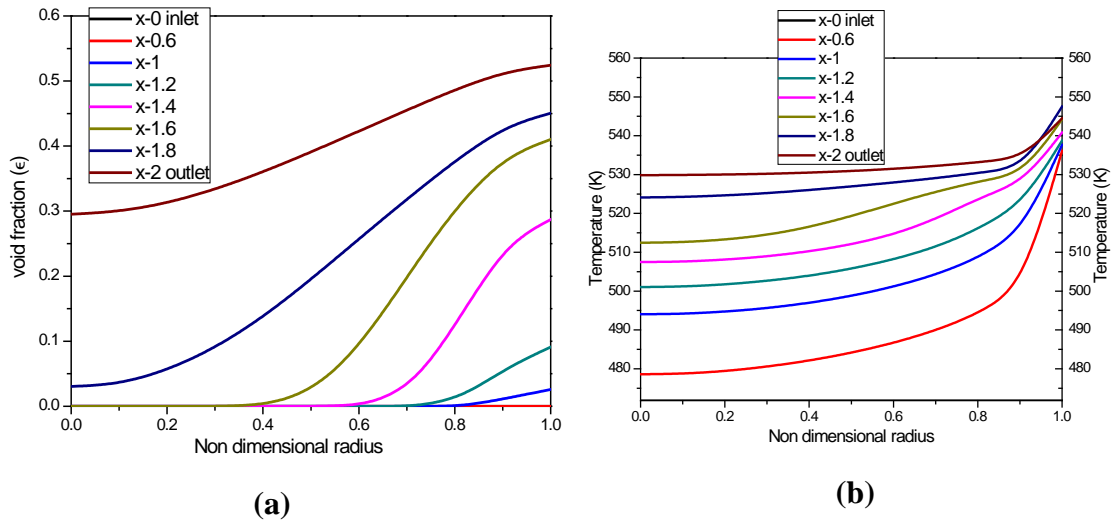


Figure-7.5 Radial variation of void and temperature

Sudden decrease in temperature just after the wall region shows condensing bubbles, when it mixes with the sub-cooled liquid bulk. This flattens out as we go toward the tube center because of lesser availability of bubble in the bulk liquid and hence lower temperature.

7.2.3 Sub models performance study

Turbulence models

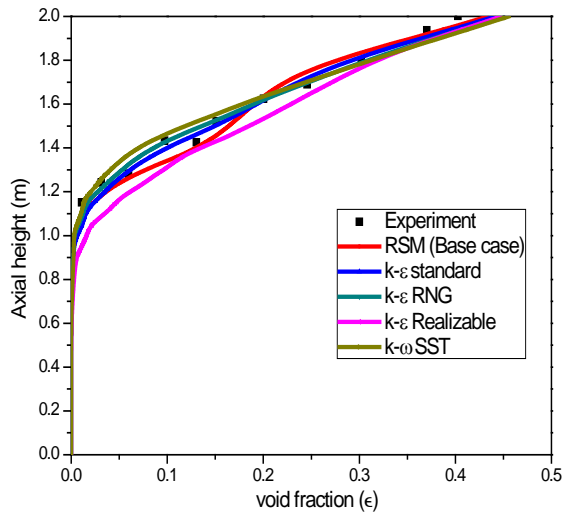
Turbulence plays an important role in simulating the flow field as two phase flows are inherently turbulent and fluctuating, that makes selection of the turbulence model more critical for the simulations. Due to the lower density of vapor, it is commonly assumed that,

in nucleate boiling flow, the motion of the dispersed vapor phase follows the fluctuations in the continuous liquid phase. Accordingly, the turbulence stresses are modeled only for the liquid phase, whereas the vapour phase is modeled by a simple zero equation model or its effect is incorporated in momentum of the continuous phase as bubble induced turbulence. When inertia of the dispersed phase becomes relatively high at high Re flow, its contribution become important and hence per phase turbulence or mixture models are used. Turbulence models being utilized for the two phase flow are simply the extension of their single phase counterpart.

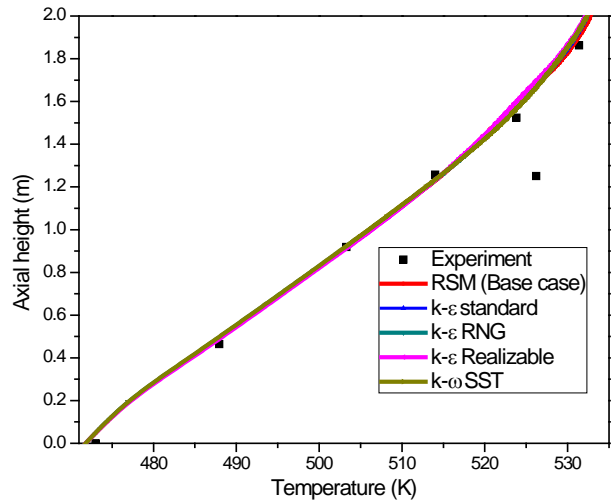
Five turbulence models including second order RSM models are selected for evaluating the performance of turbulence models during boiling. Requirement of the near wall mesh refinement is different for different turbulence models. Near wall treatment of the flow is addressed by either low Re model or wall functions models, which is reflected generally in terms of wall y^+ . $k-\varepsilon$ being the most popular turbulence model, requires its first grid to be located in turbulent region, out of the three conceptualized regions as viscous layer, buffer layer and fully turbulent region. It is apparent that viscosity affected region (viscous sub-layer and buffer layer) is not resolved with this model. Generally, $k-\varepsilon$ model is used for high Reynolds number flow with isotropic assumptions of turbulence. y^+ of near-wall mesh must larger than 11.225 using $k-\varepsilon$ model. For the flows with anisotropic behavior, two equations turbulence models are not applicable so RSM model is selected for simulation of the flow field inside the rod bundle. Considering this, RSM model is chosen for the validation cases to further analyzing the effects of other sub models. Table-7.4 shows the wall y^+ values for different turbulence models and RMS error when compared with the experiment. An average wall y^+ value of ~ 70 is observed for RSM, $k-\varepsilon$ RNG, and $k-\omega$ SST, while >100 is observed for $k-\varepsilon$ standard and $k-\varepsilon$ realizable model.

Table-7.4 Heater wall y^+ with different turbulent models

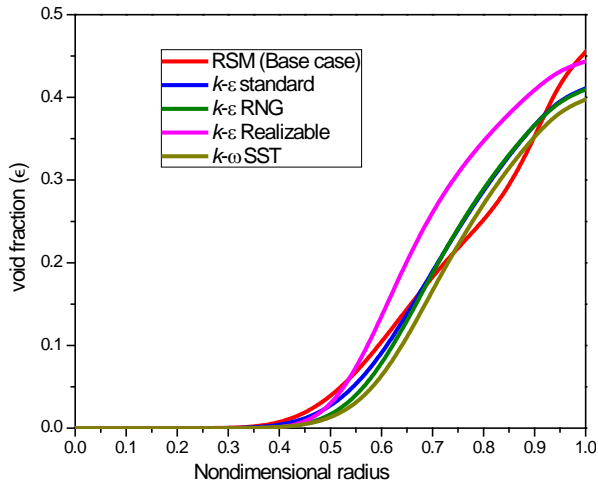
Turbulence model	Average wall y^+ for liquid phase	Average wall y^+ for vapors phase	Void RMS Error
k - ϵ standard	157.8	12.8	0.0189
k - ϵ realizable	127.75	10.79	0.0369
RSM (Base case)	71.46	6.73	0.0241
k - ϵ RNG	71.31	6.47	0.0204
k - ω SST	71.12	6.42	0.0268



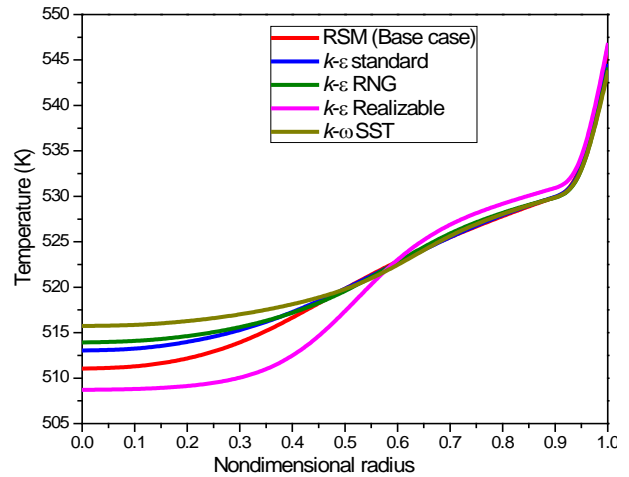
(a) Axial void distribution



(b) Axial temperature distribution



(c) Radial void distribution



(d) Radial temperature distribution

Figure-7.6 Effect of different turbulence models on flow field

Figure-7.6 shows the variation of flow parameters with different turbulent models. It is evident from Figure-7.6a that standard k - ϵ model predicts the axial profile of void close to the

experiment. Only a RMS error of 0.0189 is observed with k - ϵ model. k - ϵ reliable model under predicts the axial void and has large error as compared to other turbulence models. Axially averaged liquid temperature is well predicted by all the models as seen in Figure-7.6b. Peak void is observed at the heater wall at an axial plane (x : @1.5m) as anticipated. RSM predicts a peak void of 0.45 at wall, highest among the turbulence models (Figure-7.6c). Sharp fall in the liquid temperature is observed for all the models, just after the heater wall. A curve with prominent dip is seen for RSM model as compared to other models as shown in Figure-7.6d. A lower decrement rate of liquid temperature from radius 6.9 to 4.6 mm (non-dimensional radius 0.9 to 0.6) can be observed from Figure-7.6d, which corresponds to the condensation of bubble in the bulk raising the temperature of the bulk liquid after that relatively larger rate of temperature reduction is observed with RSM predictions.

Bubble generated turbulent

In addition to the turbulence due to wall shear and eddies in bulk liquid, movement of the dispersed phase is also a source of the turbulence. Turbulence due to wall shear and eddies in bulk liquid is taken into consideration by turbulence models like k - ω SST and RNG k - ϵ or RSM model. However, when large or medium sized bubbles are flowing through liquid, wakes are generated behind bubbles which create additional turbulence. In order to account for additional turbulence by bubbles, turbulence interaction models are used (Sato and Sekoguchi, 1981; Koncar et al., 2005). In this study, two models are compared to account effect of bubble induced turbulence. Also, a case of no BIT is analyzed. Sato et al. (1979) developed correlation based on effective viscosity to account bubble induced turbulence. Effective viscosity is a sum of molecular liquid viscosity, viscosity due to turbulent motion of bubbles relative to the surrounding fluid and viscosity due to liquid turbulence generated by

fluctuating wakes behind the large bubbles. As per the Sato model the bubble induced viscosity is given by:

$$\mu_{BIT} = \rho_l C_{\mu BIT} \epsilon_g d_b |\bar{u}_g - \bar{u}_l| \quad \dots (7.1)$$

$$\text{where } C_{\mu BIT} = 0.6$$

Troshko and Hassan (2001) stated that bubble induced turbulence destruction is more prominent than shear induced turbulence owing to its higher frequency. Considering this, they incorporated time scale ‘ τ ’ of bubble induced turbulence in their model. Troshko-Hassan (2001) model incorporates BIT as source term in the equations of turbulent kinetic energy k and turbulent dissipation ϵ as per Eq. (7.2), (7.3) and (7.4).

$$S_{BIT}^k = -F_D(u_G - u_L) \quad \dots (7.2)$$

$$S_{BIT}^\epsilon = 0.45 \frac{S_L^k}{\tau} \quad \dots (7.3)$$

$$\tau = \frac{2C_{VM}d_B}{3C_D|u_G - u_L|} \quad \dots (7.4)$$

Incorporation of bubble induced turbulence is very important for modeling of two phase flows, which can be seen from Figure-7.7. Figure-7.7a shows the axial void distribution. It is seen from the Figure-7.7a that, there is a large variation in the predictions with varying BIT models. Calculations without BIT model are having a RMS error of 0.0777 while with Troshko-Hassan (2001) model it is ~0.0503 as mentioned in Table-7.5. Void is under predicted without BIT model.

Table-7.5 RMS error for different BIT models

Model for BIT	RMS error
Troshko-Hassan	0.0503
No BIT	0.0777
Sato (Base case)	0.0241

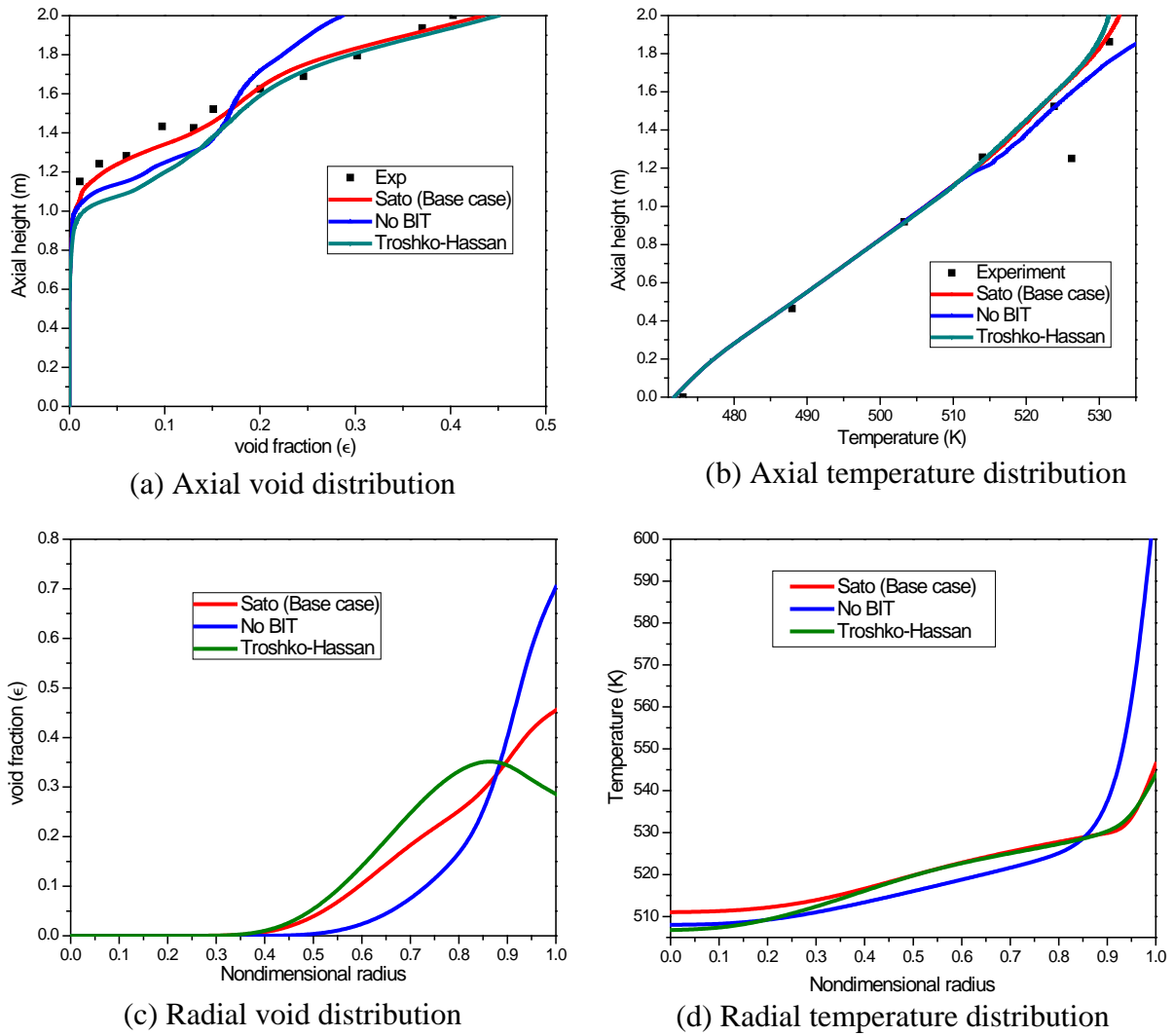


Figure-7.7 Effect of different bubble induced turbulence models on flow field

Figure-7.7b shows the axial temperature distribution as compared with base case as well as with experiment. Both Sato (1979) and Troshko-Hassan (2001) model predicts the temperature close to experiment, while the temperature distribution is found to be off without consideration of BIT in CFD modeling. Troshko-Hassan (2001) model predicts void peaking slightly away from the heater wall as seen in Figure-7.7c, while a peak void fraction of ~70% and peak radial temperatures at wall is observed with “No BIT” model as seen in Figure-7.7c and 7.7d.

Momentum closures

For accurate predictions, it is important to select appropriate correlation for the simulations. Role of closure relations for momentum equations is very significant, since they provide a weightage for different forces in momentum transport. Mainly, these forces are categorized as Drag and Non-drag force as discussed in Chapter-5. Drag is an important force deciding the total holdup in the column or the tube, while non-drag forces generally governs the radial distribution of the void.

Drag force models

In this study, 4 different drag models, listed in Table-7.6, including the one in base case have been studied for their performance. Formulation of various drag models had already discussed in section 5.4.4 of Chapter-5. Figure-7.8 shows the results of CFD predictions as compared with experiment. Figure-7.8a shows void distribution with variation of drag models. It is observed that other than Tomiyama drag model (2004), other models predict the void distribution similar to each other. Tomiyama model predicts lesser void fraction at any axial location. Axial temperature is predicted same with all drag models. RMS error of 0.023 (Table-7.6) is observed with Tomiyama model and void predictions shows better match with Tomiyama model. Relatively steep fall in radial void is observed with Tomiyama drag model, while other models predict similar behavior for radial void and temperature as seen in Figure-7.8c and 7.8d.

Table-7.6 RMS error for different Drag models

Drag Model	RMS error
Schiller Naumann	0.0234
Tomiyama	0.023
Ishii (Base case)	0.0241
Universal	0.0245

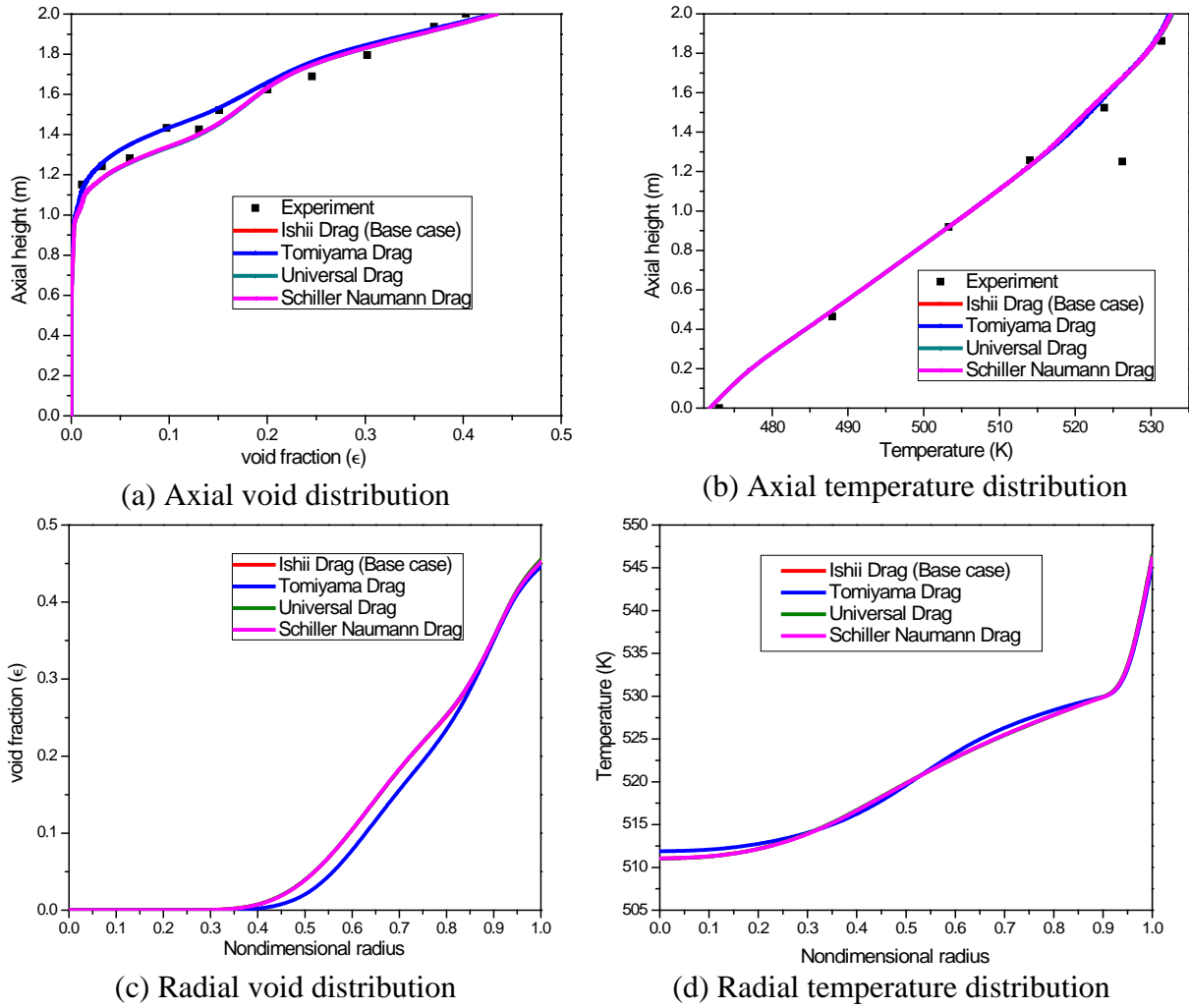


Figure-7.8 Effect of different drag models on flow field

Non-Drag force models

Lift, turbulent dispersion and wall lubrication are the major forces among non-drag forces. Wall Lubrication (WL) and Turbulent Dispersion (TD) force are considered here under the study. Lift force is important with larger bubbles and larger field gradients of velocity. Here, larger size of bubble is not expected in the bulk so lift force is not considered. Figure-7.9 shows the variation of field parameters with different wall lubrication models. Axial profiles are better matched with Antal et al (1991) model as seen in Figure-7.9a. However, inclusion of WL model reduces the void at wall and pushes it away from the wall (Figure-7.9c), which is not reasonable for subcooled wall boiling case.

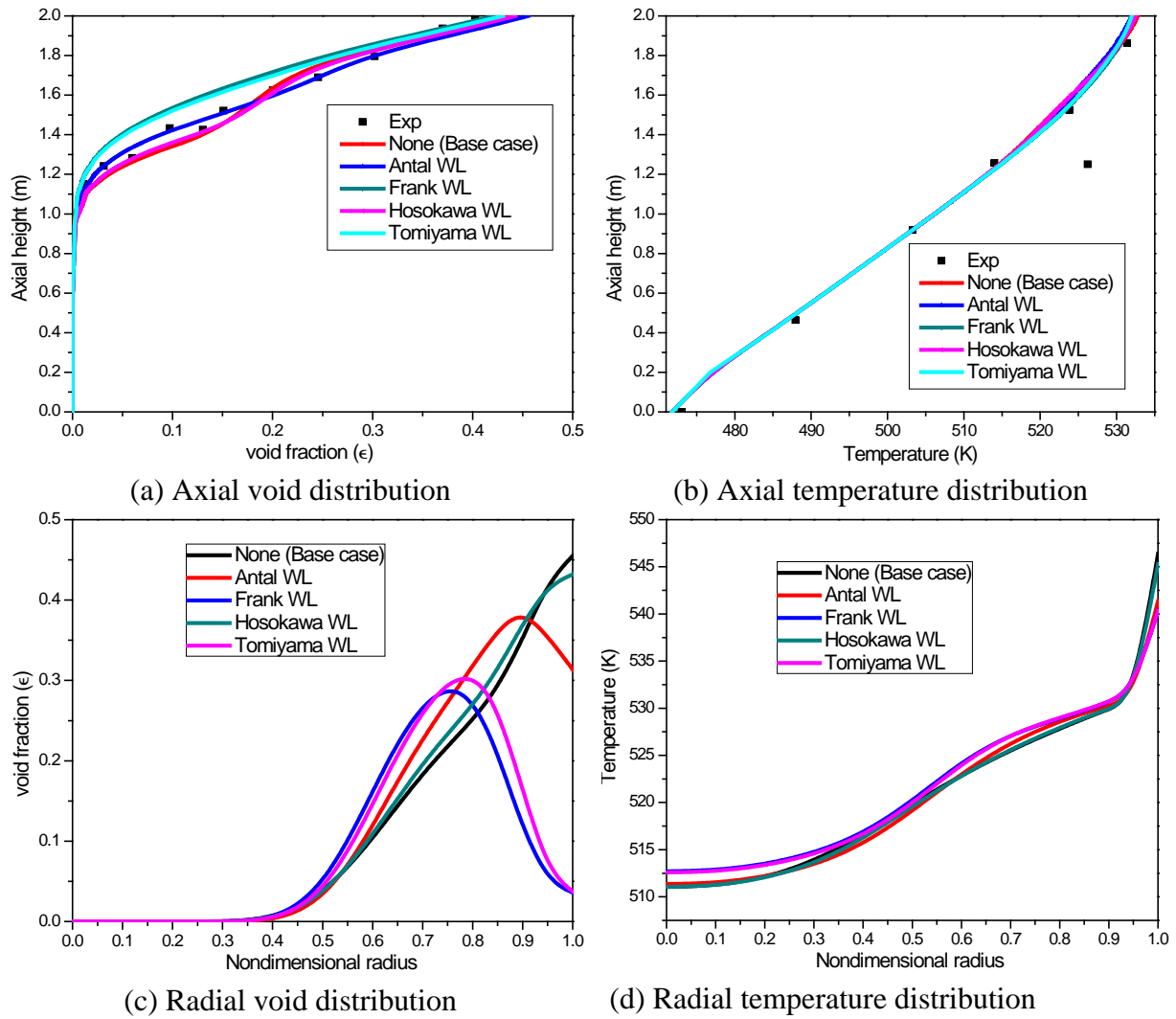


Figure-7.9 Effect of different wall lubrication models on flow field

Void will be significant at the heater wall and will reduce quickly as moving away from the heater wall due to condensation of bubbles in subcooled bulk. Axial temperature profile as predicted by all models is found to be in good agreement with experiment and radial temperature profile seems in agreement with each other.

Figure-7.10 shows the effect of TD force on flow field. Two models are considered for TD force along with “None TD” force consideration. It is having significant effect on the predictions. When compared with experimental data, the simulations without TD force modeling early predicts the boiling inception and over predict the void upto a height of 1.3 meters as shown in Figure-7.10a. After that “None TD” case under predicts the void. Because

of absence of mixing due to TD force, sufficient void would be required to drive the bubbles away from the wall and its condensation in the bulk liquid. A void fraction of ~ 0.72 is observed at the heater wall for “None TD” case seen in Figure-7.10c. With both the TD models Lopez de Bertodano Model (1997) and Burns et al. (2004), axial void distribution is predicted in good agreement with experimental data. Both TD models predict the liquid temperature very well.

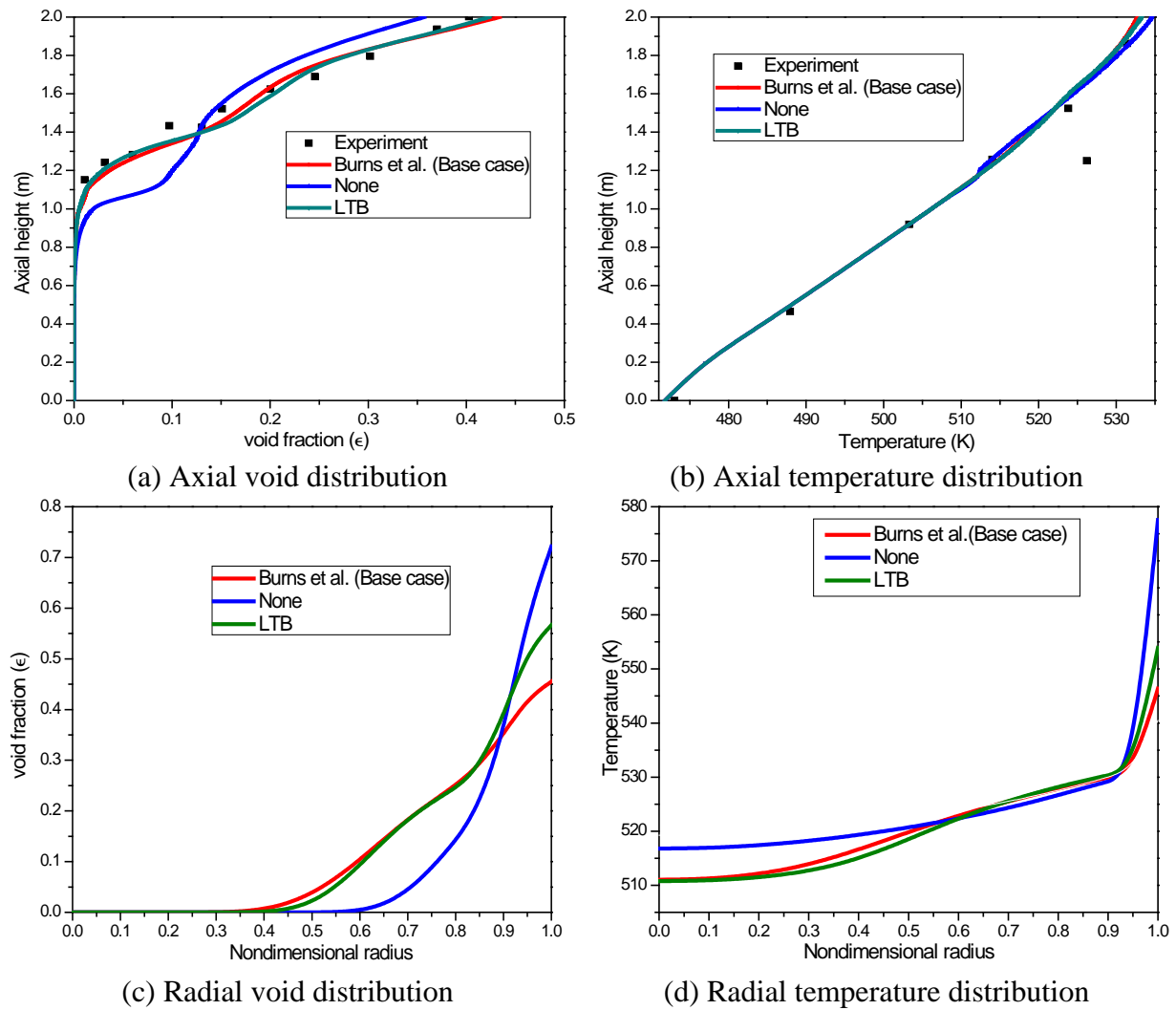


Figure-7.10 Effect of different turbulent dispersion models on flow field

Energy closures

Bubble departure diameter, bubble departure frequency and nucleation site density are important boiling parameters required closure models in RPI wall partitioning model for

subcooled boiling simulations. Various combinations of models for these parameters have been studied for observing their effect on the CFD predictions for void and liquid temperature, which are shown in Table-7.7. Different models for these parameters are discussed in Chapter-5 in details.

As seen previously that Tomiyama drag model predicts the axial void profile better than the Ishii drag model. In view of this, boiling parameters models have been studied with the two different models of the drag to study their performance for the boiling.

Figure-7.11 shows the axial and radial void and liquid temperature distribution with different boiling parameters models for Ishii and Tomiyama drag models. Five different cases have been studied including one base case. Base case with Kocamustafaogullari and Ishii (1983) models for bubble departure diameter and nucleation site density and Cole (1960) model for bubble generation frequency shows better agreement with experiment for axial void distribution as compared to other cases.

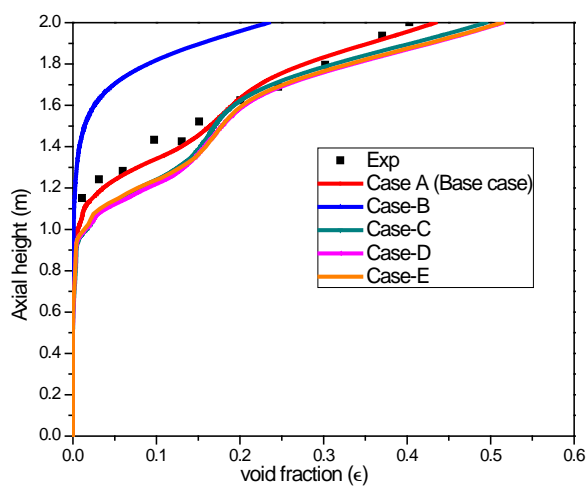
Table-7.7 Combination of boiling parameters models considered for performance study

	Model for Bubble departure diameter	Model for nucleation site density	RMS Error with Ishii drag for void	RMS Error with Tomiyama drag for void
Case-A (Base case)	Kocamustafaogullari and Ishii (1983)	Kocamustafaogullari and Ishii (1983)	0.0241	0.023
Case-B	Kocamustafaogullari and Ishii (1983)	Lemmert and Chawla (1977)	0.1422	0.1445
Case-C	Tolubinsky and Kostanchuk (1970)	Lemmert and Chawla (1977)	0.0538	0.0355
Case-D	Unal (1976)	Kocamustafaogullari and Ishii (1983)	0.0683	0.0441
Case-E	Unal (1976)	Lemmert and Chawla (1977)	0.0611	0.0416

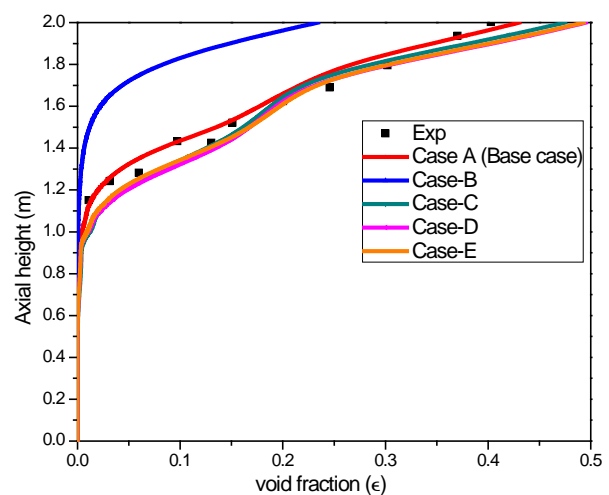
RMS error for various combination cases is shown in Table-7.7. Case-B shows a maximum RMS error of 0.1422 as compared to the 0.0241 for base case with poor predictions for void

and temperature for this case as seen in Figure-7.11a, 7.11a', 7.11b and 7.11b'. RMS errors are found to be lesser with Tomiyama drag model (Table-7.7 and Figure-7.11). RMS error remained only 0.023 with Tomiyama model in Case-A. Case-C utilizes basic models for boiling parameters, but its shows relatively better performance than the Case-D and E. Unal (1976) model for bubble departure diameter, which is developed for high pressure boiling application, shows poor predictions for the axial void distribution (Figure-7.11a) as compared to other case, it over predicts the void. Axial void temperature distribution is found to be in good agreement for all the cases except for Case-B, which is also having poor predictions for axial void. A low value of wall peak void is observed for Case-B. Behavior of rest of the case is found to be in line with each other as seen from Figure-7.11c and 7.11c'. Similar kind of behavior is observed for radial temperature profile also (Figure-7.11d and 7.11d').

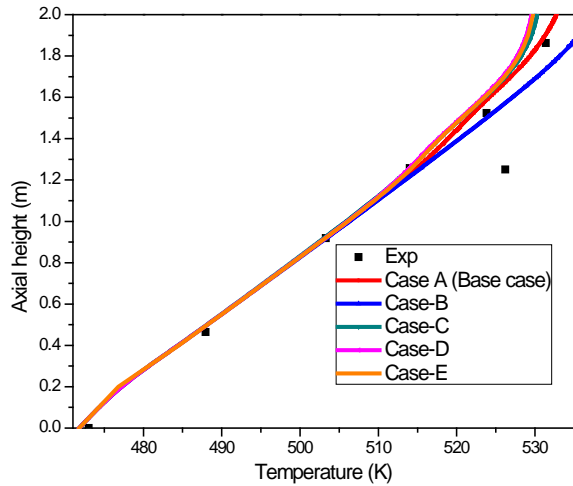
Kocamustafaogullari and Ishii (1983) model for bubble departure diameter incorporates contact angle and pressure correction in its formulation, which are fundamental properties for bubble diameter calculations. In addition, the formulation for nucleation site density also incorporates pressure dependency, which may be playing role for Case-A combination to have good agreement for axial distribution profiles of vapor fraction and liquid temperature.



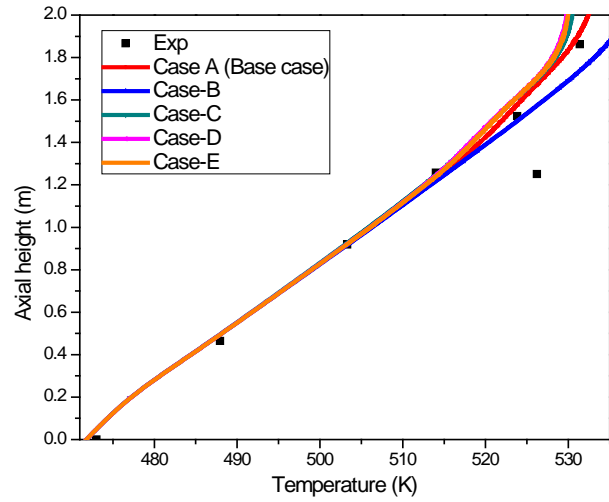
(a) Axial void distribution (Ishii drag)



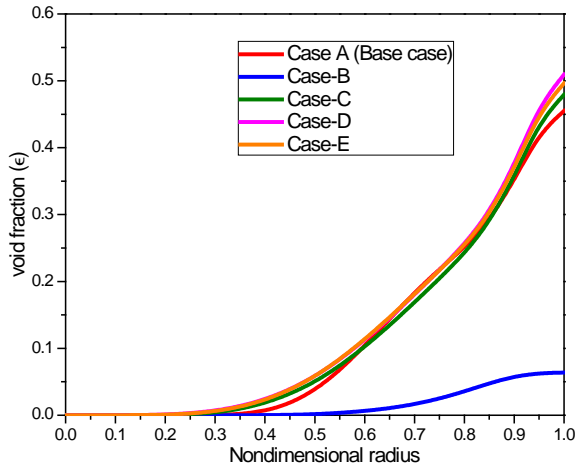
(a') Axial void distribution (Tomiyama drag)



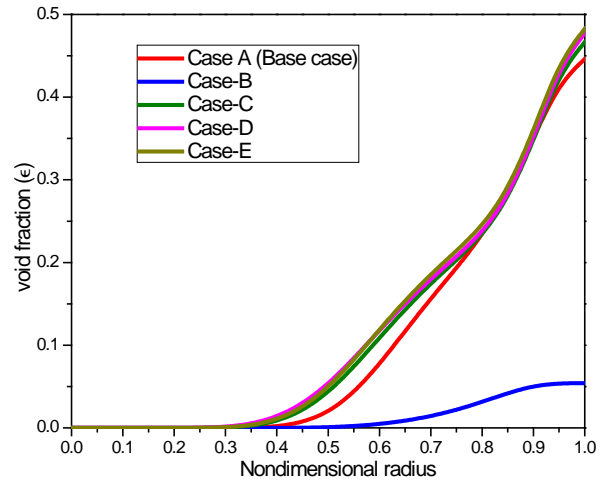
(b) Axial temperature distribution (Ishii drag)



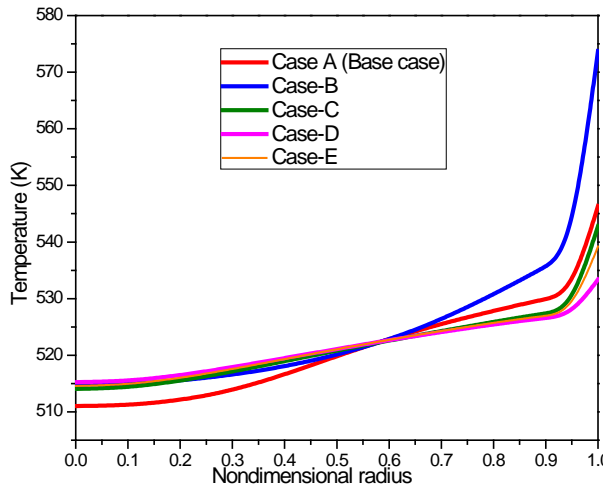
(b') Axial temperature distribution (Tomiyaama drag)



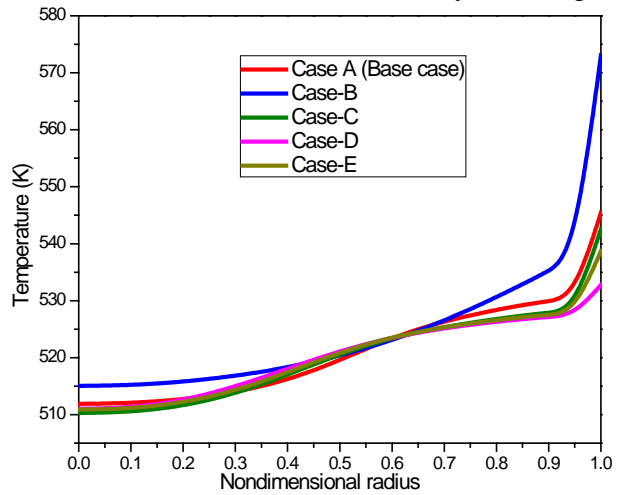
(c) Radial void distribution (Ishii drag)



(c') Radial void distribution (Tomiyaama drag)



(d) Radial temperature distribution (Ishii drag)

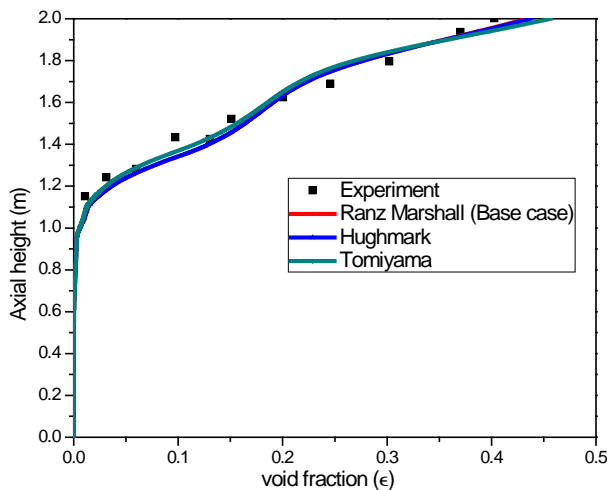


(d') Radial temperature distribution (Tomiyaama drag)

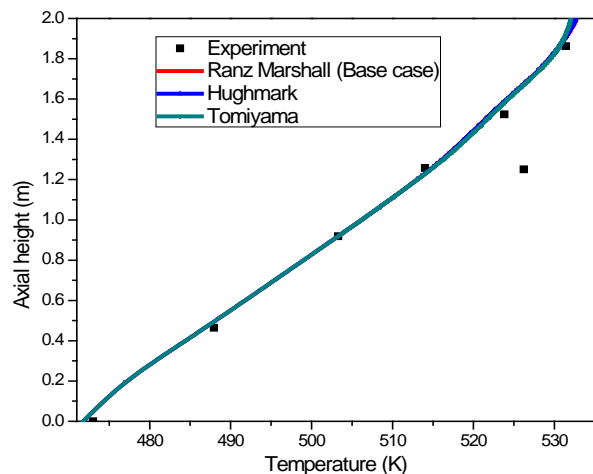
Figure-7.11 Effect of different boiling parameters model on flow field

Interfacial heat transfer models

After departing from the wall the bubble travels into the bulk liquid where it interacts with subcooled liquid in its surroundings. The heat transfer takes place through interface and bubble condenses eventually. Empirical formulations are required for modeling the phenomena at the interface for interfacial heat transfer. Performance of three models is studied for interfacial heat transfer. This includes Ranz Marshall (1952), Hughmark (1967), and Tomiyama (1998). First two models predict the exit void close to experiment, while Tomiyama model over predicts the void as seen in Figure-7.12a. After boiling inception some difference in void predictions is seen in Ranz Marshall (1952) and Hughmark (1967), but later their prediction matches with each other. A RMS error of 0.0282 is observed with Tomiyama model, while for Hughmark model it is found to be 0.0235 for void predictions. Temperature distribution is found to be in good agreement with experiment for all models. Radial void and temperature profiles are found to be similar for all models. All models predict almost same peak void and liquid temperature at wall as depicted by Figure-7.12c and 7.12d.



(a) Axial void distribution



(a) Axial temperature distribution

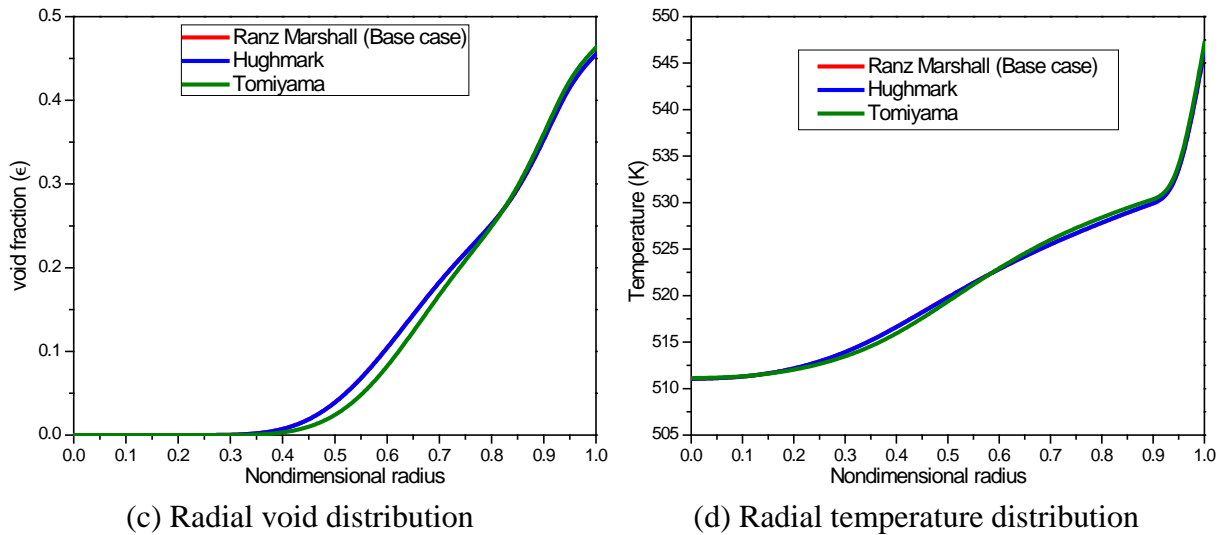


Figure-7.12 Effect of different interfacial models on flow field

7.2.4 RELAP modeling for subcooled boiling

Same case of Bartolomai (1982) has also been simulated with system code RELAP-5. The RELAP5/MOD3.2 model of the vertical tube of 2 m length and 8 mm ID has been prepared which consists of the 8 nodes with time dependent volumes at the inlet and outlet of the tube for simulating the boundary conditions. Uniform heat flux of 570 kW/m^2 is applied to the tube wall that has been simulated by heat structures. RELAP5 axial void and liquid temperature are compared with the CFD predictions and experimental data.

RELAP5 does not include models for wall voidage region between the ONB point and the NVG point. It treats fluid flow in the upstream of the NVG point as single-phase flow and fluid flow in the downstream of the NVG point as two phase flow. RELAP5 utilizes Lahey's (1978) mechanistic model to capture the effect of thermal gradient in the wall boundary layer which assumes preheating of liquid near wall and then flashing to vapor. Net Vapour Generation (NVG) point is predicted using Saha-Zuber (1974) correlation which calculates the critical enthalpy of the subcooled fluid, where RELAP5 starts treating the fluid as two phase flow. Saha-Zuber correlation is valid for pressures from 1.01 to 138 bars. At low flow rates the bubble detachment occurred at constant Nu number (thermally controlled), while at

high flow rates the bubble departure is hydrodynamically induced at a fixed St. Number. The $Pe: 70000$ is the switch between thermally or hydrodynamically controlled bubble departure (RELAP5 Manual, 1995). Interface heat transfer coefficient for subcooled bubbly flow regime is calculated by Unal (1976) correlation.

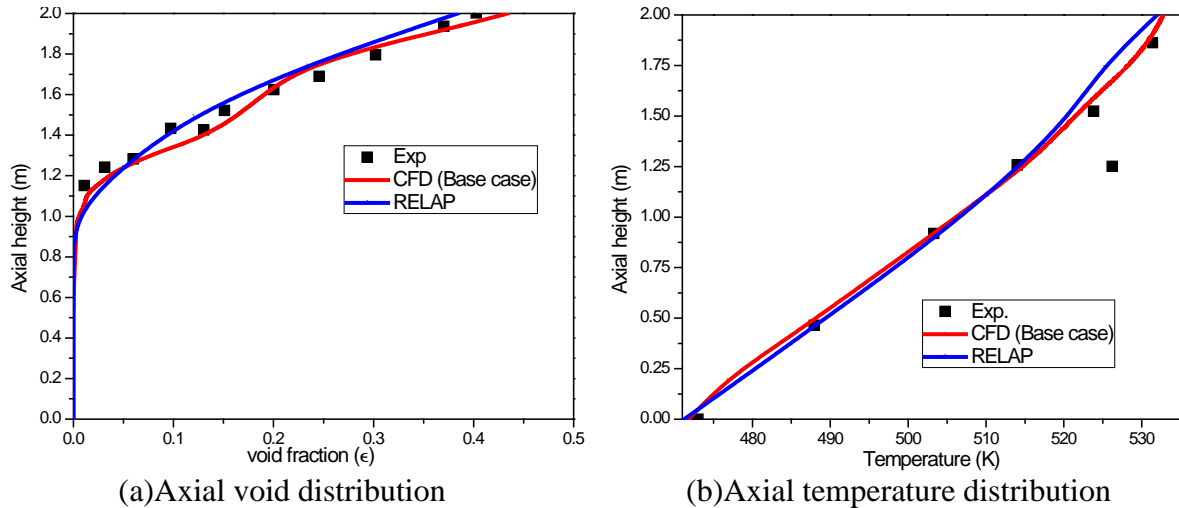


Figure-7.13 Axial void and Temperature predictions by RELAP and CFD

Figure-7.13 depicts the axial and liquid temperature distribution as predicted by RELAP and compared with CFD and experiment. RELAP5 under predicts the void fraction as compared to CFD and experiment (Figure-7.13a). Temperature distribution predicted by RELAP and CFD are found to be good agreement with experiment upto 1.5m height as seen in Figure-7.13b, RELAP5 slightly under predicts the axial temperature at outlet.

7.3 Application of the model for high pressure boiling simulation

After validation of the CFD model with experiment of Bartolomai (1982), the model is applied for another experiment conducted by Bartolomai and Chanturia (1982). The experiment was conducted in a tube of ID 12mm and length 1.6m at 6.89 MPa. Table-7.8 presents the details of the experiment simulated using CFD. Mesh for the case has been generated with a minimum size of 0.3mm, which gives a wall y^+ of ~ 80 for this case. Figure-7.14a shows the axial void distribution as predicted by CFD and compared with experiment. A fairly good agreement of void distribution is seen with experiment. Figure-7.14b shows the

radial void distribution from inlet to outlet. The void at the center of the tube is always found to be zero. Figure-7.15 shows the area average axial temperature distribution from inlet to outlet. At outlet, the liquid temperature reaches at saturation temperature.

Table-7.8 Experiment details simulated using CFD

	Exp-1
Length (m)	1.16
Tube inside diameter (mm)	12
Pressure at exit (MPa)	6.89
Heat flux (kW/m^2)	770
Mass flux ($\text{kg/m}^2\text{s}$)	1467
Inlet temperature (K)	519

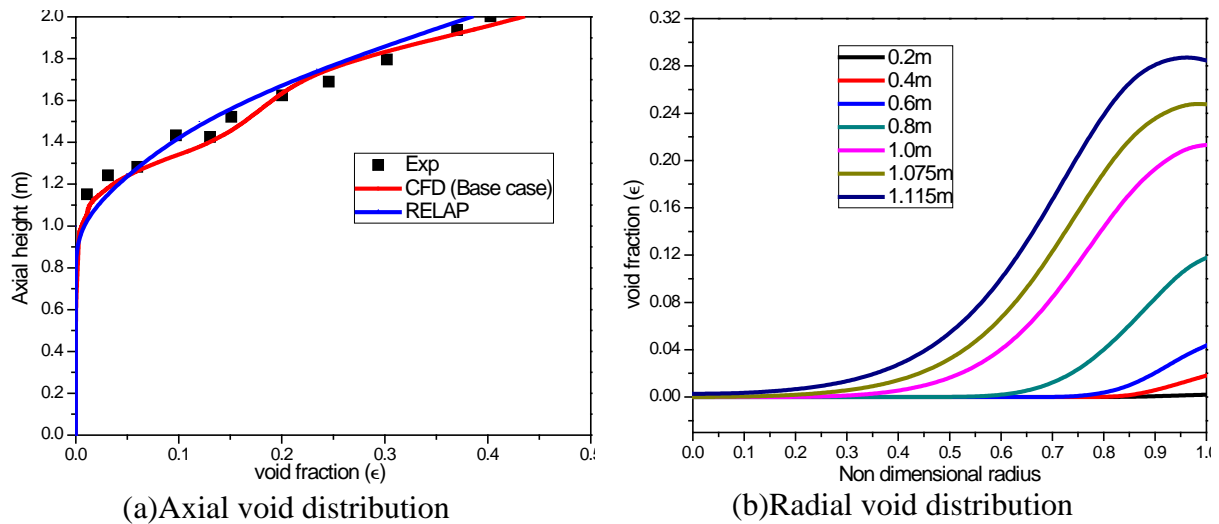


Figure-7.14 Axial and radial void distribution

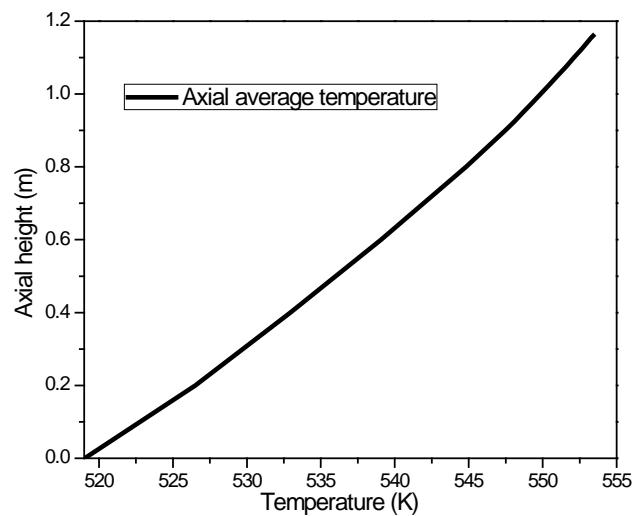


Figure-7.15 Axial temperature distribution

7.4 CFD simulation of thermal hydraulic behavior inside rod bundle

After successful validation and application of the developed boiling frame work, the CFD boiling frame work has been applied to the AHWR rod bundle case for prediction of the void distribution inside bundle for any hot spot during decay heat removal with SBO condition.

AHWR is a channel type BWR. It contains 452 channels/pressure tubes and each channel houses one fuel rod bundle. It utilizes 54 rod bundle as a fuel element. CFD simulations have been carried out for flow and void distribution over rod bundle inside the pressure tube. SBO condition has been simulated for the reactor with system code as discussed in Chapter-2 and boundary conditions for the rod bundle at various pseudo steady state instances have been obtained for simulating the multidimensional flow over heated rod bundle during decay heat conditions. This study reveals the conditions of the void and temperature distribution inside pressure tube and hence facilitates the identification of the hot spots, if present anywhere inside the pressure tube.

The 54 fuel pins of the heated rod cluster are arranged in three concentric circular pitches forming a fuel rod bundle called as 54 rod bundle. It is a rod bundle with 11.2 mm OD fuel pins having heated length of 3.5 m. Figure-7.16 shows arrangement of the fuel rod bundle inside the coolant channel. The rod bundle is having $1/12^{\text{th}}$ symmetry. However, in a $1/12^{\text{th}}$ section, some the rods becomes half of their surface area in the sub-channel. In this study, $1/6^{\text{th}}$ sector of the rod bundle has been considered which consists of 9 full fuel pins of the bundle as seen in Figure-7.17. CFD simulations have been carried out to investigate the health of the rod bundle during decay heat removal on a $1/6^{\text{th}}$ sector of the bundle. This can be confirmed with the estimation of the void, temperature and flow field inside the rod bundle. Figure-7.18 shows the MHTS depressurization curve along with the variation of flow as predicted by RELAP5 during SBO conditions. Four cases marked as case#1 to case#4 in

Figure-7.18 have been analyzed for occurrence of any local hot spot. Case#1 falls in a region of boiling, while rests of the point fall in the single phase flow region.

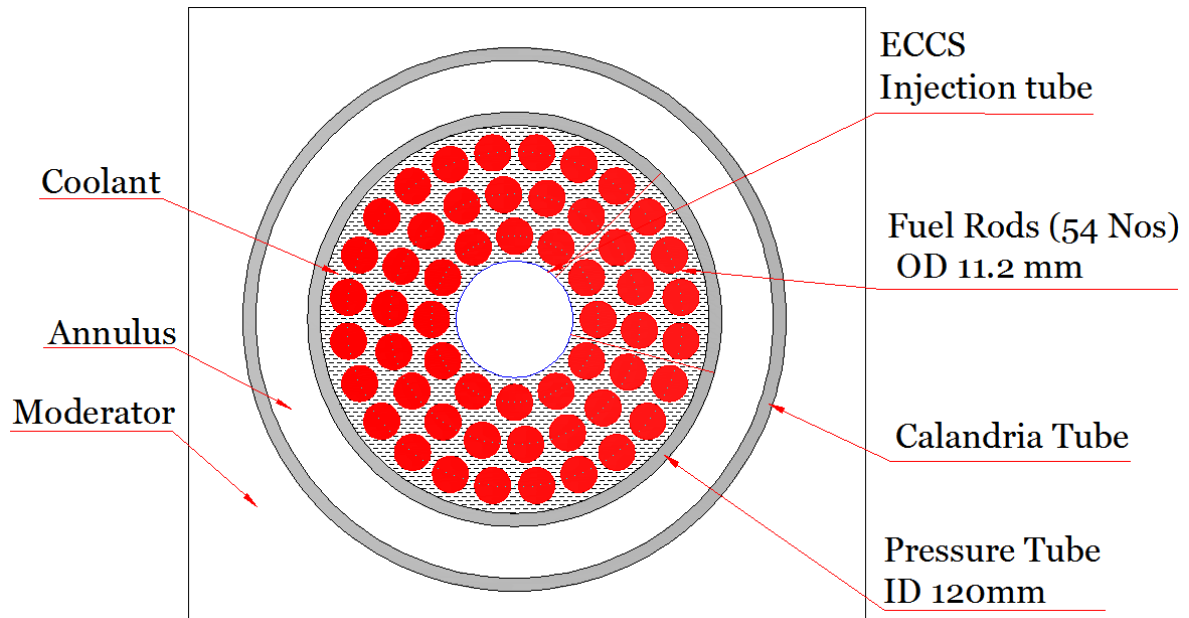


Figure-7.16 Coolant Channel with 54 Rod Bundle

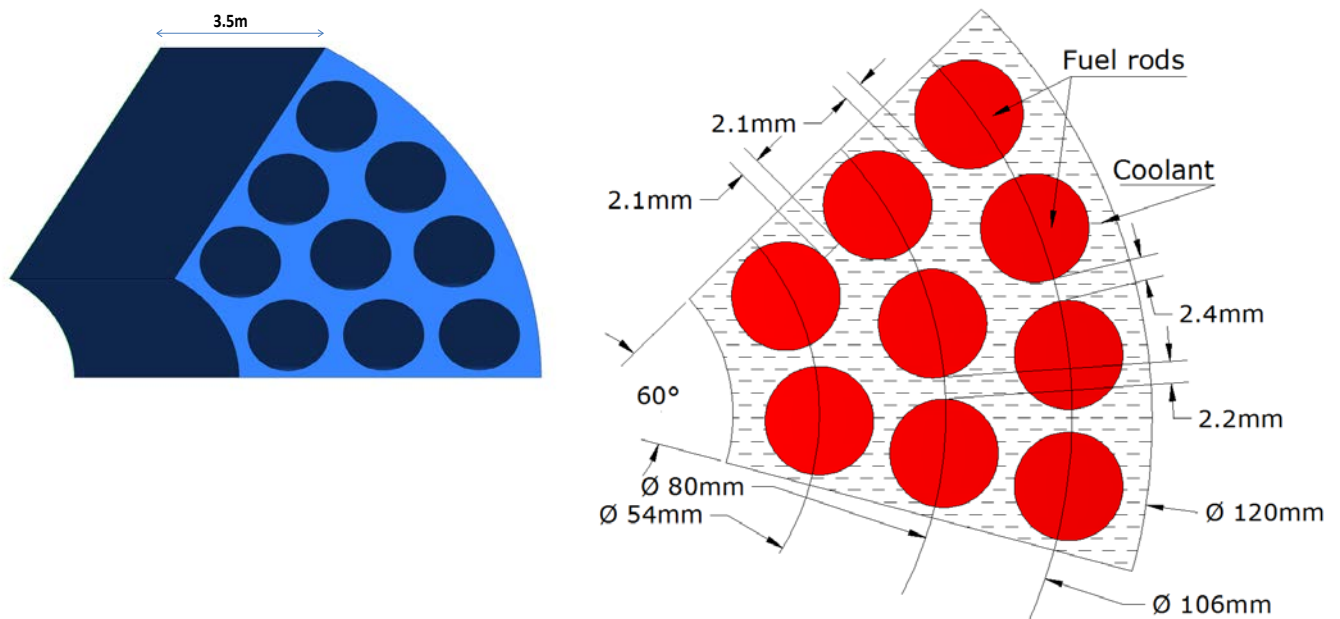


Figure-7.17 1/6th Symmetric sector of the rod bundle

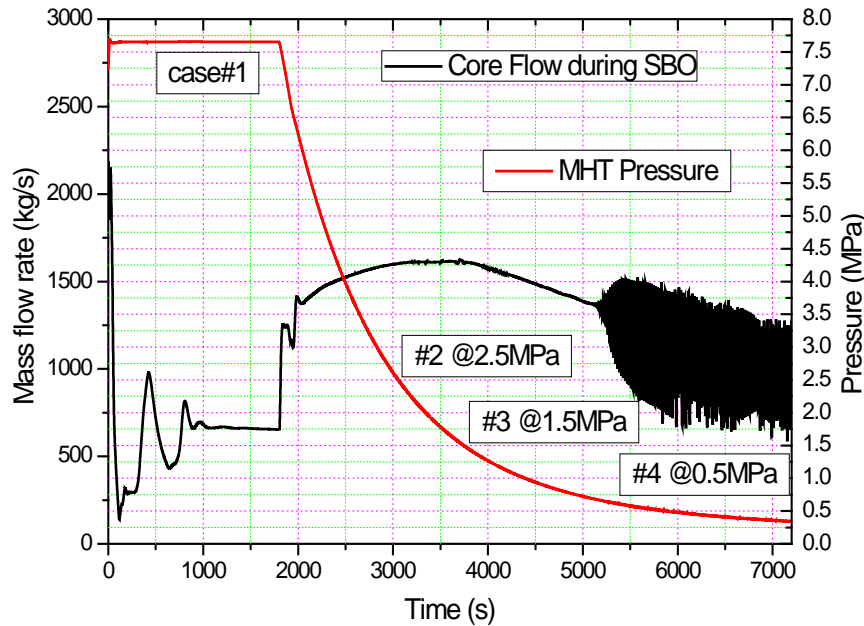
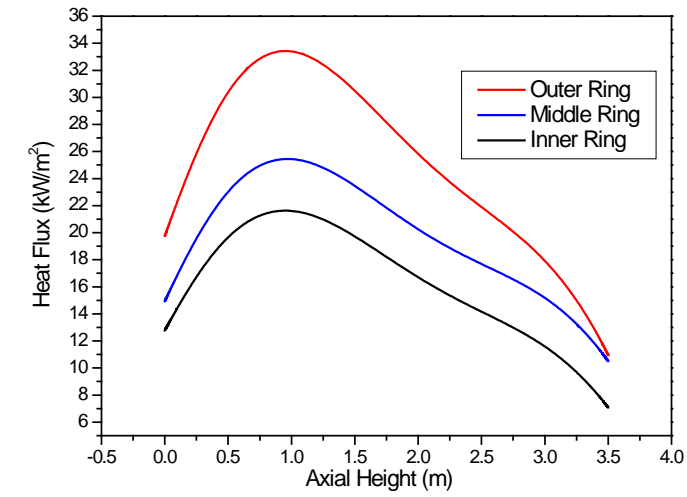


Figure-7.18 Core flow and MHTS pressure during SBO

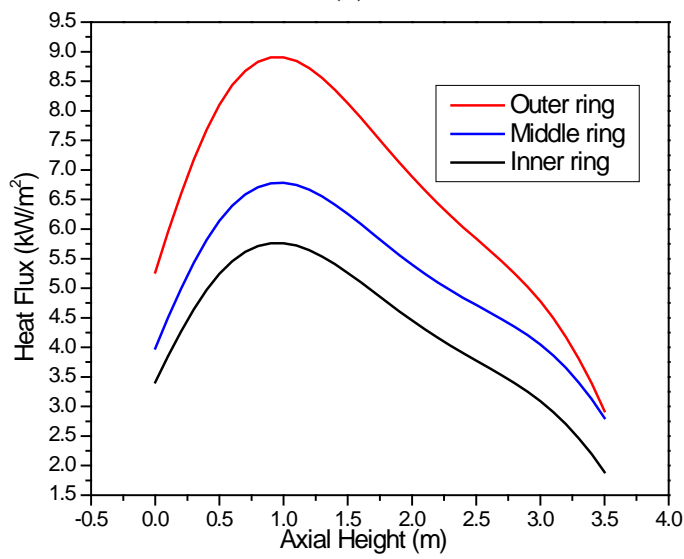
For understanding the flow behavior inside the rod bundle during these two different regimes, these cases are formulated and simulated i.e. Case#1 to Case#4. Table-7.9 shows the initial and boundary conditions obtained from RELAP5 simulations and studied with CFD. An axial and radial heat flux profile is applied to the fuel rods that simulate the decay heat for the considered instances during SBO. Figure-7.19a to 7.19c show the heat flux as applied to the fuel rods in three radial rings known as inner, middle and outer rings.

Table-7.9 Cases studied with CFD for local level thermal hydraulics

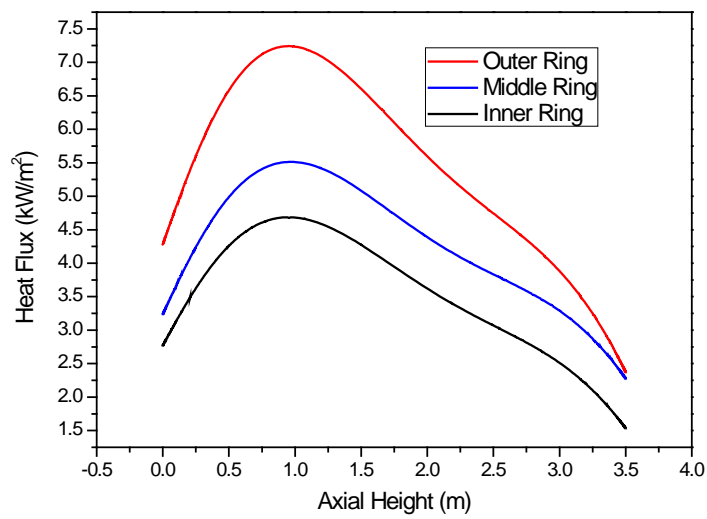
	SD Pressure (MPa)	Power	Core Inlet Temperature (°C)	Inlet Flow (kg/s)
Case #1	7.6	6.0%	285.05	0.245
Case #2	2.5	1.6%	227.0	0.627
Case #3	1.5	1.6%	201.0	0.627
Case #4	0.5	1.3%	152.0	0.480



(a)



(b)



(c)

Figure 7.19 Heat flux boundary conditions for (a) Case#1 (b) Case#2 & 3 (c) Case#4

The two phase flow is modeled through an Eulerian approach in which the phases are treated as interpenetrating continua. The ensemble averaged equations, commonly known as the Euler-Euler Two-Fluid-Model, conserves the single phase formulation by introducing a state variable to account for the volume occupied by each phase. The details of the models are discussed in chapter-5.

7.4.1 CFD Model setup for boiling flows inside rod bundle

The developed CFD frame work is validated against the experimental data as discussed in section 7.3.1. Validated and tested model is further applied for rod bundle CFD simulations. The simulations have been carried out for the three pseudo steady state instances as depicted in Table-7.9. Initial and boundary conditions for the rod bundle are shown in Table-7.9 and Figure-7.19. Table-7.10 shows the CFD models details chosen for the simulations. Variation for the boiling models has been considered for Case#1 and hence two sets of calculations have been performed. It has been seen in section 7.2.3 submodel performance studies for energy closures that the void fraction is under predicted with models of Case B. Hence, to check the consistency for rod bundle applications same models are also applied for Case#1. Figure-7.20 shows the planer mesh used for the simulations. Grid independence study has been carried out with five grid densities viz. 700K, 900K, 1400K, 1700K, and 3200K cells and the area averaged void fraction at the channel outlet has been compared. An average void of ~37% is observed at the out let of the channel as seen in Figure-7.21. A variation of less than 1% was observed from one grid to another (Figure-7.21), besides a maximum value of 30 is observed for wall y^+ as shown in Figure-7.22 for 1700K grid. The reported results correspond to simulations conducted on 1700K cell grids. The CFD data is extracted at various axial and radial planes. Figure-7.23 shows the axial and radial planes on which the results are presented for void, temperature and velocity distributions.

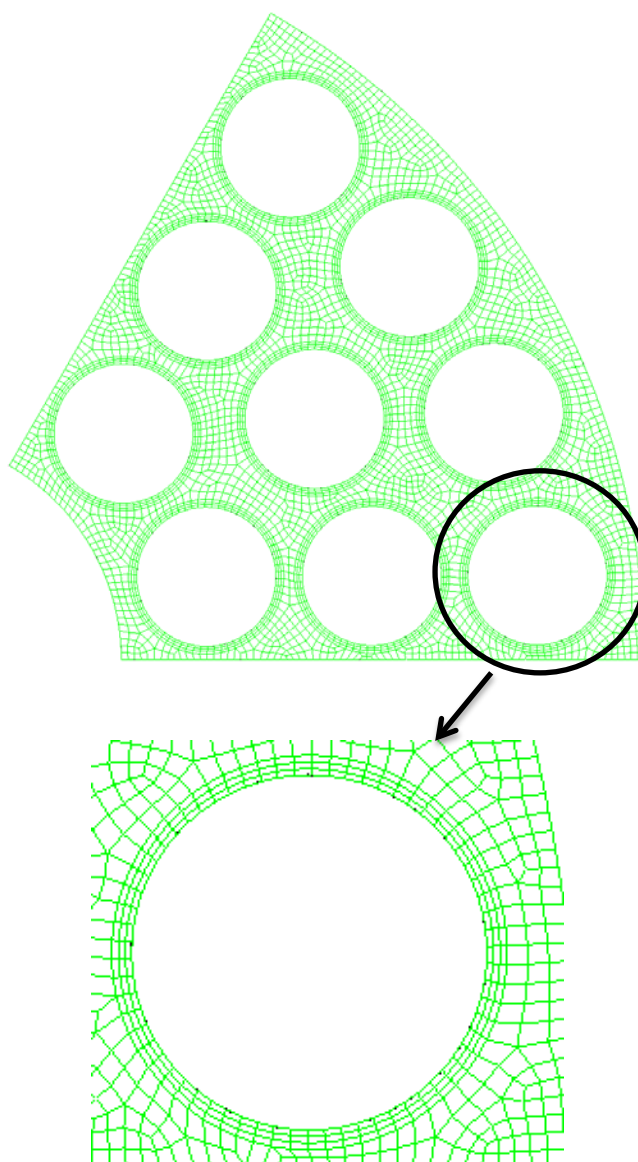


Figure-7.20 Top view of mesh for the 1/6th sector of the 54 rod bundle

Table-7.10 Details of CFD model

	Set#1	Set #2
CFD solver	Euler-Euler two phase solver	Euler-Euler two phase solver
Turbulence Model	RSM Mixture model	RSM Mixture model
Momentum closures		
Drag law	Tomiyama model (1999)	Ishii model (1979)
Turbulent dispersion	Burns et al. (2004)	Burns et al. (2004)
Bubble Induced Turbulence (BIT)	Sato et al. (1979)	Sato et al. (1979)

Energy and continuity closure		
Interface heat transfer	Ranz Marshall (1952)	Ranz Marshall (1952)
Boiling model	RPI model (1991)	RPI model (1991)
Bubble diameter	Kocamustafaogullari and Ishii (1983)	Kocamustafaogullari and Ishii (1983)
Bubble departure frequency	Cole Model (1960)	Cole Model (1960)
Nucleation Site Density	Kocamustafaogullari and Ishii (1983)	Lemmert-Chawla (1977)
Area Influence Coefficient	Delvalle-Kenning (1985)	Delvalle-Kenning (1985)
Solution procedure		
Algorithm	Coupled with void fraction	Coupled with void fraction
Convective schemes	2 nd order upwind for void distribution, momentum, energy, turbulent kinetic energy and dissipation	2nd order upwind for void distribution, momentum, energy, turbulent kinetic energy and dissipation
Convergence Criteria	Residual <1e-6	Residual <1e-6

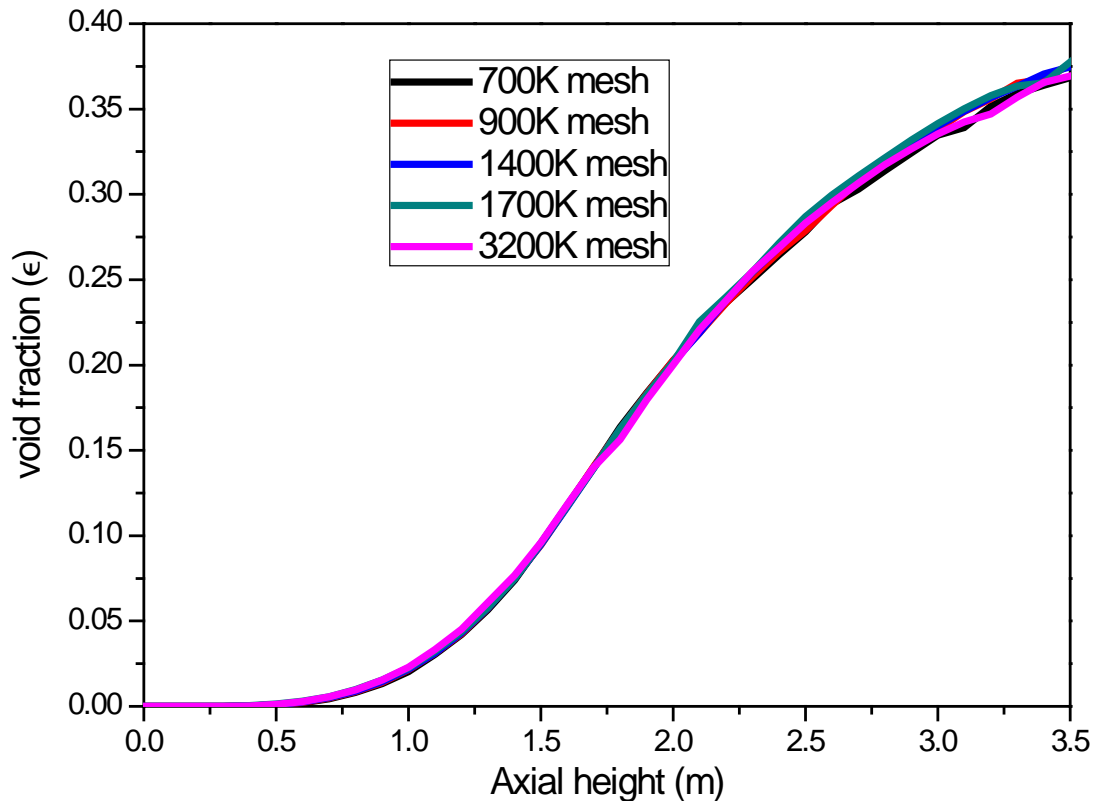


Figure-7.21 Axially averaged void distribution (Case#1) (Grid independence)

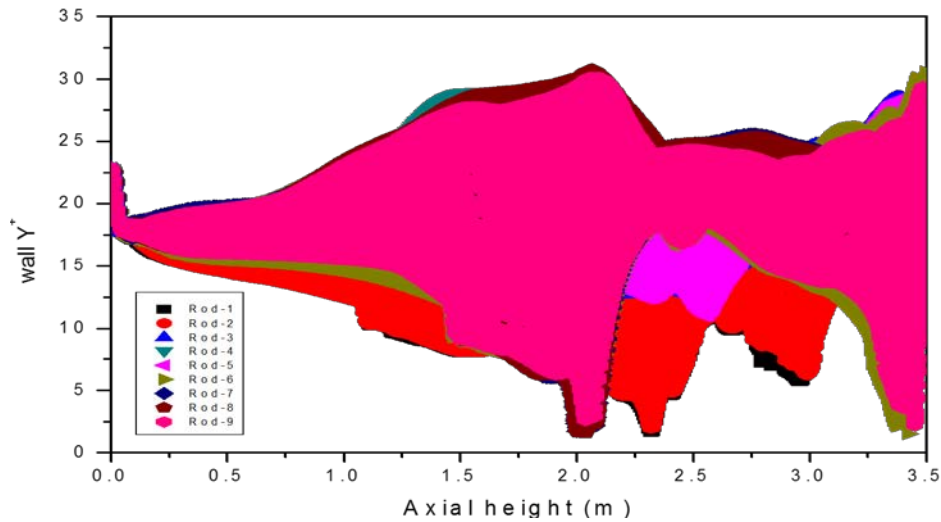
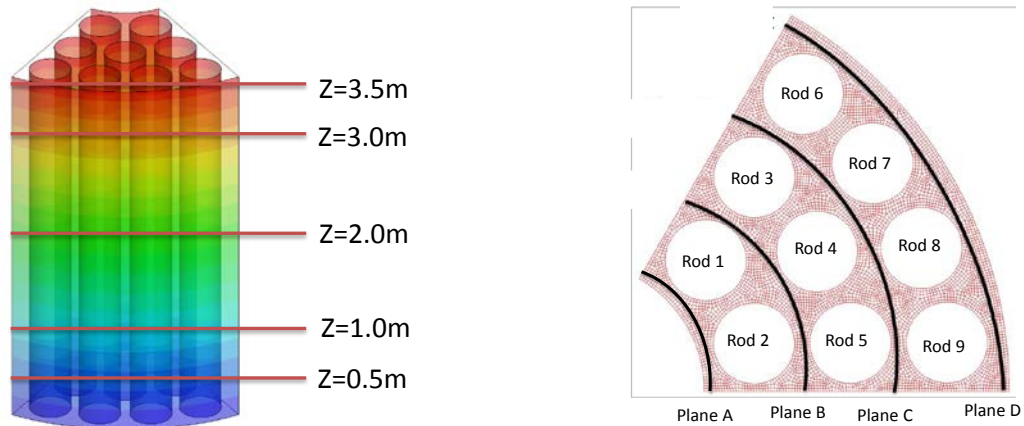


Figure-7.22 Wall y plus for heater rods



(a) Axial planes for CFD data presentation (b) Radial planes for CFD data presentation

Figure-7.23 various axial and radial planes for CFD data presentation

7.4.2 Results and discussions

Results for the void, temperature and velocity distribution are presented at various radial and axial planes (Figure-7.23).

Case#1 (Set-1 models)

Void, temperature and velocity distributions inside the rod bundle for the Case#1 are presented from Figure-7.24 to 7.35. Figure-7.24 shows the void distribution at various axial planes for Case#1 (6% decay heat). Void starts forming at ~1.0 m plane in the outer sub-channel as maximum heat is generated in the outer ring of the bundle. Substantial voiding is observed at axial location of 1.5 m from inlet with a void peak of ~35% and average of ~10%

occurring due to a bottom peaking profile of heat flux (peaking @ ~ 0.9 m from inlet). Mixing due to high void formation after 1.5 m is observed as seen from Figure-7.24 @ 2 m plane to 3.5 m plane which leads to a uniform void field after 1.5 m from inlet. Void distribution at various radial planes (Plane A, B, C and D shown in Figure-7.23b) is presented in Figure-7.25. It can be seen from the Figure-7.25 that there exist a non-uniform voiding region near to a plane @ 1.5 m from inlet before and after that uniform void distribution is observed. Few peaks in void (62%) is seen at outlet near the outer subchannel (Figure-7.24 and 7.25) due to high heat flux in the peripheral rods (Rod #6, and 9). Figure-7.26 and 7.27 show liquid temperature from inlet of the channel to the outlet. A maximum temperature of 567K is observed @ plane 1.5 m from inlet (Figure-7.26 and 7.27) near the heated wall. Temperature peaking at this plane shows existence of hot spot locations at this plane. However, maximum void at this location is only $\sim 35\%$. Temperature peak may be due to local cluttering of bubbles between the rods hindering the heat transfer phenomena. The availability of the liquid for removing the heat is less in the zone between rods, where high liquid temperature is observed.

Figure-7.28 shows the 2D angular distribution of void and liquid temperature at 5 axial planes as marked in Figure-7.23b. It is observed from temperature contours and 2D angular plots that the fluid temperature rises at angles corresponding to 17.5° and 45° for radial plane-A, 12.5° , 30° and 47.5° for radial plane-B, 10° , 30° and 50° for plane-C and 7.5° , 22.5° , 37.5° and 52.5° for radial plane D as seen in Figure-7.28. It happens due to the presence of fuel rods at these angular locations. This trend continues up to an axial location of ~ 1.25 m from inlet. After that a uniform temperature distribution is observed and temperature of the liquid remains close to the saturation temperature (564.5) of the liquid. This may be attributed to high heat transfer in sub-cooled boiling and void formation after 1.25 m in the vicinity of fuel rods. However, rise in the fluid temperature is observed slightly away from the wall where a

reduction in the void is seen after 1 m from inlet. It shows that bubble, after condensing in the bulk of the liquid, transfers its energy to the bulk fluid and raises the temperature of the fluid. Maximum average temperature is observed to be saturated temperature (564.5K). It is seen from Figure-7.28 that boiling started at a height of 0.5 m from inlet. However, area averaged fluid temperature becomes saturated at the outlet. Increase in voiding and liquid temperature is observed in the outer sub-channel due to high heat addition in this sub-channel. A high enthalpy zone is observed adjacent to the fuel rods 6 and 9.

Figure-7.29 shows the angular distribution of liquid and vapour phase velocity from inlet to outlet at radial planes A, B, C and D. Maximum velocity is found to be 0.8 m/s, while an average velocity field with 0.4 m/s has been employed at the inlet as the boundary conditions. A symmetric flow field is observed from the velocity contours. Maximum velocity is found to occur at relatively higher enthalpy zone i.e. between rods 3 & 7 and 5 & 8. In this study, it is seen that high enthalpy zone occurs between rods 3 & 7 and 5 & 8, and it does indicate a potential point for hot spot since the wall temperature rises above the saturation temperature of the liquid. It may be noted that, AHWR being a natural circulation based reactor, with increase in wall temperature, the void formation would increase which in turn would facilitate increase in flow inside the channel by increasing the buoyancy head. Figure-7.29 also shows the velocity field for the vapour phase. It shows occurrence of vapour velocity at around 0.25 m elevation from the inlet with practically no void generated at this location as depicted from Figure-7.29. Figure-7.30 shows the axially averaged velocities of the two phases from inlet to outlet and the void fraction. Around 1 m elevation from the inlet substantial vapour formed (void fraction ~2.5%) as seen from Figure-7.30 and 7.24; this point can be recognized as Net Vapour Generation (NVG) point. After 0.5 m elevation only, practical flow of the vapour is observed and a void fraction of ~10% is observed at this location. A uniform flow field is observed near the outlet of the channel because of enhanced mixing rates after 1.5 m from

inlet. Figure-7.31 shows average liquid temperature from inlet to outlet of the channel. The liquid temperature is found to be saturation temperature at the outlet of the channel. Figure-7.32 shows the typical heat flux for rod-1. It is evident from the Figure-7.32 showing various heat fluxes that all heat is transferred to the single phase liquid upto a height of 0.25 m. After that some amount of heat starts imparting to the evaporation and hence evaporative and quenching heat flux evolves. As soon as boiling starts, the single phase liquid heat transfer starts decreasing. Peak heat flux exists at an axial location of ~ 0.9 m. However, the peak in evaporation and quenching heat flux is observed slightly after 1.1 m plane and at ~ 1.5 m plane liquid phase heat transfer is found to be minimum. At this point heat could not be transferred to the liquid due to cluttering of the vapour phase near the fuel rods. Subsequently, the evaporative heat flux decreases as total heat flux also decreases after 1 m. Due to substantial mixing above 1.5 m, liquid heat flux starts rising. The bulk diameter of bubble is found to be maximum ~ 1.05 mm (Figure-7.33) at 1.5 m from inlet plane, where enhanced boiling is also observed. Further the bulk bubble diameter remained almost constant. The area average flow quality with the axial height is plotted in Figure-7.34 and it is found to be $\sim 4.23\%$ at the outlet. Figure-7.35 presents the mass transfer rate from liquid to vapour phase. A maximum mass transfer rate is observed at ~ 1.6 m from inlet, close to the minimum liquid heat flux location.

With this analysis, it is evident that substantial boiling only starts 1 m from inlet; however boiling inception is observed at a plane 0.5 m from inlet. High enthalpy zone is observed near 1.5 m plane, which is prone to have hot spots on the fuel rods.

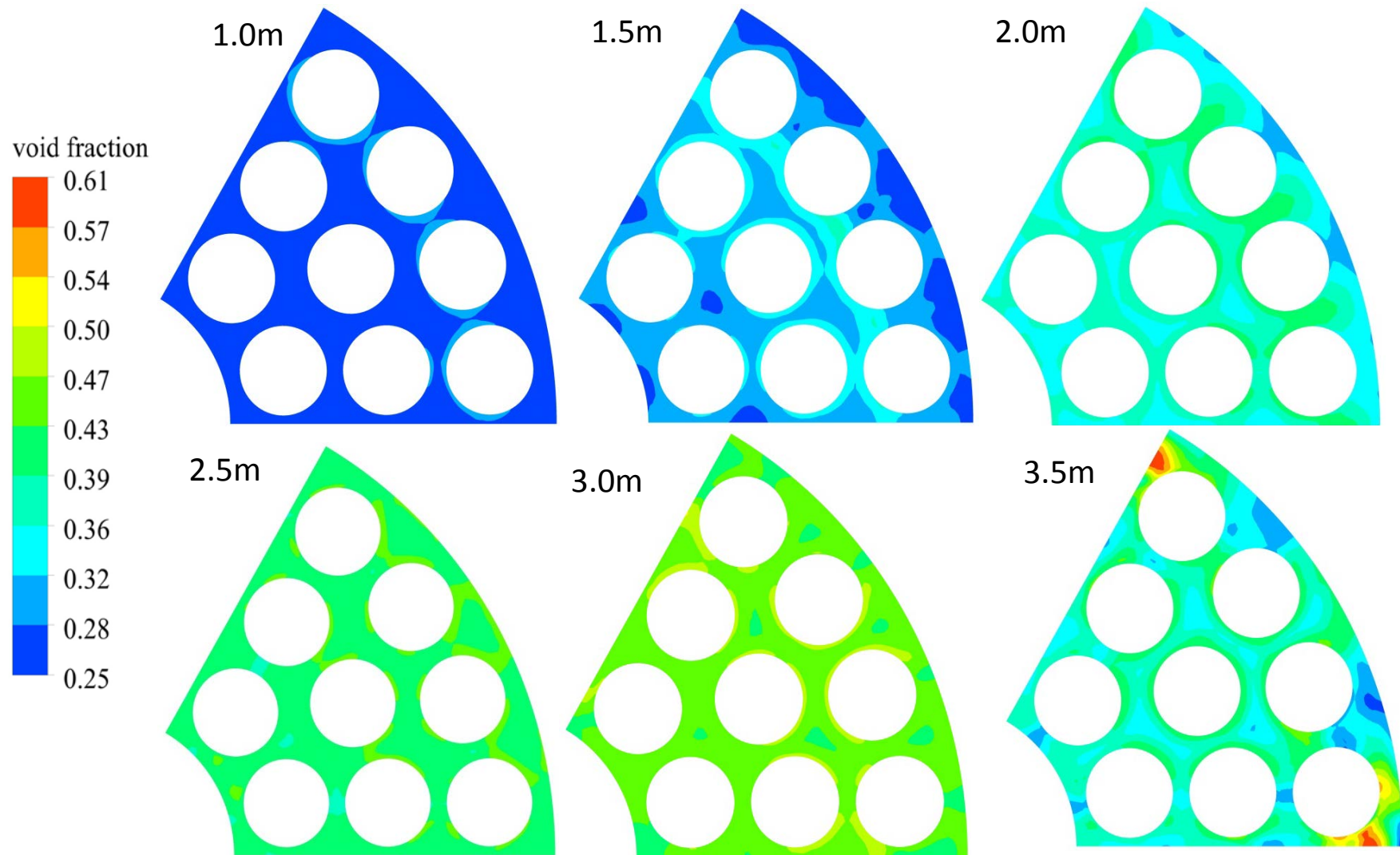


Figure-7.24 void distribution at various axial planes for Case#1

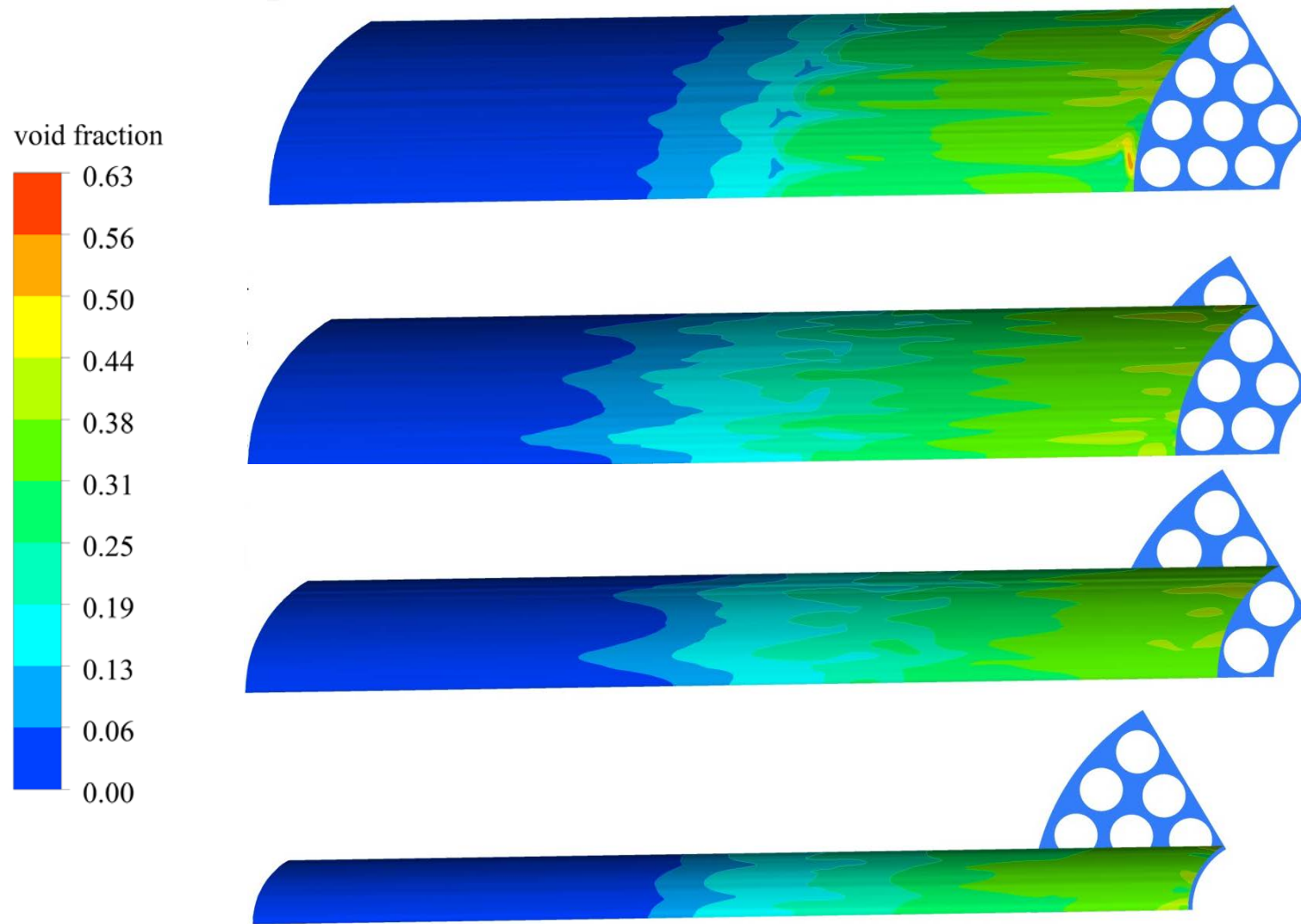


Figure-7.25 void distribution at various radial planes for Case#1

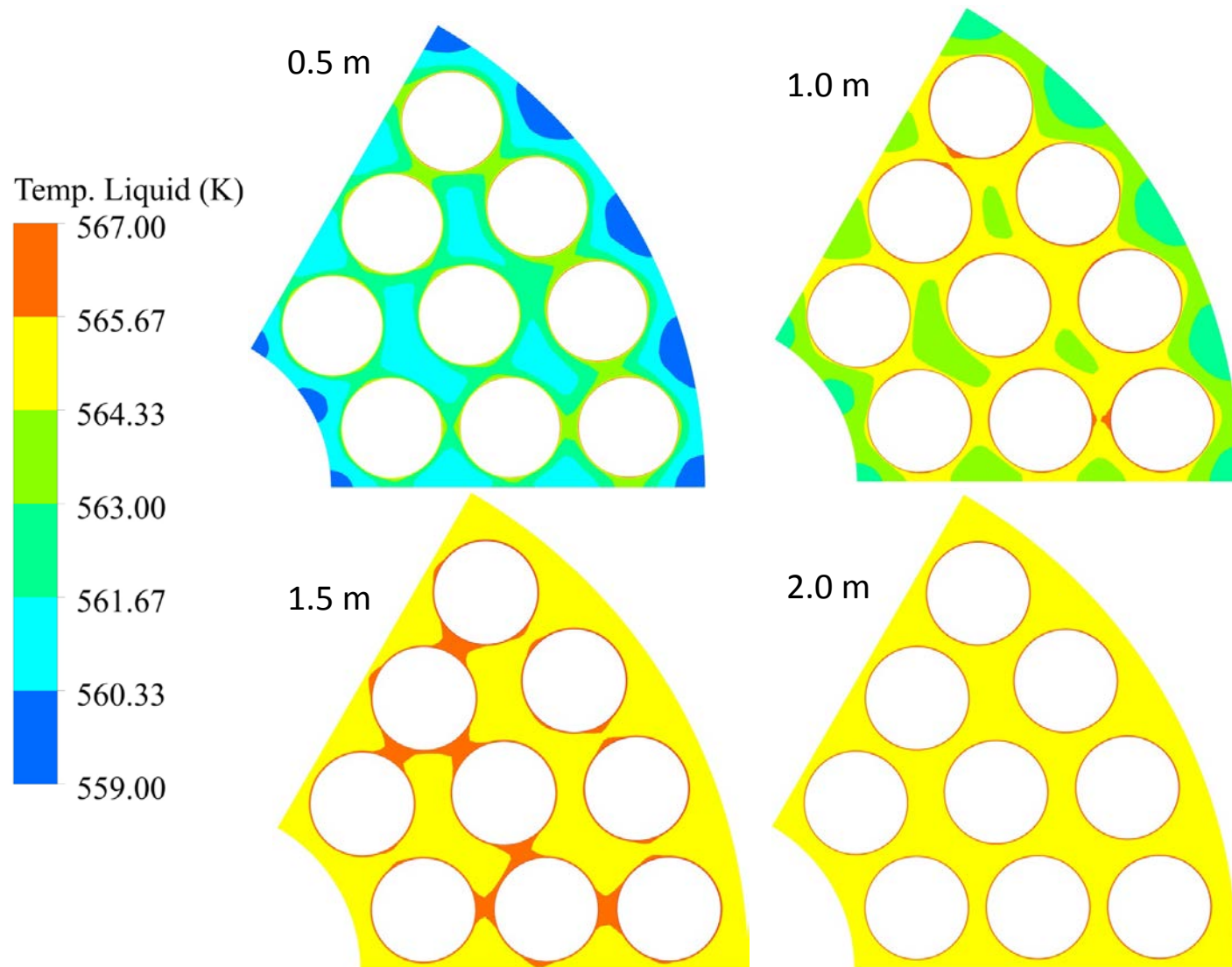


Figure-7.26 Temperature distribution at various axial planes for Case#1

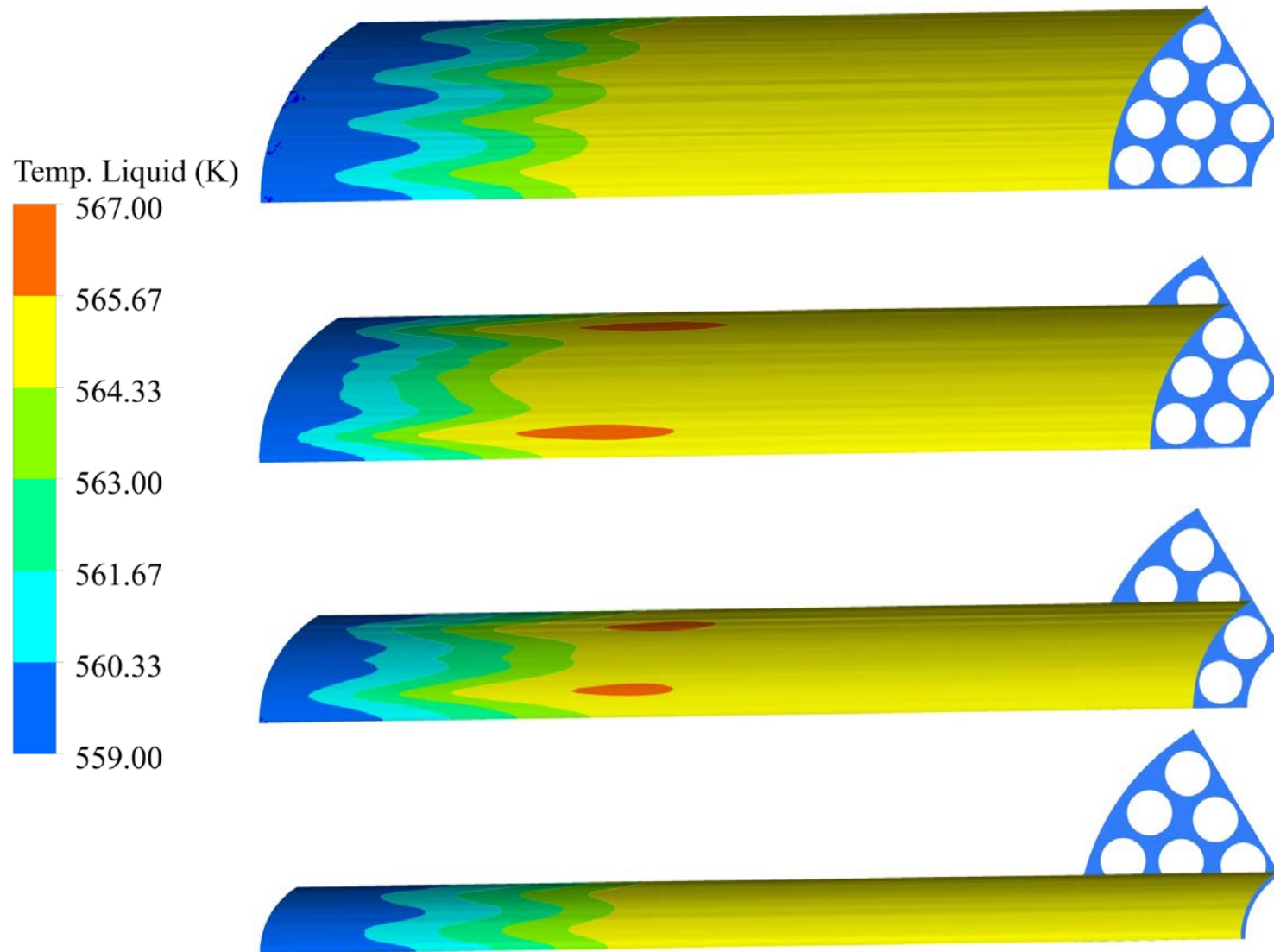
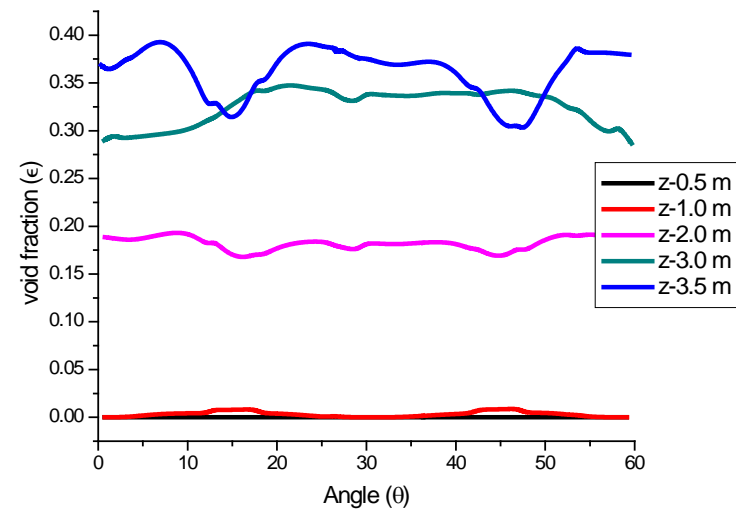
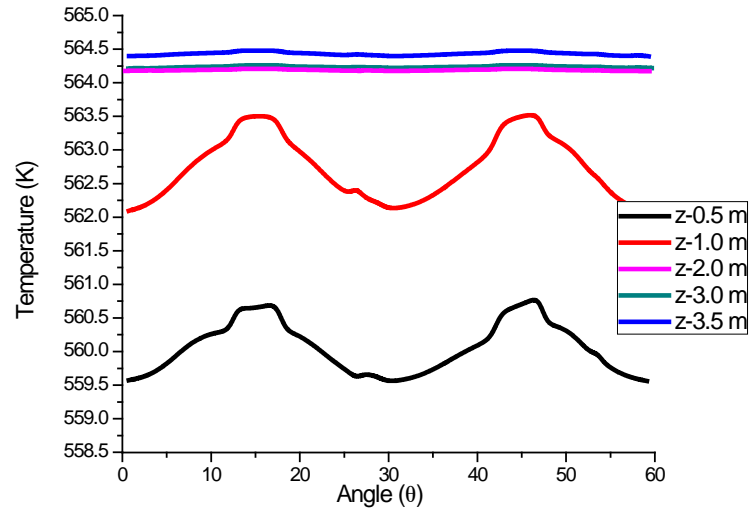
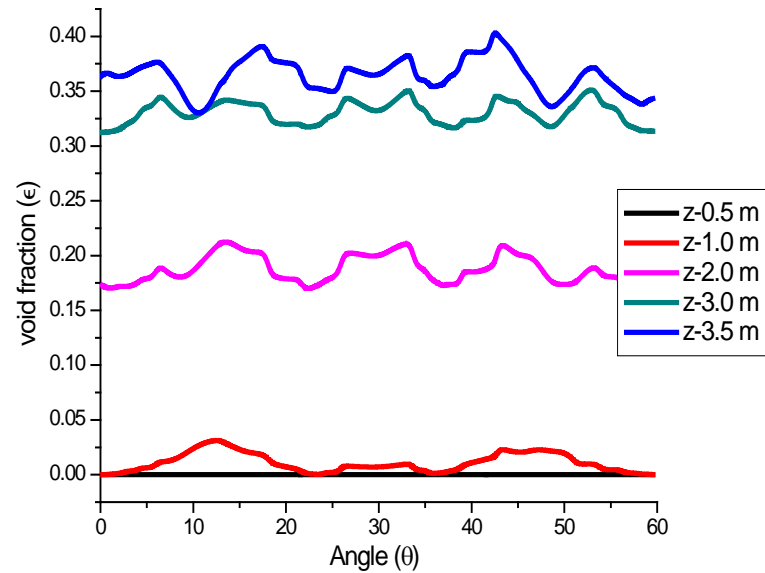
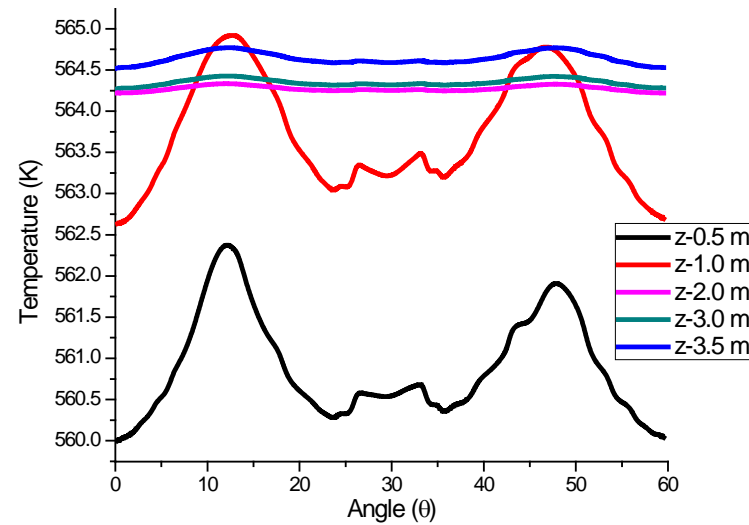


Figure-7.27 Temperature distribution at various radial planes for Case#1



Plane-A



Plane-B

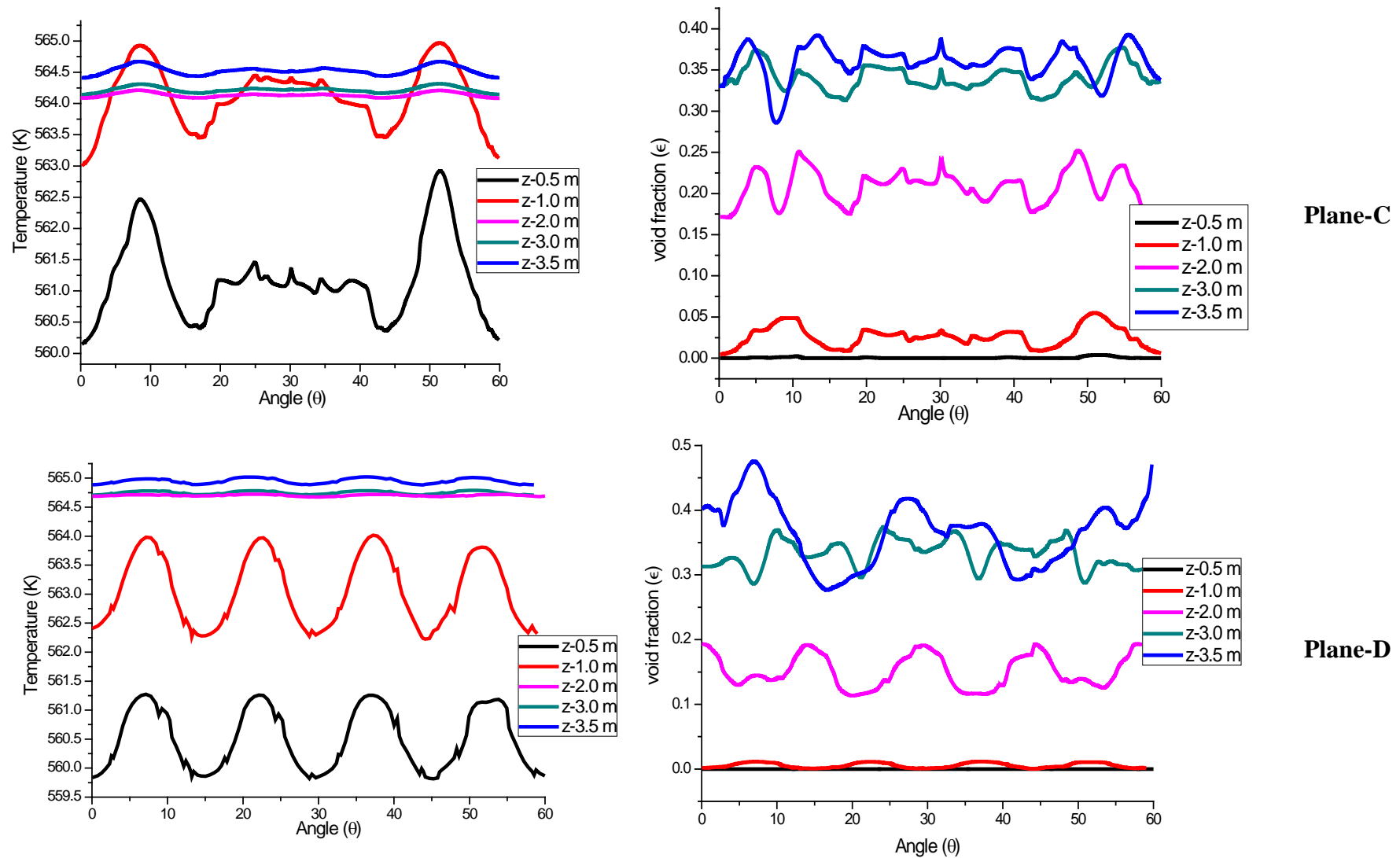
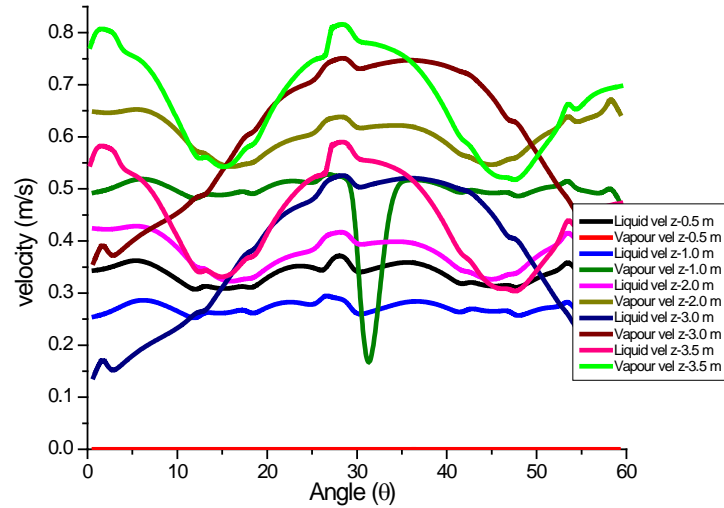
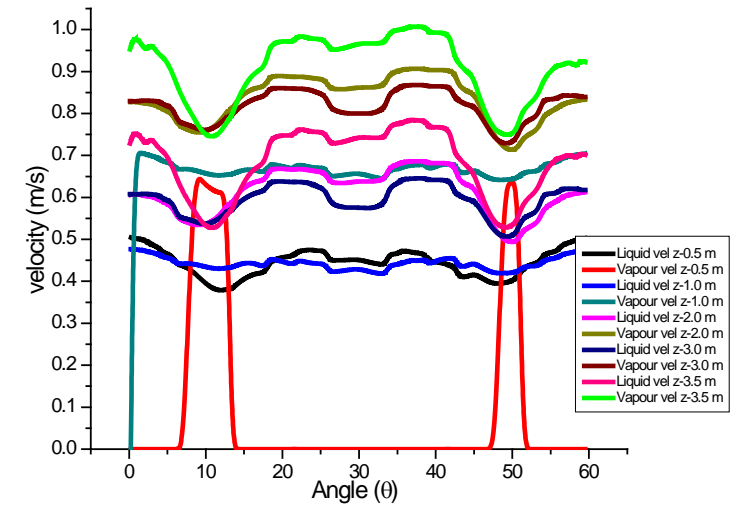


Figure-7.28 Angular temperature and void distribution on radial planes A, B, C and D for Case#1

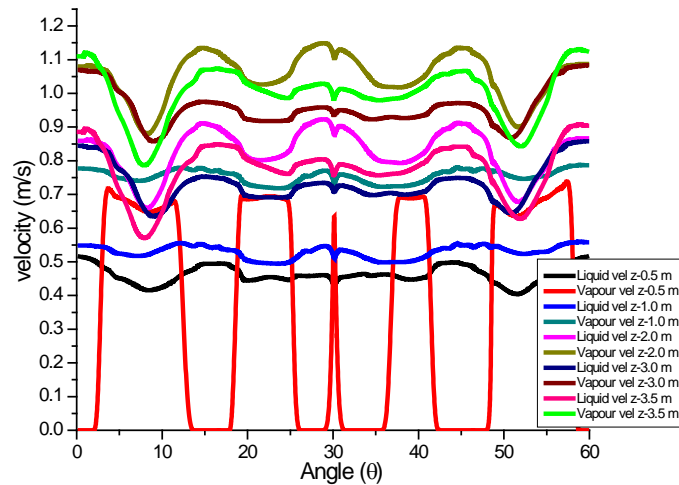


(a) Angular velocity distribution @Plane-A

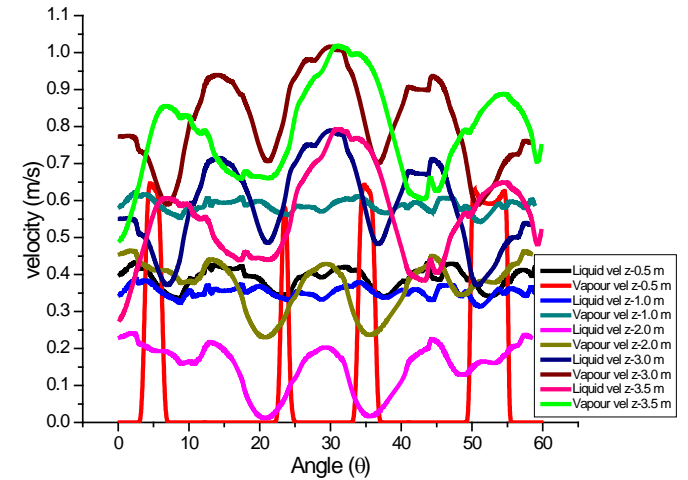
— Liquid vel z-0.5 m
— Vapour vel z-0.5 m
— Liquid vel z-1.0 m
— Vapour vel z-1.0 m
— Liquid vel z-2.0 m
— Vapour vel z-2.0 m
— Liquid vel z-3.0 m
— Vapour vel z-3.0 m
— Liquid vel z-3.5 m
— Vapour vel z-3.5 m



(b) Angular velocity distribution @Plane-B



(c) Angular velocity distribution @Plane-C



(d) Angular velocity distribution @Plane-D

Figure-7.29 Angular velocity on radial planes A, B, C and D for Case#1

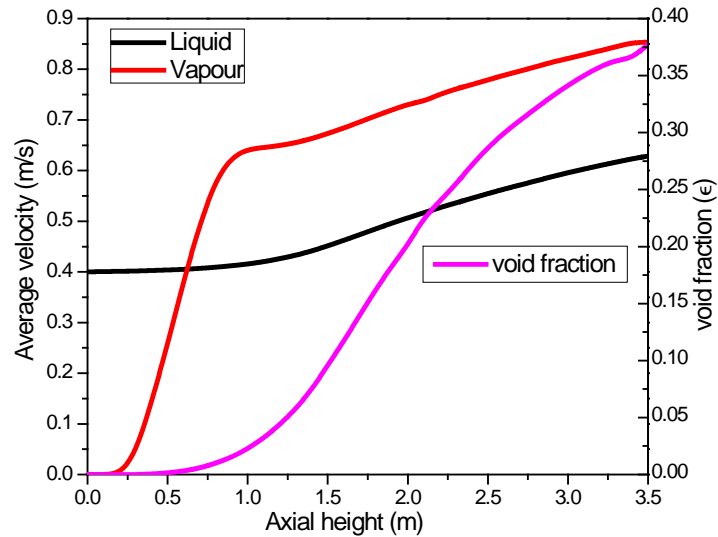


Figure-7.30 Axial phasic velocities and void distribution for Case#1

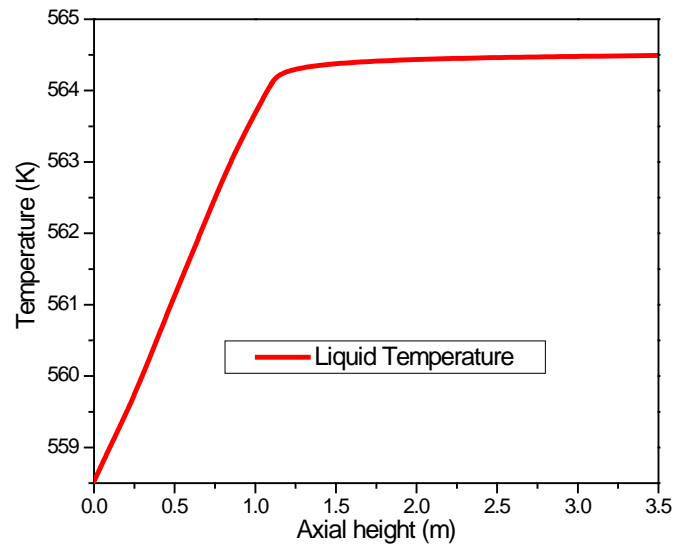


Figure-7.31 Average liquid temperature for Case#1

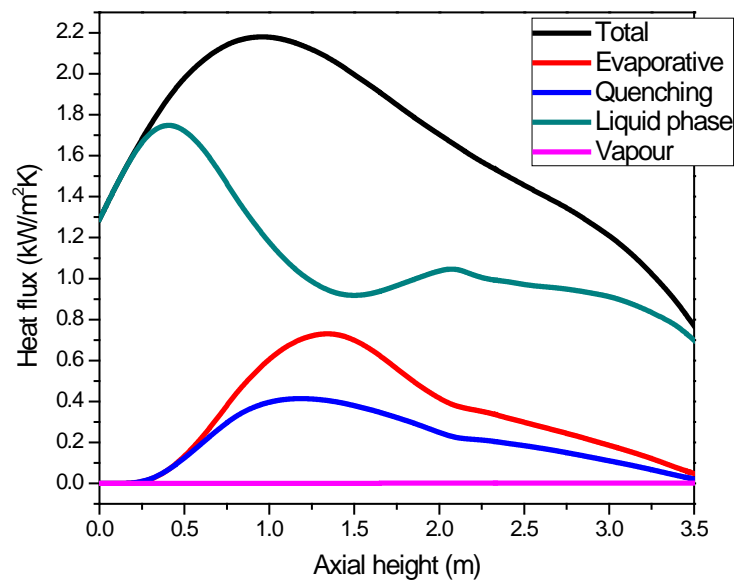


Figure-7.32 various axial heat fluxes for Case#1

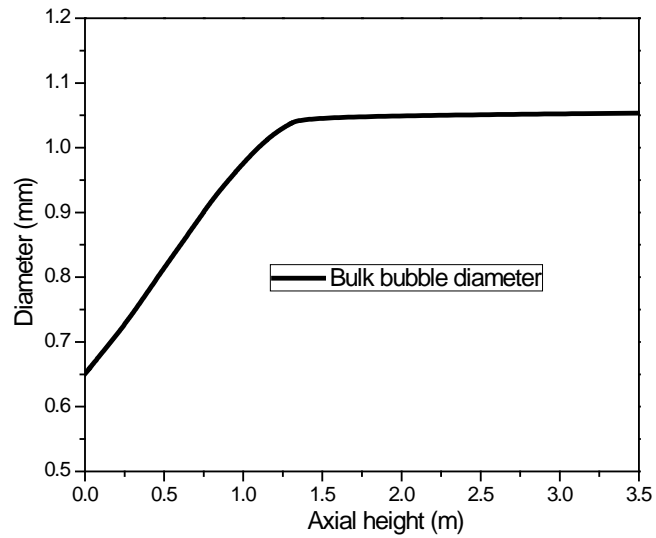


Figure-7.33 Bulk bubble diameter from inlet to outlet for Case#1

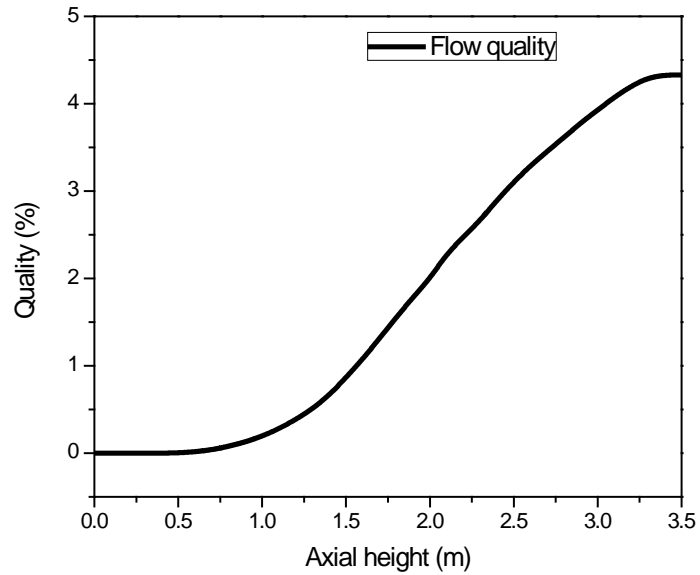


Figure-7.34 Average axial flow quality for Case#1

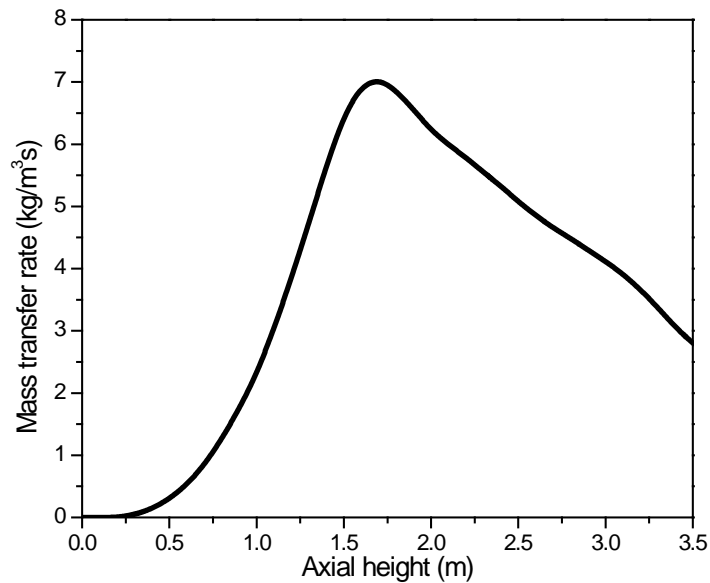


Figure-7.35 Average axial mass transfer rate for Case#1

RELAP simulation for Case#1

Case#1 has also been analysed with system code RELAP5 mod 3.2. The entire length of the bundle has been divided in 24 axial nodes of equal sizes. The boundary conditions have been simulated with time dependent volumes and junction. Two types of cases have been analysed for the bundle during SBO conditions i.e. with uniform power and with axially varying power. All the 9 rods are lumped together and radially averaged power has been applied but the power applied is varying axially. Figure-7.36 shows the details of the RELAP5 model.

A constant flow of 0.245kg/s has been simulated with Time Dependent Junction (TDJ) connected to a Time dependent Volume (TDV) @558.5K. The outlet pressure has been maintained with another TDV connected at the top of the channel @7.6MPa.

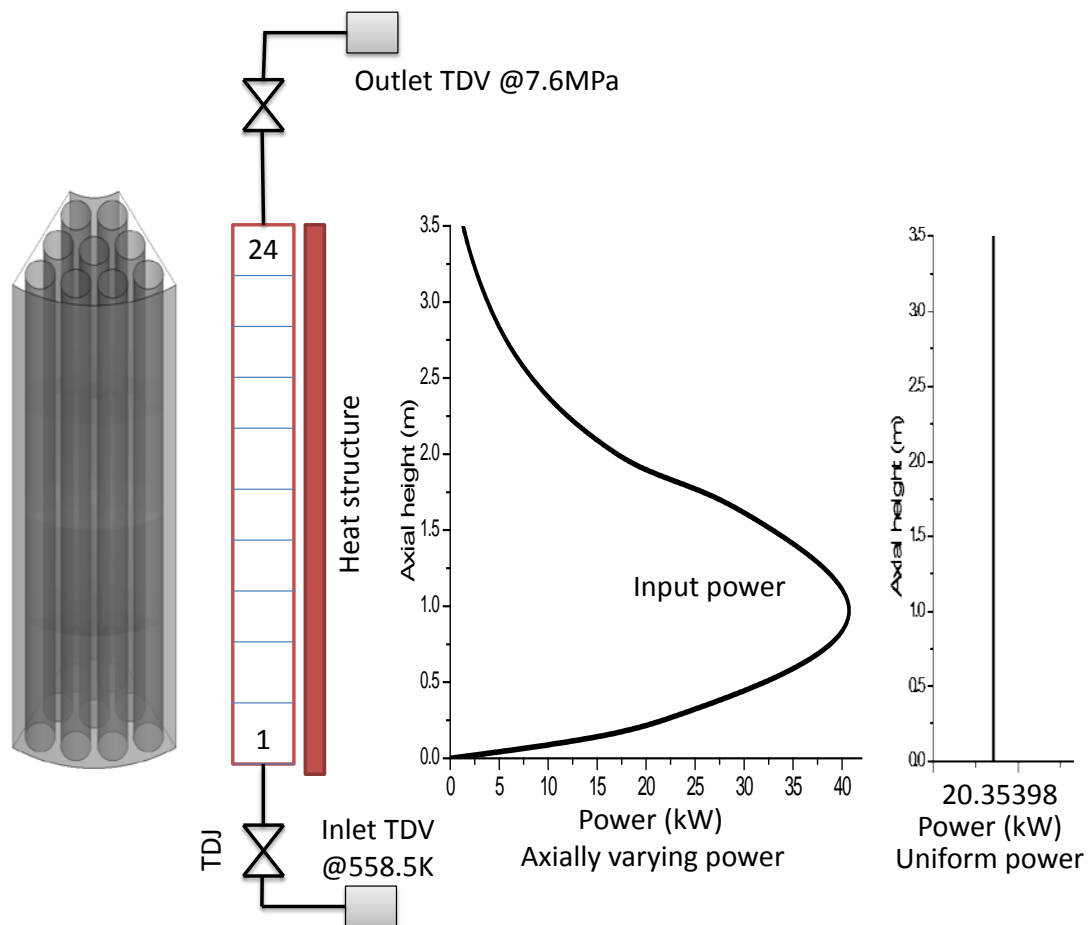


Figure-7.36 Details of the RELAP5 model for case#1

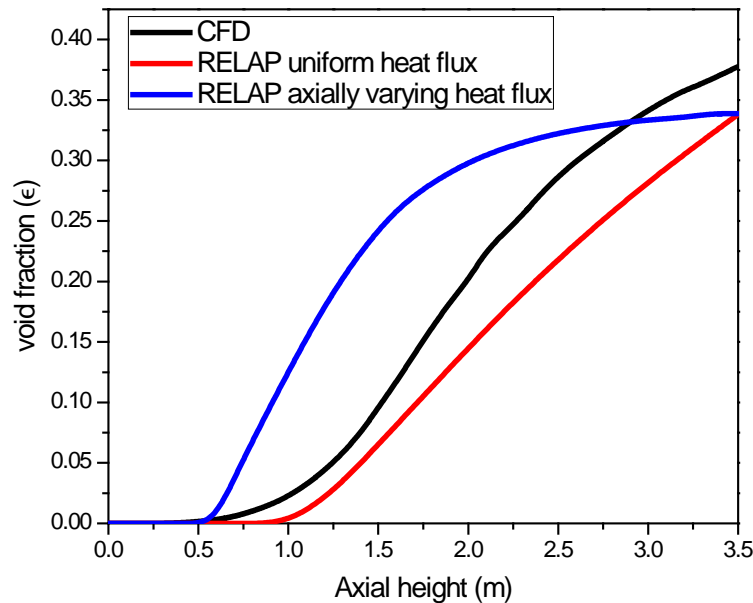


Figure-7.37 Average axial void distribution RELAP and CFD

Figure-7.37 shows area averaged axial void distribution as predicted by RELAP and compared with CFD results. In this case also RELAP under predicts the void at outlet. The outlet void fraction as predicted by RELAP is ~33% as compared to ~37% predicted by CFD. When axially varied power is applied to the bundle rods, a sharp rise in the void is observed due to higher power at the bottom. Both RELAP and CFD predicts the boiling inception in agreement. RELAP-5 utilizes Saha-Zuber correlation for location of the NVG point which fits better with the experiment. However, it under predicts the void after NVG point which may be attributed to the under prediction of wall voidages during subcooled boiling conditions.

For high void flows the interfacial friction plays dominating role. The models used by RELAP-5 for interfacial friction are developed for small diameter tubes and under predicts the interfacial area which are not applicable to the flows with larger interfacial area. Owing to this reason, RELAP over predicts the void at the outlet of the pipe flows with larger diameters. However, we have simulated the flow inside a tube of diameter 11.2 mm, which fall well within the limits of the RELAP-5 models for voidage predictions. Also, the hydraulic diameter of the rod bundle is 8.2 mm so RELAP models are able to predict the void fractions inside the rod bundle. There

found to be a variation of 10% between RELAP and CFD which is reasonable for two phase flow predictions.

However, after boiling inception further rise in CFD predictions is less than the RELAP predictions. This may be attributed to the 3D mixing effects homogenizing the void in case of CFD with lesser mean bubble diameter and interfacial area particularly inside the rod bundle (inter rod gap~2-3mm). RELAP treats the rod bundle with equivalent hydraulic diameter pipe. The real gap between the rods is very small only 2-3 mm as compared to the hydraulic diameter of 8 mm requiring multidimensional modeling treatment. The concept of equivalent hydraulic diameter is not very well explainable for rod bundles due to very small inter rod gaps. Turbulent two phase flow is essentially multidimensional in nature. CFD simulations utilize the detailed modeling of the interfacial forces based on the bubble diameter in the bulk as well as the bubble departure diameter considering the actual flow field surrounding the bubble. In case of uniform power applied for the RELAP simulations the void as predicted by RELAP is remained lesser than the CFD predictions.

Case#1 (Set-2 models)

For simulation of boiling flows over rod bundle, the boiling closures which show completely different results, as seen in section 7.3.2 case B models (energy closures), are applied for rod bundle case also. Even though applicability of those set of models is not established for high pressure boiling conditions, but to check their consistency for different geometry, their performance has been analyzed.

Typical results using those models are presented here for comparison. The area average void at the outlet is observed to be ~22% as compared to the predictions (~37%) with Set#1 models as seen in Figure-7.38. it under predicts the void, which is also found to be consistent with Bartolomei case. Maximum void is found to be 0.71 as compared to 0.62 for former models, at an axial location ~2.5m from inlet on the outer ring rods. Void and temperature distribution at

various radial planes (Plane A, B, C and D shown in Figure-7.23) is presented in Figure-7.39. It is observed from temperature contours and 2D angular plots that the fluid temperature rises at angles corresponding to 17.5° and 45° for radial plane-A, 12.5° , 30° and 47.5° for radial plane-B, 10° , 30° and 50° for plane-C and 7.5° , 22.5° , 37.5° and 52.5° for radial plane D as seen in Figure-7.39. Similar trends have been seen for the former set of models, it is due to the presence of fuel rods at these angular locations. This trend continues up to an axial location of ~ 1.25 m from inlet. After that a phase shift of 180° is observed. This may be attributed to high heat transfer in sub-cooled boiling and void formation after 1.25 m in the vicinity of fuel rods. Maximum temperature is observed to be saturated temperature and it is observed that boiling started at a height of 0.5 m from inlet. A peaking in void is observed in central location of plane-A near outlet (different from other axial locations, Fig-39a) which is capturing the nature of the vapour to move toward high velocity region (central region).

Here with these models large differences with the previous results are observed, which shows their invariability with geometry.

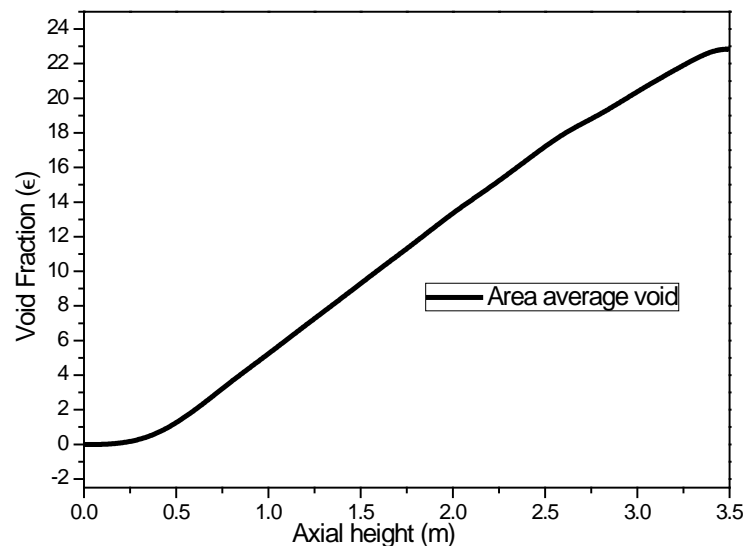
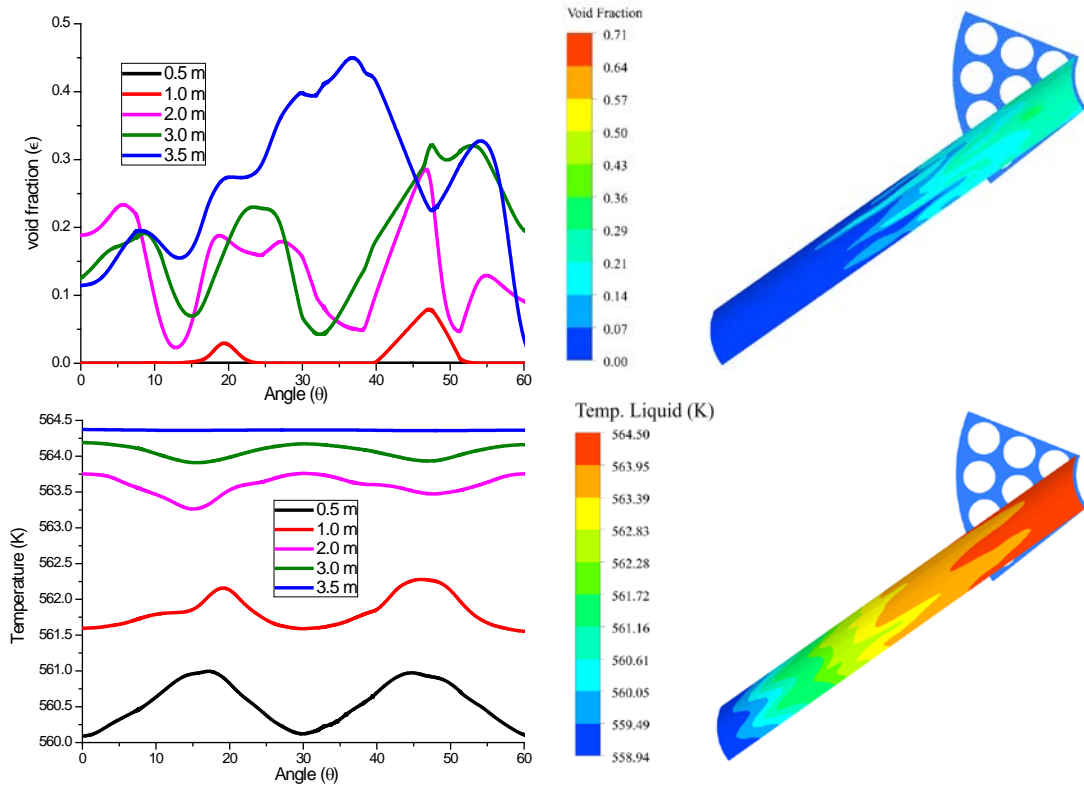
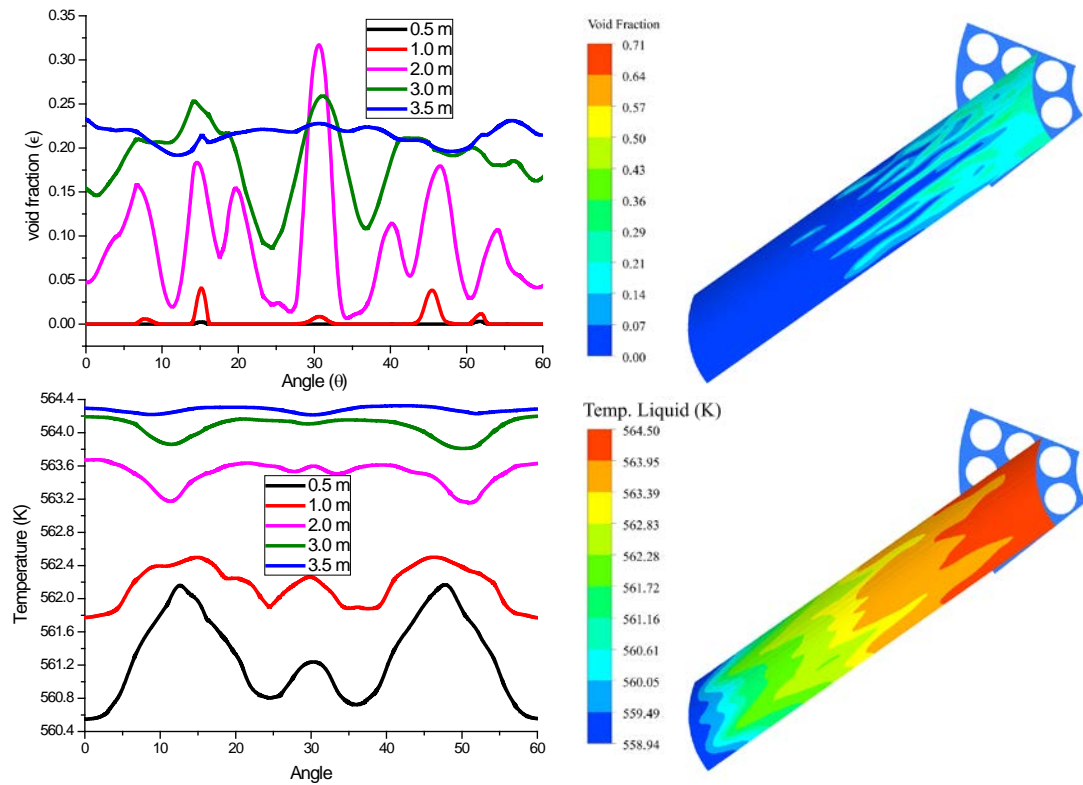


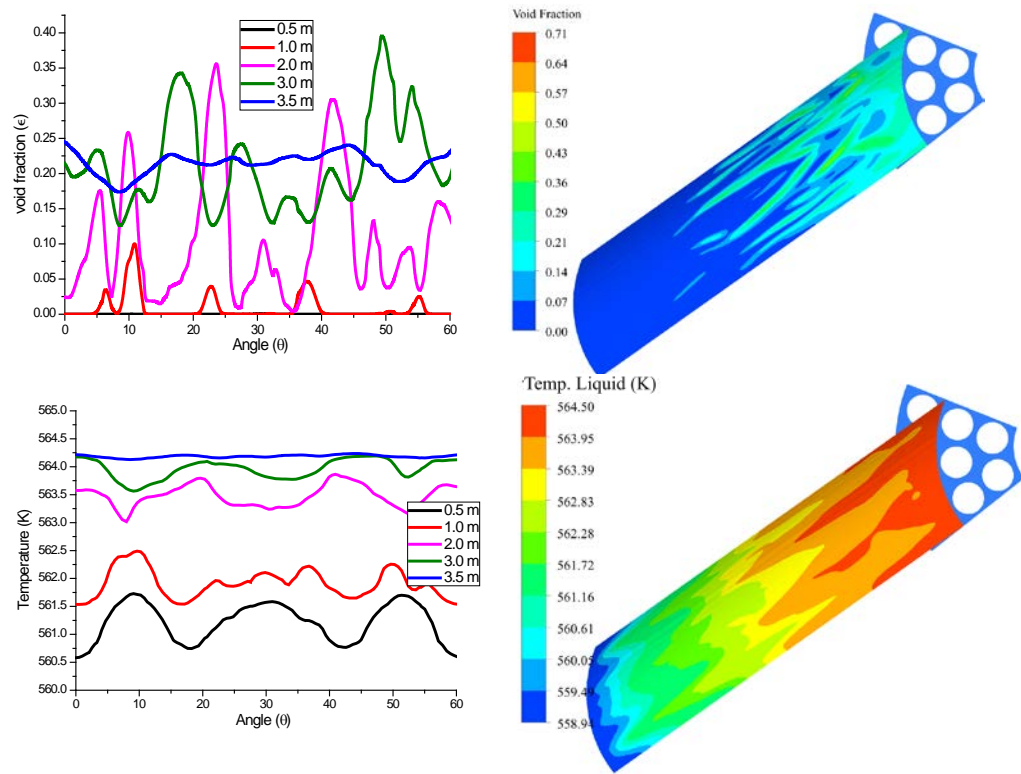
Figure-7.38 Average void fraction from inlet to outlet with Set#2 models



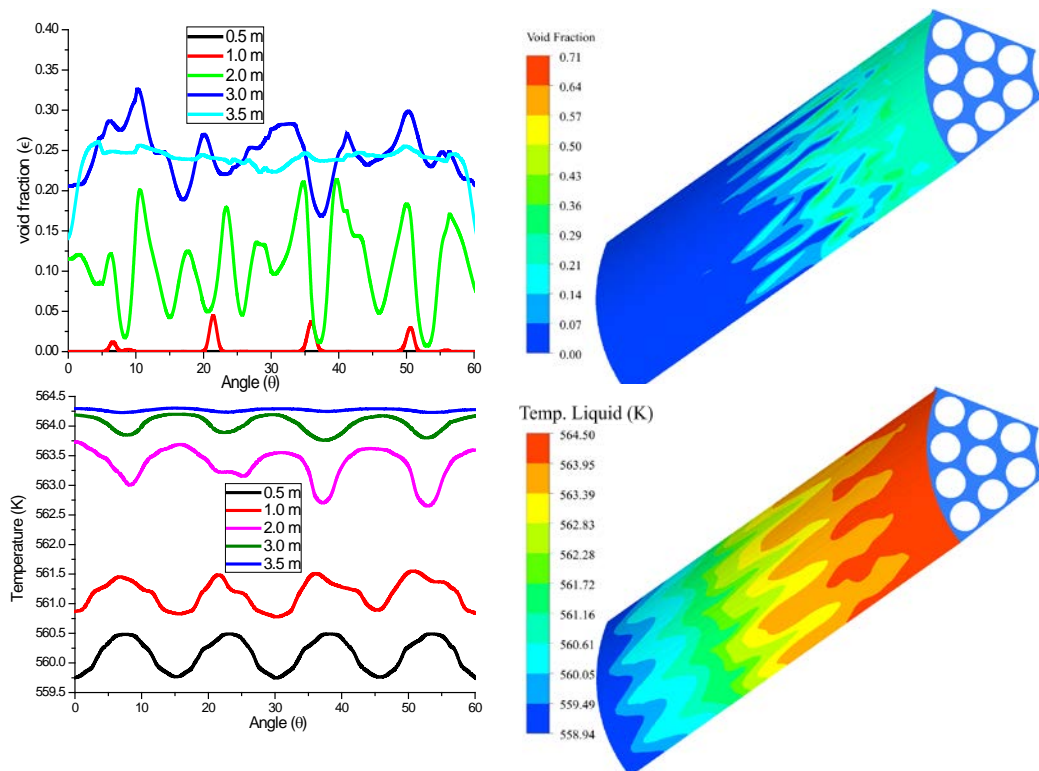
(a) Void and temperature distribution @ radial plane A from inlet to outlet



(b) Void and temperature distribution @ radial plane B from inlet to outlet



(c) Void and temperature distribution @ radial plane C from inlet to outlet



(d) Void and temperature distribution @ radial plane D from inlet to outlet

Figure-7.39 Angular void and temperature distribution from inlet to outlet for Case#1 with Set#2 models

Case#2

CFD simulations were carried out for an instance at steam drum pressure of 2.5 MPa. The fluid of 227°C temperature enters at a uniform velocity of 1.0 m/s at the inlet. Figure-5.40 and 5.41 shows radial contours of liquid temperature and liquid velocity respectively from inlet to outlet at various axial planes. A radially symmetric temperature and flow field can be observed from these figures. Prominent mixing between the sub-channels is not observed in this case unlike the former case. Therefore, it shows two-phase flow assisted turbulent mixing is more prominent than single phase turbulent mixing in rod bundle. Figure- 7.42 and 7.43 shows the temperature and velocity distribution at radial planes A, B, C, and D. Axial temperature contours and 2D angular plots show that fluid temperature rises at angles of 17.5° and 45° for radial plane-A, 12.5°, 30° and 47.5° for radial plane-B, 8°, 30° and 52° for plane-C and 7.5°, 22.5°, 37.5° and 52.5° for radial plane D as seen in Figure-7.44. This is due to the presence of fuel rods at these angular locations. Angular temperature peaks are associated with lesser velocity at those points as seen from the 2D angular velocities profiles for Planes-A, B, C, and D. Also, velocity peaks are observed at the points where temperatures are low. It is due to the fact that velocity in the vicinity of the wall will be zero due to zero slip condition and it continuously increases moving away from the wall and hence temperature will be dropped at higher velocity regions.

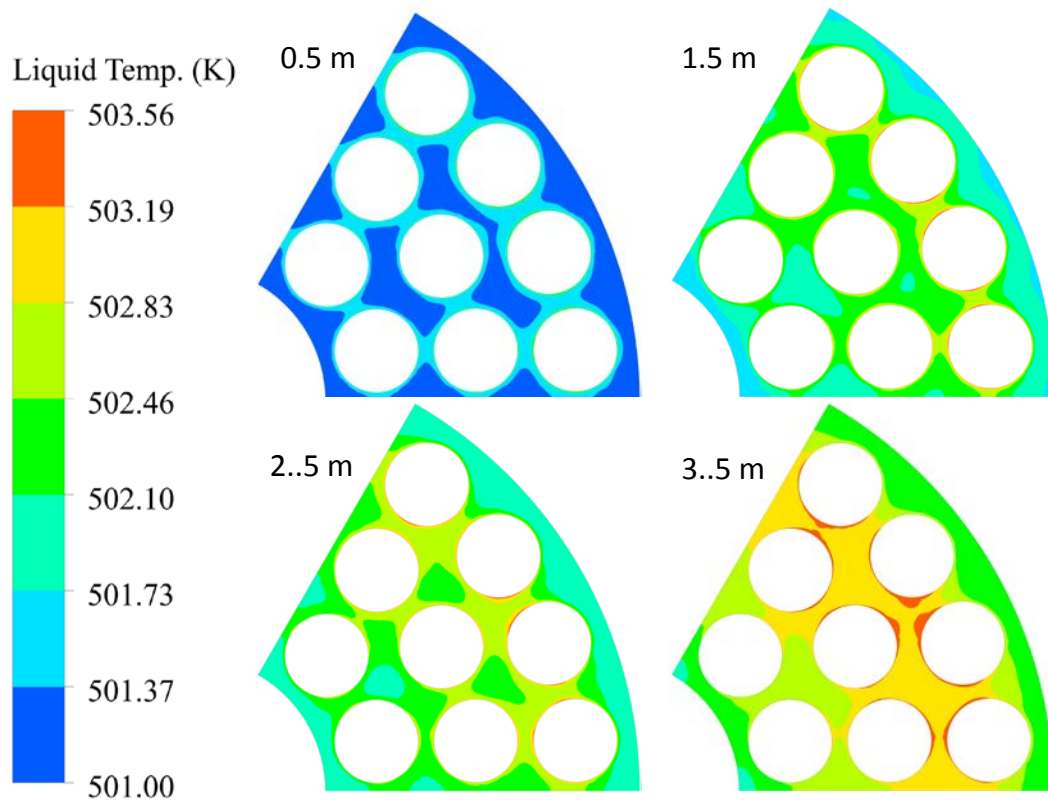


Figure-5.40 Radial temperature distribution at various axial planes

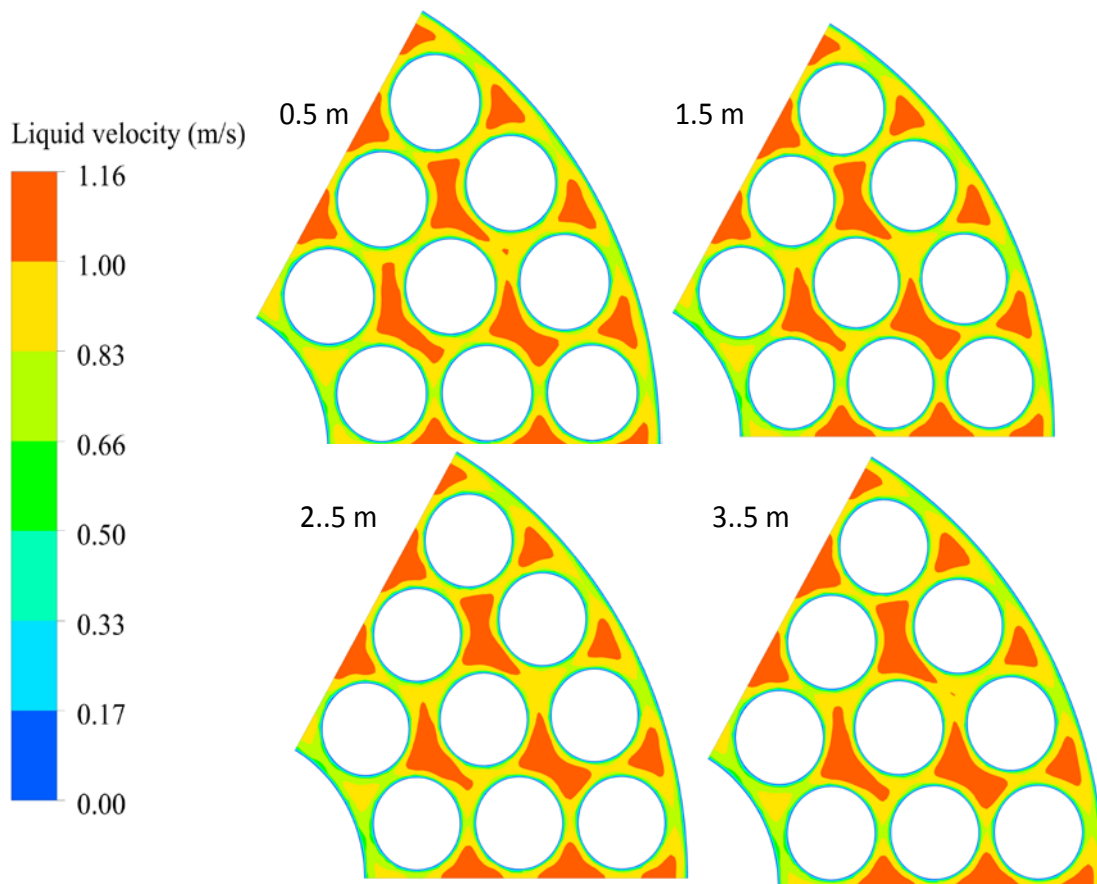


Figure-5.41 Radial velocity distribution at various axial planes

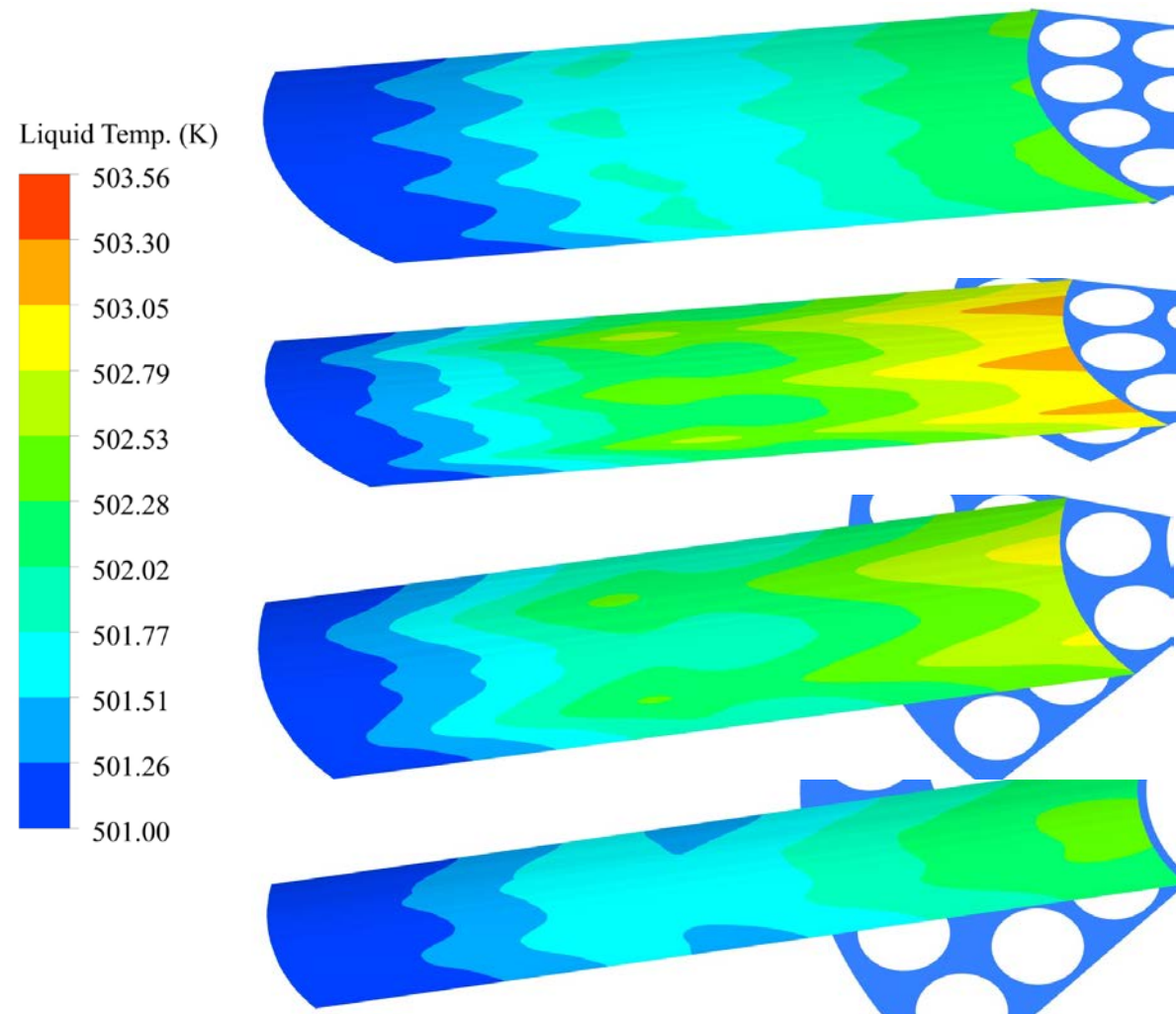


Figure-7.42 Liquid temperature distribution at various radial planes for Case#2

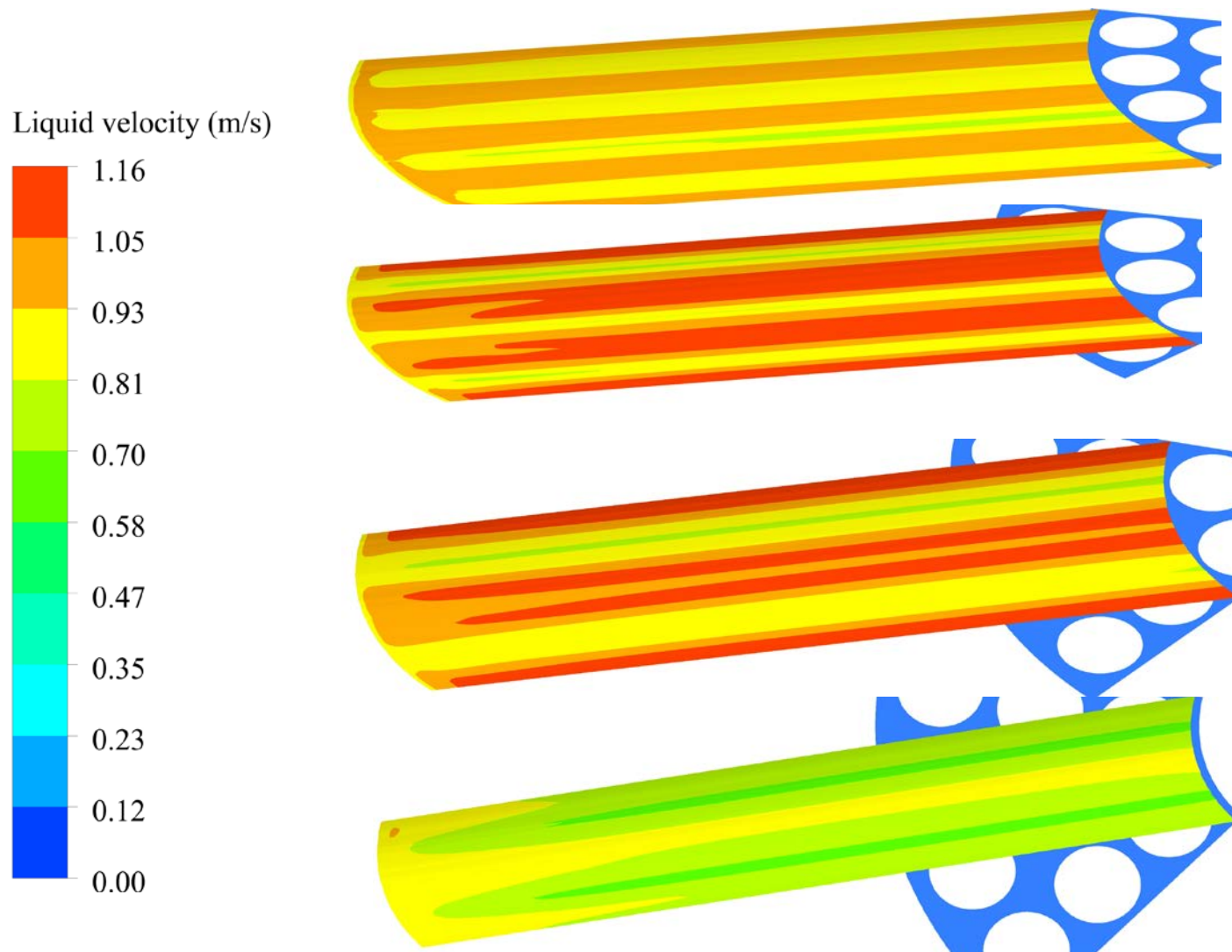
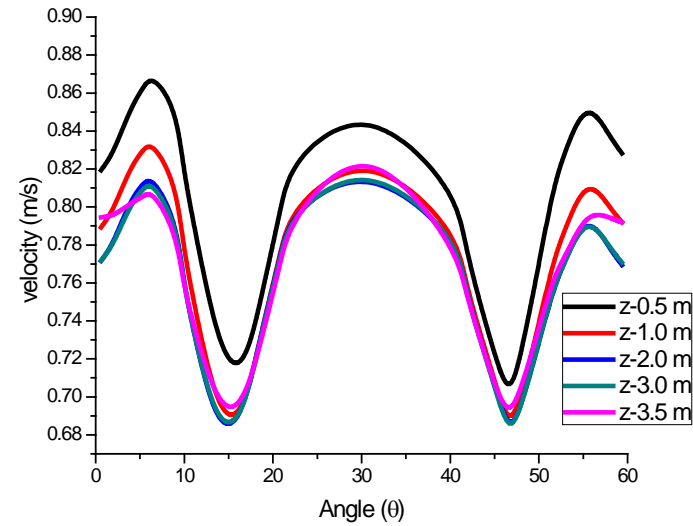
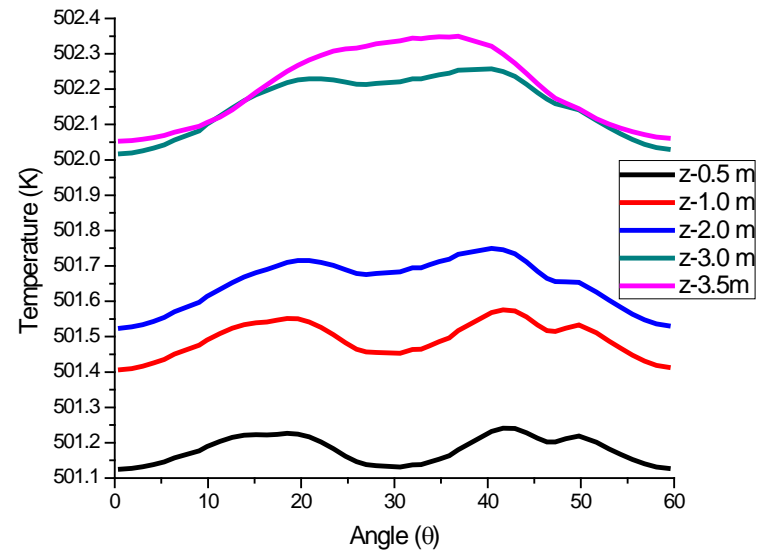
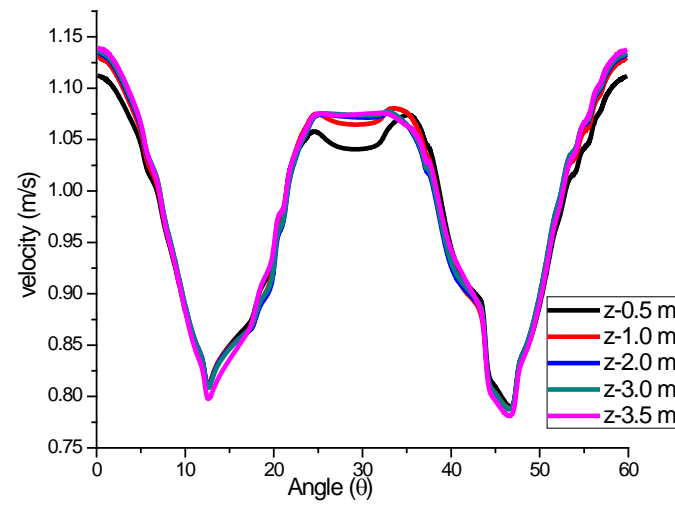
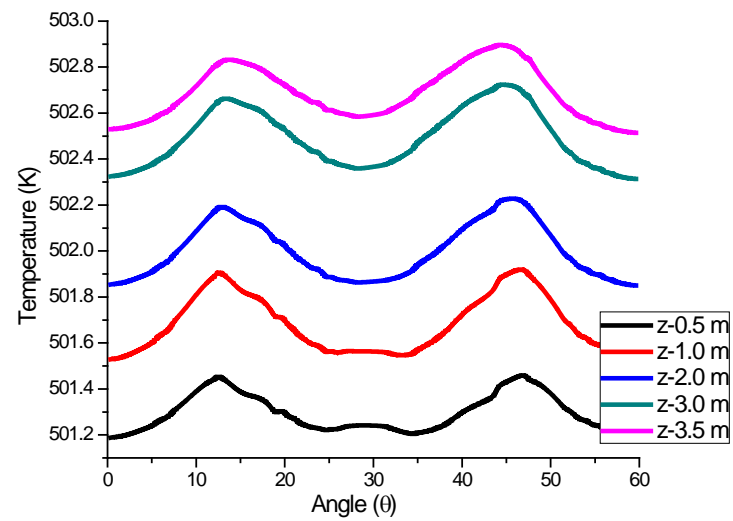


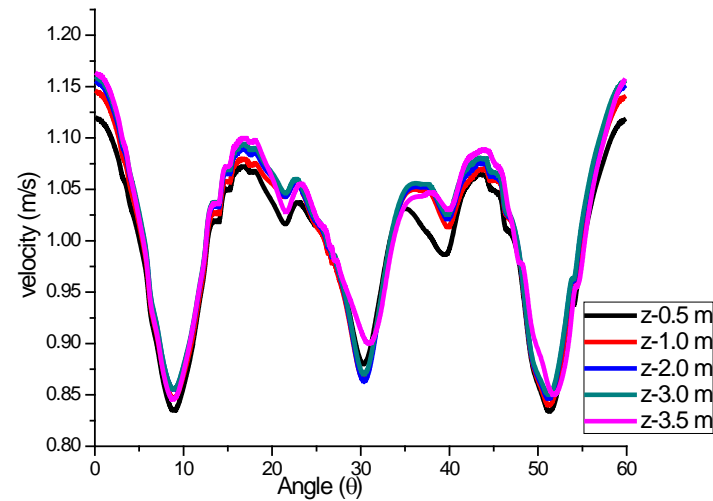
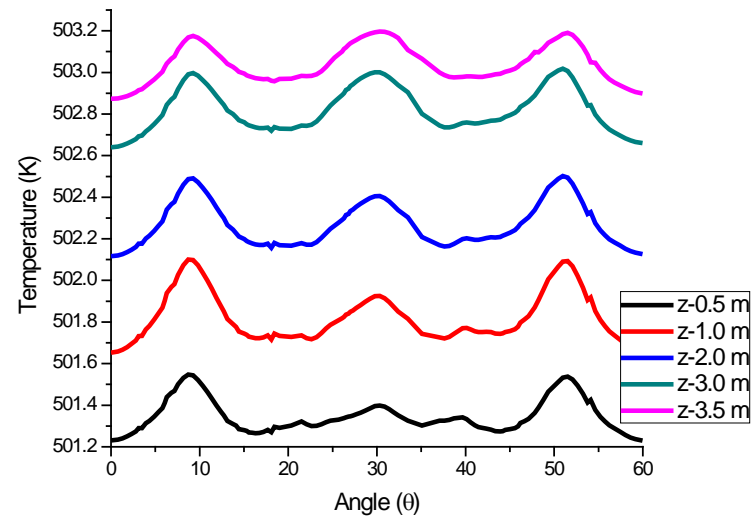
Figure-7.43 Liquid velocity distribution at various radial planes for Case#2

Plane-A

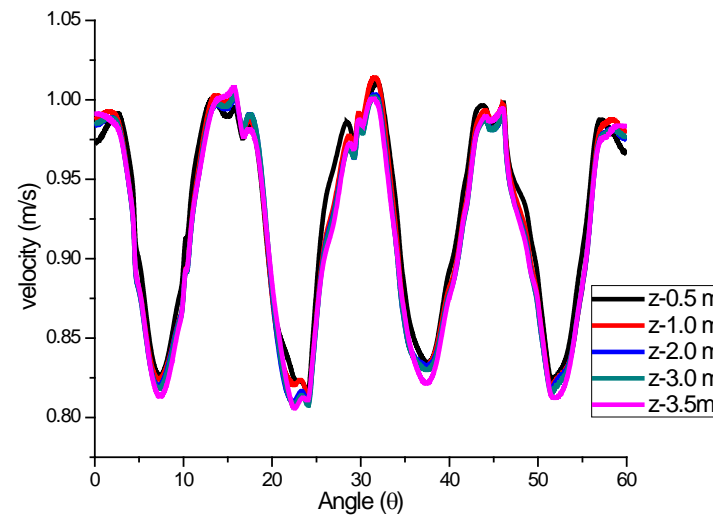
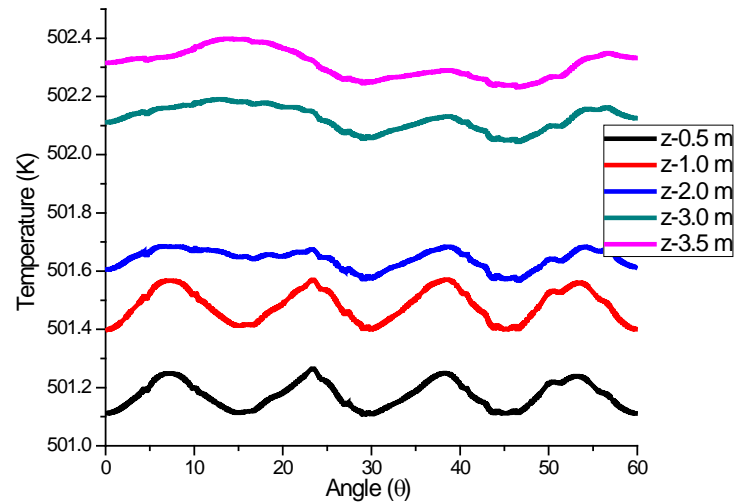


Plane-B





Plane-C



Plane-D

Figure-7.44 Angular temperature and velocity distribution on radial planes A, B, C and D for Case#2

Case#3

Comparing the initial and boundary conditions of the Case#3 with Case#2, it could be seen that the power for both the cases is almost same. On the other hand the core inlet temperature for Case#3 is substantially lower as compared to Case#2 (201°C as compared to 227°C) with same mass flow rate (0.627kg/s). Liquid density at this temperature will higher than that at Case#2. With all these considerations, it can be safely conclude that there would not be any safety issue during this phase of decay heat removal in prolonged SBO conditions.

Case#4

CFD simulations have been carried out for an instance at MHTS pressure of 0.5 MPa. The fluid of 152°C temperature enters at a uniform velocity of 0.8 m/s at the inlet. No void is observed for this case as depicted from Figure-7.45 from inlet to outlet. Figure-7.46 and 7.47 shows radial contours of liquid temperature and liquid velocity respectively from inlet to outlet. A radially symmetric temperature and flow field is observed. Prominent mixing between the sub-channels is also not observed in this case unlike the two phase flow case. Core inlet temperature for this case is 425K and maximum temperature inside the bundle is found to be 427K occurred at the outlet of the bundle. The maximum temperature (427K) of the fluid is much below saturation temperature (443K) of the fluid at local pressure, hence no boiling is observed in this case.

Axial temperature contours and 2D angular plots show that fluid temperature rises at angles of 17.5° and 45° for radial plane-A, 12.5°, 30° and 47.5° for radial plane-B, 10°, 30° and 52° for plane-C and 7.5°, 22.5°, 37.5° and 52.5° for radial plane D as seen in Figure-7.48, 7.49, 7.50 and 7.51. This is due to the presence of fuel rods at these angular locations. Similar behavior has also been observed in the former Cases.

Figure-7.48 to 7.51 also shows 2D velocity distribution from inlet to outlet at various axial as well as radial planes. Maximum velocity is observed in the outer subchannel, where maximum heat is deposited in the fluid (Figure-7.51). No hot spot is observed for this case also.



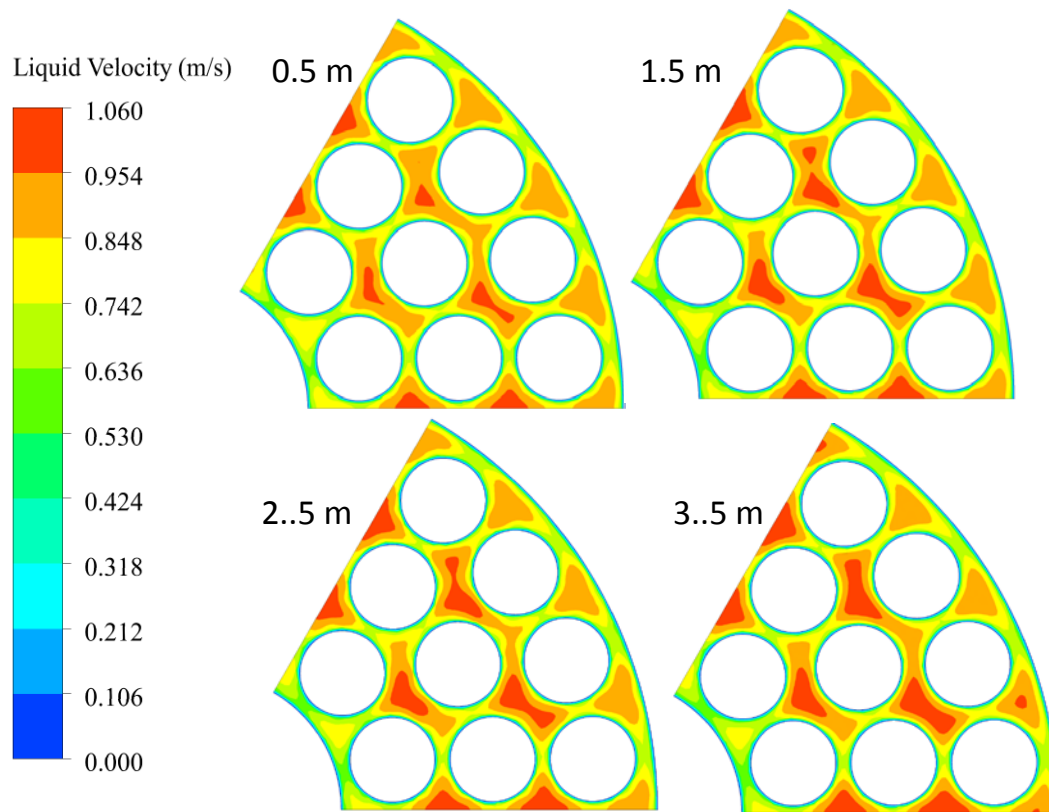


Figure-7.47 velocity distribution for liquid phase at various axial planes for case#4

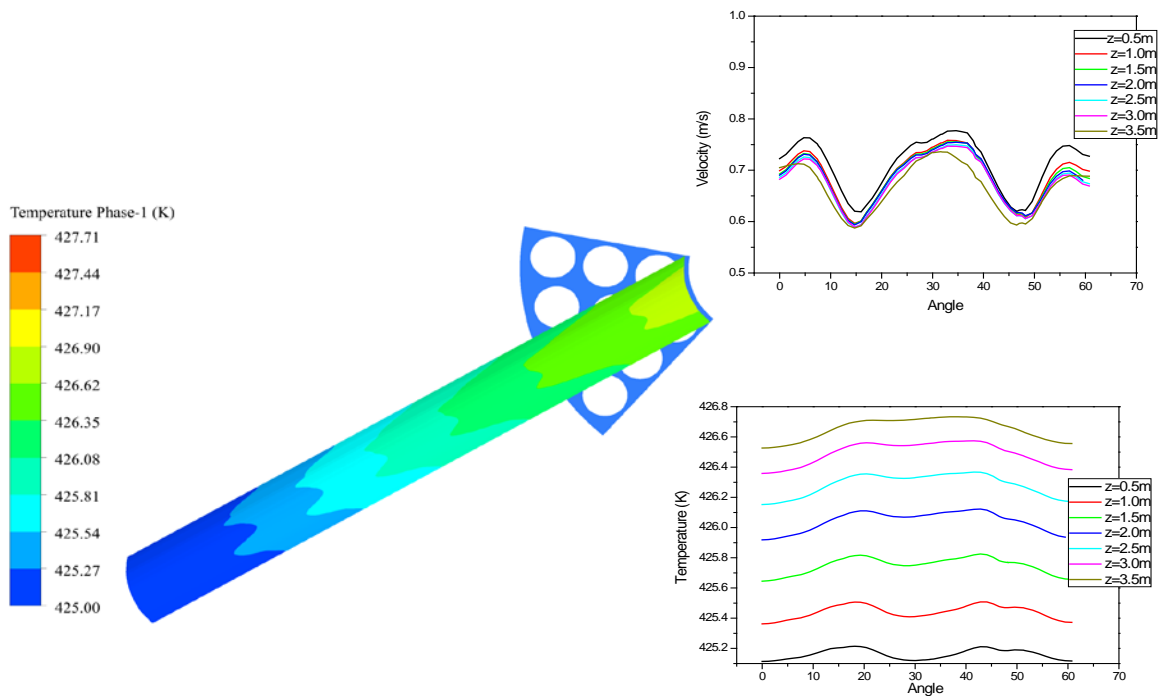


Figure-7.48 Temperature and velocity distribution for liquid phase at radial plane-A

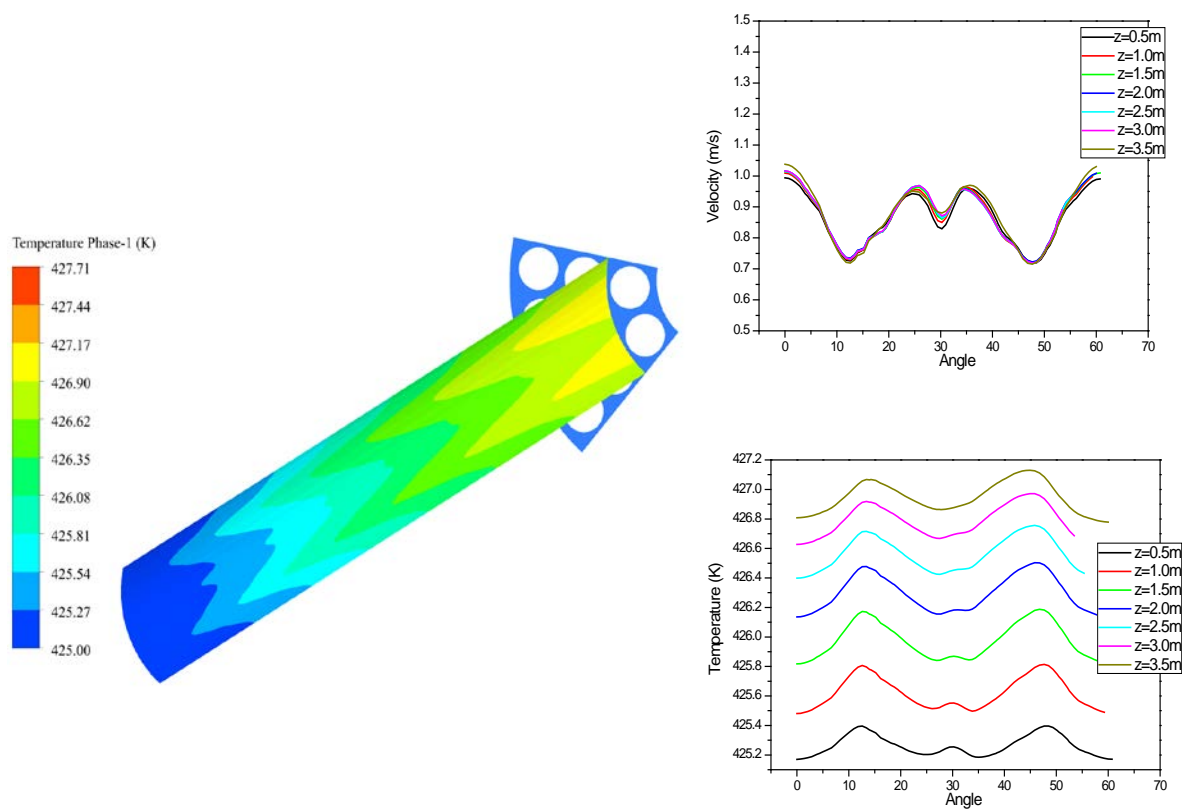


Figure-7.49 Temperature and velocity distribution for liquid phase at radial plane-B

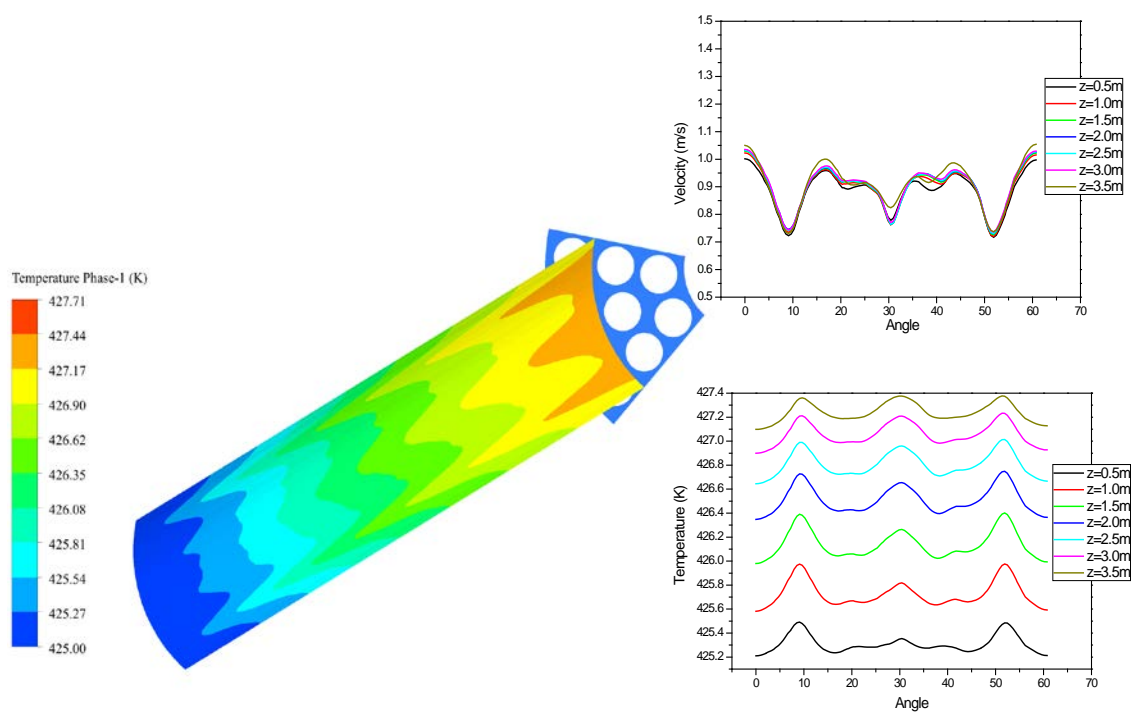


Figure-7.50 Temperature and velocity distribution for liquid phase at radial plane-C

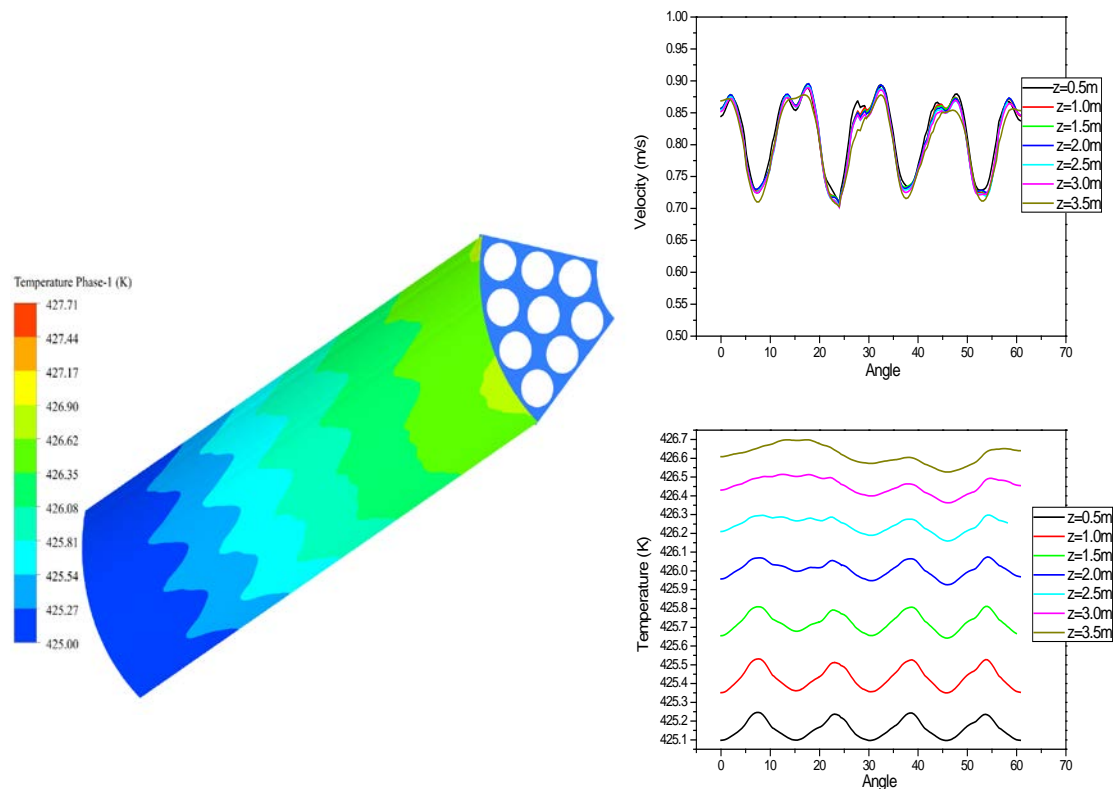


Figure-7.51 Temperature and velocity distribution for liquid phase at radial plane-D

7.5 Closure

A boiling Eulerian model is developed for estimation of the flow and void distribution inside the AHWR rod bundle during decay heat removal. The developed frame work is validated against the test data available in literature and tested for one more literature data case. Sensitivity of various closures has also been analyzed and based on that certain recommendations are evolved. Importance of various terms in conservations equations has come out as a result of this exercise. This frame work is further used to predict the flow behavior at three steady state instances (Case#1 corresponds to sub-cooled boiling regime and Case#2, and 4 as single phase heat transfer regime). Case#1 simulates the sub-cooled boiling heat transfer, in which, it is observed that the net vapor generation starts above 0.5 meter from the inlet of the bundle and void plays a key part in distribution of temperature and velocity field. The results indicate that there is no hot spot formulation inside the rod bundle, but a potential region for hot spot is identified at 1.5 m

from inlet. Maximum temperature is observed in the sub-channels located between the outer and middle rods at a plane @1.5m from inlet. CFD is able to capture the multiphase phenomena inside the rod bundle. While a fully developed flow field with radial and angular symmetries is observed for the single phase flow (Case#2 and 4) inside rod bundle.

The results of CFD are also compared with RELAP5. It is found that RELAP under predicts the void, which is also in line with Bartolomai case.

In this study, capability of the CFD is established for predictions of detailed complex flow field inside the rod bundle of a natural circulation BWR. CFD has proved itself as an indispensable tool in absence of detailed experimental data available for such complex geometries. It may be noted that it is very difficult to obtain detailed flow field inside such rod bundles where larger area of the rods are shaded by neighboring rods. Researchers in recent past are successful in extracting average information of the flow field at different axial planes. Applicability of conventional one-dimensional codes (working on hydraulic diameter principle) is limited, due to difference in flow characteristic inside rod bundles as compared to turbulent pipe flows. On the other hand, the empirical nature of the models in the Euler-Euler frame works limits its generality in extending boiling flows simulations for complex geometries. Therefore, developments of mechanistic multi-scale models are required for high fidelity simulation.

CHAPTER-8

Conclusions and Future Directions

8.1 Introduction.....	260
8.2 Major conclusions.....	260
8.2.1 Conclusions from study-1	260
<i>Establishment of decay heat removal capability by natural circulation mode of cooling during Fukushima type of scenario in integral manner</i>	<i>260</i>
8.2.2 Conclusions from study-2.....	261
<i>Demonstration of grace period of the reactor for ~7 days during SBO</i>	<i>261</i>
8.2.3 Conclusions from study-3 and 4	261
<i>Estimation of flow and void distribution inside coolant channel of AHWR during SBO conditions of heat removal</i>	<i>261</i>
8.3 Future directions	262

8.1 Introduction

The research work aimed the complete understanding of the AHWR behavior during decay heat removal in view of Fukushima accident. This includes establishment of the decay heat removal capability of reactor design during prolonged SBO. The work has been accomplished by dividing it into two parts viz.

- i. System scale simulations along with experiments in scaled test facility and
- ii. Component scale CFD for flow over Calandria tube and flow over the heated rod bundle.

Both experimental as well as numerical studies have been carried out for the undertaken research work.

8.2 Major conclusions

8.2.1 Conclusions from study-1

Establishment of decay heat removal capability by natural circulation mode of cooling during Fukushima type of scenario in integral manner

Numerical studies have been carried out for establishing the capability AHWR design against Fukushima type of accident in integral manner. Various systems of the reactor viz. MHTS, ICs, Containment (V1 and V2 volume) and GDWP are simulated for a postulated initializing event (Fukushima type) causing prolonged SBO in the reactor. Analysis shows that reactor design is capable of removing decay heat for prolonged period (more than 100 days passively) without exceeding the clad surface temperature and reactor pressure. Few new systems have been incorporated in the reactor design called as post Fukushima design modifications as a result of the outcome of this numerical study. New passive systems viz. Passive Moderator and Endshield Cooling systems (PMCS, PECS) have been incorporated in the design and integral analysis was also carried out after incorporation of PMCS and PECS.

8.2.2 Conclusions from study-2

Demonstration of grace period of the reactor for ~7 days during SBO

After incorporation of PMCS and PECS, system scale numerical studies showed that reactor is capable of removing decay heat for more than 7 days without any safety implications and hence a grace period of 7 days has been established. For experimental demonstration of the safety of the reactor a scaled test facility has been designed. Experiments have been carried out in the scaled test facility for establishing the capability of removing decay heat for more than 7 days.

Besides, 3D CFD analysis has also been carried out for assessing the integrity of the Calandria Vessel. For this purpose, 3D flow and temperature field inside the Calandria Vessel is studied for any hot pockets in the Calandria Vessel during initial period of setting up of natural circulation in the loop. The CFD model has been validated against the experimental data generated in the test facility. The CFD model showed its ability to capture the natural convection phenomena inside the vessel. A RELAP5 model for the test facility has prepared and validated against experimental data of the test facility. It has been observed that RELAP5 model predicts the gross circulation in the loop after establishment of the natural circulation in the loop. It is not able to capture the initial phase of the local convection inside the big Calandria Vessel.

8.2.3 Conclusions from study-3 and 4

Estimation of flow and void distribution inside coolant channel of AHWR during SBO conditions of heat removal

A systematic approach has been followed for estimation of the void and flow profiles inside the rod bundle for ensuring the absence of any hot spot inside the bundle while removing decay heat. An adiabatic Euler-Euler model has been developed using CFD platform Open FOAM 2.3.1. The model is able to predict the two phase flow phenomena inside a bubble

column. The model is validated against the experimental data available in literature. Experimental studies have also been carried out for the liquid velocity distributions and turbulent parameters estimation inside a bubble column with and without internals using RPT.

A boiling Eulerian frame work has been developed for estimation of the flow and void behavior inside the AHWR rod bundle during decay heat removal. The model so developed has been validated and tested for two phase flow conditions. Further, it has been used to predict the flow behavior at steady state instances during decay heat removal. The area averaged prediction of the model is also compared with the results of the RELAP5 predictions. The results of the two numerical models are found to be in good agreement within 10%. The results indicate that there is no hot spot formulation inside the rod bundle but potential locations for hot spot have been identified. Maximum void is observed in the sub-channels located at the outer periphery of the rod bundle. Temperature peaking is observed at axial locations 1.5 m from inlet of the channel.

8.3 Future directions

The main objective of the work was to establish the decay removal capability of AHWR and investigate the temperature and flow distribution inside a complex three-dimensional structure of the Calandria vessel and Fuel rod bundle.

The simulations yield the fact that although system codes can give results for overall mass flow and temperatures, it is crucial to look closely into the three dimensional temperature and flow distributions in order to ensure safety of the system. It includes the study of thermal stratification behavior of the GDWP during the decay heat removal which has substantial impact on the capacity of the GDWP water for heat removal. Thermal stratification in the pool has been studied by Verma et al (2013) and Kumar et al (2017) and performance of PDHRS has been studied by Minocha et al (2016). Verma et al (2013) and Kumar et al

(2017) suggested incorporation of shrouds for avoiding the thermal stratification and full utilization of the water pool for decay heat removal. They have optimized the shroud design and suggested to include 3 shrouds for best utilization of the pool. They have performed the separate effect tests for studying the behavior of the pool and study under integral test was not performed particularly with ICs having condensation inside the tubes. This may affect the performance of the system significantly and need to be addressed.

Besides, for big vessels like Calandria vessel, it was observed that the majority of the incoming flow impinging on the Calandria tubes is diverted outwards with low penetration into the Calandria tubes matrix. Furthermore, large fraction of this flow is recirculated within the Calandria vessel (upward flow in the tube bank and downward along the Calandria walls). The results show that during the SBO transient, the temperatures inside the Calandria are below the boiling conditions for continuous 7 days operation without any external interventions. Finally, it can be concluded that the CFD simulations provide a better understanding and estimation of the temperature and flow distribution inside a complex multidimensional system; thus giving an insight into improving the design of the system. Such an analysis is not possible by treating the flow to be one dimensional.

- i. Generally, the heat flux or temperature boundary condition of the heat source is applied directly on the fluid surface adjacent to the heater. However, in reality there exists a finite thickness of the heater wall (such as the calandria tube wall, IC tube wall, etc.) between the fluid and the heat source. In absence of these heater walls, the temperatures observed at the fluid surface become modified. This approximation generally holds true as the heater walls are made up of metals which have high thermal conductivity. The wall must be simulated in case of very fast thermal transient scenario.

- ii. Flow and heat transfer behavior in coupled natural circulation loop like in PMCS needs full 3-D CFD treatment, especially, during the flow startup in the secondary loop which is dependent on the natural circulation behavior of the primary loop. Currently, only pseudo steady state of moderator conditions are simulated, which miss the roles of the thermal inertia of the loops and their feedback.
- iii. Since, Calandria vessel is extremely critical equipment that houses all the fuel channels and control rods, changes in the design of Calandria vessel are not preferred as it is primarily governed by the reactor physics. However, the lack of penetration of flow to the centre of the lattice of the Calandria tubes can be resolved by increasing the flow in the Calandria vessel; i.e. increase in flow of the primary loop. This limitation can be overcome by increasing the elevation of the heat exchanger, or in other words, by increasing the natural circulation driving force.
- iv. A systematic sensitivity study of the various parameters in the loop needs to be carried out in order to obtain the optimized design of the system. The parameters can be the elevation between the Calandria and the heat exchanger, the piping diameter, the heat exchanger dimensions etc.
- v. While removing decay heat using ICs the distribution of the steam in the ICs tube plays an important role. It drives the performance of the ICs. The performance of ICs for any maldistribution inside the tube has been performed by Dahikar et al (2013), Ganguli et al (2013). Their study involves estimation of ICs performance in separate effect facilities and CFD simulations. However, due to strong feedback in natural circulation based systems, it needs to be studied in integral manner.

For two phase flow, adiabatic simulations inside a bubble column were carried out and further boiling and single phase conditions were simulated inside AHWR rod bundle.

- vi. Although these simulations were carried out with best suitable closures for momentum and energy as per the current understanding yet performance of these closures cannot be guaranteed. To address this issue, mechanistic model development for these closures is the need of the hour. The success of the simulations largely depends upon these models.
- vii. Currently, Euler-Euler frame work is mostly suitable and tested for bubbly flows (limited void). In view of this, development of a mathematical frame work suitable for all flow regimes is required to tackle engineering scale problems.
- viii. Turbulence modeling of two phase flow is another complexity to handle during simulations. Right now, only matured single phase turbulence models are extended for two phase flows with addition of source terms like turbulence generation in continuous phase due to presence of bubbles. Dedicated turbulence models need to be developed catering the physics of such flows.
- ix. Besides, in the existing framework for boiling flows, it is required to consider all the obstacles in the path of the fluid flow in channel that includes spacers, bottom tie plate and top tie plate. It may be noted that rod bundle are always specific for a particular reactor, with this, reliable experimental data need to be generated for bundle for ensuring safety and validation of the code, which is being taken up as future work.

.....

Finally, the research work includes a thorough study of the reactor design in experimental test facility; CFD modeling where it is feasible; and numerical modeling using system code which concludes that AHWR design is capable of removing decay heat for more than 7 days without any safety implications passively.

- *Decay heat can be safely removed for prolonged period of time (Grace period of 7 days)*
 - *Numerically established*
 - *Experimentally demonstrated*
 - *No hot spot inside Calandria Vessel and Rod Bundle during decay heat removal is seen*
-

References

- Ahmadi, G., Ma, D., "A thermo-dynamical formulation for dispersed turbulent flows-1: Basic Theory", *Int. J. Multiphase Flow* 16 (2), 323–340, 1990.
- Anklam, T. M., Miller, R.F., "Void fraction under high pressure, low flow conditions in rod bundle geometry", *Nuclear Engineering and Design* 75, 99-108, 1982.
- Antal, S. P, Lahey, R. T., and Flaherty, J.E., "Analysis of phase distribution in fully developed laminar bubbly two-phase flow". *Inte. J. of Multiphase Flow*, 635–652, 1991.
- Arai, T., Furuya, M., Kanai, T., Shirakawa, K., Nishi, Y., "Multi-dimensional void fraction measurement of transient boiling two-phase flow in a heated rod bundle", *Bulletin of the Mechanical Engineering Journal, JSME Vol.2, No.5*, 2015.
- Auton, T. R "The lift force on a spherical body in a rotational flow" *J. Fluid Mech.* 197, 241–257, 1987.
- Baek, W.P., Spinks, N.J., "CANDU Passive heat rejection using the moderator" In: *Proceedings of International Conference on New Trends in Nuclear System Thermal hydraulics*, Pisa, Italy, May 30 - June 2, 1994.
- Baglietto, E., and Ninokata, H., "A turbulence model study for simulating flow inside tight lattice rod bundles" *Nuclear Engineering and Design* 235, 773–784, 2005.
- Baroczy, C. J., "Pressure Drops for Two-Phase Potassium Flowing through a Circular Tube and an Orifice", *Chern. Eng. Prog. Symp. Ser.* 64(82): 1 2. (3), 1968.
- Bartolomei G.G. and Chanturiya V.M., "Experimental study of true void fraction whenboiling subcooled water in vertical tubes", *Therm. Eng.* 14, 123–128, 1967.
- Bartolomei, G.G., Brantov, V.G., Molochnikov, Y.S., Kharitonov, Y.V., Solodkii, V.A., Batashova, G.N., Mikhailov, V.N., "An experimental investigation of true volumetric vapor content with subcooled boiling in tubes", *Therm. Eng.* 29, 132–135, 1982.
- Basu N., Warriar G.R. and Dhir V.K., "Onset of nucleate boiling and active nucleation site density during subcooled flow boiling", *J. Heat Transfer* 124 (4) 717–728, 2002.
- Basu N., Warriar G.R. and Dhir V.K., "Wall heat flux partitioning during subcooled flow boiling: Part 1 – model development", *J. Heat Transfer-Trans. ASME* 127 (2) 131–140, 2005.
- Behzadi A., Issa R. I. and Rusche H., "Modelling of dispersed bubble and droplet flow at high phase fractions". *Chem. Eng. Sci.* 59, 759-770, 2004.

- Benjamin R.J. and Balakrishnan A.R., “Nucleation site density in pool boiling of saturated pure liquids: effect of surface micro roughness and surface and liquid physical properties”, *Exp. Therm. Fluid Sci.* 15 (1) 32–42, 1997.
- Biswas, G., Eswaran, V., “Turbulent flows: Fundamental Experiments and Modelling”, Narosa Publishing House, New Delhi, 2002.
- Boisson, N., Malin, M. R., “Numerical Prediction of Two-Phase Flow in Bubble Columns” *Int. J. for Numerical Methods in Fluids*, Vol. 23, 1289-1 3 10, 1996.
- Braz Filho, F.A., Ribeiro, G.B., Caldeira, A.D., “Prediction of subcooled flow boiling characteristics using two-fluid Eulerian CFD model”, *Nucl. Eng. Des.* 308, 30–37, 2016.
- Burns A.D., Frank T., Hamill I. and Shi J.M., “The Favre averaged drag model for turbulent dispersion in Eulerian multi-phase flows”. In: 5th International Conference on Multiphase Flow, ICMF, pp. 1–17, 2004.
- Carrica, P.M., Drew, D.A., Lahey Jr., R.T., “A polydisperse model for bubbly two phase flow around a surface ship”. *Int. J. Multiphase Flow* 25, 257–305, 1999.
- Cassanello, M., Larachi, F., Kemoun, A., Al-Dahhan, M. H., Dudukovic, M. P., “Inferring liquid chaotic dynamics in bubble columns using CARPT”, *Chemical Engineering Science*, 56, 6125- 6134, 2001.
- Chahed, J., Masbernat; L., Bellakhal, G., “k-epsilon turbulence model for bubbly flows. 2nd Int. Symposium on Two-phase flow Modelling and Experimentation”, Pisa, May 23-26, 1999.
- Chato, J. C., “Laminar Condensation inside Horizontal and Inclined Tubes”. *ASHRAE Journal*, 4, 52–60, 1961.
- Chen J. C., “Correlation for boiling heat transfer to saturated fluids in convective flow”, *IEC Process Des Dev*; 5:322-9, 1966.
- Chen, J. C., “A Correlation for Boiling Heat Transfer to Saturated Fluids in Convective Flow”, *Ind. & Eng. Chern. , Process Design and Dev.* 5:322. (4), 1966.
- Chen, J., Kemoun, A., Al-Dahhan, M. H., Dudukovic, M. P., Lee, D. J., Fan, L. S., “Comparative hydrodynamic study in a bubble column using computer-automated radioactive particle tracking (CARPT) / Computer tomography (CT) and particle image Velocimetry (PIV)”, *Chemical Engineering Science*, 54, 2199-2207, 1999.
- Cheung, S.C.P., Vahaji, S., Yeoh, G.H., Tu, J.Y., “Modeling subcooled flow boiling in vertical channels at low pressures–Part 1: Assessment of empirical correlations”, *Int. J. Heat Mass Transf.* 75, 736–753, 2014.

- Chisolm, D., "A Theoretical Bases for the Lockhart/Martinelli Correlation for Two-Phase Flow", *Int. J. Heat Mass Transfer* 10: 1 767-1 778. (3), 1 967.
- Churchill, S.W. and H. H. S. Chu. "Correlating Equations for Laminar and Turbulent Free Convection from a Horizontal Cylinder," *International Journal of Heat And Mass Transfer*, 18:1049-1053. 1975.
- Clift, R., Grace, J. R., and Weber, M. E., "Bubbles, Drops, and Particles" London: Academic Press Inc., 1978.
- Cole R., "A Photographic Study of Pool Boiling in the Region of the Critical Heat Flux", *AIChE J.* 6. 533–542. 1967.
- Colombo M. and Fairweather M., "Accuracy of Eulerian-Eulerian, two-fluid CFDboiling models of subcooled boiling flows" *Int. J. Heat Mass Transf.* 103, 28–44, 2016.
- Cui, X.Z. and Kim, K.Y., "Three-dimensional analysis of turbulent heat transfer and flow through mixing vane in a subchannel of nuclear reactor," *J. Nucl. Sci. Technol.*, 40 (10), pp. 719-724, 2012.
- Dalla Ville, J.M., "Micrometrics" Pitman Publishing Co., New York, 1948.
- Dasgupta, A., Chandraker, D. K., Nayak, A. K., Kulkarni, P.P., Chinchole, A., Rama Rao, A., "Demonstration of adequacy of passive in-bundle ECC injection of AHWR", *Annals of Nuclear Energy* 102 (2017) 11–22.
- Del Valle V. H. and Kenning D.B.R., "Subcooled flow boiling at high heat flux", *International Journal of Heat and Mass Transfer.* 28(10), 1907–1920,1985.
- Devanathan, N., Moslemian, D., Dudukovic, M. P., "Flow mapping in bubble columns using CARPT", *Chemical Engineering Science*, 45, 2285, 1990.
- Dittus, F.W., Boelter, L.M.K., "Heat transfer in automobile radiator of the tubular type" *University of California at Berkley Publ. Eng.*, 2 (1930), pp. 443-461, 1930.
- Drew D.A., "Mathematical Modeling of Two-Phase Flow", *Annual Reviews of Fluid Mechanics*, 15, 261-291, (1983).
- Frank, Th., Zwart, P. J., Krepper, E. , Prasser, H. M., and Lucas, D., "Validation of CFD models for mono and polydisperse air-water two-phase flows in pipes", *J. Nuclear Engineering & Design.* 238. 647–659, March 2008.
- Frisch, U., "Turbulence: The Legacy of A. N. Kolmogorov", Cambridge University Press, 1995
- Fritz W., "Maximum volume of vapor bubbles (Berechnung des Maximal volume von Dampfblasen)", *Phys. Z.* 36 (11) 379–384, 1935.

- Gaertner, R.F., and Westwater, J.W., “Population of active sites in nucleate boiling heat transfer”, Chem. Eng. Prog. 56 39–48. Symposium Ser. No. 30; Orig. Receipt Date: 31-DEC-61; p. Medium: X; Size, 1960.
- Gan, F., Zhu, L., “Development and application of single-phase CFD methodology for estimating flow field in rod bundles” Proceedings of the 2013 21st International Conference on Nuclear Engineering ICONE21, July 29 - August 2, Chengdu, China, 2013.
- Garnier, J., Manon, E., Cubizolles, G., “Local measurements on flow boiling of refrigerant 12 in a vertical tube”, Multiph. Sci. Technol. 13, 2001.
- Gencheva, R.V., Stefanova, A. E., Groudev, P. P., “Investigation of station blackout scenario in VVER440/v230 with RELAP5 computer code”, Nuclear Engineering and Design 295 (2015) 441–456.
- Grevskott, S., Sannaes, B.H., Dudkovic, M.P., Hjarbo, K.W., Svendsen, H.F., “Liquid circulation, bubble size distributions, and solids movement in two and three phase bubble columns”, Chem. Eng. Sci. 51 (10), 1703–1713, 1996.
- Hadamard, J., “Mouvement permanent lent d’une sphere liquid et visqueuse dans un liquide visqueux” Comptes Rendus 152, 1735, 1911.
- Hedayat, A., “Simulation and transient analyses of a complete passive heat removal system in a downward cooling pool-type material testing reactor against a complete station blackout and long-term natural convection mode using the RELAP5/3.2 code”, Nuclear Engineering and Technology 49 (2017) 953–967.
- Heindel, T. J., Ramadhyani, S., Incropera, F. P., “Assessment of turbulence models for natural convection in an enclosure”, Numerical Heat Transfer Part B 26 147–172, 1994.
- Hibiki T. and Ishii M., “Active nucleation site density in boiling systems”, Int. J. Heat Mass Transfer 46 (14) 2587–260, 2003.
- Hills, J., H., “Radial non-uniformity of velocity and voidage in a bubble column”, Transactions of Institution of Chemical Engineers, 52, 1–9, (1974).
- Holt M., Campbell, R. J., Nikitin, M. B., “Fukushima Nuclear Disaster”, Congressional Research Service, 7-5700, www.crs.gov, R41694, 2012,.
- Hosokawa, S., Tomiyama, A., Misaki, S., and Hamada, T., “Lateral Migration of Single Bubbles Due to the Presence of Wall”. ASME 2002 Joint U.S.-European Fluids Engineering Division Conference, Montreal, QC, Canada. July 14–18, 2002.
- Hou X, Sun Z and Lei W, “Capability of RELAP5 code to simulate the thermal-hydraulic characteristics of open natural circulation” Annals of Nuclear Energy 109, 2017.

- Hughmark G.A., "Mass and heat transfer from rigid spheres". *AIChE J.* 13,1967.
- IAEA-TECDOC-1624, 1-2, "Passive Safety Systems and Natural Circulation in Water Cooled Nuclear Power Plants", 2009.
- Ikeda, K., Makino, Y. and Hoshi, M., "Single phase CFD applicability for estimating fluid hot-spot locations in a 5×5 rod bundle", *Nucl. Eng. Des.*, 236 (11), pp. 1149-1154, 2006.
- Ishii M. and Zuber N., "Drag coefficient and relative velocity in bubbly, droplet or particulate flows". *AIChE J.* 25, 843–855, 1979.
- Ishii M., "Two-fluid model for two-phase flow", 2nd International Workshop on Two-phase Flow Fundamentals. RPI, Troy, NY. 1979.
- Ishii, M., Hibiki, T., "Active nucleation site density in boiling systems", *Int. J. of Heat and Mass Transfer* 46, 2587–2601, 2003.
- Ishii, M., "Thermo Fluid Dynamic Theory of Two-Phase Flow", Eyralles Press, Paris (Sci. and Medical Pub. of France, New York), 1 975.
- Ishii, M., Kataoka, I., "Similarity Analysis and Scaling Criteria for LWRs under Single Phase and Two-Phase Natural Circulation", *NUREG/CR-3267, ANL-83-32*, Argonne National Laboratory, 1983.
- Ishii, M., Revankar, S.T., Leonardi, T., Dowlati, R., Bertodano, M.L., Babelli, I., Wang, W., Pokharna, H., Ransom, V.H., Viskanta, R., Han, J.T., "The Three-Level Scaling Approach with Application to the Purdue University Multi-Dimensional Integral Test Assembly (PUMA)" *Nuclear Engg. and Design*, 186, 177-211, 1998.
- Ivey H.J., "Relationships between bubble frequency, departure diameter and rise velocity in nucleate boiling", *Int. J. Heat Mass Transfer* 10 (8) 1023–1040, 1967.
- Jain, V., Gartia, M. R., Nayak, A. K., Vijayan, P. K., Saha, D., "Study on the performance of Isolation Condenser of AHWR under degraded conditions using RELAP5/Mod3.2: Hot Shutdown", 19th National & 8th ISHMT-ASME Heat and Mass Transfer Conference, January 3 - 5, 2008, JNTU Hyderabad, India.
- Jakob, M., Fritz, W., "Versuche uber den Verdampfungsvorgang," *Forsch. Ingenieurwes*, 2, pp. 435-447, 1931.
- Johov, K., "Nucleations number during steam production, Aerodynamics and Heat Transfer in the Working Elements of the Power Facilities", Leningrad, Proceedings of CKTI, vol. 91, Russian, p. 131–135, 1969.
- Joshi, J. B., "Computational flow modelling and design of bubble column reactors", *Chemical engineering science* 56 (21-22), 5893-5933, 2001.

- Khartabil, H. F., Spink, N. J., “An Experimental Study of a Flashing-driven CANDU Moderator Cooling System”. In: Proceedings of 16th Annual Conference of Canadian Nuclear Society, Saskatoon, Canada, June 4-7, 1995.
- Kocamustafaogullari, G. and Ishii, M., “Interfacial area and nucleation site density inboiling systems” *Int. J. Heat Mass Transf.* 26, 1377–1387, 1983.
- Kolev, N.I., “How accurate can we predict nucleate boiling”, *Exp. Thermal Fluid Sci.* 10, 370–378, 1995.
- Kolmogorov, A. N., “Dissipation of energy in locally isotropic turbulence”, *Dokl. Akad. Nauk SSSR* 32, 19-21 [in Russian], 1941a.
- Kolmogorov, A. N., “The local structure of turbulence in incompressible viscous fluid for very large Reynolds numbers” *Dokl. Akad. Nauk SSSR* 30, 299-303 [in Russian], (1941 b).
- Koncar, B., Kljenak, I., Mavko, B., “Modelling of local two-phase flow parameters in upward subcooled flow boiling at low pressure”, *Int. J. Heat Mass Transf.* 47, 1499–1513, 2004.
- Koncar, B., Krepper, E., “CFD simulation of convective flow boiling of refrigerant in a vertical annulus”, *Nucl. Eng. Des.* 238, 693–706, 2008.
- Koncar, B., Krepper, E., Egorov, Y., “CFD modeling of subcooled flow boiling for nuclear engineering applications” In: International Conference Nuclear Energy for New Europe Bled, Slovenia, 2005.
- Krepper E., Koncar B. and Egorov, Y., “CFD modelling of subcooled boiling-Concept, validation and application to fuel assembly design”. *Nucl. Eng. Des.* 237, 716–731, 2007.
- Krepper, E., Rzehak, R., “CFD for subcooled flow boiling: simulation of DEBORA experiments”, *Nucl. Eng. Des.* 241, 3851–3866, 2011.
- Krepper, E., Rzehak, R., Lifante, C., and Frank, T., “CFD for subcooled flow boiling: coupling wall boiling and population balance models”, *Nuclear Engineering and Design*, vol. 255, pp. 330–346, 2013.
- Kulkarni, A.A., “Lift force on bubbles in a bubble column reactor: Experimental Analysis” *Chemical Engineering Science* 63, 1710–1723, 2008.
- Kumar, M., Nayak, A. K., Prasad, S. V., Verma, P. K., Singh, R. K., Jain, V. and Chandraker, D. K., “Experimental Demonstration of Safety of AHWR during Stagnation Channel Break Condition in an Integral Test Loop”, *ASME J of Nuclear Rad Sci* 4(2), 021005, 2018.

- Kumar, M., Chakravarty, A., Nayak, A. K., Hari Prasad, Gopika, V., “Reliability assessment of Passive Containment Cooling System of an Advanced Reactor using APSRA methodology”, *Nuclear Engineering and Design* 278 (2014) 17–28.
- Kurose, R., Misumi, R., Komori, S., “Drag and lift forces acting on a spherical bubble in a linear shear flow”, *Int. J. Multiphase Flow* 27 (7), 1247–1258, 2001.
- Kurul N. and Podowski M. Z., “On the modeling of multidimensional effects in boiling channels”, In *Proceedings of the 27th National Heat Transfer Conference*, Minneapolis, Minnesota, USA. 1991
- Lahey R.T. Jr., Drew D.A., “An Analysis of Two-Phase Flow and Heat Transfer using a Multidimensional, Multi-Field, Two-Fluid Computational Fluid Dynamics (CFD) Model”, *Japan/US Seminar on Two-Phase Flow Dynamics*, Santa Barbara, California, June 5-8, 2000.
- Lahey, R. T., “A mechanistic Subcooled boiling model,” in *Proceedings of the 6th International Heat Transfer Conference*, vol. 1, Toronto, Canada, 1978.
- Lain, S., Broder, D., Sommerfeld, M., Goz, M.F., “Modelling hydrodynamics and turbulence in a bubble column using the Euler–Lagrange procedure”, *Int. J. Multiphase Flow* 28 (8), 1381–1407, 2002.
- Larachi, F., Chaouki, J., Kennedy, G., “3-D mapping of solids flow fields in multiphase reactors with RPT”, *AIChE Journal*, 41, 439-443, 1995.
- Larachi, F., Chaouki, J., Kennedy, G., Dudukovic, M. P., “Non-Invasive Monitoring of Multiphase Flows: Chapter 11 - Radioactive Particle tracking in Multiphase Reactors: Principles and Applications”, Elsevier B.V., 335-406, 1997.
- Larachi, F., Kennedy, G., Chaouki, J., “A γ -ray detection system for 3-D particle tracking in multiphase reactors”, *Nuclear Instruments and Methods in Physics Research Section A: Accelerators, Spectrometers, Detectors and Associated Equipment*, 338, 568-576, 1994.
- Launder, B. E., G. J. Reece, and W. Rodi, “Progress in the development of a Reynolds-stress turbulence closure” *J. Fluid Mech.* 68, 537-566, 1975.
- Launder, B.E., Sharma, B.I., “Application of the Energy-Dissipation Model of Turbulence to the Calculation of Flow Near a Spinning Disc” *Letters in Heat and Mass Transfer* 1(2), 131-138, 1974.
- Lee, T.H., Park, G.C., Lee, D.J., “Local flow characteristics of subcooled boiling flow of water in a vertical concentric annulus”, *Int. J. Multiph. Flow* 28, 1351–1368, 2002.
- Legendre, D., Magnaudet, J., “The lift force on a spherical bubble in a viscous linear shear flow”, *J. Fluid Mech.* 368, 81–126, 1998.

- Lemmert M. and Chawla L.M., “Influence of flow velocity on surface boiling heat transfer coefficient”. *Heat Transf. Boil.* 237, 247, 1977.
- Levich, V.G., “Bubble motion at high Reynolds numbers”, *Zh. Eksp. Teoret. Fiz.* 19, 18–24, 1949.
- Lifante, C., Krull, B., Frank, T., Franz R., and Hampel, U., “CFD-Modeling of turbulent flows in rod bundle and comparison to experiments” *Kerntechnik*, 78, 2013.
- Liu, C.C. and Ferng, Y.M., “Numerically simulating the thermal-hydraulic characteristics within the fuel rod bundle using CFD methodology”, *Nucl. Eng. Des.*, 240, pp. 3078-3086, 2012.
- Liu, C.C., Ferng, Y.M. and Shih, C.K., “CFD evaluation of turbulence models for flow simulation of the fuel rod bundle with a spacer assembly”, *Appl. Therm. Eng.*, 40, pp. 389-396, 2012.
- Liu, W., Hidesada, T., Takase, K., Hayafune, H., Futagami, S., Kisohara, N., “Thermal-Hydraulic Experiments Under High Pressure Condition”, In: 18th International Conference on Nuclear Engineering. pp. 1101–1109, 2010.
- Lockhart, R. W., and Martinelli, R. C., “Proposed Correlation of Data for Isothermal Two-Phase, Two-Component Flow in Pipes”, *Chern. Eng Prog* 45:39. (3), 1 949.
- Lopez de Bertodano, M., “Turbulent Bubbly Flow in a Triangular Duct”. Ph.D. Thesis, Rensselaer Polytechnic Institute, Troy, New York. 1991.
- Luo, H., Svendsen, H. F., “Turbulent circulation in bubble columns from eddy viscosity distributions of single-phase pipe flow”, *Can. J. Chem. Eng.* 69, 1389-1394, 1991.
- Mangal, A., Jain V., Nayak, A. K., “Capability of the RELAP5 code to simulate natural circulation behavior in test facilities” *Progress in Nuclear Energy* 61, (2012).
- Mazzocco, T., Ambrosini, W., Kommajosyula, R. and Baglietto, E., “A reassessed model for mechanistic prediction of bubble departure and lift off diameters” *International Journal of Heat and Mass Transfer*, Vol. 117, 119-124, 2018.
- Mei, R., Klausner, J.F., Lawrence, C.J., “A note on the history force on a spherical bubble at finite Reynolds number”, *Phys. Fluids* 6 (1), 418–420, 1994.
- Menter F.R., “Two-equation eddy-viscosity turbulence models for engineering applications”. *AIAA J.* 32, 1598–1605, 1994.
- Menzel, T., Weide, T., Staudacher, O., Onken, U., “Reynold stress model for bubble column reactor”, *Ind. Engg. Chem. Res.*, 29 (1990) 988-994.

- Mikic B. B. and Rohsenow W.M., “A new correlation of pool-boiling data including the effect of heating surface characteristics”, *J. Heat Transfer* 91 (2) 245–250, 1969.
- Mimouni, S., Archambeau, F., Boucker, M., Lavieville, J., and Morel, C., “A Second-Order Turbulence Model Based on a Reynolds Stress Approach for Two-Phase Flow-Part I: Adiabatic Cases” *Science and Technology of Nuclear Installations Volume*, Article ID 792395, 2009.
- Mishima, K., Ishii, M., “Flow regime transition criteria for upward two-phase flow in vertical tubes”, *Int. J. Heat Mass Transfer* 27, 723 – 737, 1984.
- Mitsutake, T. Morooka, S., Suzuki, K., Tsunoyama, S., Yoshimura, K., “Void fraction estimation within rod bundles based on three-fluid model and comparison with X-ray CT void data” *Nuclear Engineering and Design* 120, 203-212, 1990.
- Moore, D.W., “The boundary layer on a spherical gas bubble”, *J. Fluid Mech.* 16, 161–176, 1963.
- Murallidharan, J.S., Prasad, B., Patnaik, B.S.V., Hewitt, G.F., Badalassi, V., “CFD investigation and assessment of wall heat flux partitioning model for the prediction of high pressure subcooled flow boiling”, *Int. J. Heat Mass Transf.* 103, 211–230, 2016.
- Murray, R.S., Omar, M.K., Joseph, K., Maitre Le, O.P., “Statistical analysis of small bubble dynamics in isotropic turbulence”, *Phys. Fluids* 19 (6), 065108, 2007.
- Naumann, Z., Schiller, L., “A drag coefficient correlation,” *Z. Ver Deutsch.Ing.*, vol. 77, pp. 318-323, 1935.
- Nayak, A. K., Jain, V., Gartia, M. R., Hari Prasad, Anthony, A., Bhatia, S. K., Sinha, R. K., “Reliability assessment of passive isolation condenser system of AHWR using APSRA methodology”, *Reliability Engineering & System Safety*, Volume 94, Issue 6, 2009, Pages 1064-1075.
- Nusselt, W., “Die Oberflaohen-Kondensation des Wasserdampfes *VDI Zeitung*”, 60, 541–546 & 569–575, 1916.
- OpenFOAM, “The open source CFD toolbox”, Ver.2.3.1. Paris, France: ESI Group: 2014.
- Pebles, F.N. and Garber H.J., “Studies of the motion of gas bubbles in liquids”, *Chem. Eng. Prog.* 49 (2) 88-97, 1953.
- Pope, S. B., “Turbulent Flows”, Cambridge University press, 2000.
- Ranz W.E. and Marshall W.R. Jr, “Evaporation from Drops, Part I and Part II”, *Chem. Eng. Prog.* 48(4). 173–180. April 1952.

- RELAP5 Development Team, RELAP5/Mod3.2 Code Manual, NUREG/CR-5535 Report, vols. 1-5, Idaho National Engineering Laboratory, August 1995.
- Richardson, L.F. “Weather Prediction by Numerical Process”, Cambridge University Press, 1922.
- Rohsenow, W. M., “Heat transfer with evaporation”, University of Michigan Press, 1953.
- Roy, S., Larachi, F., Al-Dahhan, M. H., Dudukovic, M. P., “Optimal design of radioactive particle tracking experiments for flow mapping in opaque multiphase reactors”, *Applied Radiation and Isotopes*, 56, 485-503, 2002.
- Rusche, H., “Computational fluid dynamics of dispersed two-phase flows at high phase fractions”, PhD Thesis, Department of Mechanical Engineering, Imperial college of Science, Technology and Medicine, London, 2002.
- Rybczynski, W., “Über die fortschreitende Bewegung einer flüssigen Kugel in einem zähen medium” *Bull. Acad. Sci. Cracovie* A40, 1911.
- Saha, P. and Zuber, N., “Point of Net Vapor Generation and Vapor Void Fraction in Subcooled Boiling,” *Proceedings of Fifth International Heat Transfer Conference*, Vol. 4, pp. 175–179, 1974.
- Sankaranarayanan, K., Sundaresan, S., “Lift force in bubbly suspensions” *Chemical Engineering Science* 57, 3521–3542, 2002.
- Sato Y. and Sekoguchi K., “Liquid velocity distribution in two-phase bubble flow”. *Int. J. Multiph. Flow* 2, 79–95, 1979.
- Sato, Y., Sadatomi, M., Sekoguchi, K., “Momentum and heat transfer in two-phase bubble flow-I. Theory”, *Int. J. Multiph. Flow* 7, 167–177, 1981.
- Sellers, J. R., Tribus, M. and Klein J. S., *Heat Transfer to Laminar Flows in a Round Tube or Flat Conduit: The Graetz Problem Extended*, *Trans. ASME*, Vol. 78, 441-451, 1956.
- Shah M. M., “A general correlation for heat transfer during subcooled boiling in pipes and annuli”. *ASHRAE Trans*;83: 202-17, 1977.
- Shah, M. M., “A New Correlation for Heat Transfer during Boiling Flow through Pipes”, *ASHRAE Trans.* 82(11):66. (4), 1976.
- Sinha, R.K., Kakkar, A., “Design and development of the AHWR—the Indian thorium fuelled innovative nuclear reactor”, *Nuclear Engg. Design* 236,683–700, 2006.
- Sokolichin, A. Eigenberger, G. Lapin, A. “Simulation of buoyancy driven bubbly flow: Established simplifications and open questions”. *AIChE J.*, 50, 24, 2004.

- Sokolichin, A., Eigenberger, G., “Gas–liquid flow in bubble columns and loop reactors: part I. Detailed modelling and numerical simulation” *Chemical Engineering Science* 49, 5735–5746, 1994.
- Stokes, G.G., “On the effect of the internal friction of fluids on the motion of pendulums”, *Trans. Cambridge Philos. Soc.* 9, Part II, 8–106, 1851.
- Takeda, T., Ohnuki, A., Kanamori, D., Ohtsu, I., “ROSA/LSTF Tests and RELAP5 Posttest Analyses for PWR Safety System Using Steam Generator Secondary-Side Depressurization against Effects of Release of Nitrogen Gas Dissolved in Accumulator Water”, Hindawi Publishing Corporation, *Science and Technology of Nuclear Installations*, Volume 2016, Article ID 7481793, 15 pages, <http://dx.doi.org/10.1155/2016/7481793>
- Tolubinsky V.I. and Kostanchuk D.M., “Vapour bubbles growth rate and heat transfer intensity at subcooled water boiling”. In: *International Heat Transfer Conference 4*, 1970.
- Tomiyaama A., “Drag lift and virtual mass forces acting on a single bubble” *Third International Symposium on Two- Phase Flow Modeling and Experimentation*, Pisa, Italy, September 22-24, 2004.
- Tomiyaama A., “Struggle with computational bubble dynamics”, *Third International Conference on Multiphase Flow*, Lyon, France. June 8–12, 1998.
- Tomiyaama, A., Tamai, H., Zun, I., Hosokawa, S., “Transverse migration of single bubbles in simple shear flows”, *Chem. Eng. Sci.* 57, 1849–1858, 2002.
- Trivedi, A. K., Allison, C., Khanna, A., Munshi, P., “AP1000 station blackout study with and without depressurization using RELAP5/SCDAPSIM”, *Nuclear Engineering and Design* 307 (2016) 299–308.
- Troshko, A.A., Hassan, Y.A., “A two-equation turbulence model of turbulent bubbly flows”, *Int. J. Multiph. Flow* 27, 1965–2000, 2001.
- Umar, E., Subki, M. H., Vecchiarlli, J., “Analysis of Passive Moderator Cooling System of CANDU-6A Reactor at Emergency Condition”, *AECL Report*, 1999.
- Umar, E., Vecchiarelli, J., “Parametric Study of Moderator Heat Exchanger for CANDU 6 Advanced Reactor” *Indonesian Journal of Nuclear Science and Technology*, 1(1), 83-98, 2000.
- Unal H.C., “Maximum bubble diameter, maximum bubble growth time and bubble growth rate during subcooled nucleate flow boiling of water up to 17.7MW/m²”, *Int. J. Heat Mass Transfer* 19, 643-649, (1976)

- Upadhyay, R. K., Roy, S., Pant, H. J., “Liquid flow patterns in rectangular air-water bubble column investigated with Radioactive Particle Tracking”, *Chemical Engineering Science*, 96, 152-164, 2013.
- Vijayan, P. K., Kamble, M. T., Nayak, A. K., Vaze, K. K., “Safety features in nuclear power plants to eliminate the need of emergency planning in public domain” *Sadhana*, Vol. 38, Part 5, pp. 925–943, 2013, Indian Academy of Sciences
- Vitankar, V. S., Joshi, J. B., “A comprehensive one-dimensional model for prediction of flow pattern in bubble columns”, *Trans. IChemE*. 80 part A, 499-512, 2002.
- Wang C.H. and Dhir V.K., “Effect of surface wettability on active nucleation site density during pool boiling of water on a vertical surface”, *J. Heat Transfer* 115 (3) 659–669, 1993.
- Warrier, G.R. and V.K. Dhir, “Heat Transfer and Wall Heat Flux Partitioning During Subcooled Flow Nucleate Boiling—A Review”, *Journal of Heat Transfer*, 128(12): p. 1243, 2006.
- Yan J., Bi Q., Liu Z., Zhu G. and Cai L., “Sub-cooled flow boiling heat transfer of water in a circular tube under high heat fluxes and high mass fluxes”, *Fusion Eng Des*;100:406-18, 2015.
- Yang, S.R. and Kim R.H., “A mathematical model of the pool boiling nucleation site density in terms of the surface characteristics”, *Int. J. Heat Mass Transfer* 31 (6) 1127–1135, 1988.
- Yang, Y. B., Devnathan, N., Dudukovic, M. P., “Liquid backmixing in bubble columns via computer automated radioactive particle tracking (CARPT)”, *Experiments in Fluids*, 16, 1-9, 1993.
- Yeoh, G. H. and Tu, J. Y., “Computational techniques for multiphase flows”, 2010 (Elsevier)
- Yun, B. J., Park, G. C., Julia, E., Hibiki, T. “Flow Structure of Subcooled Boiling Water Flow in a Subchannel of 3x3 Rod Bundles”, *Journal of Nuclear Science and Technology*, Vol. 45, No. 5, p. 402–422, 2008.
- Zeng, L.Z., Klausner, J.F., Mei, R., “A unified model for the prediction of bubble detachment diameters in boiling systems-I, Pool boiling” *Int. J. Heat Mass Transf.* 36, 2261–2270, 1993.
- Zhang, D., et al., “Numerical simulation of the dynamic flow behavior in a bubble column: a study of closures for turbulence and interface forces” *Chemical Engineering Science* 61, 7593–7608, 2006.

- Zhang, D.Z., Vander Heyden, W.B., “The effects of mesoscale structures on the macroscopic momentum equations for two-phase flows”, *Int. J. Multiphase Flow* 28 (5), 805–822, 2002.
- Zhang, K., Hou, Y. D., Tian, W. X., Fan, Y. Q., Su, G. H., Qiu S. Z., “Experimental investigations on single-phase convection and steam-water two-phase flow boiling in a vertical rod bundle” *Experimental Thermal and Fluid Science* 80, 147–154, 2017.
- Zhang, R., Cong T., Tian W., Qiu S. and Su G., “Effects of turbulence models on forced convection sub-cooled boiling in vertical pipe”. *Ann. Nucl. Energy* 80, 293–302, 2015.
- Zhou, F., Novog, D., “Mechanistic modelling of station blackout accidents for a generic 900 MW CANDU plant using the modified RELAP/SCDAPSIM/MOD3.6 code”, *Nuclear Engineering and Design* 335, 2018
- Zou, j., Li, Q., Tong, L.L., Cao, X. W., “Assessment of passive residual heat removal system cooling capacity”, *Progress in Nuclear Energy*, Volume 70, 2014, Pages 159-166.
- Zuber, N. and Findlay, J. A., Average volumetric concentration in two-phase flow systems, *J. Heat Transfer*, vol. 87, no. 4, pp. 453–468, 1965.
- Zuber, N., “Hydrodynamic aspects of boiling heat transfer (thesis), 1959.
- Zuber, N., “Nucleate boiling, The region of isolated bubbles and the similarity with natural convection”. *Int. J. Heat Mass Transf.* 6, 53–78, 1963.